LBNL-42191

ERNEST ORLANDO LAWRENCE
BERKELEY NATIONAL LABORATORY

The Growth of Thin Epitaxial Copper Films on Ruthenium (0001) and Oxygen-Precovered Ruthenium (0001) as Studied by X-ray Photoelectron Diffraction

Scott D. Ruebush

Materials Sciences Division

June 1997

Ph.D. Thesis

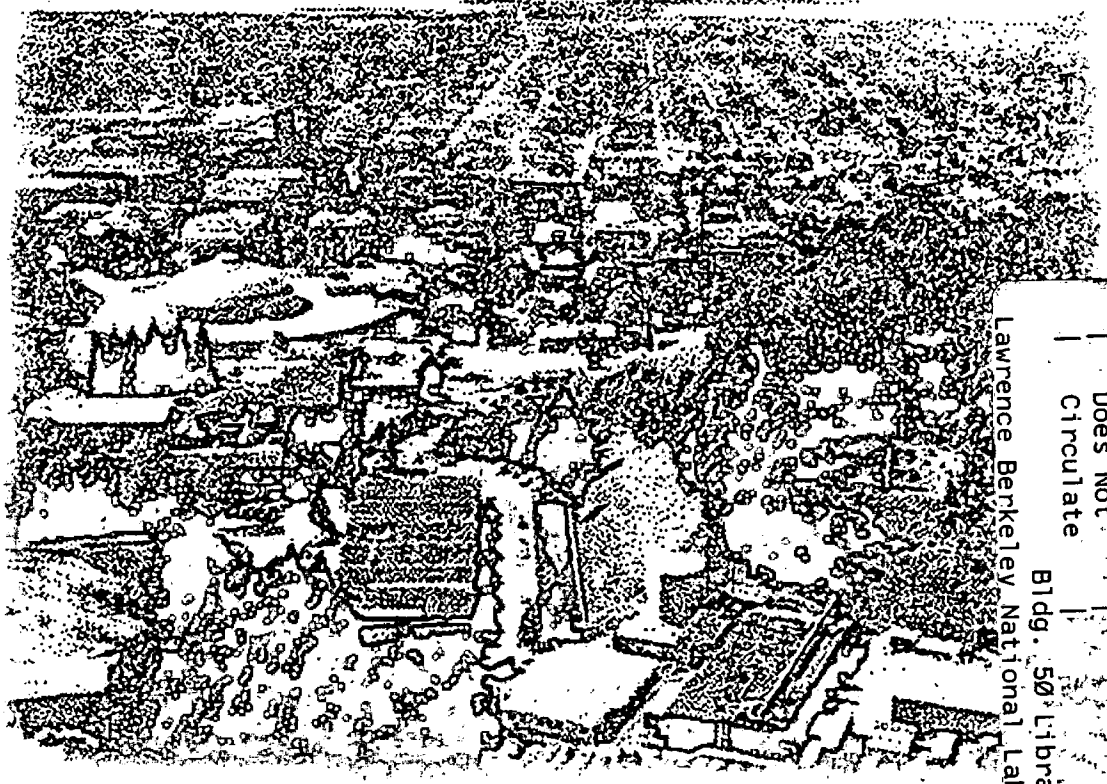

REFERENCE COPY
Does Not
Circulate
Bldg. 50 Library - Ref.
Lawrence Berkeley National Laboratory
Copy 1
LBNL-42191

DISCLAIMER

This document was prepared as an account of work sponsored by the United States Government. While this document is believed to contain correct information, neither the United States Government nor any agency thereof, nor the Regents of the University of California, nor any of their employees, makes any warranty, express or implied, or assumes any legal responsibility for the accuracy, completeness, or usefulness of any information, apparatus, product, or process disclosed, or represents that its use would not infringe privately owned rights. Reference herein to any specific commercial product, process, or service by its trade name, trademark, manufacturer, or otherwise, does not necessarily constitute or imply its endorsement, recommendation, or favoring by the United States Government or any agency thereof, or the Regents of the University of California. The views and opinions of authors expressed herein do not necessarily state or reflect those of the United States Government or any agency thereof or the Regents of the University of California.

LBNL-42191

The Growth of Thin Epitaxial Copper Films on Ruthenium (0001) and Oxygen-Precovered Ruthenium (0001) as Studied by X-ray Photoelectron Diffraction

Scott Daniel Ruebush
Ph.D. Thesis

Department of Physics
University of California, Davis

and

Materials Sciences Division
Ernest Orlando Lawrence Berkeley National Laboratory
University of California
Berkeley, CA 94720

June 1997

This work was supported by the Office of Naval Research under Contract No. N00014-90-5-1457 and N00014-94-1-0162, and by the Director, Office of Energy Research, Office of Basic Energy Sciences, Materials Sciences Division, of the U.S. Department of Energy under Contract No. DE-AC03-76SF00098.

LBNL-42191

The Growth of Thin Epitaxial Copper Films on Ruthenium (0001) and Oxygen-Precovered Ruthenium (0001) as Studied by X-ray Photoelectron Diffraction

By

Scott Daniel Ruebush
B.S. (University of Missouri, Kansas City) 1989

DISSERTATION

Submitted in partial satisfaction of the requirements for the degree of

Doctor of Philosophy

in

Physics

in the

OFFICE OF GRADUATE STUDIES

of the

UNIVERSITY OF CALIFORNIA

DAVIS

Approved:

Committee in Charge

1997

Dedication

To my parents for their support and encouragement.

Acknowledgements

I would like to thank Professor Charles S. Fadley for his support and guidance over the years. I have learned much from him. I also thank Dr. S. (Theva) Thevuthasan for his hard work in teaching me almost everything I know about the HP 5950A spectrometer, for all his help and valuable discussions, and for his friendship; Dr. Ajith P. Kaduwela for his assistance with theoretical simulations of experimental data, his stories, his friendship, and for explaining to me why one should use only alcohol soluble pens on viewgraphs; Dr. Charles Deleone, Dr. Roger King, Dr. Eric Tober, Dr. Gary Oas, Dr. Giulio Ruffini, Dr. Eric Colby, Dr. Mike Skolones, Dr. Tim Goodwin, Dr. Iad Mirshad, Dr. Ramon Ynzunza, Dr. Patrick Len, and all my other drinking buddies for friendship and occasional (er, ok frequent) sanity saving sessions at the Paragon; Dr. Michael Ashworth for teaching me some of the finer points of bujutsu; Dr. John Dykes for his constant encouragement to get done and get a real job; Dr. David Mosley for giving me a real job; Dr. Mary Anne Lee for her friendship; Mr. Britt Holbrook and Mr. Georgi Rumiansev for all the assistance with the HP electronics problems (and there were a lot of problems); Mr. Tom Anderson and Mr. Peter Dyer for assistance with precise machining; Ms. Diane Vandepeute for her assistance with purchasing items for the lab; all the other members of the UC Davis Physics Department staff for support; Ms. Margaret Louie, Ms. Jennifer Louie, and Mr. and Mrs. William Couch for friendship and emotional support; and my carpal tunnels for the sacrifices they made in this work.

Finally and most importantly, I would like to give special thanks and acknowledgment to my good friend Mr. Ryan Edward Couch who passed away in November of 1995. Ryan was a major contributor to this work, and without his assistance and support, this work would not have been completed.

This work was supported by the Office of Naval Research under Contract No. N00014-90-5-1457 and N00014-94-1-0162, and by the Director, Office of Energy Research, Office of Basic Energy Sciences, Materials Sciences Division, of the U.S. Department of Energy under Contract No. DE-AC03-76SF00098.

Abstract

In the first part of this dissertation, the variation of mean emitter depths with direction for core photoelectron emission from single crystals, including the effects of both isotropic inelastic scattering and single and multiple elastic scattering was theoretically studied. The mean emitter depth was found to vary by as much as $\pm 30\%$ with direction.

In the second part of this dissertation, x-ray photoelectron diffraction (XPD) was used to study the structure and growth mechanisms of Cu films grown on a clean and an oxygen-precovered Ru(0001) surface. Experimental Cu $2p_{3/2}$ (E_{kin} = 556 eV) and Ru 3d (E_{kin} = 1205 eV) intensities were measured for Cu coverages from submonolayer up to several monolayers (ML) on the clean Ru(0001) surface. In addition, the O 1s (E_{kin} = 958 eV) intensity was measured for Cu grown on oxygen precovered Ru(0001). These XPD intensities have been analyzed using single scattering cluster (SSC) and multiple scattering cluster (MSC) models. The first Cu layer has been found to grow pseudomorphically on the Ru(0001) surface in agreement with prior studies of the Cu/Ru(0001) system. Thus, the initial growth is layer-by-layer. For higher coverages, XPD shows that the short-range structure of the Cu films is fcc Cu(111), but with significant interlayer relaxation (compared to bulk Cu(111)) that persists up to $\geq$ 8 ML. When oxygen is preadsorbed on the Ru(0001) surface before Cu film growth (possibly to act as a surfactant promoting smoother growth), XPD shows that the first ~ 3 ML of Cu grow as 3-D islands. In addition, XPD shows that, during Cu growth, all of the oxygen "floats" on the Cu surface, in contrast to prior studies which found that 30% of the oxygen remains at the Cu/Ru interface. XPD also indicates that the oxygen is highly disordered on the Cu overlayer surface. In thicker layers with oxygen prsent, the Cu grows as Cu(111) with equal occupations of two possible domains rotated by 180° from each other. In general, this work demonstrates the considerable usefulness of XPD in studying epitaxial overlayer growth with and without surfactants present.

Table of Contents

Title Page.....i

Dedication.....ii

Acknowledgements.....iii

Abstract.....iv

List of Tables.....viii

List of Figures.....ix

List of Acronyms.....xxii

Chapter 1. **General Introduction**.....1

1.1 Background and Introduction.....1

1.2. X-ray Photoelectron Spectroscopy and Diffraction.....3

1.3. Low Energy Electron Diffraction.....8

1.4. Scanning Tunneling Microscopy.....9

1.5. Application to Mean Emission Depths and Metal-on-Metal Films.....10

References.....15

Figures.....18

Chapter 2. **Experimental Procedure and Methods of Data Analysis**.....25

2.1 Instrumentation.....25

2.2 Sample Preparation.....28

2.3 Data Treatment and Analysis.....30

2.3.1. Determination of Surface Coverages.....30

2.3.2. Normalization of Intensities.....37

2.3.3. Spline Smoothing Program.....38

2.3.4 Threefold Mapping of Data.....39

2.3.5 Global R-factor Comparison of Experiment and Theory.....39

2.3.6 Angular Broadening of Theoretical XPD Patterns.....42

2.4 Summary and Analysis of Prior STM Work on the Cu/Ru(0001) System.....44
References.....48
Tables.....50
Figures.....51
Chapter 3. **Variation of Mean Emitter Depth with Direction in Core Photoelectron Emission from Single Crystals**.....80
3.1. Introduction and Methodology.....80
3.2. Results and Discussion.....83
3.2.1 Linear Chains of Ni and Si.....83
3.2.2 A Large Cluster of Ni.....87
3.3. Conclusions.....90
References.....92
Figures.....94
Chapter 4. **X-ray Photoelectron Diffraction Study of Thin Cu Films Grown on Clean Ru(0001) and O-precovered Ru(0001)**.....102
4.1. Introduction.....103
4.2. Experiment.....106
4.3. Results and Discussion.....110
4.3.1. Cu Grown on Clean Ru(0001).....110
4.3.1.1 XPD - Experimental Results.....110
4.3.1.2 XPD - Theoretical Calculations.....116
4.3.1.2 Reference XPD results for bulk Cu(111) and comparison to theory.....131
4.3.2. Cu Grown on O-Precovered Ru(0001).....132
4.3.2.1 Experimental Results and Comparison to Cu on Clean Ru(0001).....132

4.4. Conclusion.....138

References.....140

Tables.....144

Figures.....146

Chapter 5. **Concluding Remarks**.....187

Appendix A. Spline Smoothing Program and Input files.....189

Appendix B. Gaussian Convolution Program and Input files.....214

List of Tables

Table 2.1 Parameters used in the calculation of surface coverages.....50

Table 4.1 Cu coverages as determined by QCM and XPS for Cu/Ru(0001).....144

Table 4.2 Cu coverages determined QCM and XPS for Cu/O/Ru(0001).....144

Table 4.3 Values of $d_{\perp}/d_{\parallel}$ for Cu/Ru(0001) and Cu/O/Ru(0001).....145

List of Figures

Figure 1.1 Schematic view of the three simplest topologically distinct epitaxial growth modes.....18

Figure 1.2 A schematic indication of the measurements involved in x-ray photoelectron spectroscopy (XPS) and x-ray photoelectron diffraction (XPD), scanning tunneling microscopy (STM), and low energy electron diffraction (LEED), including the complimentary information provided by each technique.....19

Figure 1.3 A typical XPS spectrum taken from a 0.6 ML Cu film on Ru(0001) with Al K α radiation as the excitation source. The core level peaks of Cu and Ru are indicated. The positions of the Cu Auger peaks are also shown although they are very weak in this spectrum. The positions of the O 1s and C 1s impurity peaks are also indicated, but were not present at a detectable level in this sample.....21

Figure 1.4 Illustration of the basic experimental geometry in the XPD experiment. The polar angle θ of electron emission is measured from the surface. The angle α between the incoming radiation and the outgoing wave vector was fixed for the experiments in this dissertation at 72°.....22

Figure 1.5 The basic process involved in photoelectron diffraction, with important physical variables indicated. Only single scattering is shown for simplicity.....23

Figure 1.6 Nickel plane-wave scattering factor amplitudes $|f(\theta_{Ni})|$ as a function of both scattering angle θ_{Ni} and the photoelectron kinetic energy (From ref. 15).....24

Figure 2.1 The Hewlett-Packard 5950A photoelectron spectrometer that has been modified so as to include LEED and automated XPD capability in a UHV environment. The major components of this system are indicated in the figure.....51

Figure 2.2 (a) Two axis sample goniometer allowing rotation in both polar and azimuthal angles so that XPD data may be taken above the nearly full 2π solid angle above the sample surface. (b) Same as (a) but top view of goniometer.....53

Figure 2.3 Custom built non-monochromatized Al $K\alpha_{1,2}$ x-ray source, yielding ~ 3x higher intensities than the original monochromatized source supplied with the HP spectrometer.....54

Figure 2.4 LEED patterns for Cu/Ru(0001) and Cu/O-precovered Ru(0001) at various coverages: (a) 1 ML Cu/Ru(0001); (b) 4ML Cu/Ru(0001) -- note the spot doubling; (c) 0.5 ML O/Ru(0001) -- two domain p(2x1) pattern; (d) 3.7 ML Cu/O/Ru(0001) prepared by annealing 6.5 ML Cu/O/Ru(0001) to 325°C briefly -- $2\sqrt{3} \times 4\sqrt{3}R30^\circ$ pattern.....56

Figure 2.5 Plot of solid angle, Ω, versus kinetic energy, E_{kin}, in the HP 5950A photoelectron spectrometer, as determined from electron trajectory calculations. This variation of Ω with E_{kin} must be taken into account in comparing any two photoelectron peaks from the spectrometer in doing quantitative analysis. This thesis made use of the standard magnification in the pre-retarding lens.....58

Figure 2.6 Compilation of experimental inelastic attenuation lengths Λ_e for various solid elements. The solid line is the so-called "universal" curve, although there is considerable variation from it for different elements and compounds.....59

Figure 2.7 Cu coverage versus polar angle for Cu grown on clean Ru(0001) as determined from the phi-averaged, spline-smoothed ratio of the Cu $2p_{3/2}$ intensity to the Ru 3d intensity.....60

Figure 2.8 O coverage versus polar angle after growing 3.7 ML Cu on O-precovered Ru(0001) as determined from the phi-averaged, spline-smoothed ratio of the O 1s to the Cu $2p_{3/2}$ intensity and of the O 1s to the Ru 3d intensity.....61

Figure 2.9 The Ru 3d XPD pattern obtained from clean Ru(0001). In (a), the raw $I(\vec{k})$ data are shown, and in (b), the normalized $\chi(\vec{k})$ data.....62

Figure 2.10 Azimuthally-averaged Cu $2p_{3/2}$ intensity, $\bar{I}(\theta)$, for 25 ML Cu/Ru(0001) and the corresponding phi-averaged, spline smoothed intensity, $I_o(\theta)$. Although not shown here, the intensity has been artificially forced to zero at a cutoff angle of -4°. This is the angle at which the sample is no longer physically exposed to the x-ray source.....63

Figure 2.11 The azimuthal Cu $2p_{3/2}$ curves obtained from 4.2 ML Cu/Ru(0001) at a polar angle of 56° as obtained from a full 360° azimuthal scan and from a partial scan over 120° that has been repeated 3 times. The anisotropy of the two sets of peaks differ from each other by about 4%, resulting in an overall threefold symmetry of the XPD pattern.....64

Figure 2.12 Illustration of the effect of angular broadening by Gaussian smoothing on the agreement between experimental and MSC theory for 1 ML Cu on Ru(0001): (a) 1 ML experiment; (b) 1 ML MSC theory without any Gaussian smoothing; (c) 1 ML MSC theory smoothed with a Gaussian of half-width at half-maximum (HWHM) = 2.4°; (d) As (c) but with HWHM = 4.8°; (e) As (c) but with HWHM = 7.1°. The XPD

patterns in (b)-(e) have all been initially broadened over a cone of 3.0° half angle via a standard multi-point calculation. The Gaussian smoothing thus represents additional angular broadening.....65

Figure 2.13 As Fig. 2.12 but for 5 ML Cu on Ru(0001): (a) 5 ML experiment; (b) 5 ML MSC theory without any Gaussian smoothing; (c) 5 ML MSC theory smoothed with a Gaussian of half-width at half-maximum (HWHM) = 2.4°; (d) As (c) but with HWHM = 4.8°; (e) As (c) but with HWHM = 7.1°.....67

Figure 2.14 As Fig. 2.12 but for experimental data from 25 ML Cu/Ru(0001) compared to six-fold symmetrized MSC theory for 5 ML Cu (assumed to be converged in depth): (a) 25 ML experiment; (b) 5 ML MSC theory without any Gaussian smoothing; (c) 5 ML MSC theory smoothed with a Gaussian of half-width at half-maximum (HWHM) = 2.4°; (d) As (c) but with HWHM = 4.8°; (e) As (c) but with HWHM = 7.1°.....70

Figure 2.15 Plot of R-factor versus HWHM of smoothing for 1 ML, 5 ML, and 25 ML Cu/Ru(0001) experimental XPD patterns compared to the corresponding theoretical XPD patterns at various degrees of smoothing.....71

Figure 2.16 STM images (from ref. 5(c)) of Cu grown on Ru(0001) for different Cu coverages: (a) 1 ML - pseudomorphic configuration (image size 77 Å x 40 Å); (b) 2 ML - uniaxially contracted from pseudomorphic configuration (image size 95 Å x 65 Å); (c) 3 ML - isotropically contracted from pseudomorpic configuration (image size 700 Å x 400 Å); (d) 4 ML - almost fully relaxed to Cu(111) and rotated azimuthally by ~ 1° from Ru(0001) to form a Moiré pattern (image size 141 Å x 86 Å; unit cell size of Moiré pattern is 49 Å x 49 Å).....72

Figure 2.17 Computer generated Moiré pattern created by placing 2D hexagonal Cu lattice on top of another 2D hexagonal Ru lattice in which the Cu lattice has a lateral lattice spacing 4.9% smaller than the underlying lattice, and has also been rotated by 0.87^{o} relative to the underlying lattice. The unit cell of the Moiré pattern is indicated by the solid lines and is approximately 49 Å x 49 Å in size. The dashed-double dotted lines indicate the atomic rows along which atoms were counted for comparison to the 4 ML STM image of Fig. 2.16(a) in arriving at the most accurate estimate of amount of contraction and rotation in the top layer. Cu is thus still 0.6% expanded from its bulk lateral lattice spacing.....74

Figure 2.18 Scanning Tunneling Microscopy (STM) image of > 5 ML Cu/Ru(0001). Image size is 3000 Å x 1500 Å.....76

Figure 2.19 Percent of layer uncovered at different Cu coverages from 1-4 ML for Cu deposited on clean Ru(0001) at room temperature. A 0% layer uncovered means the layer is completely covered or does not exist. A large % uncovered indicates the dominant coverage. Note that these curves are peaked around the nominal coverage.....78

Figure 2.20 As Fig. 2.20 but for 4.15 ML deposited at room temperature and annealed at different temperatures.....79

Figure 3.1: Mean emitter depth $\overline{Z}(\vec{k})$ including both elastic and inelastic scattering (from Eq. 1) as a function of polar angle θ for Ni 2p emission at 636 eV from vertical Ni(001) chains with an interatomic spacing of 3.52 Å. The geometry for the calculation is shown in (a), with the surface defined by the topmost atom, the emitter atom j being anywhere from the surface (j = 0) to the bottom atom of the chain (j = n-1), and emission along the chain direction corresponding to $\theta = 0^{o}$. $\overline{Z}(\vec{k})$ curves for chains of 2, 3, 4,...10 atoms in

length are shown in (b) for single scattering and in (c) for multiple scattering. The dashed curves superimposed on these results represent the reference intensities $\overline{Z}_0(\vec{k})$ including inelastic scattering, but no elastic scattering.....94

Figure 3.2 The normalized difference between forward scattering intensities $\overline{Z}(\theta = 0^0)$ and the reference intensity $\overline{Z}_0(\theta = 0^0)$ (from Eq. 4) for a vertical Ni(001) chain; filled circles represent results for single scattering and filled squares represent results for multiple scattering.....96

Figure 3.3 As Fig. 1, but for Si 2p emission at 600 eV from vertical Si(001) chains with an interatomic spacing of 5.43 Å.....97

Figure 3.4 As Fig. 1, but for Si 2p emission at 600 eV from vertical Si(111) chains with alternating interatomic spacings of 2.35 Å and 7.05 Å.....98

Figure 3.5 Normalized intensities $\chi(\vec{k})$ and mean emission depths $\overline{Z}(\vec{k})$ over the full 2π solid angle for Ni 2p emission at 636 eV from a large cluster representing a Ni(001) single crystal. (a),(b): Three-dimensional renderings of $\chi(\vec{k})$ in single scattering and multiple scattering as projected down onto the k_x-k_y plane. (c),(d) Three-dimensional renderings of $\overline{Z}(\vec{k})$ in single scattering and multiple scattering.....99

Figure 3.6 $\overline{Z}(\vec{k})$ and $\overline{Z}_0(\vec{k})$ as a function of polar angle (θ) at two different azimuthal angles (a): $\phi = 0^o$ and (b): 45°, as extracted from the results of Figs. 5(c),(d). $\overline{Z}(\vec{k})$ from multiple scattering is shown as a dotted curve, $\overline{Z}(\vec{k})$ from single scattering is shown as a solid curve, and the reference $\overline{Z}_0(\vec{k})$ is shown as a dashed curve.....100

Figure 3.7 Kikuchi-band calculations of $\overline{Z}(\theta')$ and $I(\theta')$ as a function of the deviation angle θ' from directions parallel to a given set of (hkl) planes. (a) Cu(111) planes. (b) Cu(002) planes. (c) Cu(022) planes. (d) Cu (024) planes.....101

Figure 4.1 Illustration of the basic experimental geometry in the XPD experiment. The polar angle θ of electron emission is measured from the surface. The angle α between the incoming radiation and the outgoing wave vector was fixed for the experiments in this dissertation at 72°.....146

Figure 4.2 (a)-(i) Experimental XPD patterns for Cu $2p_{3/2}$ emission (E_{kin} = 556 eV) for several Cu coverages on clean Ru(0001): (a) 0.4 ML; (b) 1.1 ML; (c) 2.0 ML; (d) 2.9 ML; (e) 4.2 ML; (f) 4.9 ML; (g) 6.5 ML; (h) 8.0 ML; (i) 25.2 ML; (j) Experimental XPD patterns for Cu $2p_{3/2}$ emission from Cu(111) (E_{kin} = 556 eV), as artificially sixfold symmetrized by adding (k) and (k) with a 180° rotation; (k) As (j), but raw data from Cu(111) with expected threefold symmetry; (k) Experimental XPD pattern for Ru 3d emission (E_{kin} = 1206 eV) from clean Ru(0001).....147

Figure 4.3 (a) Experimental relative anisotropies = $\Delta I(\theta)/I_{max}(\theta)$ versus polar angle for various Cu coverages from 0.4 ML to 25.2 ML on clean Ru(0001) and for bulk Cu(111) with sixfold symmetrization; each value is calculated over a given azimuthal scan. These anisotropies range from 5% to 30% depending on the polar angle. (b) As (a), but for various Cu coverages from 0.6 ML to 30.5 ML on Ru(0001) precovered with 0.5 ML O. The magnitudes of the anisotropies here are about half as large as those for Cu grown on clean Ru(0001). (c) As (a), but derived from multiple scattering cluster (MSC) calculations, as described in the text. Here the magnitudes of the anisotropy here are slightly larger than in experiment in (a). (d) As (b), but derived from single scattering

cluster (SSC) calculations. Here, the magnitudes are often significantly larger than in experiment in (a).....149

Figure 4.4 (a) Atomic structure of the Cu(111) surface. The white circles represent the surface layer, the gray circles represent the second layer, and the black circles represent the third layer. Various low index azimuthal directions are indicated. (b) A cross section through a $(1\bar{1}0)$ plane at ϕ = 30°, with various forward scattering direction indicated. The white circles represent atoms in the plane of the cut, and the gray circle represent atoms just behind the cut.....150

Figure 4.5 Illustration of the effect angular broadening by gaussian smoothing on comparison of experiment and MSC theory: (a) 25.2 ML Experiment; (b) 5 ML MSC theory without gaussian smoothing (but with $\pm 3^{\circ}$ angular broadening using a multi-point average); (c) 5 ML MSC theory smoothed with a gaussian of half-width at half-maximum (HWHM) = 2.4°; (d) As (c) but with HWHM = 4.8°; (e) As (c) but with HWHM = 7.1°.....152

Figure 4.6 Global sum over five normalized R-factors plotted for 5 ML SSC and 5 ML MSC calculations as compared to 25.2 ML experiment for various degrees of gaussian angular smoothing.....154

Figure 4.7 R-factor plots versus the structural parameters $Z_{Cu\text{-}Ru}$ and derived from comparing experiment to SSC and MSC calculations at various Cu coverages on

Ru(0001): (a) 1 ML; (b) 2 ML; (c) 3 ML; (d) 4 ML; (e) 5 ML; (f) 6.5 ML; (g) 8 ML; (h) 25.2 ML. Note the divergence of results for SSC and MSC, which begins at about 4 ML as multiple scattering effects become more important. The fraction of occupation of domain #1 (=f_1) was also optimized for each case ≥2 ML, and is plotted in Fig. 4.16(b).....155

Figure 4.8 Experimental and theoretical XPD patterns for Cu $2p_{3/2}$ emission: (a) 1.1 ML experiment; (b) 1 ML MSC theory; (c) 1 ML SSC theory; (d) Positions of simple forward scattering directions in the 1 ML, which in fact are not observable, (e) 2.0 ML experiment; (f) 2 ML MSC theory; (g) 2 ML SSC theory, (h) Positions of simple forward scattering directions in the 2 ML cluster.....157

Figure 4.9 Experimental and theoretical XPD patterns for Cu $2p_{3/2}$ emission: (a) 2.9 ML experiment; (b) 2 ML MSC theory (sixfold symmetrized); (c) 2 ML SSC theory (sixfold symmetrized); (d) Positions of simple forward scattering directions in the 2 ML cluster (sixfold symmetrized); (e) 4.2 ML experiment; (f) 4 ML MSC theory; (g) 4 ML SSC theory, (h) Positions of simple forward scattering directions in the threefold symmetric 4 ML cluster.....159

Figure 4.10 Experimental and theoretical XPD patterns for Cu $2p_{3/2}$ emission: (a) 4.9 ML experiment; (b) 5 ML MSC theory; (c) 5 ML SSC theory; (d) Positions of simple forward scattering directions in the 5 ML cluster; (e) 6.5 ML experiment; (f) 5 ML MSC

theory; (g) 5 ML SSC theory, (h) Positions of simple forward scattering directions in a 5 ML cluster.....161

Figure 4.11 Experimental and theoretical XPD patterns for Cu $2p_{3/2}$ emission: (a) 8.0 ML experiment; (b) 5 ML MSC theory; (c) 5 ML SSC theory; (d) Positions of simple forward scattering directions for a 5 ML cluster (sixfold symmetrized in order to simulate two domains); (e) 25.2 ML experiment; (f) 5 ML MSC theory; (g) 8 ML SSC theory, (h) Positions of forward scattering directions for a 5 ML cluster cluster (sixfold symmetrized in order to simulate two domains).....163

Figure 4.12 MSC calculations from (a) 1 ML up to (h) 8 ML for the bulk value of $d_{\perp}/d_{\parallel}$ = 0.816. Visually, the MSC calculation appears to have converged to a bulklike description by about 5 ML.....165

Figure 4.13 (a) Global R-factor comparison of MSC theory for n ML to MSC theory for 8 ML, as shown in Fig. 4.12. (b) Global R-factor comparison of 25.2 ML experiment and 8 ML experiment to n ML theory for n = 1, 2, ...,8.....167

Figure 4.14 (a) Plot of $d_{\perp}/d_{\parallel}$ = (Cu-Cu interplanar distance)/(Cu-Cu in-plane nearest-neighbor distance) versus coverage in monolayers (ML), as derived by different methods. ● = Estimate of $d_{\perp}/d_{\parallel}$ using Cu areal densities derived from a 2D Frenkel-Kontorova model by Hamilton and Foiles [4.3] combined with a constant-atomic-volume assumption; ◊ = Estimate of $d_{\perp}/d_{\parallel}$ using Cu areal densities derived from a 2D Frenkel-

Kontorova model by Hamilton and Foiles [4.3] combined elasticity theory [4.38, 4.39]; (■ = $d_{\perp}/d_{\parallel}$ determined by R-factor comparisons between experimental XPD data from various Cu coverages on Ru(0001) and MSC calculations for Cu $2p_{3/2}$ emission at a photoelectron kinetic energy of 556 eV; ◆ and □ = $d_{\perp}/d_{\parallel}$ determined by R-factor comparisons to experimental Cu $2p_{3/2}$ data obtained from Cu(111) by Naumovic et al. at photoelectron kinetic energies of 321 eV and 808 eV, respectively [4.21]; O = $d_{\perp}/d_{\parallel}$ determined by an R-factor comparison between experimental Cu $2p_{3/2}$ XPD data obtained in our laboratory from a Cu(111) single crystal and MSC calculations at an energy of 556 eV; (b) Plot of relative occupation of domain #1 versus coverage, with rotational symmetry indicated.....168

Figure 4.15 Experimental XPD patterns for Cu $2p_{3/2}$ emission at three different energies from from a Cu(111) single crystal, as compared to corresponding MSC and SSC calculations for the optimum interlayer spacing; (a)-(c) Kinetic energy equals 321 eV. (d)-(f) Energy equals 556 eV. (g)-(i) Energy equals 808 eV. The 321 eV and 808 eV data are due to Naumovic and Osterwalder [4.21].....170

Figure 4.16 Global summed R-factor plot for MSC comparisons to the Cu(111) data shown in Figs. 4.15(a), (d) and (g).....172

Figure 4.17 XPD patterns from a 0.5 ML saturation coverage of oxygen on Ru(0001) for: (a) Experimental O 1s peak; (b) MSC calculation of O 1s pattern, assuming three domains of p(2x1)-O/Ru(0001); (c) As for (b) but SSC calculation; (d) Experimental Ru 3d pattern (cf. Fig. 4.2(l)).....173

Figure 4.18 Experimental XPD patterns from Cu/O/Ru(0001) at 1.1 ML and 2.2 ML Cu coverages: (a) O 1s emission at 1.1 ML Cu coverage; (b) Cu $2p_{3/2}$ emission at 1.1 ML Cu coverage; (c) comparison to Cu $2p_{3/2}$ emission at 1.1 ML Cu coverage on clean Ru(0001); (d) O 1s emission at 2.2 ML Cu coverage; (e) Cu $2p_{3/2}$ emission at 2.2 ML Cu coverage; (f) comparison to Cu $2p_{3/2}$ emission at 2.0 ML Cu coverage on clean Ru(0001).....175

Figure 4.19 Experimental XPD patterns from Cu/O/Ru(0001) at 3.2 ML and 3.7 ML Cu coverages: (a) O 1s emission at 3.2 ML Cu coverage; (b) Cu $2p_{3/2}$ emission at 3.2 ML Cu coverage; (c) comparison to Cu $2p_{3/2}$ emission at 2.9 ML Cu coverage on clean Ru(0001); (d) O 1s emission at 3.7 ML Cu coverage; (e) Cu $2p_{3/2}$ emission at 3.7 ML Cu coverage; (f) comparison to Cu $2p_{3/2}$ emission at 4.2 ML Cu coverage on clean Ru(0001).....177

Figure 4.20 Experimental XPD patterns from Cu/O/Ru(0001) at 4.8 ML and 6.5 ML Cu coverages: (a) O 1s emission at 4.8 ML Cu coverage; (b) Cu $2p_{3/2}$ emission at 4.8 ML Cu coverage; (c) comparison to Cu $2p_{3/2}$ emission at 4.9 ML Cu coverage on clean Ru(0001); (d) O 1s emission at 6.5 ML Cu coverage; (e) Cu $2p_{3/2}$ emission at 6.5 ML Cu coverage; (f) comparison to Cu $2p_{3/2}$ emission at 6.5 ML Cu coverage on clean Ru(0001).....179

Figure 4.21 Experimental XPD patterns from Cu/O/Ru(0001) at 8.0 ML and 30.5 ML Cu coverages: (a) O 1s emission at 8.0 ML Cu coverage; (b) Cu $2p_{3/2}$ emission at 8.0 ML Cu coverage; (c) comparison to Cu $2p_{3/2}$ emission at 8.0 ML Cu coverage on clean Ru(0001); (d) O 1s emission at ~30.5 ML Cu coverage; (e) Cu $2p_{3/2}$ emission at ~30.5 ML Cu coverage; (f) comparison to Cu $2p_{3/2}$ emission at ~25.2 ML Cu coverage on clean Ru(0001).....181

Figure 4.22 Global R-factor plots comparing experiment to SSC calculations (for 1-3 ML) and MSC calculations (for all coverages) at various Cu coverages on O-precovered Ru(0001): (a) 1.1 ML; (b) 2.2 ML; (c) 3.2 ML; (d) 3.7 ML; (e) 4.8 ML; (f) 6.5 ML; (g) 8.0 ML; (h) 30.5 ML.....183

Figure 4.23 As Fig. 4.14, but for oxygen-precovered Ru(0001). (a) Plot of $d_{\perp}/d_{\parallel}$ = (Cu-Cu interplanar distance)/(Cu-Cu in-plane nearest-neighbor distance) versus coverage in monolayers (ML): ● = Estimate of $d_{\perp}/d_{\parallel}$ using Cu areal densities derived from a 2 D Frenkel-Kontorova model by Hamilton and Foiles [4.3] combined with a constant-atomic-volume assumption; ■ = $d_{\perp}/d_{\parallel}$ determined by R-factor comparisons between experimental XPD data from Cu/O/Ru(0001) and MSC calculations for Cu $2p_{3/2}$ emission at a photoelectron kinetic energy of 556 eV; ◆ and □ = $d_{\perp}/d_{\parallel}$ determined by R-factor comparisons to experimental Cu $2p_{3/2}$ data obtained from Cu(111) by Naumovic and Osterwalder at photoelectron kinetic energies of 321 eV and 808 eV, respectively [4.21]; O = $d_{\perp}/d_{\parallel}$ determined by an R-factor comparison between experimental Cu $2p_{3/2}$ XPD data obtained in our laboratory from a Cu(111) single crystal and MSC calculations at an energy of 556 eV; (b) Plot of relative occupation of domain #1 versus coverage, with rotational symmetry indicated.....185

List of Acronyms

AES	Auger electron spectroscopy
BE	binding energy
FM	Frank-van der Merwe
LEED	low energy electron diffraction
ML	monolayer
MS	multiple scattering
MSC	multiple scattering cluster
PD	photoelectron diffraction
QCM	quartz-crystal microbalance
SK	Stranski-Krastonov
SS	single scattering
SSC	single scattering cluster
STM	scanning tunneling microscopy
UHV	ultrahigh vacuum
VW	Volmer-Weber
XPD	x-ray photoelectron diffraction
XPS	x-ray photoelectron spectroscopy

Chapter 1

General Introduction

1.1 Background & Introduction

The electronic, vibrational, and magnetic properties of thin epitaxial films are particularly sensitive to the atomic structure of the film. A detailed knowledge of the structure of thin epitaxial films is thus essential to developing a fully quantitative understanding of surface phenomena and processes such as catalytic activity, oxidation and corrosion, adhesion, alloying, overlayer and nanostructure formation, and other electronic and magnetic properties of relevance to integrated circuits and magnetic storage devices. Because of the numerous technological applications of epitaxial films, epitaxy has been a subject of interest for many years [1.1-1.3]. Epitaxial films may grow by different mechanisms which depend upon many factors (e.g. the surface free energies of the substrate and overlayer, lattice misfit between the substrate and the overlayer, deposition temperature, deposition rate, presence of defects or steps on the surface, contaminants, etc.). In the simplest view, three distinct classic growth modes have been established: Franck-van der Merwe (FM) or layer-by-layer growth, Stranski-Krastanov (SK) or layer-by-layer growth followed by 3D island growth, and Volmer-Weber (VW) or 3D island growth. These three modes are shown in Fig. 1.1. Bauer was the first to point out that a very important factor in controlling the growth morphology is the balance between the surface free energy of the overlayer ,σ_o, the surface free energy of the substrate, σ_s, and the overlayer-substrate interface free energy, σ_i [1.1(a)]. In particular, one may expect: layer-by-layer growth (FM) if $\sigma_s > \sigma_o + \sigma_i$; three dimensional island growth (VW) if $\sigma_s < \sigma_o + \sigma_i$; and finally, layer-by-layer followed by 3D island growth (SK) if $\sigma_s \cong \sigma_o + \sigma_i$. The additional influence of strain on epitaxial growth modes may, however, become important when large misfits occur between the overlayer lattice geometry and the substrate lattice geometry, as is often the case in heteroepitaxy (the

ordered growth of one material on a different material). Heteroepitaxy is of special interest because the strain caused by misfit between the overlayer and the substrate lattice geometries may lead to altered growth modes in the overlayer [1.4] that do not simply fit into any of the three modes shown in Fig. 1.1 [1.5]. Finally, the growth mode of the overlayer may be influenced by the deposition temperature [1.4(d)] as well as by the presence of contaminants [1.6-1.9]. A contaminant introduced in a controlled way may even act as a "surfactant" for growth, leading to smoother layers more nearly approximating the FM mode [1.7, 1.8]. An understanding of how the various factors mentioned above influence the growth and structure of thin epitaxial overlayers is thus vital the development of new materials, magnetic storage devices, optoelectronic devices, integrated circuits, and other nanostructured materials with new and useful properties. In this dissertation, we have used x-ray photoelectron spectroscopy (XPS), x-ray photoelecton diffraction (XPD), and low energy electron diffraction (LEED) as experimental probes of the surface atomic structure of heteroepitaxial systems, considering both some fundamental theoretical and experimental questions of how XPD can be used to more accurately probe such structures, and then applying XPS, XPD, and LEED to the growth of Cu on Ru(0001) and the growth of Cu on oxygen-precovered Ru(0001), a case for which surfactant behavior has been observed. We have also made considerable use of prior STM studies [1.4] on the Cu/Ru(0001) system to aid in the interpretation of our data. A schematic illustrating the three complimentary surface techniques of PS/PD, STM, and LEED is shown in Fig. 1.2.

An important consideration in the quantitative analysis of surfaces, surface concentration profiles, and epitaxial surface structures using photoelectrons is the variation of the mean emission depth or mean sensing depth of photoelectrons due to both *inelastic* scattering events and single and multiple *elastic* scattering events. Such variations with emission direction, for example, may drastically affect quantities determined via XPS (e.g. thin film thicknesses). Therefore, in this dissertation, the

variation of mean emitter depths with direction for core photoelectron emission from single crystals, including the effects of both isotropic *inelastic* scattering and single and multiple *elastic* scattering, has been theoretically studied. The number of layers of material needed for convergence of a given calculated XPD pattern involving both of these effects has also been studied quantitatively.

1.2 X-ray Photoelectron Spectroscopy and Diffraction

X-ray photoelectron spectroscopy is a technique which has been widely used in studying surface electronic and atomic structure [1.10]. In this technique, a source of radiation is directed at a sample, and if the radiation is of high enough energy, photons can be adsorbed by the sample and cause the emission of electrons, called photoelectrons. This is the well known photoelectric effect which was first explained by Einstein [1.11]. The photoelectric equation describing the conservation of energy is

$$E_{kin} = h\upsilon - E_b^v(i), \tag{1.1}$$

where E_{kin} is the kinetic energy of the photoelectron, $h\upsilon$ is the exciting photon energy, and $E_b^v(i)$ is the binding energy of an electron emitted from the ith level as referenced to the vacuum level. A typical XPS spectrum excited with a photon energy of 1486.6 eV from a clean Ru(0001) crystal is shown in Fig. 1.3. As an alternative of the same experiment, ultraviolet photoelectron spectroscopy (UPS) uses radiation sources of about 5-40 eV and can be used to study valence levels, as for example in band structure studies [1.12]. In x-ray photoelectron spectroscopy (XPS), higher energy radiation such as Al $K\alpha_{1,2}$ x-rays are used to study the core levels. In this dissertation, Al $K\alpha_{1,2}$ x-rays from a standard x-ray tube at an energy of 1486.6 eV are used. X-ray photoelectron spectroscopy is particularly useful in the quantitative analysis of surface coverages (i.e. overlayer

thicknesses), and the theoretical model used to determine surface coverages has been described in much detail elsewhere [1.10], as well as in Chapter 2 of this dissertation.

In x-ray photoelectron diffraction (XPD), one typically measures the intensity as a function of emission angle for photoelectrons emitted from a specific core-level. Shown in Fig. 1.4 is the experimental geometry used for our measurements. The angle between photon incidence and electron exit is fixed at 72° for the experimental apparatus used in this dissertation (a specially-modified photoelectron spectrometer located in the UC Davis Department of Physics). The intensities are measured over essentially the full 2π solid angle above the sample surface by varying both the azimuthal angle, ϕ, and the polar angle, θ, where θ is measured from the sample surface. Strong angular dependent variations of the intensity, $I(\theta,\phi)$, are observed when photoelectron measurements are made above an ordered surface. These variations are caused by the scattering of photoemitted electrons from neighboring atoms and the resultant interference between the unscattered or direct photoelectron wave, ϕ_o, and the scattered photoelectron wave, ϕ_j.

For the simple case of single scattering, the intensity resulting from this interference can be written as [1.13],

$$\begin{aligned} I(\vec{k}) &= \left|\phi_o + \sum_j \phi_j\right|^2 \\ &\propto |\phi_o|^2 + \sum_j \left(\phi_o^* \phi_j + \phi_o \phi_j^*\right) + \sum_j \sum_k \phi_j \phi_k^*, \end{aligned} \tag{1.2}$$

where $\vec{k}$ is the electron wave vector and ϕ_j and ϕ_k are arbitrary scattered waves. For the simple reference case of photoelectron emission from an s subshell into an outgoing ϕ_o with p character, the individual wave components may be written more explicitly as:

$$\phi_o = \hat{\varepsilon} \cdot \hat{k} \exp\left(-L_o/2\Lambda_e\right), \tag{1.3}$$

and:

$$\phi_j = \frac{\hat{\varepsilon}\cdot\hat{r}_j}{r_j}\left|f\left(\theta_j, r_j\right)\right| W_j \exp\left(-L_j/2\Lambda_e\right)\exp\left[i\left\{kr_j\left(1-\cos\theta_j\right)+\Psi_j\left(\theta_j, r_j\right)\right\}\right], \tag{1.4}$$

where: $\hat{\varepsilon}$ is the radiation polarization direction; $\hat{k}$ is the photoelectron emission direction; $\hat{r}_j$ is a unit vector pointing from the emitting atom to the scattering atom j; r_j is the distance from the emitting atom to the scattering atom j; $\exp\left(-L_o/2\Lambda_e\right)$ and $\exp\left(-L_j/2\Lambda_e\right)$ are exponential decay factors, with L_o and L_j being equal to the total lengths for paths below the surface for ϕ_o and ϕ_j, respectively; Λ_e is the inelastic attenuation length; $f_j\left(\theta_j\right)$ is the spherical wave scattering factor involving both an amplitude $\left|f_j\left(\theta_j\right)\right|$ and a phase shift $\Psi_j\left(\theta_j\right)$ that are functions of the scattering angle θ_j; W_j is the Debye-Waller factor for the jth scatterer that allows for attenuation of interference due to vibrational effects; and $\exp\left[ikr_j\left(1-\cos\theta_j\right)\right]$ is the phase factor due to path-length related differences where $r_j\left(1-\cos\theta_j\right)$ is the path length difference between ϕ_o and ϕ_j. All structural information is contained in this last factor. The basic processes involved in such a single scattering model and various important parameters are outlined in Fig. 1.5. For emission from a subshell with initial angular momentum $l_{initial} > 0$, the above expressions in Eqns. 1.3 and 1.4 become more complex due to sums over initial and final magnetic quantum numbers $m_{initial}$ and m_{final}, as well as interference between the two final-state channels $l_{final} = l+1$ and $l-1$ that are allowed by the dipole selection rules [1.14, 1.15]. The sum on j above must be over sufficient scatterers to include all important scattering events, and so includes a finite cluster of up to ~100 atoms approximately centered on the emitter. Thus, this approach is called the single scattering cluster (SSC) model. This model can also be generalized to include a more precise description of the spherical-wave scattering involved, as well as all multiple

scattering events [1.16, 1.17], as is typically done in the theory of LEED. It is this more accurate approach, the multiple scattering cluster (MSC) model, that will be used in deriving all of the quantitative conclusions in this thesis. Two additional effects on the outgoing electron are refraction which can occur in crossing the surface potential barrier V_0 and angular smearing of the diffraction pattern due to the finite acceptance cone of the spectrometer, which in general subtends some solid angle Ω_0.

X-ray photoelectron diffraction (XPD) is particularly well suited for deriving detailed structural information about surfaces and epitaxial overlayers. First, because inelastic attenuation lengths are very small (typically about 5 to 20 Å for the photoelectron energies used in XPD [1.18]), photoelectrons from only about the top 5-10 layers of the surface are able to escape, making XPD a surface sensitive probe. In addition, XPD is a probe of the short-range structural order because the direct wave has the limiting spherical wave form, $\phi_o \propto \exp(ikr)/r$, and is also attenuated exponentially by inelastic scattering (cf. Fig. 1.5), so that the strongest scattering/interference effects are seen for atoms closest to the emitting atom. Thus, long-range order is not essential for seeing an XPD pattern, by contrast with LEED. Another important aspect of XPD is that for photoelectron kinetic energies higher than about 500 eV, the scattering amplitude $|f_j(\theta_j)|$ is highly peaked in the forward direction near $\theta_j = 0$. An illustration of this strong forward scattering and the kinetic energy dependence of atomic scattering factors for the simple, but illustrative, case of plane-wave scattering is shown in Fig. 1.6 for Ni [1.19]. It is clear from this figure that, for the energies used in this thesis (> 500 eV), strong scattering occurs only along the forward direction. This strong forward scattering effect can be used for identifying bond directions for adsorbed molecules or near-neighbor directions in epitaxial overlayers [1.10, 1.13, 1.20]. Thus, in the case of epitaxial films, the forward-scattering peaks along near-neighbor directions in the overlayer can be used to determine not only how many layers of growth one has, but also whether there have been vertical relaxations in the interlayer distances during growth (via

the polar angles at which such peaks occur). Another important aspect of XPD is that, since it samples photoelectrons from core levels which are unique to a particular atom, it is also an element specific structural probe of the local environment surrounding an atom. Thus, diffraction patterns for the overlayer element as well as the substrate element can be measured simultaneously, allowing information such as the preferred orientation of the overlayer relative to the substrate to be determined as well [1.21]. Finally, core binding shifts with chemical state or binding site can also make it possible to study the local atomic environment of atoms in different chemical states or binding sites separately [1.21-1.23], although this aspect has not been used in the work presented in this dissertation.

In order to interpret the experimental XPD data obtained in this dissertation, single scattering cluster (SSC) calculations and fully-converged multiple-scattering cluster (MSC) calculations of photoelectron diffraction patterns were performed utilizing codes developed by Freidman et al. [1.15] and by Kaduwela et al [1.17], respectively. These codes are based on the Rehr-Albers formalism [1.16] of separable Green's functions, carried out at the 2nd-order level and involving (6x6) matrix multiplications. Cluster sizes for these codes typically consisted of 80-120 atoms and incorporate all of the physical variables discussed above, including surface refraction due to the the inner potential V_0 (usually a minor effect for all but the lowest takeoff angles in XPD); the solid angle of acceptance of the photoelectron spectrometer, Ω_o; and the angular momenta and interferences between the two possible final state channels, $l+1$ and $l-1$. We also comment in Chapters 2 and 4 on a more accurate way to determine the effective angular broadening in the theoretical calculations. Details on the various parameters used in the calculations are discussed further in the appropriate chapters.

1.3 Low Energy Electron Diffraction

In 1927, Davisson and Germer [1.24] performed an experiment which first demonstrated the wave nature of the electron. This experiment provided the basis for what has today become one of the most widely used methods for surface structural analysis, low energy electron diffraction (LEED). In LEED, a focussed beam of monoenergetic electrons of energies between about 20-300 eV is directed toward a sample surface, where the electrons are then elastically scattered and diffracted. These diffracted electrons are usually observed by means of a phosphor screen held at a fixed potential and constant radial distance from the point at which the beam hits the surface. Because of the very short inelastic mean-free path, Λ_e, and the strong backscattering occuring at the low energies involved, LEED is primarily sensitive to only the top few layers of the surface, and thus it is a very surface sensitive structural probe (probably somewhat more surface sensitive than photoelectron spectroscopy at the same energy). The surface atom periodicities of the sample act as diffraction gratings, and therefore the most intense diffraction spots in a LEED pattern probe long-range two-dimensional order. The two-dimensional Bragg condition can be expressed as [1.25]:

$$\vec{k}_{\parallel}' = \vec{k}_{\parallel} + \vec{g}_{hk}\,, \tag{1.5}$$

with

$$\vec{g}_{hk} = h\vec{a}^{*} + k\vec{b}^{*}\,, \tag{1.6}$$

and,

$$\vec{a}^* = 2\pi \frac{\vec{b} \times \hat{n}}{A},\ \vec{b}^* = 2\pi \frac{\hat{n} \times \vec{a}}{A},\ A = \vec{a} \cdot \vec{b} \times \hat{n}, \tag{1.7}$$

where $\vec{a}^*$ and $\vec{b}^*$ are the primitive translation vectors of the two dimensional surface recripical lattice, $\hat{n}$ is a unit vector normal to the surface, $\vec{g}_{hk}$ is a reciprocal lattice vector, and $\vec{k}_{\|}$ and $\vec{k}_{\|}'$ are the incident and emerging wave vectors parallel to the surface, respectively. Each spot in the LEED pattern can be associated with one of the reciprical lattice vectors $\vec{g}_{hk}$ describing the periodicity of the surface.

In addition to the long range 2D periodicities at the surface, LEED can be used to determine other information such as the presence of disorder or limited long range order. Blurriness or streaking of the diffraction spots is often a sign of poor ordering over long distances. More quantitative information about the surface structure (e.g. interlayer spacings of the top surface layers) may also be determined by measuring the intensities of different diffraction spots as a function of energy (referred to as LEED I-V curves) and then comparing these curves to multiple-scattering theory for different possible atomic structures via reliability factors or R-factors [1.26] in order to determine the best estimate of the structure. In this dissertation, however, we have only used LEED for the determination of the long-range order of our surface structures. R-factors developed specifically for XPD analysis [1.20], have however been used to derive all final structural conclusions.

1.4 Scanning Tunneling Microscopy

A third important experimental technique for this dissertation is scanning tunneling microscopy (STM). Although no measurements of this type have been performed as part of this thesis, I will make frequent reference to some elegant and very detailed STM studies of the Cu/Ru system by Behm and co-workers [1.4].

STM is another very powerful and broadly used technique for studying surface atomic morphologies [1.27]. Its basic principle is to scan an atomically sharp tip over a surface at a distance of several Å from the surface atoms. If a bias voltage V_b is applied between the surface and the tip, a tunneling current develops. This tunneling current is extremely sensitive to the height of the tip above the surface, approximately following the relationship

$$I_{tunneling} \propto V_b e^{-d\bar{\phi}^{1/2}}, \tag{1.8}$$

where d is the distance between tip and surface, and

$$\bar{\phi} = \frac{1}{2}[\phi_{tip} + \phi_{sample} - |eV_b|], \tag{1.9}$$

with the two additional quantities being the work functions of tip and sample, respectively. For small bias voltages and work functions of the order of 4 eV (as for Cu), a change in d of 1 Å leads to a change in tunneling current of an order of magnitude. Thus, STM can be used to probe the surface atomic geometry, or more precisely, the surface electronic density of states that is responsible for the tunneling on a resolution scale of as high as 0.1 Å, if not better [1.27]. STM cannot directly see atomic structure below the surface layer however, and we have thus used XPD as a complement to it in our study of the Cu/Ru system.

1.4 Application to Mean Emission Depths and Metal-on-Metal Films

The ability to understand the atomic scale structure and growth modes of thin films is thus becoming increasingly more important because of the vast technological

applications of such films in, for example, the magnetic recording industry where thin film technology is used in the fabrication of both magnetic disks and magneto-resistive heads. The thicknesses of layers and the lateral feature sizes are also approaching nanometer dimensions for which atomic-scale growth control is crucial. The study of thin films is also important from the purely scientific perspective of trying to acquire a better fundamental understanding of such nanometer-scale phenomena. Thin film growth, structure, and morphology often play an important role in the other physical properties (e.g. magnetic, electronic, catalytic) of the film. Therefore, it is important not only to understand the relation between the atomic scale structure of thin films and their other physical properties, but also to clarify how the choice of substrate and growth conditions can affect the thin film growth and structure. The techniques discussed above all provide excellent tools for determining such information about thin films.

This dissertation is divided into two parts. First, the variation of the mean emitter depth with direction of photoelectrons ejected from core levels in single crytals was studied from a theoretical point of view. The combined effects of inelastic and elastic scattering and diffraction on this mean depth of emission has been considered for the first time in an ordered array of atoms. Such elastic scattering and diffraction effects are important in the quantitative characterization of surfaces, surface concentration profiles, and epitaxial surface structures using photoelectrons and Auger electrons. Second, the growth and structure of thin epitaxial Cu films on Ru(0001) were studied. As part of this work, the influence of oxygen on the growth and structure of the Cu thin films has also been investigated. For this case, the oxygen is preadsorbed on the Ru(0001) surface before Cu deposition, and its potential influence as a surfactant explored. These two parts of the dissertation are introduced in more detail below.

Part 1: Mean Emitter Depth

A crucial ingredient in accurately using XPS and XPD data is the electron inelastic attenuation length, Λ_e. Various discussions, tabulations, and calculations of this quantity appear in the literature [1.18]. Through Λ_e and the assumed exponential attenuation of elastically scattered intensity along path lengths associated with it (cf. Fig. 1.5), the well-known and much-used variation of mean emitter depth with takeoff angle arises [1.13]; that is, the mean depth in an isotropic or amorphous material is expected to go as $\Lambda_e . sin\theta_i$, where θ_i is the emission angle inside the surface and before refraction has occurred. However, the possible importance of elastic scattering in determining effective electron propagation distances and mean emitter depths has also been pointed out, in particular by Nefedov and co-workers [1.28], and more recently by others [1.29]. In theoretical simulations, Nefedov and co-workers simultaneously treated both inelastic scattering and elastic scattering in core emission from amorphous atomic arrays. This work suggested that elastic scattering could significantly alter the effective inelastic attenuation length, and with it also mean emitter depths, especially as the detection direction is varied from normal to grazing [1.28], conclusions that have been confirmed in later work [1.29]. Beyond these studies aimed at the analysis of polycrystalline or amorphous samples, photoelectron diffraction effects on peak intensities, as produced by single and multiple elastic scattering, and their resultant influence on quantitative analyses, have also been considered for both adsorbates [1.30] and multilayer single crystals [1.31]. However, there have been no attempts to look in detail at the expected variation in effective mean emission depths from single crystals with full allowance for photoelectron diffraction. This is the aim of Chapter 3 of this dissertation.

Part 2: Cu/Ru(0001) and Cu/O/Ru(0001)

The heteroepitaxial system Cu/Ru(0001) has become a model system for strained heteroepitaxial growth due to the several interesting structural transformations which

occur in the Cu overlayer as the film thickness is increased from 1 ML to 4 ML [1.4]. These structural transitions are driven by a balance between the misfit energy and the strain energy of the Cu overlayer [1.32]; the misfit is such that the fcc Cu(111) lateral lattice constant is 5.5% smaller than that of hcp Ru(0001) on which it finally grows.

Although prior scanning tunneling microscopy (STM) studies [1.4] and low energy electron diffraction (LEED) studies [1.33-1.35] have revealed much about the growth mode and misfit dislocation structures formed when Cu is deposited on Ru(0001), these studies were unable to determine whether the misfit dislocation structures thread to the Cu-Ru interface or occur only in the top Cu layer or layers. Nor does STM permit determining the vertical spacing between adjacent Cu layers. We have thus applied x-ray photoelectron diffraction (XPD) to both of these issues, finally arriving at some interesting conclusions concerning the rate at which the interlayer spacing converges to the bulk value as coverage is increased.

Recent studies have also suggested that, when oxygen is preadsorbed on the Ru(0001) surface, Cu grows layer-by-layer up to as high as 50 ML, thus qualifying oxygen as a surfactant [1.6-1.9]. These studies also found that 70-85% of the oxygen floats on top of the Cu overlayer while the rest remains at the Cu-Ru interface, and in addition that the oxygen forms a disordered overlayer. In an effort to confirm these reports, we investigated the effect of oxygen using XPD, and found that <u>all</u> of the oxygen floats on top of the Cu overlayer and that it is disordered and/or highly mobile on the Cu surface. In addition, we found that oxygen promotes multilayer or 3D island growth of Cu on Ru(0001) up to at least 3 ML coverage.

The outline of the following chapters is as follows: In Chapter 2, the experimental instrumentation is discussed, as well as various experimental procedures. In addition, discussions of various methods for processing and analyzing XPS and XPD are included. Chapter 3 is a theoretical investigation of the variation of the mean emitter

depth with direction of core photoelectrons emitted from single crystals. Chapter 4 discusses the epitaxial growth modes and interlayer relaxation of Cu grown on Ru(0001), as well as the influence of oxygen on such growth. Finally, Chapter 5 presents specific conclusions concerning mean emission depths and the Cu/Ru(0001) and Cu/O/Ru(0001) systems, as well as some suggestions about possible future directions for such studies of epitaxial growth. Also included are some appendices containing various special items developed for this dissertation, such as computer programs used for data analysis.

References:

[1.1] (a) E. Bauer, Z. Krist. **110**, 372, 395 (1958); (b) E. Bauer, Applic. Surf. Sci. **11/12**, 479 (1982).

[1.2] Epitaxial Growth A & B, J.W. Matthews, ed., (Materials Science Series, Academic Press, London, 1975).

[1.3] Ultrathin Magnetic Structures I: An Introduction to the Electronic, Magnetic and Structural Properties, J.A.C. Bland and B. Heinrich, eds., (Springer-Verlag, Berlin, 1994).

[1.4] (a) G. Potschke, J. Schroder, C. Guenther, R.Q. Hwang, and R. J. Behm, Surf. Sci. **252,** 592 (1991); (b) G.O. Potschke, and R.J. Behm, Phys. Rev. B **44,** 1442 (1991); (c) C.Guenther, J. Vrijmoeth, R.Q. Hwang, and R.J. Behm, PRL **74,** 754 (1995); (d) C. Guenther, Ph.D. Thesis, Univ. Muenchen (1994).

[1.5] R. Kern, G. Le Lay, and J.J. Metois in Current Topics in Materials Science, edited by Kaldis (North-Holland, Amsterdam, 1979) Vol. 3.

[1.6] K. Kalki, M. Schick, G. Ceballos, and K. Wandelt, Thin Solid Films **228**, 36 (1993).

[1.7] H. Wolter, M. Schmidt, and K. Wandelt, Surf. Sci., **298**, 173 (1993).

[1.8] M. Schmidt, H. Wolter, M. Nohlen, and K. Wandelt, J. Vac. Sci. Technol. A **12**, 1818 (1994).

[1.9] Y.G. Shen, D.J. O'Connor, H. van Zee, K. Wandelt, R.J. MacDonald, Thin Solid Films **263**, 72 (1995).

[1.10] C. S. Fadley in Electron Spectroscopy: Theory, Techniques, and Applications, C. R. Brundle and A. D. Baker, eds., Vol. II, Chap 1 (Academic Press, London, 1978); C. S. Fadley, Review of Angle Resolved X-ray Photoelectron Spectroscopy in Prog. in Surf. Sci., edited by S. G. Davidson (Pergamon Press, New York, 1985) Vol. 16 no. 3.

[1.11] A. Einstein, Ann. Physik **17**, 132 (1905).

[1.12] K.T. Park, M. Richards-Babb, J.S. Hess, J. Weiss, and others, Phys. Rev. B**54**, 5471 (1996); Daimon, H.; Imada, S.; Nishimoto, H.; Suga, S. J. Electron Spectrosc. and Relat. Phenom. **76**, 487 (1995).

[1.13] (a) C.S. Fadley in Synchrotron Radiation Research: Advances in Surface and Interface Science, Vol. 1, ed. by R.Z. Bachrach, (Plenum Press, New York 1992).

[1.14] C.H. Li and S.Y. Tong, Phys. Rev. Lett. **42**, 901 (1979).

[1.15] (a) D.J. Friedman and C.S. Fadley, J. Electron Spectrosc. Relat. Phenom. **48**, 689 (1990).

[1.16] J.J. Rehr and R.C. Albers, Phys. Rev. B **41**, 8139 (1990).

[1.17] (a) A.P. Kaduwela, G.S. Herman, D.J. Friedman, C.S. Fadley and J.J. Rehr, Phys. Scr. **41**, 948 (1990); (b) A.P. Kaduwela, D.J. Friedman, and C.S. Fadley, J. Electron Spectrosc. Relat. Phenom. **57**, 223 (1991).

[1.18] M.P. Seah and W.A. Dench, Surf. and Int. Anal. **1**, 2 (1979); C.J. Powell, Scanning Electron. Microsc. **4**, 1649 (1984); S. Tanuma, C.J. Powell, and D.R. Penn, Surf. and Int. Anal. **11**, 577 (1988).

[1.19] M. Sagurton, E.L. Bullock, and C.S. Fadley, Surf. Sci. **182**, 287 (1987).

[1.20] (a) R.S. Saiki, A.P. Kaduwela, M. Sagurton, J. Osterwalder, D.J. Friedman, C.S. Fadley, and C.R. Brundle, Surf. Sci. **282**, 33 (1993).

[1.21] C.S. Fadley, M.A. Van Hove, Z. Hussain, A.P. Kaduwela, J. Electron Spectrosc. and Relat. Phenom. **75**, 273 (1995).

[1.22] R.X. Ynzunza, E.D. Tober, J. Palomares, Z. Wang, Z. Hussain, A.P. Kaduwela and C.S. Fadley, to be published.

[1.23] E.D. Tober, R.X. Ynzunza, Z. Wang, J. Palomares, Z. Hussain, A.P. Kaduwela and C.S. Fadley, to be published.

[1.24] C.J. Davidson and L.H. Germer, Phys. Rev. 30, 705 (1927).

[1.25] J.B. Pendry, Low Energy Electron Diffraction, Academic Press, New York (1974); M.A. Van Hove, W.H. Weinbergand, C.-M Chan, Low Energy Electron Diffraction, Springer Verlag, Heidelberg (1986).

[1.26] M.A. Van Hove, S.Y. Tong and M.H. Elconin, Surf. Sci. **64**, 85 (1977).

[1.27] F. Ogletree and M. Salmeron, Prog. Solid St. Chem., **20**, 235 (1990).

[1.28] O.A. Baschenko and V.I. Nefedov, J. Electron Spectrosc. **17**, 405 (1979); **21**, 153 (1980); **27**, 109 (1982); O.A. Baschenko, G.V. Machavariani, and V.I. Nefedov, J. Electron Spectrosc. **34**, 304 (1984).

[1.29] A. Jablonski and J. Zemek, Phys. Rev. **B48**, 4799 (1993); V. M. Dwyer, Surf. Interface Anal. **20**, 687 (1993); W. S. M. Werner, Surf. Interface Anal. **18**, 217 (1992); W. S. M. Werner *et al.*, Surf. Interface Anal. **21**, 38 (1994); P. J. Cumpson, Surf. Interface Anal. **20**, 727 (1993); P. F. A. Alkemade *et al.*, Appl. Surf. Sci. **70/71**, 24 (1993); A. Jablonski and S. Tougaard, J. Vac. Sci. Tech. **A8**, 106 (1990); W. H. Gries and W. Werner, Surf. Interface Anal. **16**, 149 (1990); and other references contained therein.

[1.30] R.E. Connelly, C.S. Fadley, and P.J. Orders, J. Vac. Sci. Tech. **A2**, 1333 (1984).

[1.31] P. Alnot, J. Olivier, F. Wyczisk, and C.S. Fadley, J. Electron Spectrosc. **43**, 263 (1987); P. Alnot, J. Olivier, and C.S. Fadley, J. Electron Spectrosc. **49**, 159 (1989).

[1.32] J. C. Hamilton and S.M Foiles, PRL **75,** 882 (1995)

[1.33] K. Christmann, G. Ertl, and H. Shimizu, Thin Solid Films 57 (1979) 247; J. Catalysis **61,** 397 (1980).

[1.34] J.E. Houston, C.H.F. Peden, D.S. Blair, and D.W. Goodman, Surf. Sci. **167,** 427 (1986); J. E. Houston, C. H. F. Peden, and Peter J. Feibelman, PRL **56,** 375 (1986); D. G. O'Neill and, J.E. Houston, Phys. Rev. B **42,** 2792 (1990)

[1.35] C. Park, E. Bauer, and H. Poppa, Surf. Sci. **187,** 86 (1987).

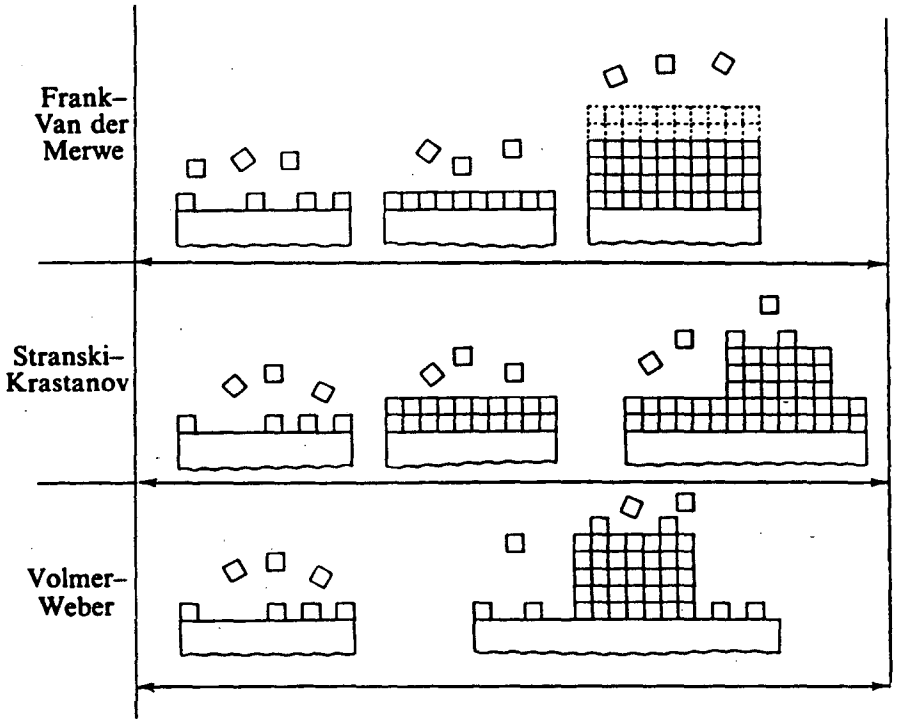

Fig. 1.1 Schematic view of the three simplest topologically distinct epitaxial growth modes (From ref. 1.5).

Fig. 1.2 A schematic indication of the measurements involved in x-ray photoelectron spectroscopy (XPS) and x-ray photoelectron diffraction (XPD), scanning tunneling microscopy (STM), and low energy electron diffraction (LEED), including the complementary information provided by each technique.

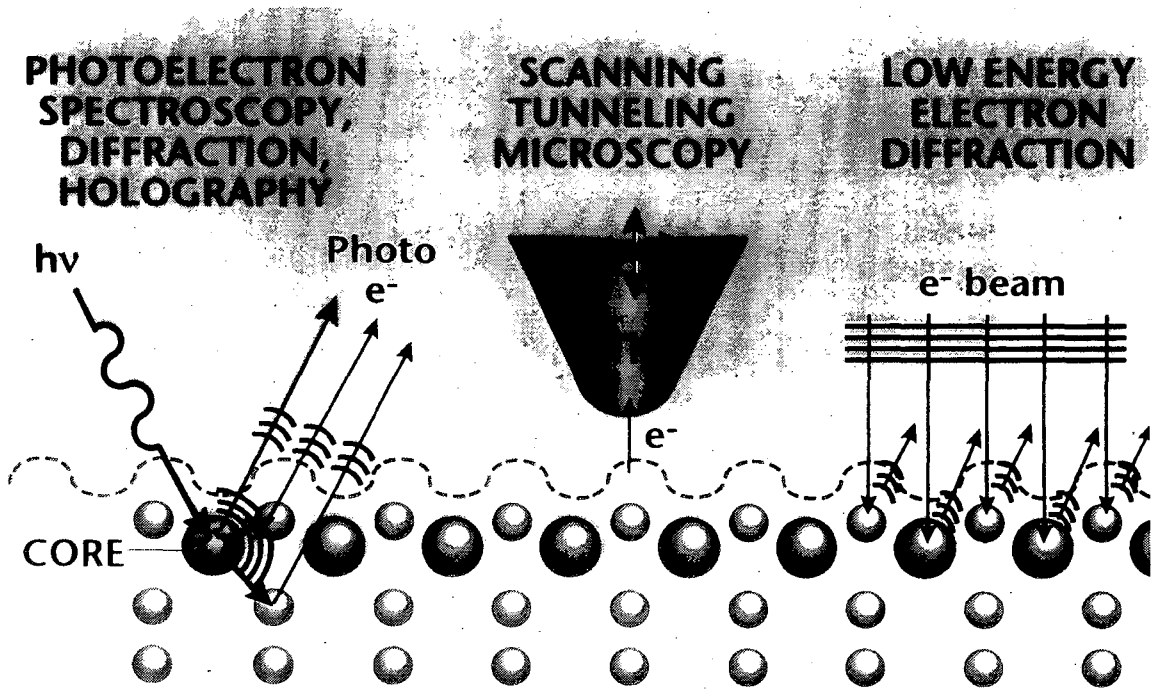

-Short-range order	-Short- and long-range order & disorder	-Long-range order
-Atom/state specific	-Not atom specific	-Not atom specific
-First few layers	-Surface contours (D.O.S.) only	-First few layers

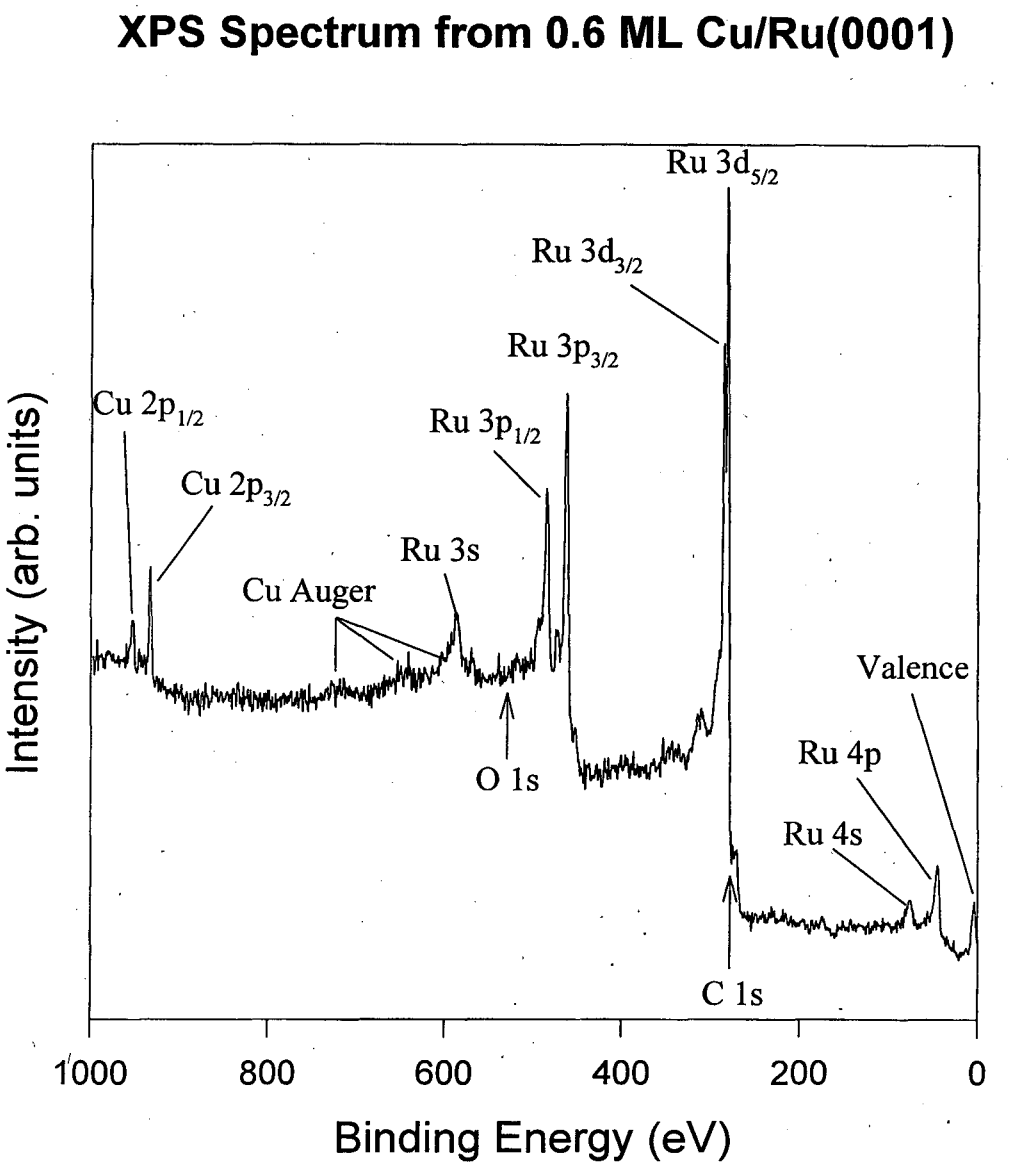

Fig. 1.3 A typical XPS spectrum taken from a 0.6 ML Cu film on Ru(0001) with Al Kα radiation as the excitation source. The core level peaks of Cu and Ru are indicated. The positions of the Cu Auger peaks are also shown although they are very weak in this spectrum. The positions of the O 1s and C 1s impurity peaks are also indicated, but were not present at a detectable level in this sample.

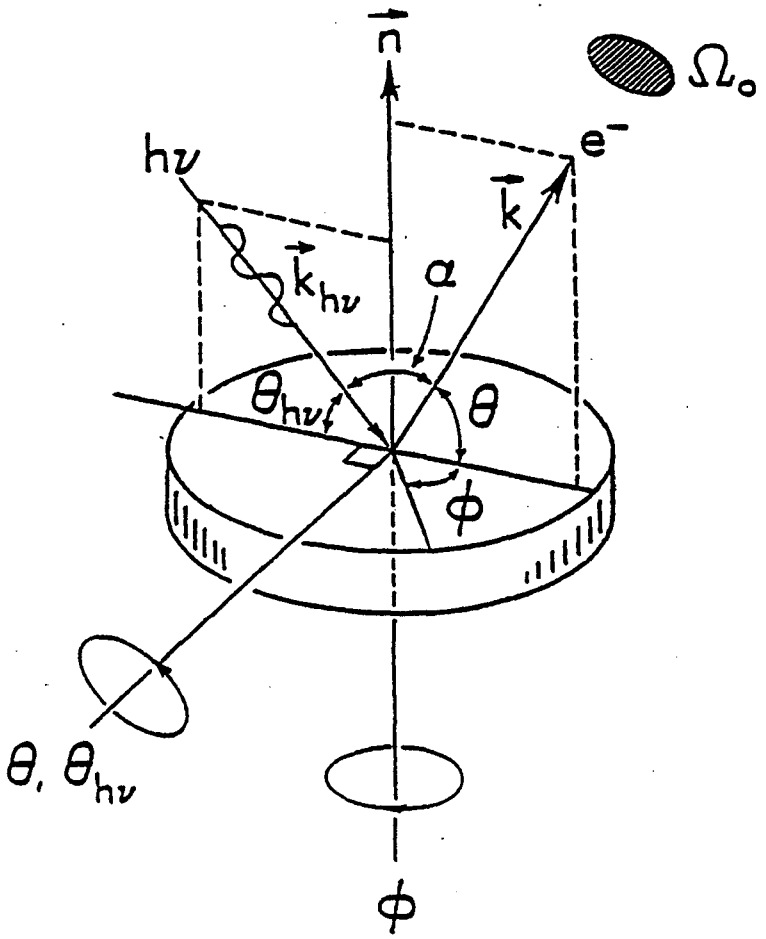

Fig. 1.4 Illustration of the basic experimental geometry in the XPD experiment. The polar angle θ of electron emission is measured from the surface. The angle α between the incoming radiation and the outgoing wave vector was fixed for the experiments in this dissertation at 72°.

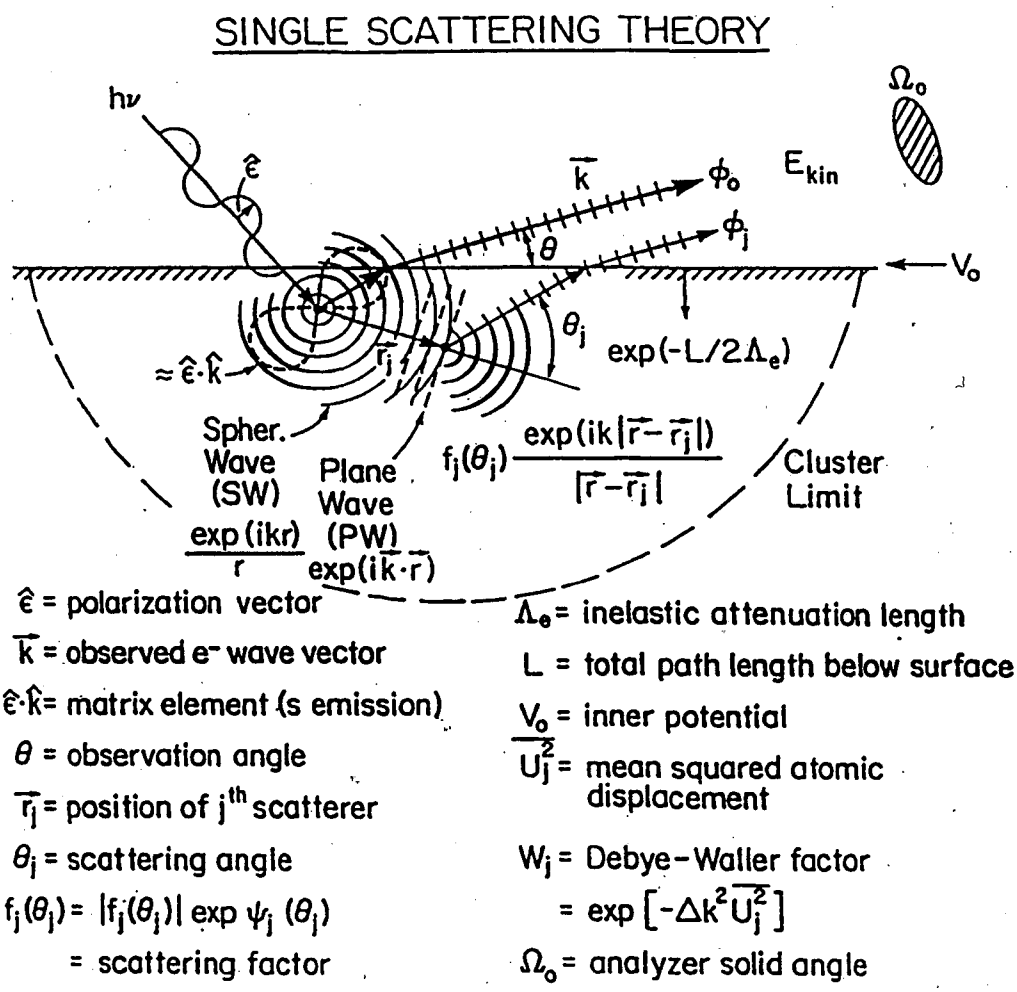

$\hat{\epsilon}$ = polarization vector

$\vec{k}$ = observed e⁻ wave vector

$\hat{\epsilon}\cdot\hat{k}$ = matrix element (s emission)

θ = observation angle

$\vec{r}_j$ = position of jth scatterer

θ_j = scattering angle

$f_j(\theta_j) = |f_j(\theta_j)| \exp \psi_j(\theta_j)$

= scattering factor

Λ_e = inelastic attenuation length

L = total path length below surface

V_0 = inner potential

$\overline{U_j^2}$ = mean squared atomic displacement

W_j = Debye–Waller factor

$= \exp\left[-\Delta k^2 \overline{U_j^2}\right]$

Ω_0 = analyzer solid angle

Fig. 1.5 The basic process involved in photoelectron diffraction, with important physical variables indicated. Only single scattering is shown for simplicity.

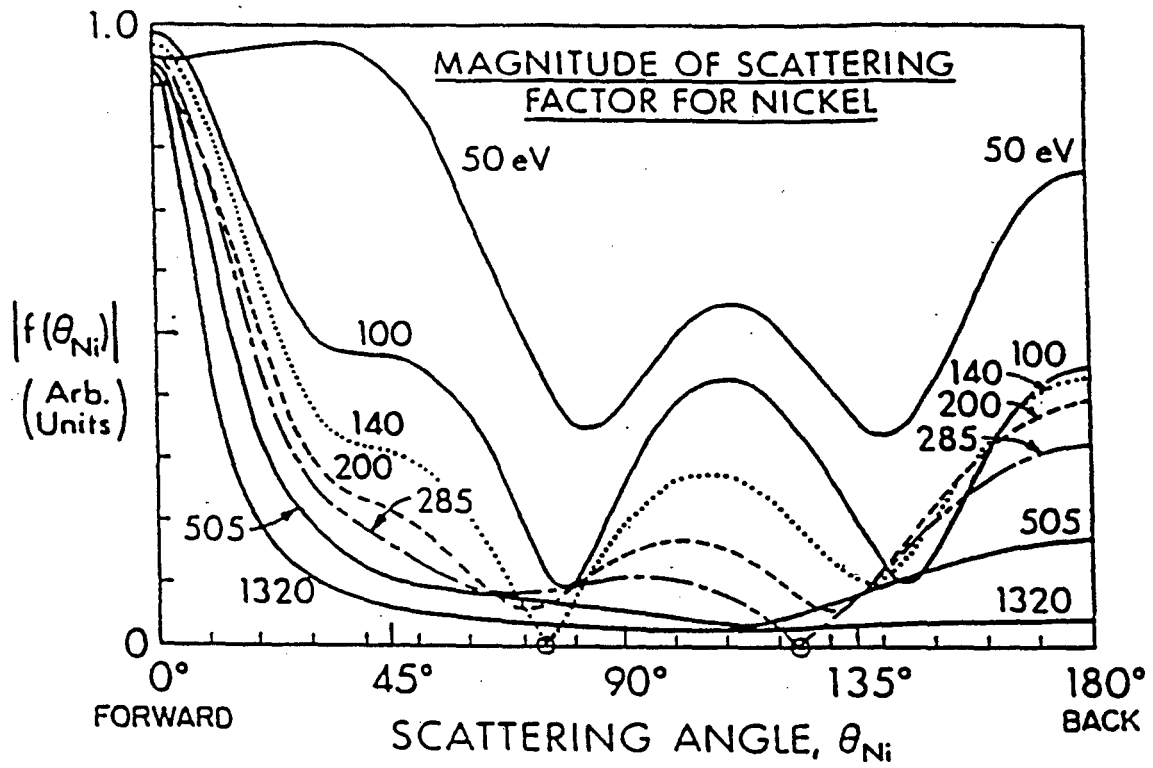

Fig. 1.6 Nickel plane-wave scattering factor amplitudes $|f(\theta_{Ni})|$ as a function of both scattering angle θ_{Ni} and the photoelectron kinetic energy (From ref. 15).

Chapter 2

Experimental Procedure and Methods of Data Analysis

2.1 Instrumentation

The experimental work for this thesis was performed using a Hewlett-Packard 5950A photoelectron spectrometer that has been specially modified for x-ray photoelectron diffraction (XPD) studies, as shown in Fig. 2.1. This modification [2.1, 2.2] consists of an sample preparation chamber which can be isolated from the main chamber and a custom built variable temperature two axis sample goniometer shown in Fig. 2.2 which allows rotation in both polar and azimuthal angles such that data may be taken above nearly the full 2π solid angle above the sample surface and with angular accuracies $\leq \pm 0.3^{o}$ in both angles. This goniometer is described in more detail in ref. 2.3. The experimental system shown in Fig. 2.1 thus consists of the sample preparation chamber where *in situ* surface preparation and characterization are made and a main chamber where XPD data are taken. Both of these chambers operate in the ultrahigh vacuum (UHV) regime, with base pressures in the mid-10^{-11} torr range in the main chamber, and in the low-10^{-10}-mid-10^{-11} range in the preparation chamber. The sample may be transferred between the sample preparation chamber and the main chamber by means of a long manipulator in which the goniometer is housed. The sample preparation chamber may be isolated from the main chamber during sample preparation by means of an isolation valve in order to minimize contamination of the main chamber.

The sample preparation chamber is equipped with an ion gun (Phi Model 20-005F) for surface cleaning by Ar^{+} ion bombardment, a water cooled, shutter-controlled evaporation system for metal vapor deposition, a quartz crystal microbalance (QCM, Infocon Model 751-001-G1) for monitoring thin film thicknesses and deposition rates, a thermocouple-calibrated infrared pyrometer (Wahl pyrometer, Model HSM-671) for monitoring sample temperature, a low energy electron diffraction (LEED) unit (Varian

Model 981-2148) for monitoring long range surface order, and a quadrapole mass spectrometer (UTI Model 100C) for identifying chamber contaminants and for performing vacuum chamber helium leak checks.

The main chamber is equipped with a hemispherical electron energy analyzer which has been discussed in detail elsewhere [2.3]. The main chamber is also equipped with two Al Kα x-ray sources, one monochromatized and the other non-monochromatized. The custom built non-monochromatized x-ray source, shown in Fig. 2.3 and designed by Z. Wang and S. Thevuthasan in our group, was added to provide a higher intensity source of x-rays [2.4]. While some energy resolution is lost by not monochromatizing the x-rays, for the same operating power of 800 W, the x-ray intensity is increased such that the photoelectron yield is finally about 3 times higher than with the normal HP monochromator. The natural linewidth of the Al K$\alpha_{1,2}$ line of approximately 0.8 eV, combined with the energy width derived from the 6.0 mm entrance slit of the HP spectrometer (which is now not operated in dispersion-compensated mode [2.3]), lead finally to an inherent instrumental width of about 2 eV. By contrast, for the monochromatized x-ray source on the HP system as operated with dispersion compensaton, the overall linewidth is approximately 0.5 eV full width at half maximum (FWHM) [2.1]. Thus, for XPD studies in which high energy resolution is not important, the added intensity achieved by using an non-monochromatized x-ray source decreases the counting time required to achieve high quality diffraction patterns with a high signal-to-noise ratio. This non-monochromatized source was therefore used for all of the experimental data reported in this thesis. The resistive-anode multichannel detector (a Surface Science Laboratories Model 239) was always operated at $\leq$~10,000 counts/sec over its entire surface to avoid saturation problems.

As part of this thesis, the sample goniometer was also modified by the addition of an extra idler spur gear so as to provide for more space around the sample barrel. This is shown in Fig. 2.2. The electron bombardment sample heater assembly was also modified

with a larger diameter so as to make it more robust and easy to use; this also is shown in Fig. 2.2.

A final important improvement to the HP 5950A photoelectron spectrometer system has been the addition of a Windows-based software system written by H. Xiao in our group which fully automates the process of taking XPS and XPD data on this system. The program steps the sample in both polar (θ) and azimuthal (ϕ) angles during XPD data collection, with simultaneous plotting of intensities in a two dimensional format. This software also added the capability that up to 10 different photoelectron peaks could be measured at each emission direction in order to make sure that the XPD data from each element were obtained for exactly the same sample positions and surface conditions. For the data in this dissertation, the Cu $2p_{3/2}$ peak and the close-lying Ru $3d_{3/2}$ and Ru $3d_{5/2}$ peaks were measured simultaneously for Cu deposited on clean Ru(0001), and the O 1s peak, Cu $2p_{3/2}$ peak, and Ru $3d_{3/2}$ and Ru $3d_{5/2}$ peaks were measured simultaneously for Cu deposited on O-precovered Ru(0001). Data were taken over one-third of the nearly full 2π solid angle above the sample surface, thus exploiting the threefold symmetry of the Cu/Ru system to reduce scan time. However, the threefold symmetry was verified for all overlayers studied by performing full 360° azimuthal scans at selected polar angles. Thus, both the polar (θ) and azimuthal (ϕ) emission angles were varied, with θ being measured from the sample surface, and ϕ from the [001] direction lying in the Ru surface. Scanning was over the ranges $6^{o} \leq \theta \leq 90^{o}$ and $0^{o} \leq \phi \leq 120^{o}$, with full-hemisphere intensity patterns then being generated by threefold repetition of each set of data. The step size in θ was 2°. The step size in ϕ was initially 2° at $\theta = 6^{o}$, and was increased as θ increased so that the data density in solid angle would remain roughly constant over the full data set above the sample surface. The formula used to adjust the size of the ϕ step was

$$\Delta\phi = \Delta\phi_{init.} \frac{\sin\left(\frac{90^\circ - \theta_{init.}}{2}\right)}{\sin\left(\frac{90^\circ - \theta}{2}\right)}, \tag{2.1}$$

where $\Delta\phi_{init.} = 2^o$ and $\theta_{init.} = 6^o$ for our data.

2.2 Sample Preparation

Ru(0001) Sample

The Ru(0001) surface was prepared by mechanically polishing a Ru single crystal, 0.5 inches in diameter, until the sample face attained a mirror finish. This was accomplished by starting with 6 micron diamond paste and finishing with 0.05 micron alumina micropolish. The polished Ru single crystal was oriented by Laue back reflection and the surface was found to be within 0.5° of the (0001) orientation. The polished and oriented Ru(0001) crystal was cleaned further in the UHV preparation chamber, with a base pressure near 5×10^{-11} Torr. The *in situ* cleaning consisted of mild Ar^+ ion bombardment (30 mA, 800 V, 5.5×10^{-5} Torr), followed by several oxygen/heat cleaning treatments in which the Ru sample was heated to about 800°C in an oxygen atmosphere of 3×10^{-7} Torr for ~5 minutes and then briefly vacuum annealed at ~1400°C [2.5-2.8]. Surface cleanliness was verified by x-ray photoelectron spectroscopy (XPS) [2.1], with details concerning the quantitative analysis to be presented later in this chapter. The presence of a well ordered Ru(0001) surface was verified by a sharp hexagonal LEED pattern, one example of which is shown in Fig. 4(a). In order to insure that the Ru(0001) surface remained clean and well ordered, oxygen/heat treatments, XPS, and LEED were performed before each Cu deposition.

Cu Film Deposition - Cu on Clean Ru(0001)

The thin Cu films were made by evaporating Cu onto the Ru substrate from a resistively heated W wire wrapped with high purity (99.998%) Cu wire. The amount of Cu deposited was determined using the QCM, and the final Cu coverage on the surface was determined for thinner layers ≤ 8 ML in thickness using angular dependent XPS [2.1], with the details of this also to follow. The Ru substrate temperature during deposition was ~ 600°C for Cu coverages less than 4 ML and ~300°C for Cu coverages ≥ 5 ML to suppress evaporation effects, as in prior studies [2.5-2.8]. An intermediate-thickness 4 ML film was obtained by annealing a 7.7 ML film at 600°C briefly. After annealing, XPS indicated a Cu coverage of 4.2 ML. The LEED pattern for this 4.2 ML overlayer is shown in Fig. 2.4(b).

Cu Film Deposition - Cu on O-Precovered Ru(0001)

For Cu grown on O-precovered Ru(0001), the clean Ru surface was first exposed to 90 Langmuirs of oxygen until a saturation coverage of 0.5 ML was reached. A well ordered p(2x1)-O/Ru(0001) structure was confirmed by LEED, and an example of this is shown in Fig. 4(c). Copper was then evaporated as for Cu/clean Ru(0001), but at a substrate temperature of ~ 125°C as in prior work [2.9-2.11]. An intermediate-thickness 3.7 ML Cu film, however, was obtained by annealing a 6.5 ML Cu film to 325°C briefly so as to obtain a $2\sqrt{3} \times 4\sqrt{3}R30^{\circ}$ LEED structure as seen previously by Wolter et al. [2.10]. This LEED pattern is shown in Fig. 4(d). After annealing, XPS indicated a Cu coverage of 3.7 ML.

2.3 Data Treatment and Analysis

2.3.1 Determination of Surface Coverages

We first introduce the standard XPS quantitative analytical expression applicable to the case of a semi-infinite substrate with uniform overlayer of thickness t from Eq. (3) of ref. [2.12]. This equation will be applied to the case of Cu/Ru(0001) and Cu/O-precovered Ru(0001). The polar angle θ dependence of the substrate and overlayer intensities are expressed as:

Peak k from substrate with E_{kin} ð E_k:

$$N_k(\theta) = I_o\Omega_o(E_k)A_o(E_k,\theta)D_o(E_k)\rho_k(d\sigma_k/d\Omega)\Lambda_e(E_k)\exp\left(-t/\Lambda_e'(E_k)\sin\theta\right)$$

$$= N_k^{\infty}(\theta)\exp\left(-t/\Lambda_e'(E_k)\sin\theta\right), \tag{2.2}$$

Peak l from overlayer with E_{kin} ð E_l:

$$N_l(\theta) = I_o\Omega_o(E_l)A_o(E_l,\theta)D_o(E_l)\rho_l(d\sigma_l/d\Omega)\Lambda_e'(E_l)\left[1-\exp\left(-t/\Lambda_e'(E_l)\sin\theta\right)\right]$$

$$= N_l^{\infty}(\theta)\left[1-\exp\left(-t/\Lambda_e'(E_l)\sin\theta\right)\right] \tag{2.3}$$

where

I_o = the incident x-ray flux

Ω_o = the kinetic-energy-dependent effective solid angle seen by the spectrometer

A_o = the kinetic-energy- and angle- dependent effective specimen area seen by

the spectrometer

D_o = the kinetic-energy-dependent efficiency of the detector

$d\sigma_{k,(l)}/d\Omega$ = the differential cross section, which depends on the subshell k(or l) and the photon energy

Λ_e = the inelastic attenuation length in the substrate

$\Lambda_e^{'}$ = the inelastic attenuation length in the overlayer

ρ_k = an atomic density in the substrate associated with subshell k

ρ_l = an atomic density in the substrate associated with subshell l, and

N_k^{∞} and N_l^{∞} = the absolute peak intensities at a certain θ resulting from atomically clean and semi-infinite specimens of the substrate and overlayer material, respectively (in our case N_k^{∞} for Ru, N_l^{∞} for Cu), and given by:

$$N_k^{\infty} = I_o\Omega_o(E_k)A_o(E_k,\theta)D_o(E_k)\rho_k(d\sigma_k/d\Omega)\Lambda_e(E_k) \tag{2.4}$$

$$N_l^{\infty} = I_o\Omega_o(E_l)A_o(E_l,\theta)D_o(E_l)\rho_l(d\sigma_l/d\Omega)\Lambda_e^{'}(E_l). \tag{2.5}$$

It is more convenient to deal with peak ratios in which the x-ray intensity I_o and any purely instrumental variations with θ cancel:

Overlayer/substrate ratio:

$$R(\theta) \equiv \frac{N_l(\theta)}{N_k(\theta)} = \frac{N_l^{\infty}}{N_k^{\infty}}\left[1-\exp\left(-t/\Lambda_e^{'}(E_l)\sin\theta\right)\right]\exp\left(t/\Lambda_e^{'}(E_k)\sin\theta\right) \tag{2.6}$$

where $N_k(\theta)$ and $N_l(\theta)$ are the measured peak intensities of substrate and overlayer at a certain coverage, respectively. Eqs. (2.5) and (2.6) can be used to experimentally

calibrate the two reference intensities from semi-infinite samples, and these can then be inserted in Eq. (2.6) to determine t via the angular dependence of the ratio *R(6)*, provided good estimates for the two mean free paths in the overlayer are known. Alternatively, N_k^∞ and N_l^∞ can be determined from their theoretical expressions. For the further simplified case of fractional monolayer coverage in which the overlayer can be assumed to be non-attenuating, Eq. (2.6) becomes:

$$R(\theta) \equiv \frac{N_l(\theta)}{N_k(\theta)} = \left[\frac{s'}{s}\right] \times \frac{D_o(E_l)A_o(E_l)\Omega_o(E_l)(d\sigma_l/d\Omega)d}{D_o(E_k)A_o(E_k)\Omega_o(E_k)(d\sigma_k/d\Omega)\Lambda_e(E_k)\sin\theta} \tag{2.7}$$

where

s' = the mean surface density of overlayer atoms in which peak l originates (cm^{-2})

s = the mean surface density of substrate atoms (cm^{-2})

s'/s = the fraction monolayer coverage of the atomic species in which peak l originates, as measured with respect to the substrate atomic density

d = the mean separation between layers of density s in the substrate (calculable as an average number from s/ρ or more precisely from the known atomic structure of a given low-index surface).

The differential cross section for the *nl* subshell excited with unpolarized radiation is [2.13]:

$$d\sigma_{nl}(E_{kin})/d\Omega = \left(\sigma_{nl}(E_{kin})/4\pi\right)\left[1 - \tfrac{1}{2}\beta_{nl}(E_{kin})P_2(\cos\alpha)\right], \tag{2.8}$$

where $\beta_{nl}(E_{kin})$ is termed the asymmetry parameter, $P_2(\cos\alpha) = \frac{1}{2}(3\cos^2\alpha - 1)$, and α is the angle between the incident x-ray direction and the outgoing photoelectron direction. For the Hewlett-Packard 5950A photoelectron spectrometer, $\alpha = 72^o$.

The product $D_o(E_{kin})A_o(E_{kin})\Omega_o(E_{kin})$ can be described as an overall analyzer "transmission", and for the HP 5950A, it has been found adequate [2.14] to use only the variation of the solid angle accepted into the lens with E_{kin}, as calculated by R.J. Baird from an electron trajectory analysis [2.15] and shown in Fig. 2.5. (However, in connection with the quantitative analysis of XPD patterns, we comment below on the fact that this analysis does not seem to allow for all of the effective sources of angular broadening in the experiment.)

Theoretical cross sections and asymmetry parameters, from which the differential cross section can be calculated, appear in both extensive tables and graphs for the entire periodic table by Yeh and Lindau [2.16], and in the prior tabulation by Goldberg et al. based on the same computer program [2.13].

For the effective inelastic electron attenuation length (EAL), Λ_e, we use the inelastic mean free path (IMFP), as tabulated from experimental data by Seah and Dench [2.17], or as calculated theoretically from optical constant data on a number of materials by Tanuma, Powell, and Penn (TPP) [2.18]. Several different measures of electron propagation lengths are used, depending on how they are measured and how they are to be used, as discussed in more detail by Jablonski and Powell [2.19] and by Powell, Jablonski, Tanuma, and Penn [2.20]. Qualitatively, elastic scattering effects usually act to make the EAL smaller than the IMFP, sometimes by as much as 30-40%; although for grazing angles of electron emergence, the EAL can actually be greater than the IMFP. In practice, we use the more accessible IMFP, although the average effective electron escape depths are expected to be somewhat shorter. Values for the IMFP are given for O, Cu, and Ru in Table 2.1, and have been determined using the formula given by Seah and Dench [2.17], which is in turn based on the "universal" curve for the elements shown in Fig. 2.6:

$$\Lambda_e = \frac{1430}{E_{kin}^2} + 0.54 \cdot E_{kin}^{1/2}, \tag{2.9}$$

and also the formula based on optical constant data and known as "TPP-2M" [2.20]:

$$\Lambda_e = \frac{E_{kin}}{E_p^2\left[\beta \ln(\gamma E_{kin}) - C/E + \left(D/E_{kin}^2\right)\right]}, \tag{2.10}$$

where Λ_e is in units of Angstroms, and where

$E_{kin=}$ electron kinetic energy

$E_p = 28.8(N_v\, \rho / M)^{\frac{1}{2}}$

$\rho \equiv$ density (g-cm^{-3})

$M \equiv$ atomic or molecular weight

$N_v \equiv$ number of valence electrons per atom (elements)

$\beta = -0.10 + \dfrac{0.944}{\left(E_p^2 + E_g^2\right)^{\frac{1}{2}}} + 0.069\rho^{0.1}$

$E_g \equiv$ bandgap energy for nonconductors

$\gamma = 0.191\rho^{-0.50}$

$C = 1.97 = 0.91U$

$D = 53.4 - 20.8U$

$U = N_v \rho / M = E_p^2 / 829.4$.

As shown in Table 2.1, Eq. (2.10) gives somewhat higher values for Λ_e than Eq. (2.9), by a factor of 1.2-1.7. We have therefore used Eq. (2.9) in all our calculations since, as stated above, the actual electron escape depths are expected to be somewhat shorter.

Values for the various parameters in Eq. (2.5) are shown in Table 2.1 for O 1s, Cu $2p_{3/2}$, and Ru 3d photoelectron peaks. The resulting coverage equations with no experimental inputs are:

(1) Cu on clean Ru(0001):

$$\left(1-e^{-t/6.11\sin\theta}\right)e^{t/9.01\sin\theta}=0.666\frac{N_{Cu2p_{3/2}}(\theta)}{N_{Ru3d}(\theta)},\ t\geq 1\text{ ML},\tag{2.11}$$

where t is the coverage in monolayers and, for submonolayer coverages,

$$\frac{s'}{s}=2.938\left(\frac{N_{Cu2p_{3/2}}(\theta)}{N_{Ru3d}(\theta)}\right)\sin\theta,\ s'/s<1.\tag{2.12}$$

(2) O on Ru(0001):

$$\frac{s'}{s}=30.0\left(\frac{N_{O1s}(\theta)}{N_{Ru3d}(\theta)}\right)\sin\theta,\ s'/s<1.\tag{2.13}$$

where, again, s'/s is the fractional monolayer coverage, and is always ≤0.5 ML = the saturation coverage.

For Cu on O-precovered Ru(0001), the oxygen floats on top of the growing Cu overlayer as discussed in more detail in Chapter 4, and therefore we use Eq. (2.7) above with the assumption that the floating oxygen overlayer is a non-attenuating overlayer [2.12]. To determine the O coverage on the Cu overlayer, the following equations were used:

(1) O coverage based on O 1s to Cu 2p3/2 peak ratio

$$\frac{s'}{s}=\frac{N_{O1s}(\theta)}{N_{Cu2p_{3/2}}(\theta)}59.52\left(1-e^{-t/12.73\sin\theta}\right)\sin\theta,\tag{2.14}$$

(2) O coverage based on O 1s to Ru 3d peak ratio

$$\frac{s'}{s} = \frac{N_{O1s}(\theta)}{N_{Ru3d}(\theta)} 28.60\left(e^{-t/18.74\sin\theta}\right)\sin\theta, \tag{2.15}$$

where t is the thickness of the Cu overlayer in ML as determined from Eq. (2.7). In the above coverage equations, values for N_l^∞ / N_k^∞ where determined by substituting in theoretical values (given in Table 2.1) for the various parameters. However, the resulting value for N_l^∞ / N_k^∞ may also be determined experimentally by first measuring N_l^∞ from a very thick Cu overlayer. This was done in connection with determining Cu coverages by first growing a very thick Cu layer on Ru(0001) until the Ru 3d signal could no longer be seen due to attenuation through the thick Cu layer. At this Cu coverage the Cu $2p_{3/2}$ intensity was measured and used as N_l^∞. The Cu was then immediately removed from the Ru sample by heating to 1400°C, and the Ru 3d intensity was then measured from the clean Ru sample, and this intensity was used as N_k^∞. The ratio N_l^∞ / N_k^∞ was about 0.653, which is very close (within about 2%) to the calculated value of 0.666. Thus, our theoretical inputs to these calculations seem quite accurate.

An additional complication in the determination of surface coverages related to the electron escape depth arises from the effect of diffraction. Since photoelectron diffraction can change peak intensities, and therefore also the mean depth of emission (as discussed in more detail in Chapter 3), by as much as ±50%, such effects also can constitute a major source of error in determining surface coverages or stoichiometries. Thus, averaging over many different emission directions is necessary for the most accurate estimates. The best procedure for averaging over diffraction in surface coverage determinations involves measuring the two (or three) intensities involved over the full 2π solid angle above the sample surface, averaging over the azimuth at each polar angle, and then using a spline smoothing program (see description in Section 2.3.3) to smooth out any remaining polar-angle-dependent variations in the average azimuthal intensities

which are caused by diffraction. Taking the ratio of the final smoothed overlayer intensities to the final smoothed substrate intensities as a function of polar angle then allows the coverage to be determined as a function of polar angle by using Eq. (2.6). Furthermore, past work [2.12] indicates that the angular range over which these ratios are most reliable is for polar angles above 30°-40° since additional affects due to surface refraction, surface roughness, and elastic scattering even from amorphous materials in which photoelectron diffraction is not observed can cause larger differences from simple models for more grazing electron emission [2.19, 2.20]. Examples of this method for determining surface coverages are shown in Fig. 2.7 for a nominal Cu coverage of 5 ML on clean Ru(0001) (as derived from the QCM) and in Fig. 2.8 for an oxygen coverage after depositing 3.7 ML Cu on O-precovered Ru(0001). Note that at low polar angles the coverage changes drastically while at polar angles above about 30°, the coverages are fairly constant. In addition, note that the oxygen coverage can only be determined to within $\pm$ 0.05 ML, due to a combination of the θ dependence, the small difference in values depending on whether we use the O/Ru ratio or the O/Cu ratio, and the noise level in the rather weak.oxygen signal. But in any case, the overall average over the two methods of determination of 0.48 $\pm$ 0.05 ML is in excellent agreement with the expected saturation coverage of 0.5 ML. This value for the oxygen coverage furthermore did not change significantly in going from clean Ru to the various coverages of Cu on O-precovered Ru.

2.3.2 Normalization of Intensities

The XPD intensities in this dissertation have been normalized so as to include only the diffraction features. The normalized intensity, $\chi(\vec{k})$, is defined as $\chi(\vec{k}) = \left[I(\vec{k}) - I_o(\vec{k})\right] / I_o(\vec{k})$, where $I(\vec{k})$ is the photoelectron intensity, $I_o(\vec{k})$ is the photoelectron intensity in the absence of any scattering, and $\vec{k}$ is the photoelectron wave

vector. In this dissertation, we estimate $I_o(\vec{k})$ by applying a spline smoothing routine (as described in the next section 2.3.3) to $I(\vec{k})$ so that the diffraction features have been smoothed out [2.21]. To provide some idea as to the effect of this, we show in Fig. 2.9 a comparison of (a) $I(\vec{k})$ and (b) $\chi(\vec{k})$ for the Ru 3d peak from a clean Ru(0001) sample. Note the typical falloff of $I(\vec{k})$ for low electron takeoff angles, and the resulting loss of visibility of diffraction features. However, in $\chi(\vec{k})$ these low-angle features are much easier to see and analyze.

2.3.3 Spline Smoothing of Diffraction Features

A spline smoothing routine written by Dierckx [2.21] was incorporated into a special program for analyzing XPD data. This program reads in XPD data as $I(\theta,\phi)$, and then carries out both the azimuthal averaging to yield $\bar{I}(\theta,\phi)$ and the spline fitting to $\bar{I}(\theta,\phi)$ necessary to generate the best final estimate of $I_o(\vec{k})$. Finally, $\chi(\vec{k})$ is determined for subsequent plotting, as in Fig. 2.9(b). A copy of the program is included in Appendix A. For more details on spline smoothing, I refer the reader to the paper by Dierckx [2.21]. The input file for the program is also shown in Appendix A. The first line of the input file is the number of smoothed output files created. The second line is the name of the input XPD data file. The rest of the lines specify the smoothing factors used followed by the respective output smoothed file. The smoothing factor determines the degree of smoothing performed and can be any number between 0 and 1.0. Using a smoothing factor of 0 will cause the program to interpolate (i.e. the spline will go through all data points). Using a smoothing factor of 1.0 will cause the maximum amount of smoothing. The input data file is a full 2π XPD data set in a (θ, ϕ, Intensity) format. The output file is only in a (θ, Intensity) format. The program first averages over phi for each polar angle. These phi averaged intensities, $\bar{I}(\theta)$, are then read into the spline smoothing routine and smoothed. The spline is forced to go to zero for a cutoff takeoff

angle that is near the negative of the estimated half-angle of acceptance of the analyzer, and the parameter specifying this can be adjusted in the program (as the variable CUTOFFANG). The output is then in the (θ, Intensity) format. For $I_o(\theta,\phi)$ subtraction, $I_o(\theta) = I_o(\theta,\phi)$ for all ϕ, and $I_o(\theta,\phi)$ is then subtracted from the 2π XPD data. An example of $\bar{I}(\theta)$ and its smoothed intensity, $I_o(\theta)$, is shown in Fig. 2.10.

2.3.4 Threefold Mapping of Data

As mentioned previously in section 2.3.1, the intensities of the O 1s, Cu $2p_{3/2}$, and Ru 3d peaks were measured over only one third of the nearly full 2π solid angle above the sample surface. Azimuthal scans of the Cu $2p_{3/2}$ intensities from full-360° and threefold-mapped data at a polar angle of 55° are shown for 4 ML Cu/Ru(0001) in Fig. 2.11. The two curves are both threefold symmetric, and the difference in anisotropy between the two sets of peaks is only about 4%; thus, there is in general excellent agreement between them. Similar checks of symmetry between full-360° and threefold-mapped data were made for all cases reported in this thesis. No curves are shown for O data, since the O overlayer is disordered and therefore the O 1s XPD pattern shows no or very weak diffraction features.

2.3.5 Global R-Factor Comparison of Experiment and Theory

In order to compare experimental and theoretical XPD patterns in a more quantitative manner, a reliability factor or "R-factor" is used to determine the goodness of fit between experiment and theory. Theoretical calculations are performed for various predicted structures, lattice spacings, or interlayer spacings, and then compared to experiment via R-factors, with the minimum R-factor indicating the best fit.

The R-factors used in this dissertation are based on a global summed R-factor which is the normalized average of the quantities "R_1" - "R_5". These R-factors were first developed by Saiki et al. [2.22(a)] for use in XPD, and are based on a set of five R-factors proposed previously for LEED analyses [2.22(b)]. The experimental and theoretical intensities are first normalized so that they have the same average anisotropy and the same overall amplitude. These normalized intensities $\overset{*}{I}_{expt}$ and $\overset{*}{I}_{theo}$ are then substituted into expressions for the five different R factors. The quantity, R_1, is a measure of the difference between the experimental and theoretical intensities,and is defined as:

$$R_1 = \frac{\sum_n \left| I^*_{expt}(n) - I^*_{theo}(n) \right|}{\sum_n \left| I^*_{expt}(n) \right|}. \tag{2.16}$$

R_2 is a measure of the squared difference between experimental and theoretical intensities:

$$R_2 = \frac{\sum_n \left| I^*_{expt}(n) - I^*_{theo}(n) \right|^2}{\sum_n \left| I^*_{expt}(n) \right|^2}. \tag{2.17}$$

R_3 is the percentage of angle range over which the experimental and theoretical intensities have slopes of different sign (+/-). R_4 is a measure of the difference between the first derivative of the experimental and theoretical intensities:

$$R_4 = \frac{\sum_n \left| I^{*\prime}_{expt}(n) - I^{*\prime}_{theo}(n) \right|}{\sum_n \left| I^{*\prime}_{expt}(n) \right|}. \tag{2.18}$$

Finally, R_5 is a measure of the squared difference between the first derivative of the experimental and theoretical intensities:

$$R_5 = \frac{\sum_n \left| I^{*'}_{expt}(n) - I^{*'}_{theo}(n) \right|^2}{\sum_n \left| I^{*'}_{expt}(n) \right|^2}. \tag{2.19}$$

These R-factors are discussed in more detail in ref. [2.22]. The R-factors have been determined by first calculating R_i at each individual polar angle in the nearly full 2π XPD pattern and then summing R_i over the polar angles from $\theta = 6^{\circ}$ to $\theta = 88^{\circ}$. We will refer to these summed R-factors as R_i^S. In this analysis, we have varied the interlayer spacing and calculated the resulting summed R-factors as a function of $d_\perp/d_\parallel$. The global summed R-factor is then calculated by first normalizing R_2^S - R_5^S to the average of R_1^S, i.e.,

$$R_i^N\left(d_\perp/d_\parallel\right) = R_i^S\left(d_\perp/d_\parallel\right) \cdot \frac{\sum_{d_\perp/d_\parallel} R_i^S\left(d_\perp/d_\parallel\right)}{\sum_{d_\perp/d_\parallel} R_1^S\left(d_\perp/d_\parallel\right)}, \quad \text{i} = 2, 3, 4, \text{ or } 5, \tag{2.20}$$

where $R_i^N(d_\perp/d_\parallel)$ is the ith normalized R-factor, and $R_1^N\left(d_\perp/d_\parallel\right) = R_1^S\left(d_\perp/d_\parallel\right)$. The global R-factor is then,

$$R_{global}\left(d_\perp/d_\parallel\right) = \frac{1}{5}\sum_{i=1}^{5} R_i^N\left(d_\perp/d_\parallel\right). \tag{2.21}$$

We finally take this number to be the best representative of the goodness-of-fit of theory to experiment.

2.3.6 Angular Broadening of Theoretical XPD Patterns

Another consideration in the comparison of experimental and theoretical XPD patterns via R-factors is that theoretical XPD patterns, and in particular MSC XPD patterns, were found in this work to show much more fine structure than is present in the experimental XPD patterns. Qualitatively, similar observations have been made for other cases in our group. This may be due to several reasons. One is that the $\pm 3^{o}$ angular broadening included in our calculations may not accurately represent the true amount of angular broadening in our experimental system, which may be slightly larger. In addition, there may be other effects in experiment such as defects and imperfections in the sample which tend to smear out the experimental XPD patterns as compared to the theoretical XPD patterns. Quasi-elastic vibrational excitations may also lead to some smearing of features beyond the simple attenuation included in Debye-Waller factors. Finally, there may also be deficiencies in the way the MSC code includes the effects of angular broadening in that it samples too few points over the assumed solid angle. This extra fine structure seen in theoretical XPD patterns thus may affect not only the overall R-factors, but the positions of the R-factor minima as well. Therefore, to account for angular broadening in a more quantitative way than has been attempted previously, we have performed a systematic smoothing of the theoretical XPD patterns by convolution with a gaussian of various widths, and this has in fact been found to both lower the overall R-factors and improve the visual comparison of theory with experiment. Thus, the amount of angular broadening now becomes one of the non-structural parameters in the analysis that is varied to yield the final best agreement between experiment and theory. The gaussian convolution program, filter.f, used for the 2D smoothing of the theoretical data is presented in Appendix B and it includes modifications made to a program written by Patrick Len of our group [2.23]. The convolution procedure, originally suggested by

Harp et al. in connection with the holographic analysis of photoelectron diffraction data [2.24], is simple and is given by:

$$I_F\left(\hat{k}\right) = \frac{\iint_S I\left(\hat{k}'\right) e^{-\sigma^2\left|\bar{k}-\bar{k}'\right|^2} k'^2 \, d\Omega_{\hat{k}}}{\iint_S e^{-\sigma^2\left|\bar{k}-\bar{k}'\right|^2} k'^2 \, d\Omega_{\hat{k}}}, \tag{2.18}$$

where σ is a variable parameter which determines the degree of angular broadening, $I_F\left(\hat{k}\right) = I_F(\theta,\phi)$ is the broadened theoretical intensity, and $I\left(\hat{k}'\right) = I(\theta',\phi')$ is the raw unbroadened theoretical intensity. The parameter, σ, determines the half width at half maximum of the gaussian used, and it can be redefined in terms of this width,

$$\theta_{\frac{1}{2}} = \sin^{-1}\left(\frac{0.8344\sigma}{\left|\bar{k}\right|}\right), \tag{2.19}$$

where both σ and $|\bar{k}|$ are expressed in units of $Å^{-1}$. The angle steps used in this broadening are approximately 2.4°. The gaussian broadening extends however, over all angles. The program in Appendix B contains the program as modified for broadening XPD data. The other modification made to the program is to output the broadened intensity with 2° step sizes in both θ and ϕ. The input intensities do not need a constant step size in θ or ϕ, however, at each θ, there must be an equal number of ϕ steps. This can be accomplished by simply repeating the last data point at each θ, so that each azimuthal scan has an equal number of ϕ steps. The program, map.f, in Appendix B will accomplish this task. The input file with descriptions of each input parameter, filter.in, is also given in Appendix B.

As an example of the effect of this smoothing procedure on both the visual comparisons and the R-factor comparisons of experimental and theoretical XPD patterns,

we show, in Figs. 2.12(a), 2.13(a), and 2.14(a), experimental XPD patterns at 1 ML, 5 ML, and 25 ML, respectively, and in Figs. 2.12(b)-(e), 2.13(b)-(e), and 2.14(b)-(e), the corresponding theoretical XPD patterns that have been smoothed to various degrees. Visually, the theoretical XPD patterns that have been smoothed using a gaussian with a HWHM between 2.4° and 4.8° appear to provide the best fits to experiment. A more quantitative R-factor comparison shows that this is indeed the case, as illustrated in Fig. 2.15 with a plot of the global R-factor versus HWHM for the coverages of 1 ML, 5 ML, and 25 ML. The R-factor minima occur at HWHM values of 5.6°, 4.0°, and 4.8°, respectively. The procedure used for analyzing the experimental data presented in this thesis has been to use the minimum amount of angular broadening consistent with minimizing the global R-factor and yielding a best visual fit. This yields a broadening HWHM of 4.0° that was finally applied to all of the theoretical diffraction patterns.

2.4 Summary and Analysis of Prior STM Work on the Cu/Ru(0001) System,

Although no STM images were obtained as part of this dissertation, the prior STM work by Behm and co-workers on Cu deposited on clean Ru(0001), culminating in a very detailed doctoral thesis by C. Günther [2.5], provides some key background for the present study. Thus, we briefly review this work here.

In order to present a clearer picture of the dislocation structures that are formed by Cu when grown on Ru(0001), we show in Figs. 2.16(a)-(d), STM images for 1-4 ML Cu/Ru(0001), as obtained from ref. 2.5(c). In Fig. 2.16(a) is the STM image for 1 ML Cu/Ru, and clearly the Cu film has conformed to the hexagonal hcp Ru(0001) structure below it, forming what is termed a pseudomorphic overlayer. Our LEED pattern for the same structure shown in Fig. 2.4(a) is consistent with this, consisting of a simple set of sharp spots associated with the Ru(0001) periodicity. At 2 ML, shown in Fig. 2.16(b), a striped dislocation pattern is seen. Here, the layer is assumed to contract uniaxially from

the pseudomorphic configuration, and the bright stripes are assumed to be due to Cu atoms which are sitting in bridge sites of the underlying layer, while the dark stripes are assumed to be due to Cu atoms which are in registry with the underlying layer and are sitting in threefold hollow sites. From this STM picture it was not possible to tell whether only the top Cu layer contracted uniaxially, or whether both layers contracted uniaxially together, and this is one question we want to answer using our XPD data. At 3 ML, shown in Fig. 2.16(c), a complex threefold star pattern is seen and this is believed to be due to the Cu overlayer contracting along three directions. Again, the bright stripes are believed to be due to Cu atoms sitting in bridge or atop sites, while the dark spots are believed to be due to Cu atoms sitting in threefold hollow sites. Finally, at 4 ML, shown in Fig. 2.16(d), the Cu contracts almost fully to the bulk fcc Cu(111) lateral lattice spacing, and forms a large scale incommensurate lateral superlattice or Moiré pattern. At 4 ML the Cu lattice is also believed to be rotated slightly compared to the Ru(0001) lattice, thus producing the observed rotation of the Moiré pattern with respect to the individual atomic rows. By comparing the 4 ML STM image to a computer generated Moiré pattern in which a 2D hexagonal lattice of various lateral lattice spacings and rotations is placed on top of a hexagonal lattice with no rotation and a lateral lattice spacing equal to the Ru(0001) lattice spacing, it is possible to estimate that the Cu lattice is still about 0.6% expanded from a bulk fcc Cu(111) lateral lattice spacing, and that it is rotated by about 0.9^{o} as compared to the Ru(0001) lattice. Such a computer generated Moiré pattern is shown in Fig. 2.17. The dashed-dotted lines indicate the atomic rows along which atoms where counted on both the experimental 4 ML image and the simulated structures in order to optimize agreement The angle between the bottom dashed-dotted line and one side of the unit cell (indicated by the solid lines) was also measured and compared to the corresponding angle in the STM image. In the prior STM studies, it was estimated in the same manner that the Cu lattice is expanded about 0.4% [2.5(d)] from the bulk fcc Cu(111) lateral lattice spacing, and that it is rotated by about 1°

[2.5(c)] as compared to the Ru(0001) lattice, in good agreement with our own estimates of 0.6% and 0.87°.

As one other type of data on the growth mode of a 4 ML overlayer, we note that the LEED pattern in Fig. 2.4(b) exhibits two sets of spots that might be thought to be due to the two slightly different lattice parameters for Cu and Ru, and/or to the influence of the Moiré structure in producing additional spot fine structure. The two sets of spots are in fact found to have a separation ratio of 0.95 that is suggestive of an almost fully relaxed Cu overlayer.

It would be difficult to determine from our XPD measurements whether there is a 0.9^{o} rotation of the Cu lattice relative to the Ru lattice without taking very high angular resolution azimuthal scans, and even then, such data could be confused if there are two equally populated domains present in which the Cu lattice is rotated by $\pm 1^{o}$ with respect to the Ru lattice. Our XPD measurements do, however, permit determining whether these misfit dislocation structures occur only in the top Cu layer or in all the Cu layers, as will be discussed in more detail in Chapter 4. In addition, with XPD, it is possible to determine whether there is any interlayer contraction in the Cu overlayer. This will also be discussed in more detail in Chapter 4.

An additional consideration in the analysis of the XPD patterns is that the growth of Cu on Ru(0001) is not simply layer-by-layer, but under most conditions involves the presence of several layer heights. This is illustrated in the STM image of Fig. 2.18 (From ref. 2.5(a)) where the nominal coverage is > 5 ML, but a distribution of island heights exists. In Fig. 2.19, we have plotted the percentage of each layer that is uncovered by overlying Cu atoms for coverages from 1-4 ML, as derived from ref. 2.5(d). The percentage of each layer that is uncovered was determined by subtracting the amount of total surface area that the next higher layer covers from the total surface area that the layer in question covers. Thus if layer 1 covers 100% of the total surface area, layer 2 covers 95% of the total surface area, layer 3 covers 20% of the total surface area, layer 4 covers

20% of the total surface area, and higher layers cover 0% of the total surface area, then layer 1 is 5% uncovered, layer 2 is 75% uncovered, layer 3 is 0% uncovered, layer 4 is 20% uncovered, and the higher layers are 0% uncovered since they do not exist. Thus, a 0 % uncovered layer means the layer is either completely covered or does not exist. A large % uncovered layer indicates the dominant coverage. These curves in Fig. 2.19 should thus be peaked around the nominal coverage if growth is mostly layer-by-layer, and this is generally what is seen. A similar plot is shown in Fig. 2.20 but for 4.15 ML annealed at different temperatures. Here, the peak shifts from near the nominal-coverage layers #4 and #5 at room temperature (RT) to layer #2 at 647°C, indicating the formation of a more stable filled second layer upon which are thick 3D islands that cover very little of the total surface. Thicknesses of 3 ML and 6 ML also appear to show extra stability for an intermediate annealing temperature od 387°C. Thus, the higher the temperature, the less the growth is layer-by-layer, and the more the special stability of the 2 ML overlayer might be expected to manifest itself in the XPD patterns.

Various aspects of these STM results will thus become important in the discussion of our XPD data in Chapter 4.

References:

[2.1] (a) C. S. Fadley in Electron Spectroscopy: Theory, Techniques, and Applications, C. R. Brundle and A. D. Baker, eds., Vol. II, Chap 1 (Academic Press, London) (1978); (b) C. S. Fadley, review of angle resolved x-ray photoelectron spectroscopy in Prog. in Surf. Sci., edited by S. G. Davidson (Pergamon Press, New York, 1984) Vol. 16 no. 3.

[2.2] P. J. Orders, R. E. Connelly, N. F. T. Hall, and C. S. Fadley, Phys. Rev. B 24, 6163 (1981); and K. A. Thompson and C. S. Fadley, Surf. Sci. 146, 281 (1984).

[2.3] R. J. Baird and C. S. Fadley. J. Elect. Spect. 11, 39 (1977).

[2.4] Z. Wang, Ph.D. Thesis, Univ. of California-Davis (1997).

[2.5] (a) G. Pötschke, J. Schröder, C. Günther, R.Q. Hwang, and R. J. Behm, Surf. Sci. **252,** 592 (1991); (b) G.O. Pötschke, and R.J. Behm, Phys. Rev. B **44,** 1442 (1991); (c) C.Günther, J. Vrijmoeth, R.Q. Hwang, and R.J. Behm, PRL **74,** 754 (1995); (d) C. Günther, Ph.D. Thesis, Univ. Muenchen (1994).

[2.6] K. Christmann, G. Ertl, and H. Shimizu, Thin Solid Films 57 (1979) 247; J. Catalysis **61,** 397 (1980).

[2.7] J.E. Houston, C.H.F. Peden, D.S. Blair, and D.W. Goodman, Surf. Sci. **167,** 427 (1986); J. E. Houston, C. H. F. Peden, and Peter J. Feibelman, PRL **56,** 375 (1986); D. G. O'Neill and, J.E. Houston, Phys. Rev. B **42,** 2792 (1990)

[2.8] C. Park, E. Bauer, and H. Poppa, Surf. Sci. **187,** 86 (1987).

[2.9] K. Kalki, M. Schick, G. Ceballos, and K. Wandelt, Thin Solid Films **228**, 36 (1993).

[2.10] H. Wolter, M. Schmidt, and K. Wandelt, Surf. Sci., **298**, 173 (1993).

[2.11] M. Schmidt, H. Wolter, M. Nohlen, and K. Wandelt, J. Vac. Sci. Technol. A **12**, 1818 (1994).

[2.12] C. S. Fadley, Prog. in Surf. Sci. 16, 275 (1984).

[2.13] S. M. Goldberg, C. S. Fadley and S. Kono, J. Elect. Spectrosc. and Rel. Phenom. 21, 285 (1981).

[2.14] C.S. Fadley, private communication.

[2.15] R.J. Baird, Ph.D. Thesis, Univ. of Hawaii (1977).

[2.16] J. J. Yeh and I. Lindau, Atomic Data and Nuclear Data Tables 32, 1 (1985).

[2.17] M. P. Seah and W. A. Dench, Surf. and Interface Anal. 1, 2 (1979).

[2.18] S. Tanuma, C. J. Powell, and D. R. Penn, Surf. and Interface Anal. 17, 911 (1991).

[2.19] A. Jablonski and C. J. Powell, Surf. and Interface Anal. 20, 771 (1993).

[2.20] C. J. Powell, A. Jablonski, S. Tanuma, and D. R. Penn, J. Elec. Spectrosc. and Rel. Phenom. 68, 605 (1994).

[2.21] P. Dierckx, J. Comp. and Applied Mathematics 1, 165 (1975).

[2.22] (a) R.S. Saiki, A.P. Kaduwela, M. Sagurton, J. Osterwalder, D.J. Friedman, C.S. Fadley, and C.R. Brundle, Surf. Sci. **282**, 33 (1993); (b) M.A. Van Hove, S.Y. Tong and M.H. Elconin, Surf. Sci. **64**, 85 (1977).

[2.23] P.M. Len, Ph.D. Thesis, Univ. of California-Davis (1997).

[2.24] G.R. Harp, D.K. Saldin, X. Chen, Z.-L. Han, and B.P. Tonner, J. Electron Spectrosc. Relat. Phenom. **57**, 331 (1991).

Table 2.1:

peak	E_b (eV)	E_{kin} (eV)	β_{nl}	σ_{nl} (Mbarns)	$d\sigma/d\Omega$ (Mbarns)	Ω_o (Steradian)	Λ_e (Å) (ref. 17)	Λ_e (Å) (ref. 20)	ρ (g/cm^3)
O 1s	531.6	955	2.000	0.0400	4.56×10^{-4}	100	16.72	28.77	0.99 *
Cu 2p3/2	930.6	556	1.429	0.2292	0.02289	300	12.73	18.23	8.93
Ru 3d	280.6	1206	1.201	0.1717	0.1659	135	18.74	22.05	12.36

* The oxygen density is based on the density of oxygen in the p(2x1) structure formed on Ru(0001).

Fig. 2.1 The Hewlett-Packard 5950A photoelectron spectrometer that has been modified so as to include LEED and automated XPD capability in a UHV environment. The major components of this system are indicated in the figure.

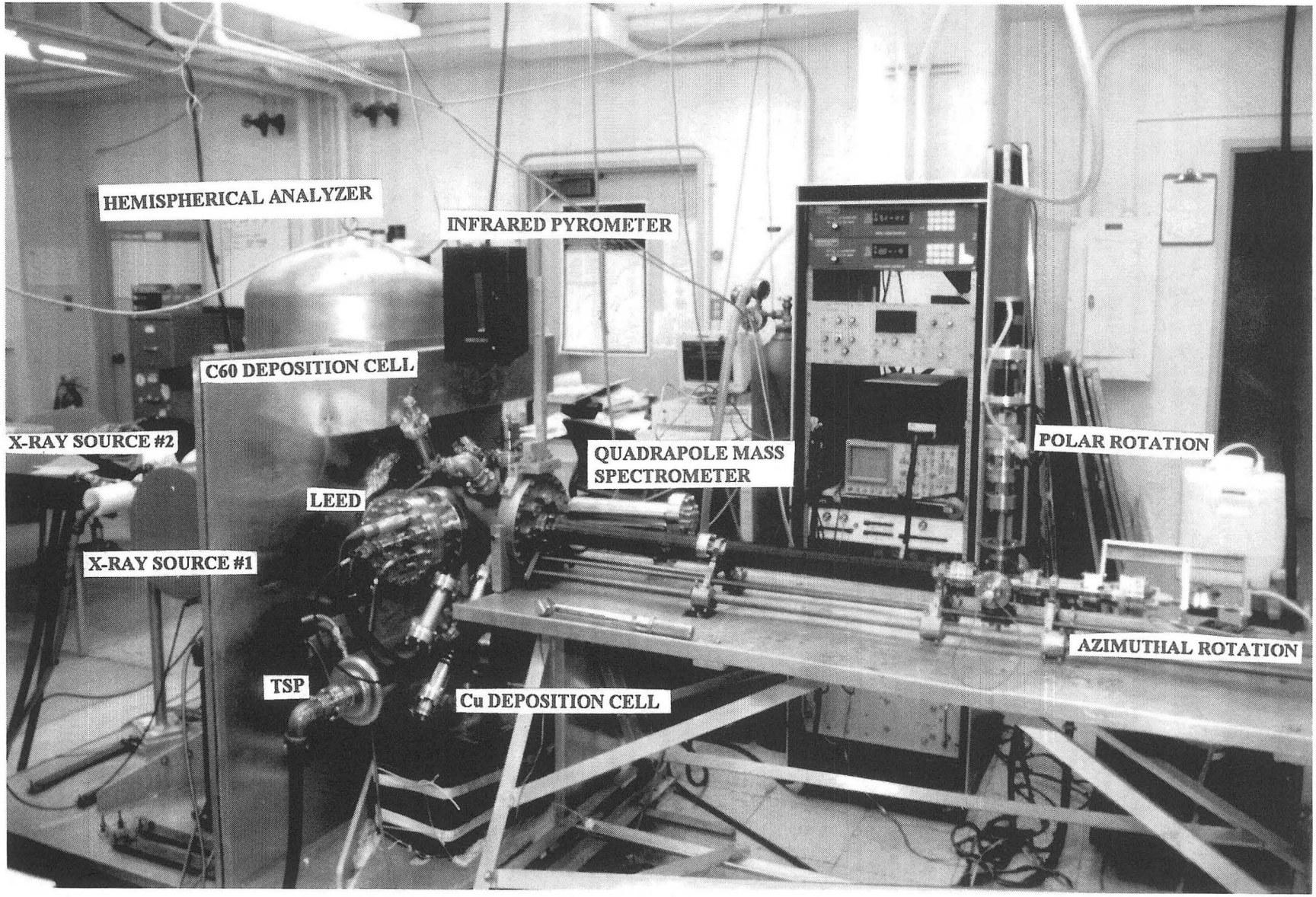
HEMISPHERICAL ANALYZER
INFRARED PYROMETER
C60 DEPOSITION CELL
X-RAY SOURCE #2
QUADRAPOLE MASS SPECTROMETER
POLAR ROTATION
LEED
X-RAY SOURCE #1
AZIMUTHAL ROTATION
TSP
Cu DEPOSITION CELL

(a)

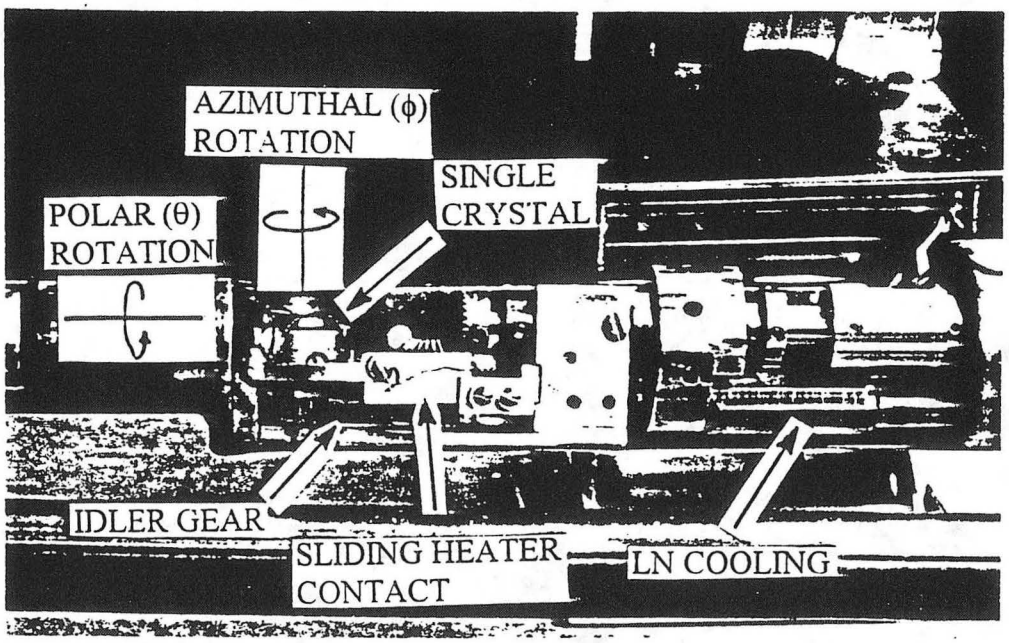

(b)

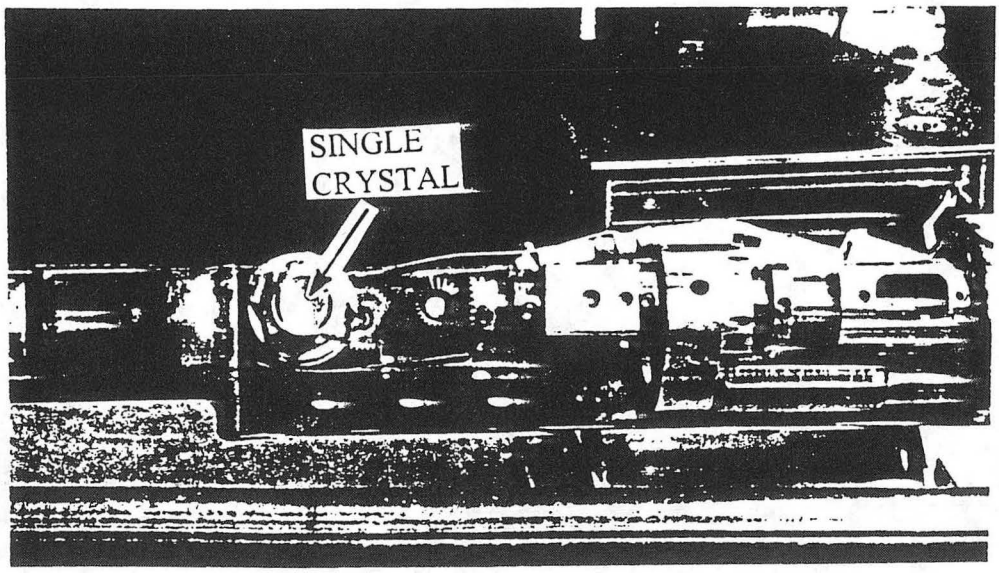

Fig. 2.2 (a) Two axis sample goniometer allowing rotation in both polar and azimuthal angles so that XPD data may be taken above the nearly full 2π solid angle above the sample surface. (b) Same as (a) but top view of goniometer.

Fig. 2.3 Custom built non-monochromatized Al $K\alpha_{1,2}$ x-ray source, yielding ~ 3x higher intensities than the original monochromatized source supplied with the HP spectrometer.

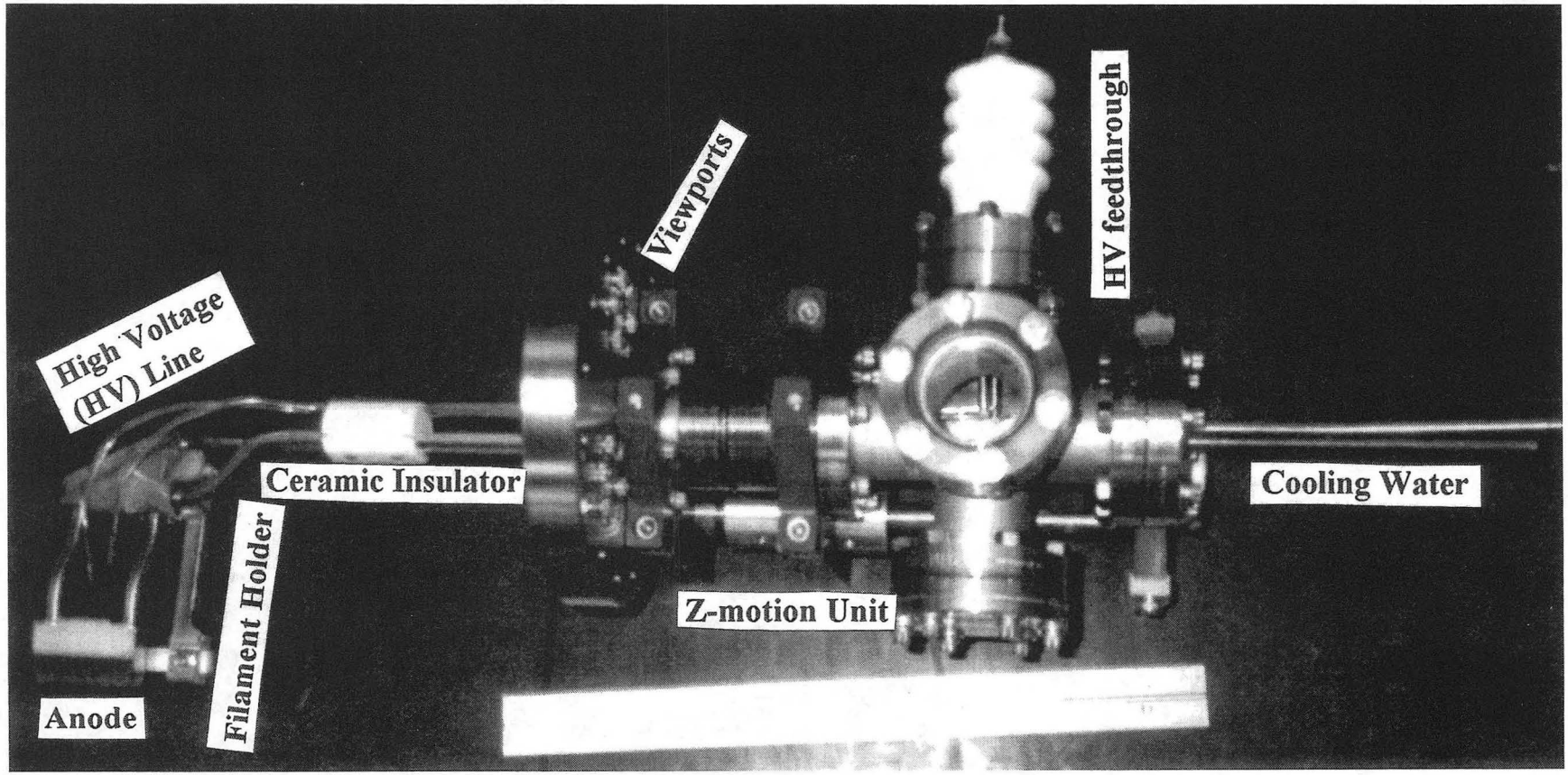
High Voltage
(HV) Line
Viewports
HV feedthrough
Ceramic Insulator
Cooling Water
Filament Holder
Z-motion Unit
Anode

Fig. 2.4 LEED patterns for Cu/Ru(0001) and Cu/O-precovered Ru(0001) at various coverages: (a) 1 ML Cu/Ru(0001); (b) 4ML Cu/Ru(0001) -- note the spot doubling; (c) 0.5 ML O/Ru(0001) -- two domain p(2x1) pattern; (d) 3.7 ML Cu/O/Ru(0001) prepared by annealing 6.5 ML Cu/O/Ru(0001) to 325°C briefly -- $2\sqrt{3} \times 4\sqrt{3}R30^{\circ}$ pattern.

(a) 1 ML Cu/Ru(0001)

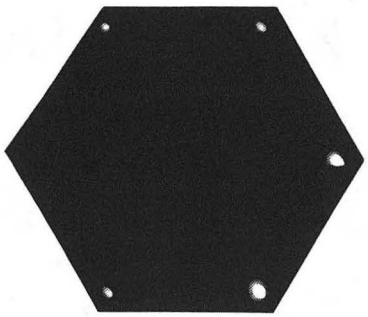

(c) 0.5 ML O/Ru(0001)

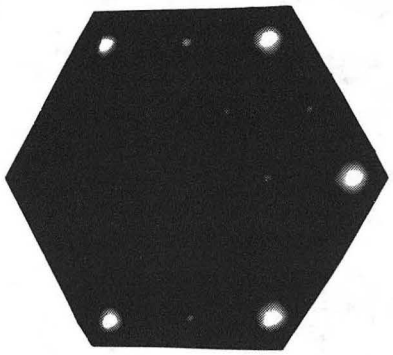

(b) 4 ML Cu/Ru(0001)

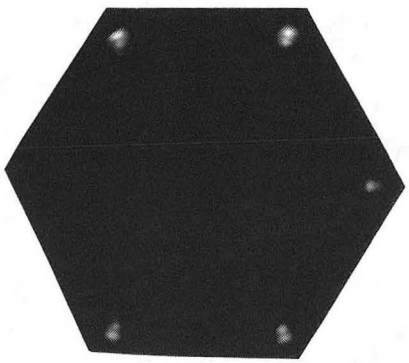

(d) 3.7 ML Cu/O/Ru(0001)

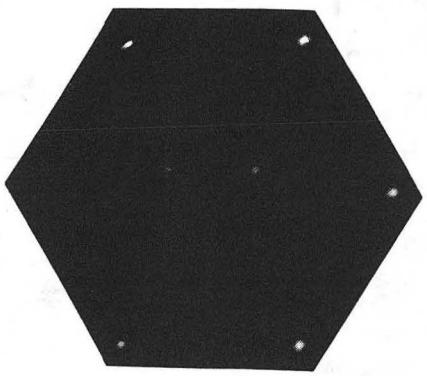

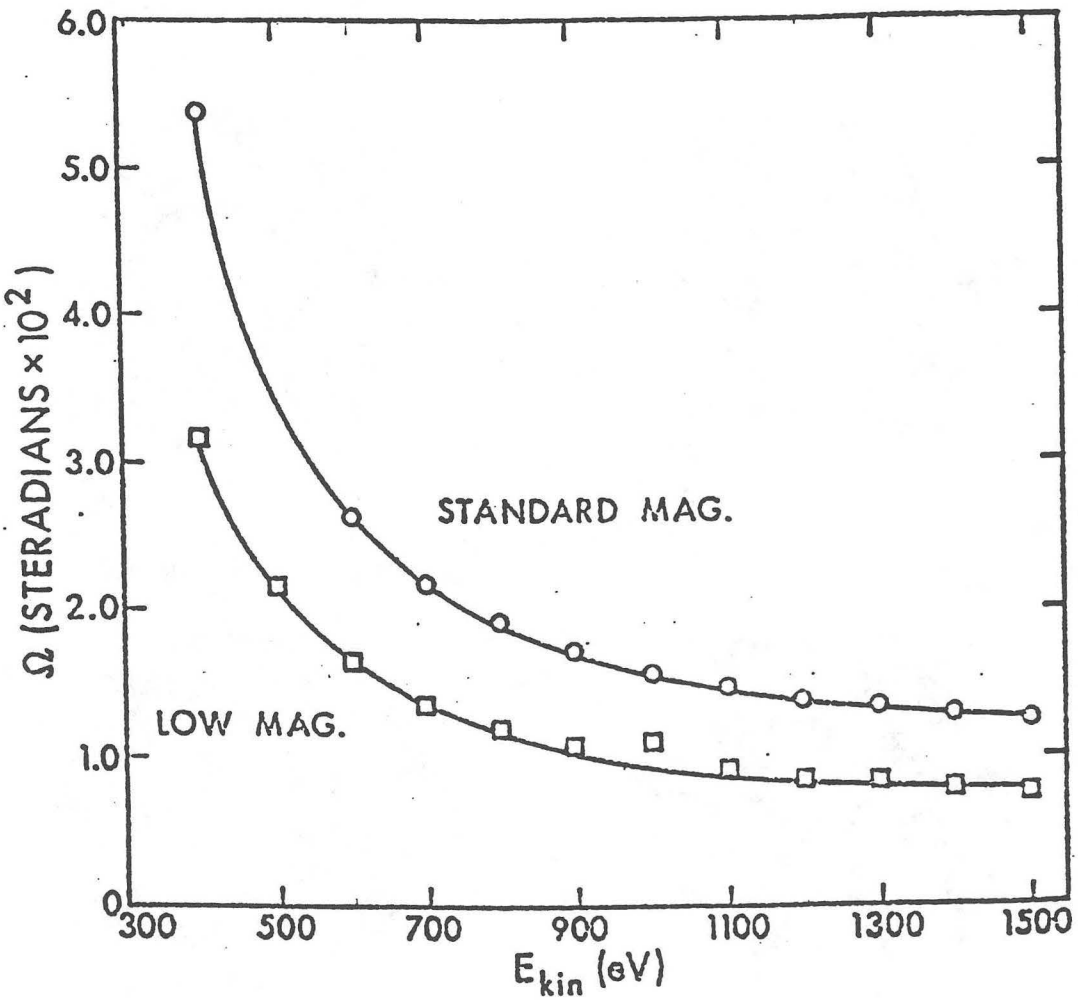

Fig. 2.5 Plot of solid angle, Ω, versus kinetic energy, E_{kin}, in the HP 5950A photoelectron spectrometer, as determined from electron trajectory calculations. This variation of Ω with E_{kin} must be taken into account in comparing any two photoelectron peaks from the spectrometer in doing quantitative analysis. This thesis made use of the standard magnification in the pre-retarding lens [From ref. 3].

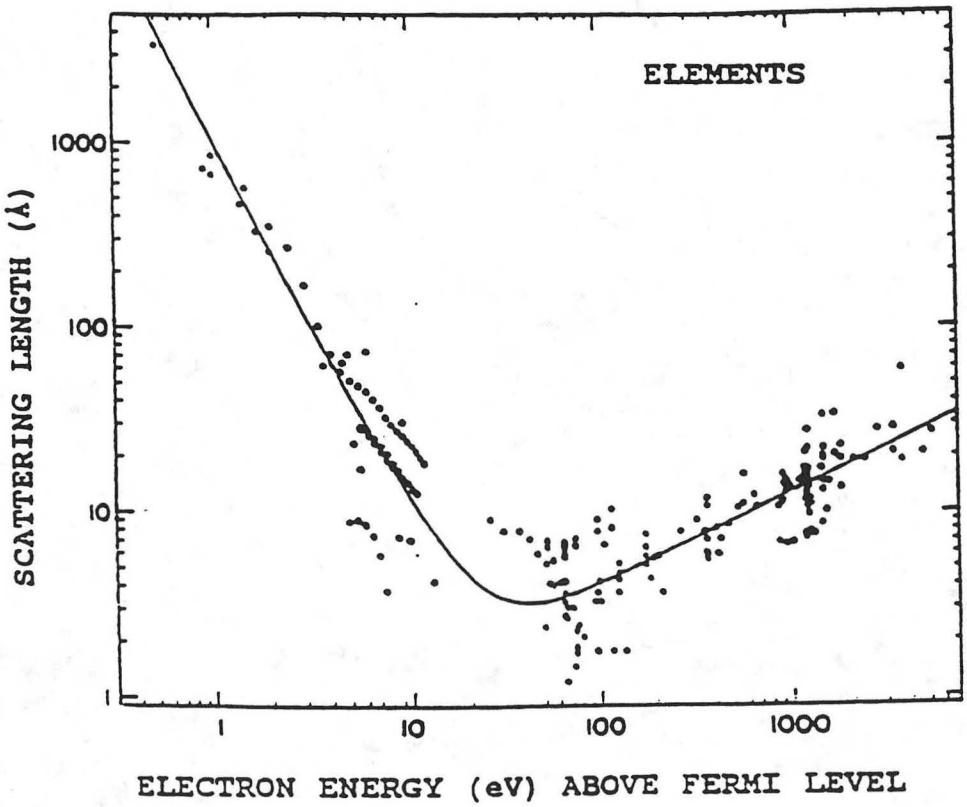

Fig. 2.6 Compilation of experimental inelastic attenuation lengths Λ_e for various solid elements. The solid line is the so-called "universal" curve, although there is considerable variation from it for different elements and compounds [From ref. 17].

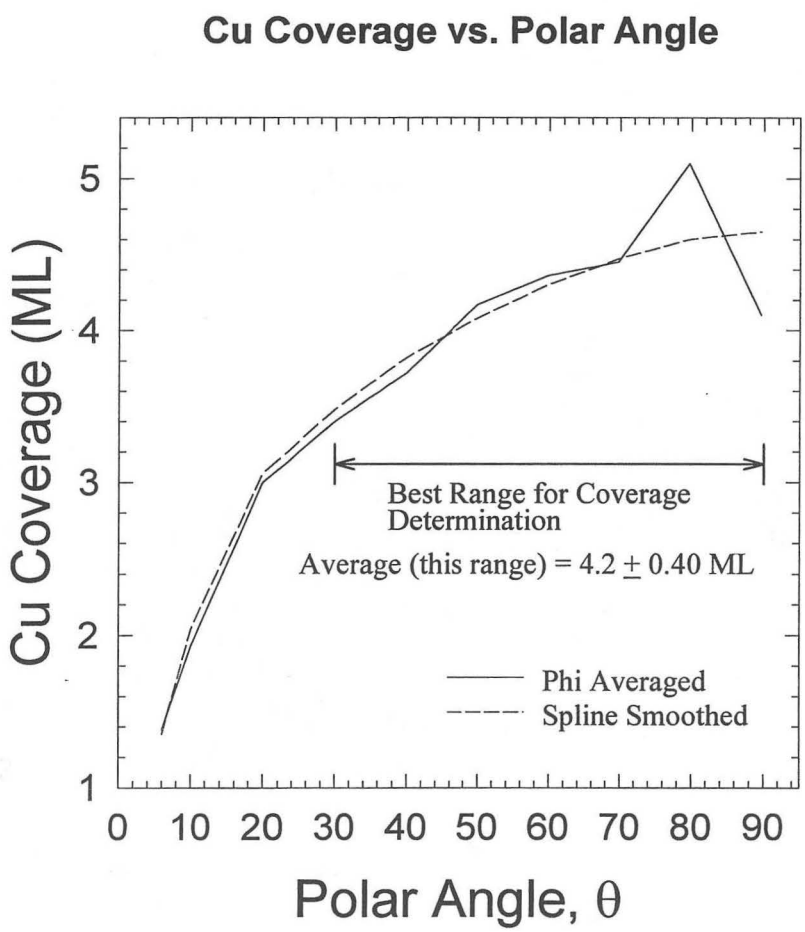

Fig. 2.7 Cu coverage versus polar angle for Cu grown on clean Ru(0001) as determined from the phi-averaged, spline-smoothed ratio of the Cu $2p_{3/2}$ intensity to the Ru 3d intensity.

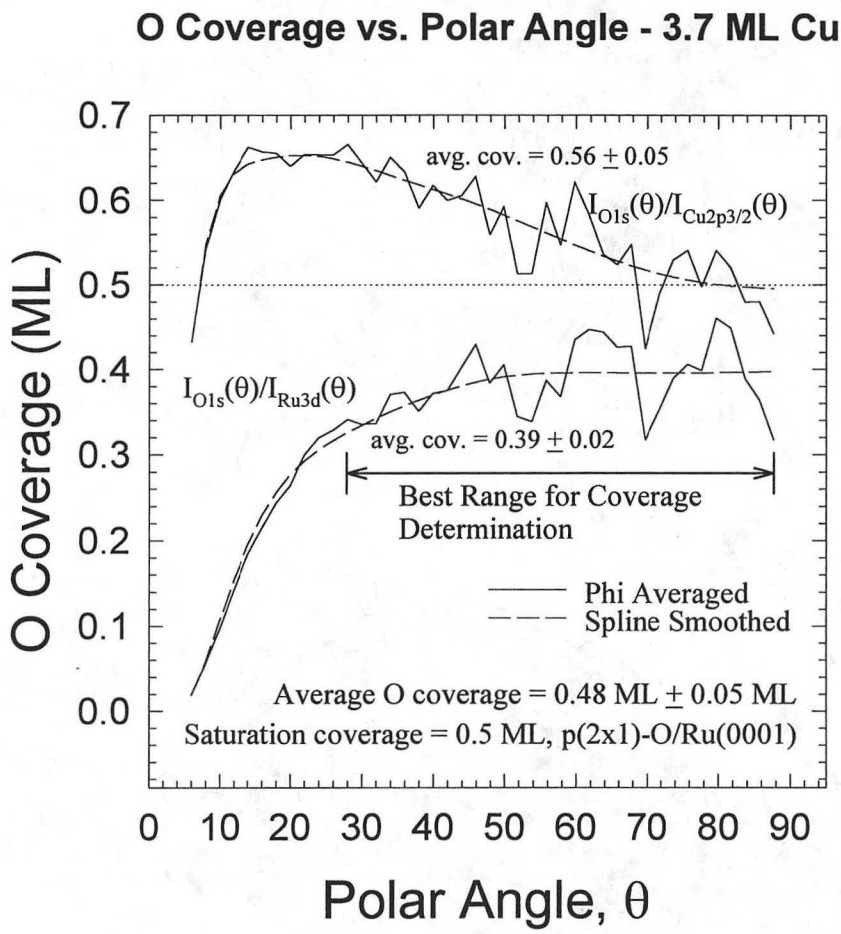

Fig. 2.8 O coverage versus polar angle after growing 3.7 ML Cu on O-precovered Ru(0001) as determined from the phi-averaged, spline-smoothed ratio of the O 1s to the Cu $2p_{3/2}$ intensity and of the O 1s to the Ru 3d intensity.

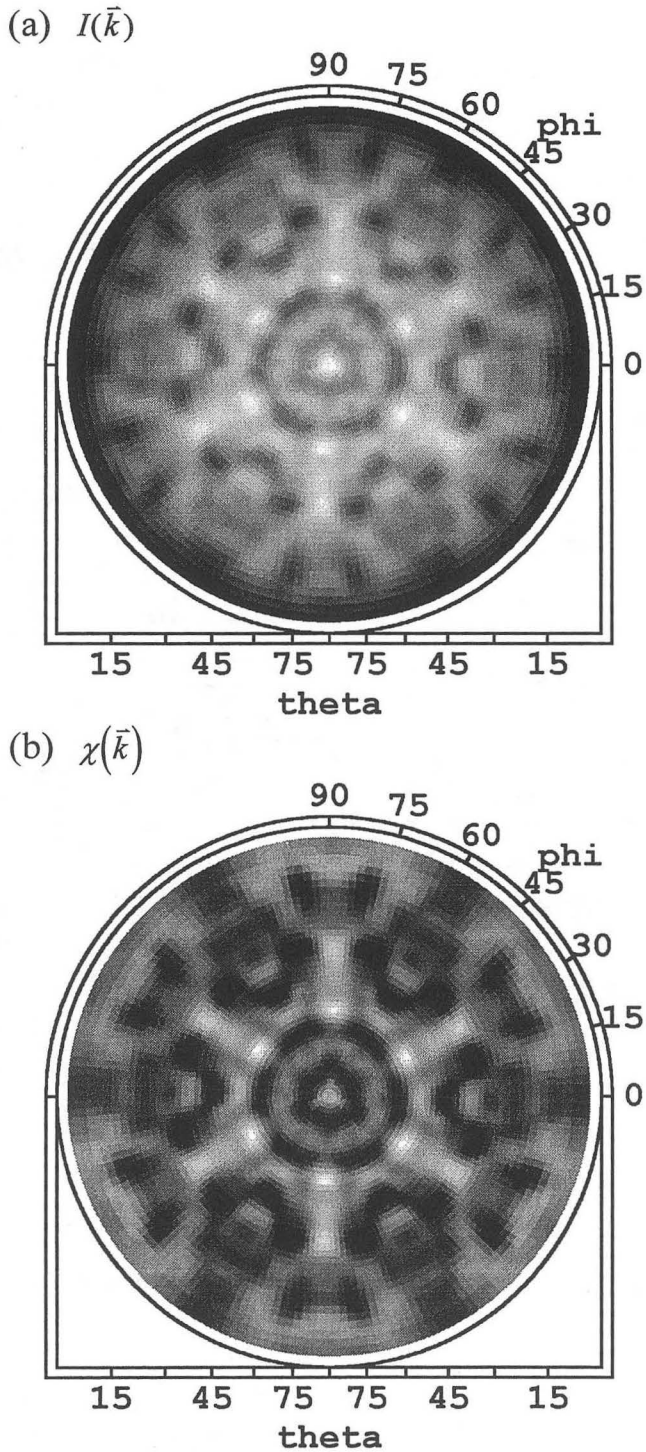

Fig. 2.9 The Ru 3d XPD pattern obtained from clean Ru(0001). In (a), the raw $I(\vec{k})$ data are shown, and in (b), the normalized $\chi(\vec{k})$ data.

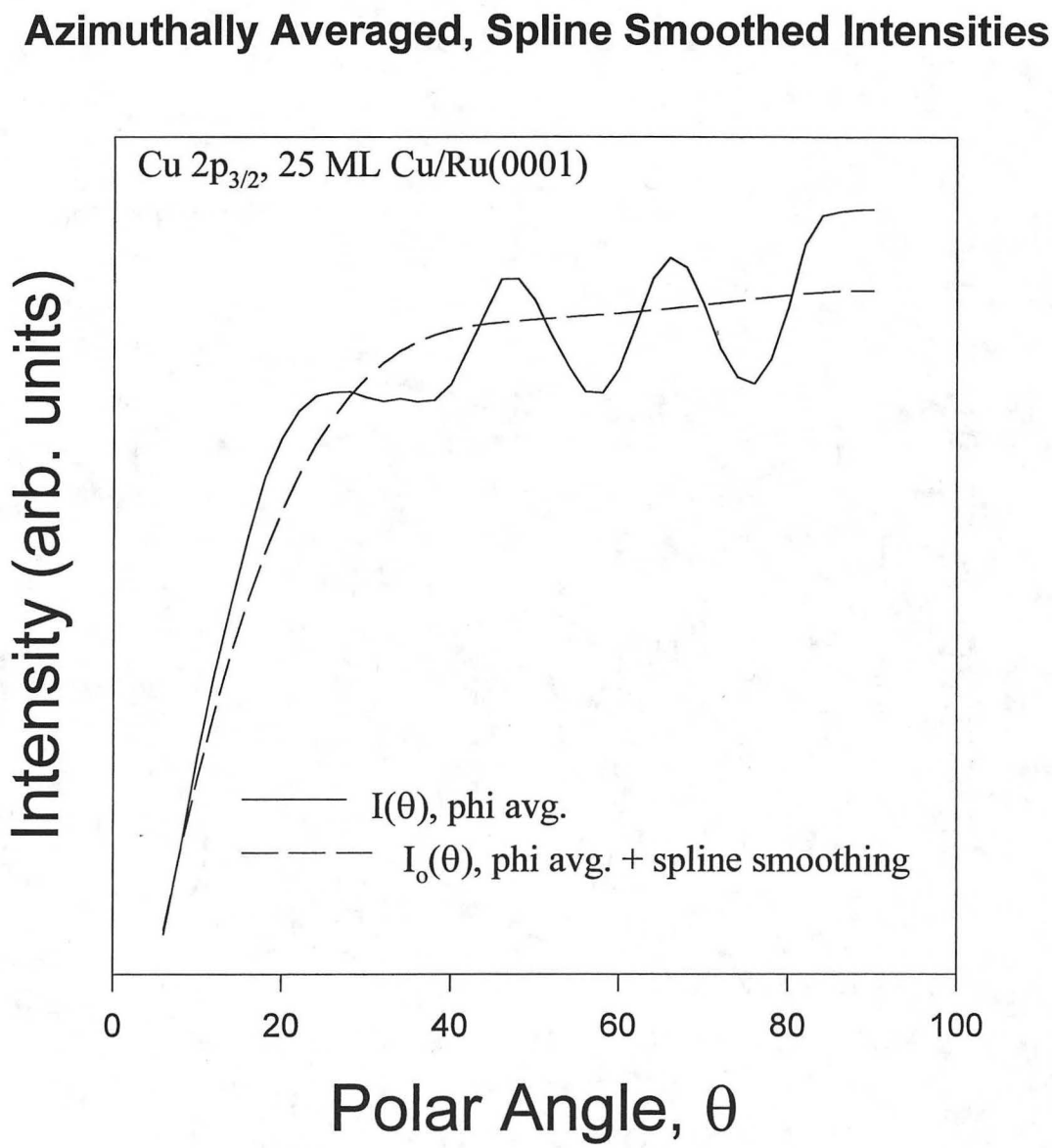

Fig. 2.10 Azimuthally-averaged Cu $2p_{3/2}$ intensity, $\bar{I}(\theta)$, for 25 ML Cu/Ru(0001) and the corresponding phi-averaged, spline smoothed intensity, $I_o(\theta)$. Although not shown here, the intensity has been artificially forced to zero at a cutoff angle of -4°. This is the angle at which the sample is no longer physically exposed to the x-ray source.

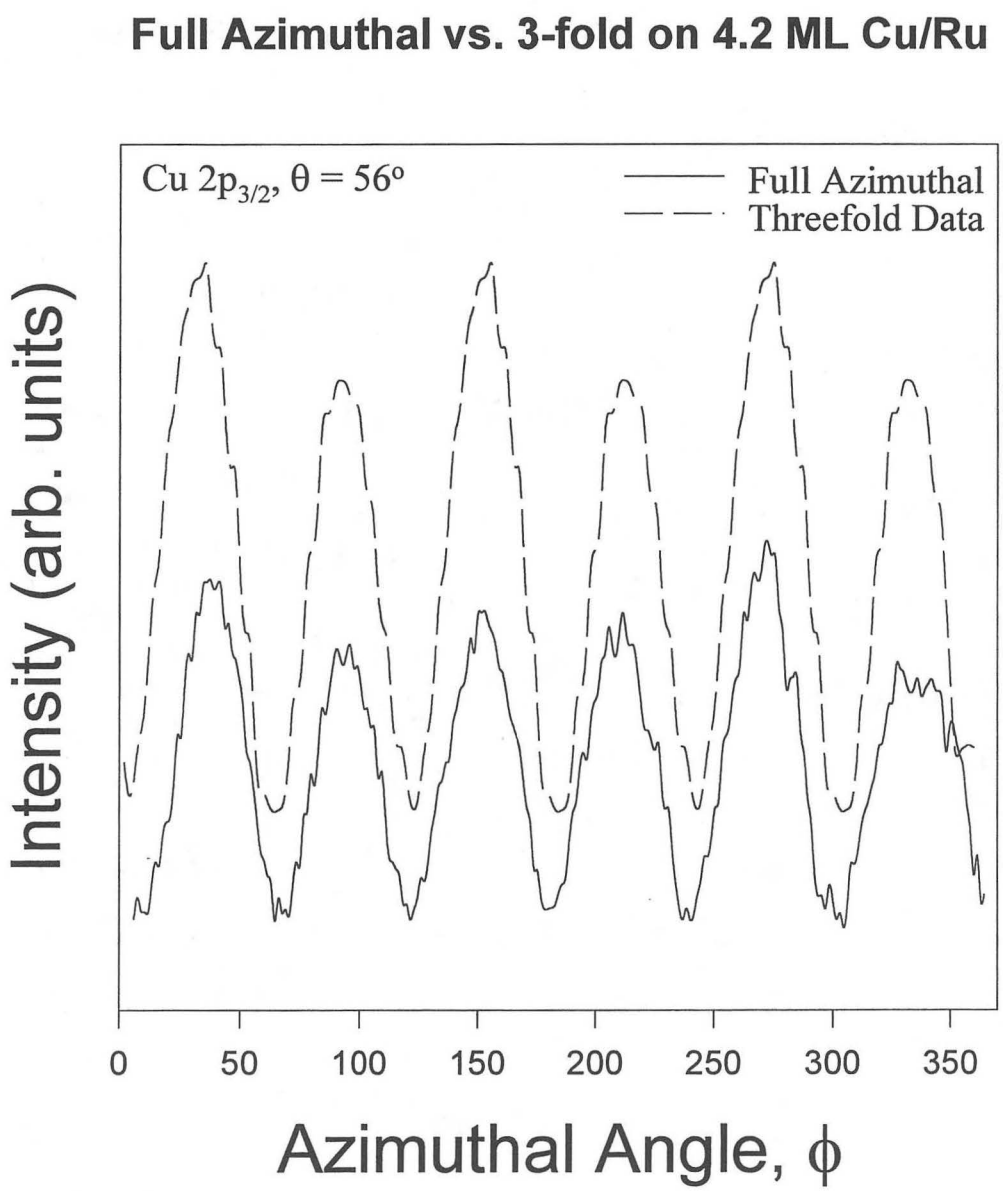

Fig. 2.11 The azimuthal Cu $2p_{3/2}$ curves obtained from 4.2 ML Cu/Ru(0001) at a polar angle of 56° as obtained from a full 360° azimuthal scan and from a partial scan over 120° that has been repeated 3 times. The anisotropy of the two sets of peaks differ from each other by about 4%, resulting in an overall threefold symmetry of the XPD pattern.

Fig. 2.12 Illustration of the effect of angular broadening by Gaussian smoothing on the agreement between experimental and MSC theory for 1 ML Cu on Ru(0001): (a) 1 ML experiment; (b) 1 ML MSC theory without any Gaussian smoothing; (c) 1 ML MSC theory smoothed with a Gaussian of half-width at half-maximum (HWHM) = 2.4^{o}; (d) As (c) but with HWHM = 4.8^{o}; (e) As (c) but with HWHM = 7.1^{o}. The XPD patterns in (b)-(e) have all been initially broadened over a cone of 3.0^{o} half angle via a standard multi-point calculation. The Gaussian smoothing thus represents additional angular broadening.

XPD - Effect of Smoothing MSC Theory

(a)

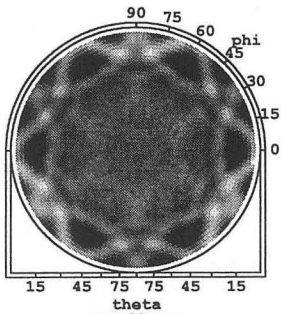

Experiment - 1 ML

(b)

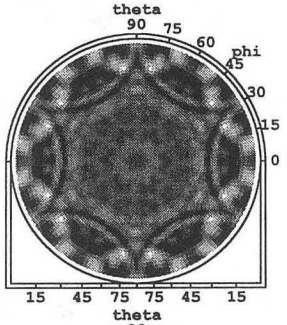

Theory - 1 ML

HWHM = 0o

(c)

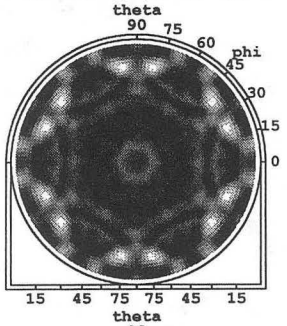

HWHM = 2.4o

(d)

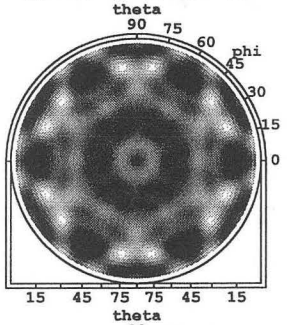

HWHM = 4.8o

(e)

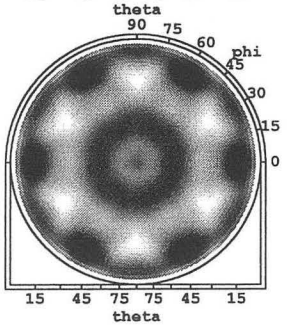

HWHM = 7.1o

Fig. 2.13 As Fig. 2.12 but for 5 ML Cu on Ru(0001): (a) 5 ML experiment; (b) 5 ML MSC theory without any Gaussian smoothing; (c) 5 ML MSC theory smoothed with a Gaussian of half-width at half-maximum (HWHM) = 2.4^{o}; (d) As (c) but with HWHM = 4.8^{o}; (e) As (c) but with HWHM = 7.1^{o}.

XPD - Effect of Smoothing MSC Theory

(a)

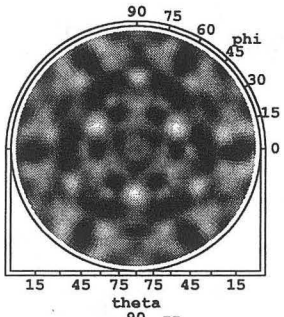

Experiment - 5 ML

(b)

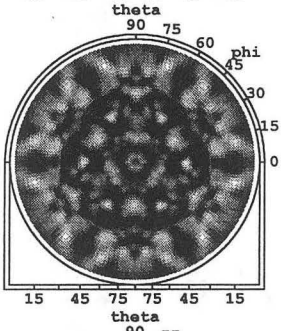

Theory - 5 ML

HWHM = 0o

(c)

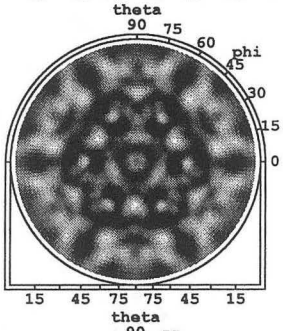

HWHM = 2.4o

(d)

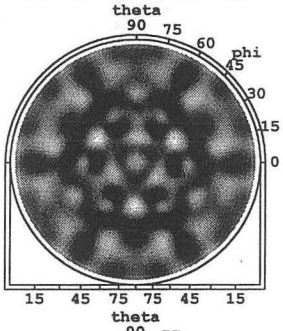

HWHM = 4.8o

(e)

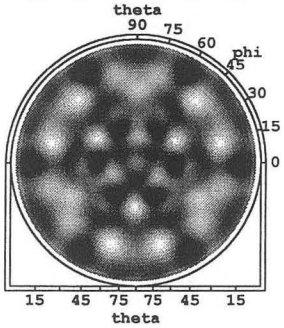

HWHM = 7.1o

Fig. 2.14 As Fig. 2.12 but for experimental data from 25 ML Cu/Ru(0001) compared to six-fold symmetrized MSC theory for 5 ML Cu (assumed to be converged in depth): (a) 25 ML experiment; (b) 5 ML MSC theory without any Gaussian smoothing; (c) 5 ML MSC theory smoothed with a Gaussian of half-width at half-maximum (HWHM) = 2.4^{o}; (d) As (c) but with HWHM = 4.8^{o}; (e) As (c) but with HWHM = 7.1^{o}.

XPD - Effect of Smoothing MSC Theory

(a)

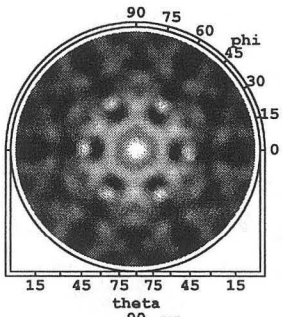

Experiment - 25 ML

(b)

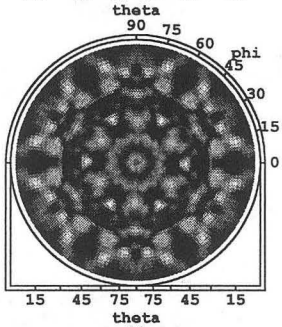

Theory - 5 ML

HWHM = 0o

(c)

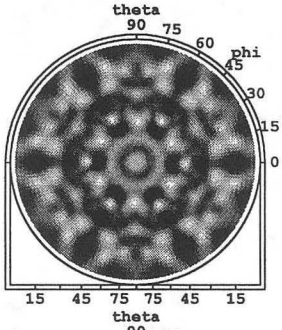

HWHM = 2.4o

(d)

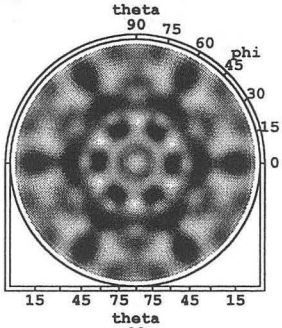

HWHM = 4.8o

(e)

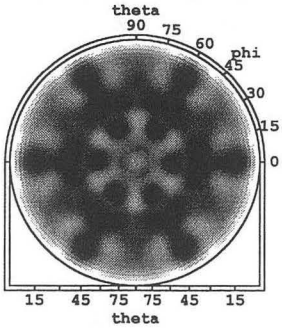

HWHM = 7.1o

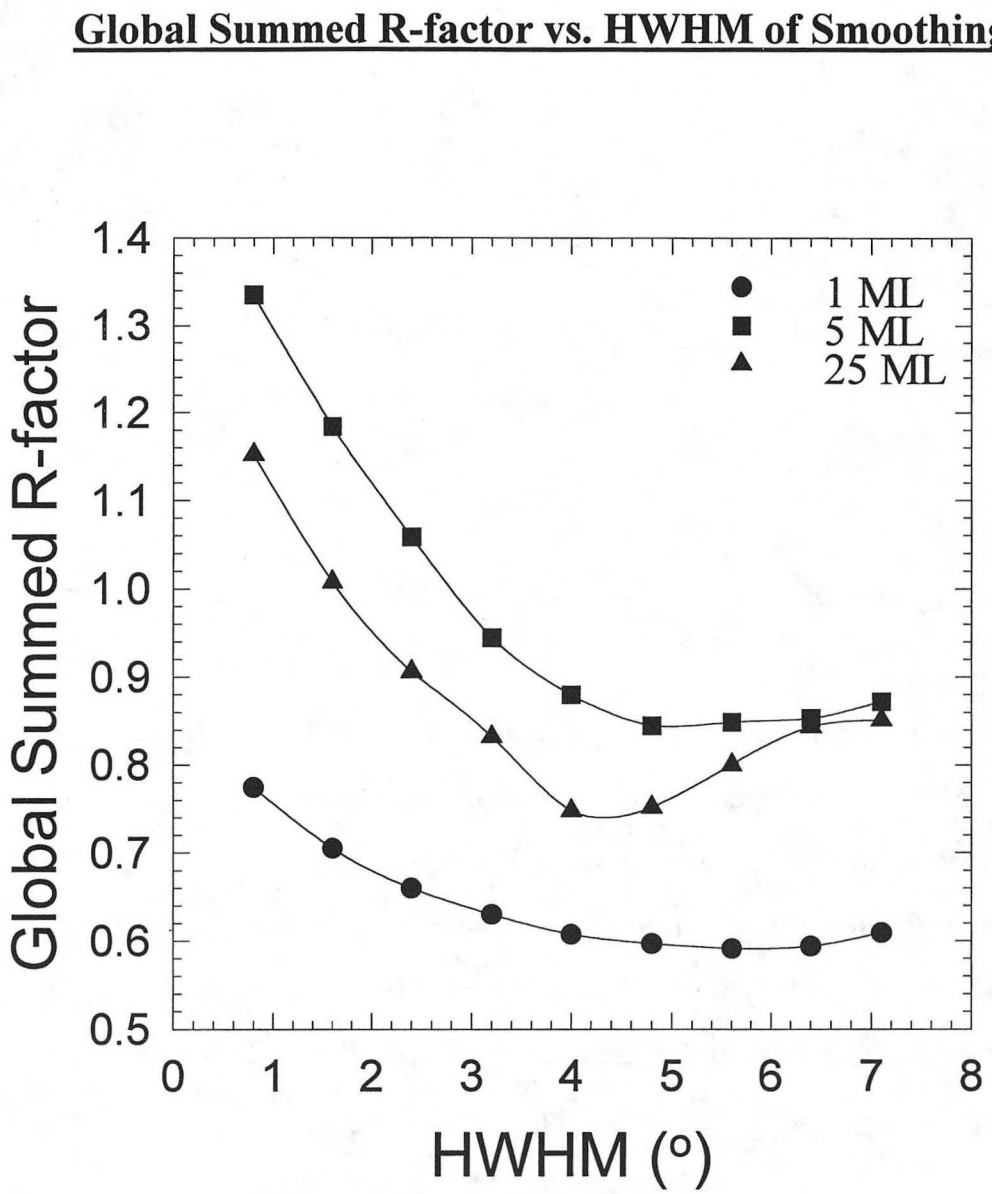

Fig. 2.15 Plot of R-factor versus HWHM of smoothing for 1 ML, 5 ML, and 25 ML Cu/Ru(0001) experimental XPD patterns compared to the corresponding theoretical XPD patterns at various degrees of smoothing.

Fig. 2.16 STM images (from ref. 5(c)) of Cu grown on Ru(0001) for different Cu coverages: (a) 1 ML - pseudomorphic configuration (image size 77 Å x 40 Å); (b) 2 ML - uniaxially contracted from pseudomorphic configuration (image size 95 Å x 65 Å); (c) 3 ML - isotropically contracted from pseudomorpic configuration (image size 700 Å x 400 Å); (d) 4 ML - almost fully relaxed to Cu(111) and rotated azimuthally by ~ 1° from Ru(0001) to form a Moiré pattern (image size 141 Å x 86 Å; unit cell size of Moiré pattern is 49 Å x 49 Å).

(a) 1 ML

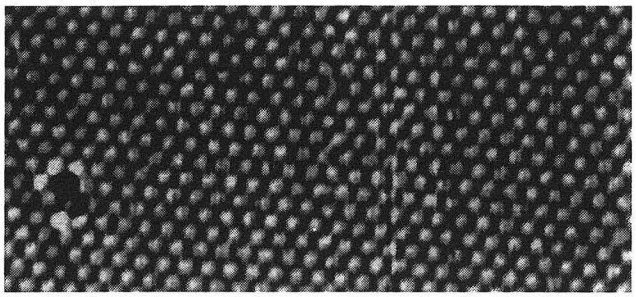

(b) 2 ML

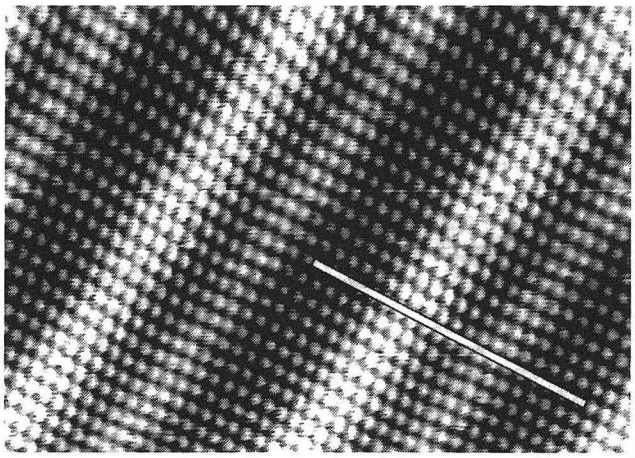

(c) 3 ML

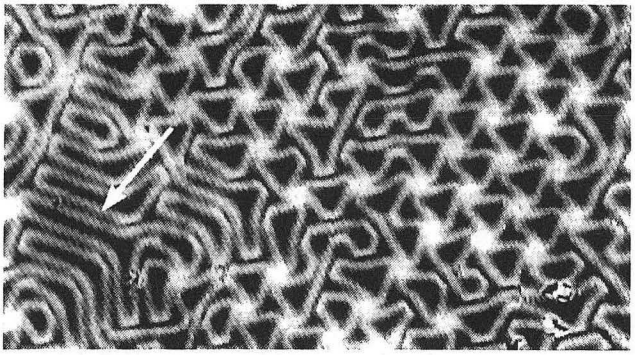

(d) 4 ML

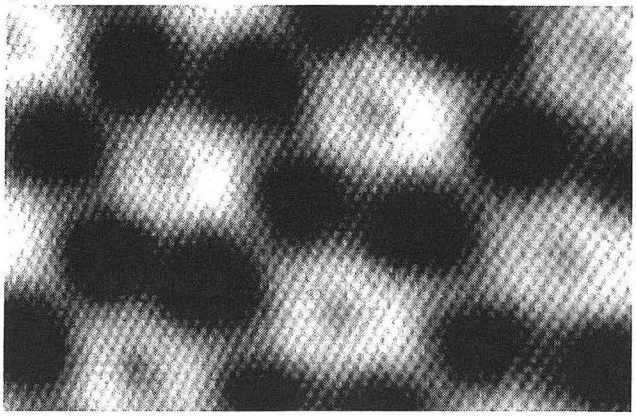

Fig. 2.17 Computer generated Moiré pattern created by placing 2D hexagonal Cu lattice on top of another 2D hexagonal Ru lattice in which the Cu lattice has a lateral lattice spacing 4.9% smaller than the underlying lattice, and has also been rotated by 0.87^{o} relative to the underlying lattice. The unit cell of the Moiré pattern is indicated by the solid lines and is approximately 49 Å x 49 Å in size. The dashed-double dotted lines indicate the atomic rows along which atoms were counted for comparison to the 4 ML STM image of Fig. 2.16(a) in arriving at the most accurate estimate of amount of contraction and rotation in the top layer. Cu is thus still 0.6% <u>expanded</u> from its bulk lateral lattice spacing.

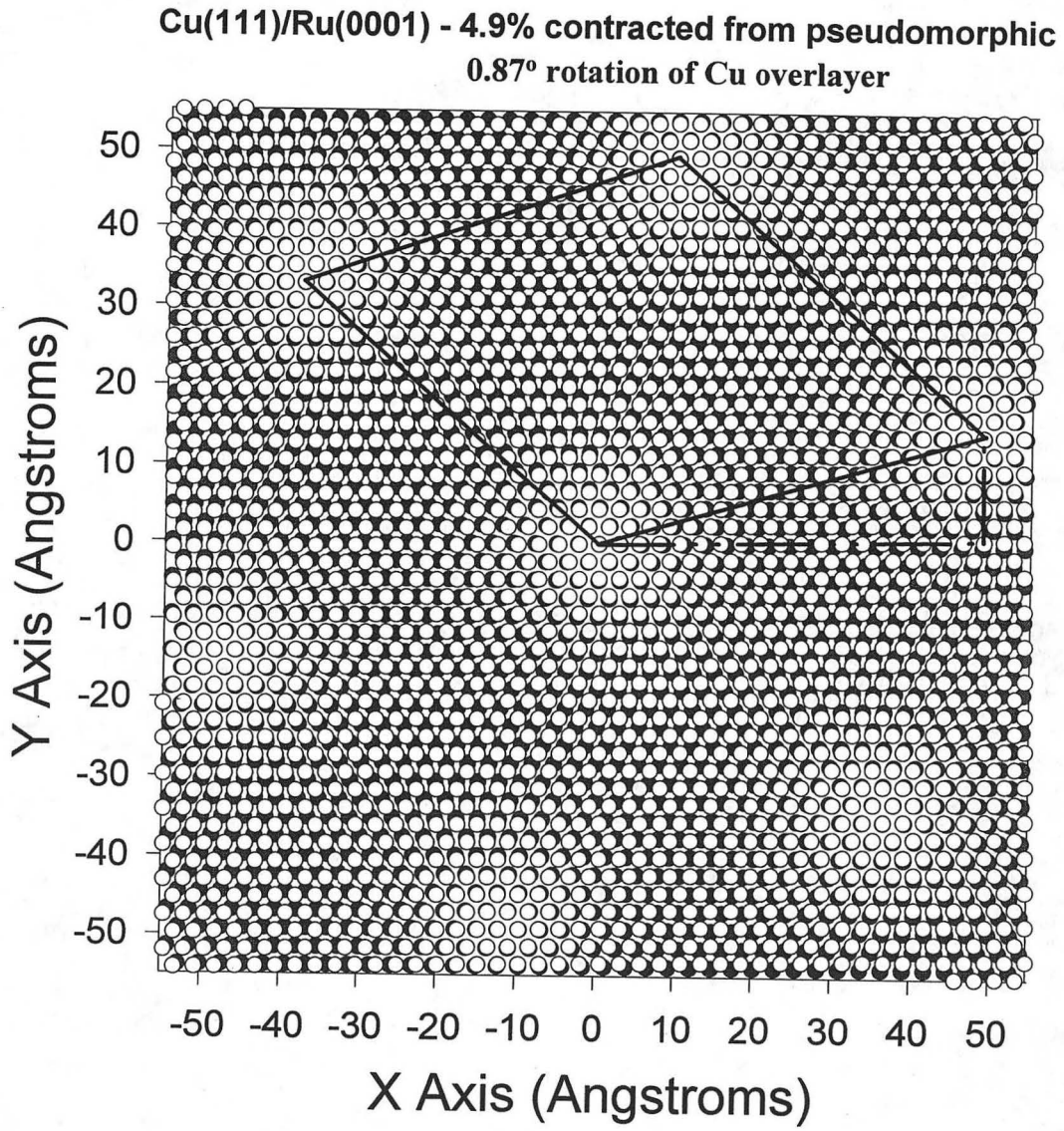
Cu(111)/Ru(0001) - 4.9% contracted from pseudomorphic
0.87° rotation of Cu overlayer
Y Axis (Angstroms)
50
40
30
20
10
0
-10
-20
-30
-40
-50
-50 -40 -30 -20 -10 0 10 20 30 40 50
X Axis (Angstroms)

Fig. 2.18 Scanning Tunneling Microscopy (STM) image of > 5 ML Cu/Ru(0001). Image size is 3000 Å x 1500 Å. [From ref. 2.5(a)].

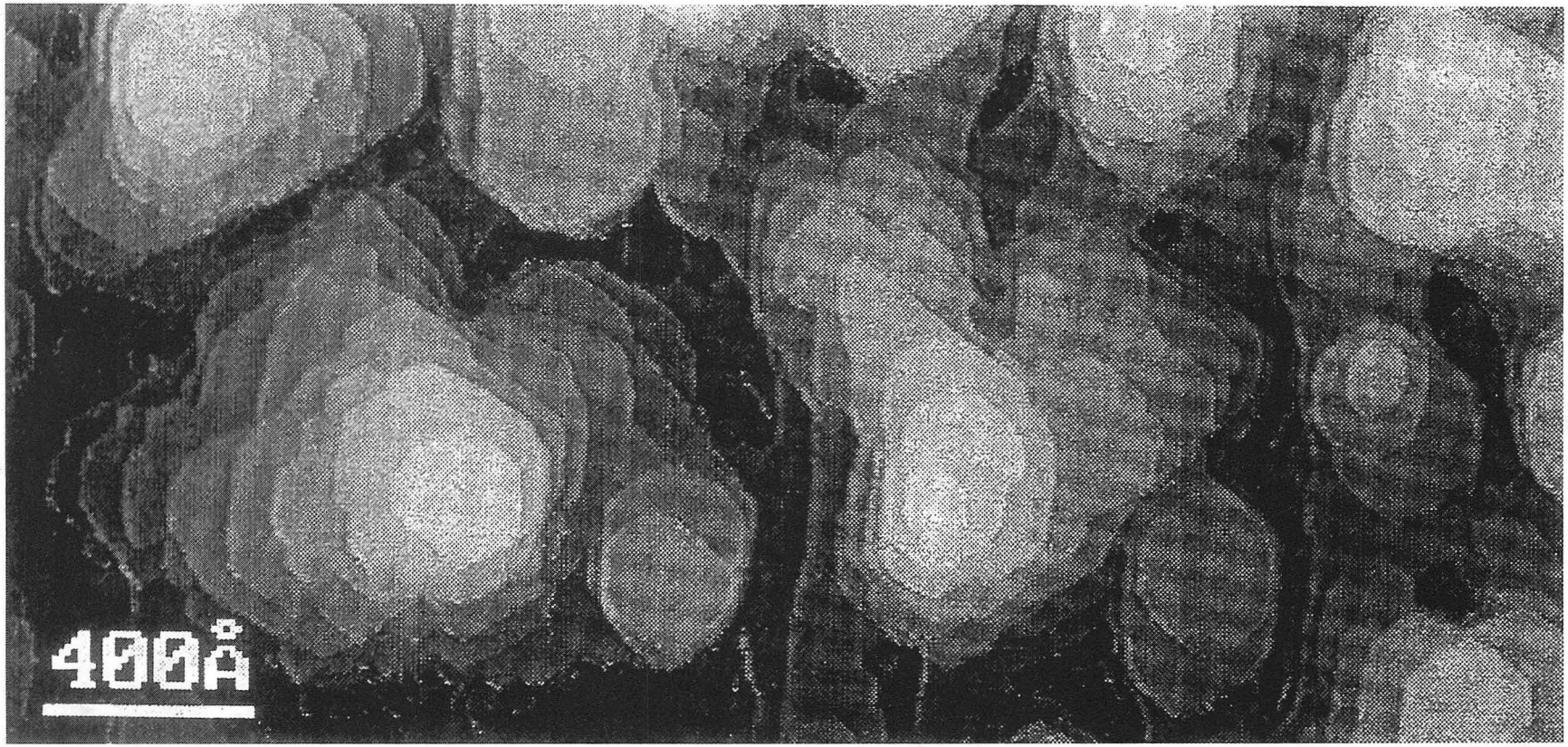
400Å

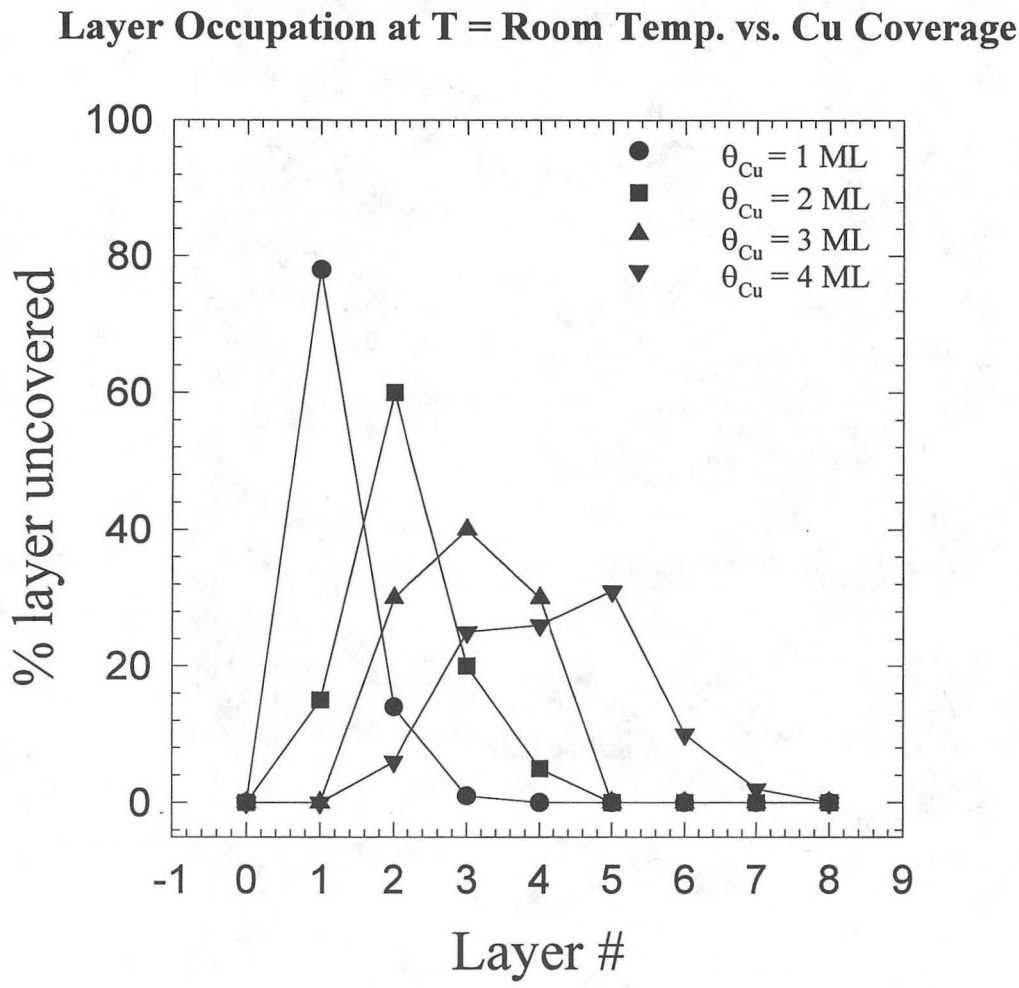

Fig. 2.19 Percent of layer uncovered at different Cu coverages from 1-4 ML for Cu deposited on clean Ru(0001) at room temperature. A 0% layer uncovered means the layer is completely covered or does not exist. A large % uncovered indicates the dominant coverage. Note that these curves are peaked around the nominal coverage. [Percentages obtained from ref. 2.5(d)]

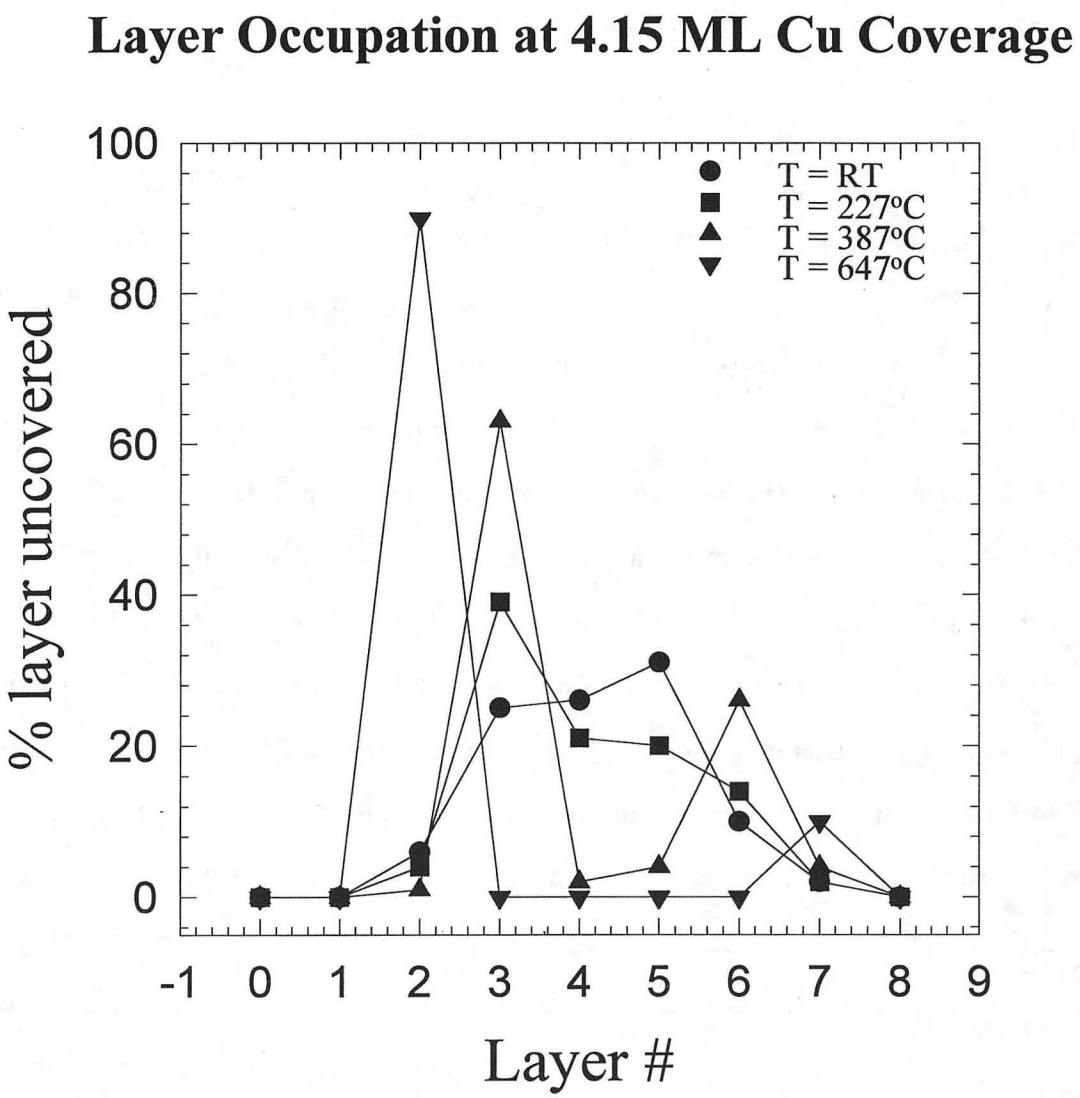

Fig. 2.20 As Fig. 2.20 but for 4.15 ML deposited at room temperature and annealed at different temperatures. [Percentages obtained from ref. 2.5(d)]

Chapter 3

Variation of Mean Emitter Depth with Direction in Core Photoelectron Emission from Single Crystals

Abstract:

We have theoretically studied the variation of mean emitter depths with direction for core photoelectron emission from single crystals, including the effects of both isotropic inelastic scattering and single and multiple elastic scattering. Our calculations were carried out for emission in the 1 keV energy range on both simple chains of atoms embedded in an isotropic inelastic medium and on larger atomic clusters that should more realistically simulate emission from a semi-infinite single-crystal substrate or epitaxial overlayer. The mean emitter depth is found to vary by as much as $\pm$30% with direction. It is lowest just adjacent to low-index chains of atoms because of destructive interferences in photoelectron diffraction. It is highest along low-index directions due to forward scattering, in spite of well-known reductions in intensity along such directions due to multiple-scattering defocusing effects. These variations of mean emission depth, due to photoelectron diffraction effects (as well as analogous Auger diffraction effects), should be taken into account in the quantitative characterization of surfaces, surface concentration profiles, and epitaxial surface structures using photoelectrons and Auger electrons.

3.1 Introduction and Methodology

Angle-resolved core-level x-ray photoelectron spectroscopy (XPS) is by now a standard tool for the quantitative analysis of surfaces [3.1]. A crucial ingredient in accurately using such XPS data is the electron inelastic attenuation length, Λ_e. Various discussions and tabulations of this quantity appear in the literature [3.2]. Through Λ_e and

the assumed exponential attenuation of elastically scattered intensity along path lengths associated with it, the well-known and much-used variation of mean emitter depth with takeoff angle arises [3.1]. However, the possible importance of elastic scattering in determining effective electron propagation distances and mean emitter depths has also been pointed out, in particular by Nefedov and co-workers [3.3], and more recently by others [3.4]. In theoretical simulations, Nefedov and co-workers simultaneously treated both inelastic scattering and elastic scattering in core emission from amorphous atomic arrays. This work suggested that elastic scattering could significantly alter the effective inelastic attenuation length, and with it also mean emitter depths, especially as the detection direction is varied from normal to grazing [3.3], conclusions that have been confirmed in later work [3.4]. Beyond these studies aimed at the analysis of polycrystalline or amorphous samples, photoelectron diffraction effects on peak intensities, as produced by single and multiple elastic scattering, and their resultant influence on quantitative analyses, have also been considered for both adsorbates [3.5] and multilayer single crystals [3.6]. However, there have been no attempts to look in detail at the expected variation in effective mean emission depths from single crystals with full allowance for photoelectron diffraction. This is the aim of the present chapter.

One diffraction effect of particular interest in this context is multiple-scattering (MS) in photoelectron diffraction and Auger electron diffraction at higher energies above ~500 eV from multilayer systems [3.7-3.9], especially along low-index chains of atoms. MS is expected to be enhanced along such rows due to the strong forward scattering or forward focusing expected at energies above about 500 eV [3.7-3.9]. One effect of such MS (first predicted theoretically by Tong et al. [3.7] and later studied by Xu, Barton, and Van Hove [3.8], and by Kaduwela et al. [3.9]) is a "defocusing" of scattered intensity along chain directions such that single scattering (SS) calculations can significantly overestimate intensities along such directions. Indications of such defocusing effects in experimental data were first reported by Egelhoff for epitaxial films of Cu and Ni grown

on Ni(001) [3.10]. Various calculations have also shown that, at medium-to-high energies in the 500-1500 eV range, contributions from deeper atoms along low-index directions will be diminished by such MS effects, and thus, that it may be possible to consider only contributions from atoms in the top 5-10 layers in quantitative analyses of experimental data [3.7-3.9]. We return to this point also in Chapter 4. More detailed MS simulations of such effects have also shown that there is a decrease in the full width at half maximum (FWHM) peaks along the direction of an atomic chain as the number of atoms in the chain is increased [3.9].

In this paper, we study the variation with direction of the effective mean emitter depth above a single-crystal sample, considering not only emission along low-index chains, but also emission over the full range of angles away from such chains. Emitters in n layers, j = 0,...n-1, at vertical distances, z_j, below the surface are weighted by their intensity contributions in a given direction, as calculated from a photoelectron diffraction calculation which includes both inelastic and elastic scattering effects. Inelastic scattering is included along all portions of single and multiple scattering path lengths below the surface plane. Thus, in some of our calculations, an isolated chain is embedded in an isotropic inelastic medium. The mean emitter depth $\overline{Z}(\vec{k})$ is then calculated according to:

$$\overline{Z}(\vec{k}) = \frac{\sum_{j=0}^{n-1} z_j I_j(\vec{k})}{\sum_{j=0}^{n-1} I_j(\vec{k})} \tag{3.1}$$

where $I_j(\vec{k})$ is the intensity in the $\vec{k}$ direction due to an emitter in the jth layer of atoms, z_j is the depth of the jth layer, and n is the total number of layers in the cluster or number of atoms in the chain. For a constant layer spacing a, z_j = ja. j = 0 corresponds to the surface layer of emitters.

Another important reference against which to judge the behavior of $\overline{Z}(\vec{k})$ is the mean depth, as calculated with complete neglect of any elastic scattering effects. This we denote by $\overline{Z}_0(\vec{k})$, and it is determined in a standard way by assuming that the intensity from each emitting layer in a given direction is the same except for exponential inelastic attenuation, and further that the inelastic attenuation length, Λ_e, is isotropic:

$$\overline{Z}_0(\vec{k}) = \frac{\sum_{j=0}^{n-1} ja \cdot \exp(-ja / \Lambda_e \cos\theta)}{\sum_{j=0}^{n-1} \exp(-ja / \Lambda_e \cos\theta)}. \tag{3.2}$$

Any difference between $\overline{Z}(\vec{k})$ and $\overline{Z}_0(\vec{k})$ is thus due to elastic scattering and diffraction effects.

We have calculated mean emitter depths for two different geometries: small clusters of linear chains with up to 10 atoms in 10 layers and large clusters with up to 79 atoms in 7 layers. The interatomic separations and geometries of these clusters are chosen to represent emission from both the fcc lattice of Ni and the more open diamond lattice of Si. Mean emitter depths have been calculated in both spherical-wave single-scattering [3.11] and fully-converged spherical-wave multiple-scattering approaches [3.9]. As a reference, such depths were also calculated in the limit for which only inelastic scattering attenuation is included via an isotropic Λ_e (as usually assumed in surface analysis). The diffraction calculations were carried out using a multiple scattering code developed by Kaduwela and co-workers [3.9] and based on the separable Green's function matrix method developed by Rehr and Albers [3.12].

3.2 Results and Discussion

3.2.1 Linear Chains of Ni and Si

First we present results for the simple case of linear chains in Figs. 3.1-3.4. Fig. 3.1(a) shows the geometry of a chain of Ni atoms positioned along the vertical (z) direction so as to represent a [001] chain at a Ni(001) surface, thus the spacing here is a = 3.52 Å. For each choice of j in a series, the jth atom at the bottom of the chain is considered to be the emitter and the surface is defined at the topmost scatterer. The emission angle, θ, is defined relative to the surface normal (i.e. 0° along the normal and $\pm 90^o$ along the surface). SS and MS calculations were carried out for choices of n = 2 to 10 atoms along the chain. We considered the example of Ni 2p emission through Al Kα excitation, and used correct $l \pm 1$ final-state interference. The kinetic energy of the photoelectron is thus 636eV, and an appropriate inelastic attenuation length is Λ_e = 10.0 Å [3.2,3.5]. Fig. 3.1(b) shows the variation of $\overline{Z}(\vec{k})$ with emission angle θ for SS. Analogous results for MS are presented in Fig. 3.1(c). The results for $\overline{Z}(\vec{k})$ are shown as stacked solid curves for chain lengths from 2 to 10 atoms. Corresponding results for the inelastic-only reference $\overline{Z}_0(\vec{k})$ are shown as dashed curves superimposed on each solid curve.

The $\overline{Z}(\vec{k})$ results in Fig. 3.1 show the expected peaks and valleys associated with successive constructive and destructive interference of the direct and scattered photoelectron wave components. These effects have been discussed in detail previously [3.1], with the forward scattering peak along the chain being designated "zeroth order" constructive interference, the next peak at about 22° in SS and $24\text{-}26^o$ in MS being "first order", etc. In single scattering, the locations, θ_m, of the peaks corresponding to these different diffraction orders, m, are given by

$$2\pi m = kr_k(1-\cos\theta_m) + \psi(\theta_m), \quad m = 1,2,\ldots, \tag{3.3}$$

where r_k is the distance to a given scatterer along the chain, $r_k(1-\cos\theta_m)$ is the path-length difference between direct and scattered waves, and $\psi(\theta_m)$ is the additional phase difference between the direct and the scattered waves produced by elastic scattering. The first-order peaks for pairs of atoms 3.52 Å apart occur very close to second-order peaks for 7.04 Å pairs, third-order peaks for 10.56 Å pairs, fourth-order peaks for 14.08 Å pairs, etc. Thus, the "first-order" peak in $\overline{Z}(\vec{k})$ is due to a superposition of different orders from different emitter-scatterer pairs in the chain. Multiple scattering also tends through the superposition of components with additional path-length-dependent phase shifts to slightly shift and sharpen these diffraction features as the number of atoms in the chain is increased.

Another important observation from Fig. 3.1 is that $\overline{Z}(\vec{k})$ is much higher along the atomic rows in SS as compared to MS. In SS, this is simply the result of strong forward scattering from the various atoms in the chain. In MS, defocusing effects tend to markedly reduce $\overline{Z}(\vec{k})$ along the chain axis, <u>but it still has a strong local maximum along this direction</u>. As the chain length increases in both SS and MS, the mean emitter depth increases also, with a slow convergence to the value that would be expected for an infinitely long chain (semi-infinite substrate). Defocusing causes this convergence to be much more rapid in MS, and it is very nearly complete by a 10-atom chain.

Finally, the MS mean emission depths along the chain direction ($\theta = 0^o$) seem to converge for longer chains to the mean emission depth, $\overline{Z}_0(\vec{k})$, that is expected in the absence of any elastic scattering. However, this does not occur in SS, where the long-chain limit for $\theta = 0^o$ remains well above $\overline{Z}_0(\vec{k})$. As a normalized measure of this relationship between $\overline{Z}(\vec{k})$ and $\overline{Z}_0(\vec{k})$, we can use

$$\frac{\Delta\overline{Z}(\theta=0^0)}{\overline{Z}_0(\theta=0^0)} = \frac{\overline{Z}(\theta=0^0)-\overline{Z}_0(\theta=0^0)}{\overline{Z}_0(\theta=0^0)}, \tag{3.4}$$

and this is plotted versus chain length in Fig. 3.2. In MS, $\Delta\overline{Z}(\theta=0^0)/\overline{Z}_0(\theta=0^0)$ decreases with increasing number of atoms in the chain, going to zero for about 10 atoms in the chain. In SS, it remains about 60% above the inelastic-only limit. Although the exact value of $\Delta\overline{Z}(\theta=0^0)/\overline{Z}_0(\theta=0^0)$ at high chain length in MS depends on the degree of inelastic attenuation, the decrease can be qualitatively understood by noting that longer chains permit more and more MS events to occur, but each class of these can have a slightly different phase shift due to elastic scattering (i.e., different contributions like $\psi(\theta_m)$ in Eq. 3.3). As all the scattered waves are added together, the effective randomness of the phases will make it appear as though very little elastic scattering occurs in the forward direction, a point that has been quantitatively discussed recently by Li et al. [3.13]. On the other hand, in SS, all events involve the same forward scattering phase shift $\psi(\theta_m=0^0)$, even as the number of atoms in the chain increases; thus, the intensity along the chain continues to increase until purely inelastic damping leads to convergence. Thus, $\Delta\overline{Z}(\theta=0^0)/\overline{Z}_0(\theta=0^0)$ remains well above zero for SS in Fig. 3.2.

In Figs. 3.3 and 3.4, we show similar results for $\overline{Z}(\vec{k})$ and $\overline{Z}_0(\vec{k})$ for the case of Si 2p emission from atomic chains corresponding to [001] and [111] in silicon. Again, correct $l\pm1$ final-state interference was included in the calculations, solid curves represent $\overline{Z}(\vec{k})$, and dashed curves represent $\overline{Z}_0(\vec{k})$. Here the kinetic energy of the photoelectron is taken to be 600 eV (an energy used in a prior synchrotron radiation study of this system [3.14(a)]), and the attenuation length to be 18.4 Å [extrapolated from higher-energy XPS data [3.14(b)]). The structure of the diamond lattice leads to a constant interatomic spacing along [001] of 5.43 Å [Fig. 3.3(a)] and alternating short and long distances of 2.35 Å and 7.05 Å along [111] [Fig. 3.4(a)]. Although most of the features in these figures are similar to those in Fig. 1, the convergence of $\overline{Z}(\theta=0^0)$ to $\overline{Z}_0(\theta=0^0)$ for MS in longer chains is poor [Figs. 3.3(c) and 3.4(c)]. This difference compared to Fig. 3.1(c) for Ni could be due to the weaker scattering along the Si chains, as caused by both larger interatomic distances and lower atomic number. Also, both the SS and MS curves for

$\overline{Z}(\vec{k})$ along a [111] chain [Figs. 3.4(b) and 3.4(c)] have more diffraction features than the corresponding curves along a [100] direction [Figs. 3.3(b) and 3.3(c)]. This is due to the alternating atomic spacing along the [111] chain which causes two sets of diffraction features to beat against one another.

3.2.2 A large cluster of Ni

In order to determine whether the effects noted above for isolated chains would also occur along chain directions in a real multilayer substrate system, we have, in addition, performed SS and MS calculations on large clusters made up of atoms in Ni(001) planes. For this purpose, we have carried out calculations for a 79-atom cluster containing seven (001) layers and occupying somewhat more than a 45° wedge in azimuth, the minimum needed by symmetry to accurately calculate the intensity in the full hemisphere above the surface. Each layer has an emitter, and the number of atoms in each layer (ordered from the surface inward) is 16, 16, 15, 13, 10, 8, and 1. The kinetic energy of the photoelectron is again 636 eV, and full SS and MS calculations were done for Ni 2p emission with correct $l\pm1$ final state interference.

In Figs. 3.5(a) and 3.5(b), we first present the total SS and MS intensity, respectively, over the full 2π solid angle above the surface, as projected down onto the (001) = k_x,k_y plane. This intensity has been normalized in a standard way into a chi function via $\chi(\vec{k})=[I(\vec{k})-I_0(\vec{k})]/I_0(\vec{k})^{1/2}$ before projection. The forward scattering peaks along several low index directions such as {001}, {011}, {101}, and {112} are labeled in the figures. As expected, MS defocusing effects reduce the relative intensities along these directions, especially for the highest-density {011} directions. However, away from these directions, there are, in general, very similar diffraction features in both SS and MS. The mean emitter depth, $\overline{Z}(\vec{k})$, for these two cases is shown in similar k_x,k_y plots in Figs. 3.5(c) and 3.5(d), with the same low-index directions labeled. In general,

the behavior of $\overline{Z}(\vec{k})$ is similar to what we have observed before for the chains: an increase along the different chain directions due to forward scattering and a decrease adjacent to these chains due to destructive interference in between zeroth-order and first-order diffraction peaks. To examine this situation in more detail, we show, in Fig. 3.6, $\overline{Z}(\vec{k})$ and $\overline{Z}_0(\vec{k})$ as a function of polar angle θ for two different azimuthal angles, $\phi = 0^o$ and 45°, that correspond to scans in high-symmetry planes of the fcc lattice ([001] through [101] and [001] through [112], respectively). Again, certain low-index directions are labeled: [101] and [001] in Fig. 3.6(a) and [112] and [001] in Fig. 3.6(b). SS results for $\overline{Z}(\vec{k})$ are shown here as solid curves, MS as dotted curves, and $\overline{Z}_0(\vec{k})$ as dashed curves. Within the 7 layers of this cluster, there were several chains of atoms: a 6-atom chain with interatomic spacing 2.49 Å in the [101] direction, a 4-atom chain with spacing 3.52 Å in the [001] direction, and a 4-atom chain with spacing 4.31 Å in the [112] direction. The number of scatterers along these low-index directions is too low to make any quantitative statements about the convergence to $\overline{Z}_0(\vec{k})$ seen in the MS results of Figs. 3.1 and 3.2. They also lead to lower overall $\overline{Z}(\vec{k})$ values than seen with the longer chains. Nevertheless, all of the systematic trends seen before for isolated chains are again found in Fig. 3.6: forward scattering peaks along low-index directions are much reduced in intensity and narrowed in width in going from SS to MS, as noted before; even in the more accurate multiple scattering curves, the mean emitter depth is enhanced by as much as 25-30% relative to that expected with no elastic scattering due to forward scattering along low-index directions, <u>and</u> is decreased by as much as 25-30% just adjacent to these directions, due to destructive interference effects.

Finally, we point out that a similar sort of variation of mean emitter depth with direction occurs if the photoelectron emission from a localized site is treated in a Kikuchi-band picture which emphasizes long-range order and Bragg reflections from low-index sets of planes, but in the limit of strong inelastic damping. Although the Kikuchi-band model is not as quickly convergent a method for describing photoelectron

or Auger electron diffraction as the short-range order cluster approach used here, it has been pointed out before by Goldberg et al. [3.15(a)] and Trehan et al. [3.15(b)] that both of these approaches are essentially describing the same physics and agree with one another in the limit of a large cluster with long-range order and/or strong inelastic damping. To illustrate this correspondence more quantitatively, we have carried out calculations of intensity and $\overline{Z}$ using a simple two-beam Kikuchi model that has been applied previously to photoelectron diffraction [3.15]. An expression for intensity I as a function of the deviation angle θ' from a given set of (hkl) planes appears elsewhere [3.15]. The function $|\psi(z,\theta')|^2$, which represents the probability of emission at angle θ' from a depth z below the surface [3.15], has been appropriately integrated over z to yield $\overline{Z}(\theta')$:

$$\overline{Z}(\theta') = \frac{\int_0^\infty z|\psi(z,\theta')|^2 dz}{\int_0^\infty |\psi(z,\theta')|^2 dz} = \frac{a/d^2 + b(d^2-c^2)/(d^2+c^2)^2}{a/d + bd/(d^2+c^2)}, \tag{3.5}$$

where

$a = 2x^2 - 2x + 1,$

$b = 2x(1-x),$

$c = (1+y^2)^{1/2}(2m/\hbar^2 E)V'_{hkl},$

$d = 1/\Lambda_e \cos\theta',$

$x = \frac{1}{2}\left[1 + (y-1)/(1+y^2)^{1/2}\right],$

$y \cong (2E/V'_{hkl})\sin\theta_{hkl}(\sin\theta_{hkl} - \sin\theta'),$

θ' = the angle of emission relative to the *hkl* planes,

θ_{hkl} = the first-order Bragg angle for the *hkl* planes,

m = electron mass,

E = the photoelectron kinetic energy, and

V'_{hkl} is the Fourier coefficient for a given set of planes *hkl* as determined from a Hartree-Slater central-field potential with a Debye-Waller factor included.

The quantity d is here defined such that the surface boundary of inelastic scattering is perpendicular to the (hkl) planes under consideration, so as to be analogous to the chain geometries of Figs. 3.1, 3.3, and 3.4.

Using values for the above parameters from prior work [3.15], we have carried out calculations for Cu 3p emission from crystalline Cu with Al Kα excitation, corresponding to an electron kinetic energy of 1420 eV. The inelastic attenuation length was taken to be 9.8 Å [3.15]. Fig. 7 shows $I(\theta')$ and $\overline{Z}(\theta')$ for θ' relative to the lowest-index (111), (002), (022), and (024) planes from which Bragg reflections can occur. For all of these cases, there is qualitative similarity to the chain calculations of Figs. 3.1, 3.3, and 3.5: a maximum in $\overline{Z}(\theta')$ near the planes on which rows of atomic scatterers are situated (actually slightly below the relevant Bragg angle for those planes), adjacent to which there is a minimum in which $\overline{Z}(\theta')$ drops by 5-10%. In the Kikuchi model, the mean depth near a low-index set of planes is thus higher due to constructive interference in Bragg scattering, but just adjacent to each set of planes is a region of destructive interference in which the mean depth is lower. Making a more quantitative connection between these two pictures is not possible via this simple two-beam approach, but it is clear that both the cluster approach and the Kikuchi model lead to qualitatively similar expectations for the variation of $\overline{Z}(\theta')$ close to a low-index direction in a single crystal.

3.3 Conclusions

We have calculated the directional dependence of the mean emitter depth for core-level photoelectron emission from single crystal overlayers and substrates, including both inelastic and elastic scattering and using both single-scattering and fully-converged multiple scattering approaches. In calculations on both isolated chains of Ni and Si

atoms, and a more realistic large cluster of Ni atoms, we have shown that this mean emission depth may vary by as much as $\pm$25-30% from a reference value based only upon isotropic inelastic scattering. Even in the presence of multiple scattering defocusing along low-index directions, the dominance of net forward scattering effects in the first few layers along such directions usually leads to the highest mean emission depths; conversely, just adjacent to such directions, destructive interference effects lead to the lowest mean emission depths. For dense atomic chains with a high number of strong scatterers, our results further suggest that intensities should tend toward that expected from isotropic inelastic scattering alone; this is due to the effective randomizing of scattering phase shifts from the many different MS scattering paths. Although not explicitly treated here, similar effects would be expected in Auger electron emission. Such variations in mean emission depth due to electron diffraction effects in outgoing electrons thus represent additional important considerations in the use of XPS or Auger electron spectroscopy for the quantitative characterization of surfaces, surface concentration profiles, epitaxial overlayers, and other nanostructures.

References:

[3.1] C.S. Fadley, (a) Prog. in Surf. Sci. **16**, 275 (1984), and (b) in Synchrotron Radiation Research: Advances in Surface and Interface Science, R.Z. Bachrach, Ed. (Plenum Press, New York, 1992) Vol. 1.

[3.2] M.P. Seah and W.A. Dench, Surf. and Int. Anal. **1**, 2 (1979); C.J. Powell, Scanning Electron. Microsc. **4**, 1649 (1984); S. Tanuma, C.J. Powell, and D.R. Penn, Surf. and Int. Anal. **11**, 577 (1988).

[3.3] O.A. Baschenko and V.I. Nefedov, J. Electron Spectrosc. **17**, 405 (1979); **21**, 153 (1980); **27**, 109 (1982); O.A. Baschenko, G.V. Machavariani, and V.I. Nefedov, J. Electron Spectrosc. **34**, 304 (1984).

[3.4] A. Jablonski and J. Zemek, Phys. Rev. **B48**, 4799 (1993); V. M. Dwyer, Surf. Interface Anal. **20**, 687 (1993); W. S. M. Werner, Surf. Interface Anal. **18**, 217 (1992); W. S. M. Werner *et al.*, Surf. Interface Anal. **21**, 38 (1994); P. J. Cumpson, Surf. Interface Anal. **20**, 727 (1993); P. F. A. Alkemade *et al.*, Appl. Surf. Sci. **70/71**, 24 (1993); A. Jablonski and S. Tougaard, J. Vac. Sci. Tech. **A8**, 106 (1990); W. H. Gries and W. Werner, Surf. Interface Anal. **16**, 149 (1990); and other references contained therein.

[3.5] R.E. Connelly, C.S. Fadley, and P.J. Orders, J. Vac. Sci. Tech. **A2**, 1333 (1984).

[3.6] P. Alnot, J. Olivier, F. Wyczisk, and C.S. Fadley, J. Electron Spectrosc. **43**, 263 (1987); P. Alnot, J. Olivier, and C.S. Fadley, J. Electron Spectrosc. **49**, 159 (1989).

[3.7] S.Y. Tong, H.C. Poon, and D.R. Snider, Phys. Rev. **B32**, 2096 (1985).

[3.8] M.-L. Xu, J.J. Barton, and M.A. Van Hove, Phys. Rev. **B39**, 8275 (1989).

[3.9] (a) A.P. Kaduwela, G.S. Herman, D.J. Friedman, and C.S. Fadley, Physica Scripta **41**, 948 (1990); (b) A.P. Kaduwela, D.J. Friedman, and C.S. Fadley, J. Electron Spectrosc. Relat. Phenom. **57** 223 (1991).

[3.10] W.F. Egelhoff, Phys. Rev. Lett. **59**, 559 (1987).

[3.11] D.J. Friedman and C.S. Fadley, J. Electron Spectrosc. **51**, 689 (1990).

[3.12] J.J. Rehr, and R.C. Albers, Phys. Rev. **B41**, 8139 (1990).

[3.13] Li *et al.*, Surf. Sci. Letters **281**, L347 (1993).

[3.14] (a) E. Puppin, C. Carbone, R. Rochow, Phys. Rev. **B46**, 13215 (1992); (b) J.M. Hill, D.G. Royce, C.S. Fadley, L.F. Wagner, and F.J. Grunthaner, Chem. Phys. Lett. **44**, 225 (1979).

[3.15] (a) S.M. Goldberg, R.J. Baird, S. Kono, N.F.T. Hall, and C.S. Fadley, J. Electron Spectrosc. **21**, 1 (1980); (b) R. Trehan, C.S. Fadley, and J. Osterwalder, J. Electron Spectrosc. **42**, 187 (1987).

Fig. 3.1: Mean emitter depth $\overline{Z}(\vec{k})$ including both elastic and inelastic scattering (from Eq. 1) as a function of polar angle θ for Ni 2p emission at 636 eV from vertical Ni(001) chains with an interatomic spacing of 3.52 Å. The geometry for the calculation is shown in (a), with the surface defined by the topmost atom, the emitter atom j being anywhere from the surface (j = 0) to the bottom atom of the chain (j = n-1), and emission along the chain direction corresponding to $\theta = 0^{o}$. $\overline{Z}(\vec{k})$ curves for chains of 2, 3, 4,...10 atoms in length are shown in (b) for single scattering and in (c) for multiple scattering. The dashed curves superimposed on these results represent the reference intensities $\overline{Z}_0(\vec{k})$ including inelastic scattering, but no elastic scattering (from Eq. 2).

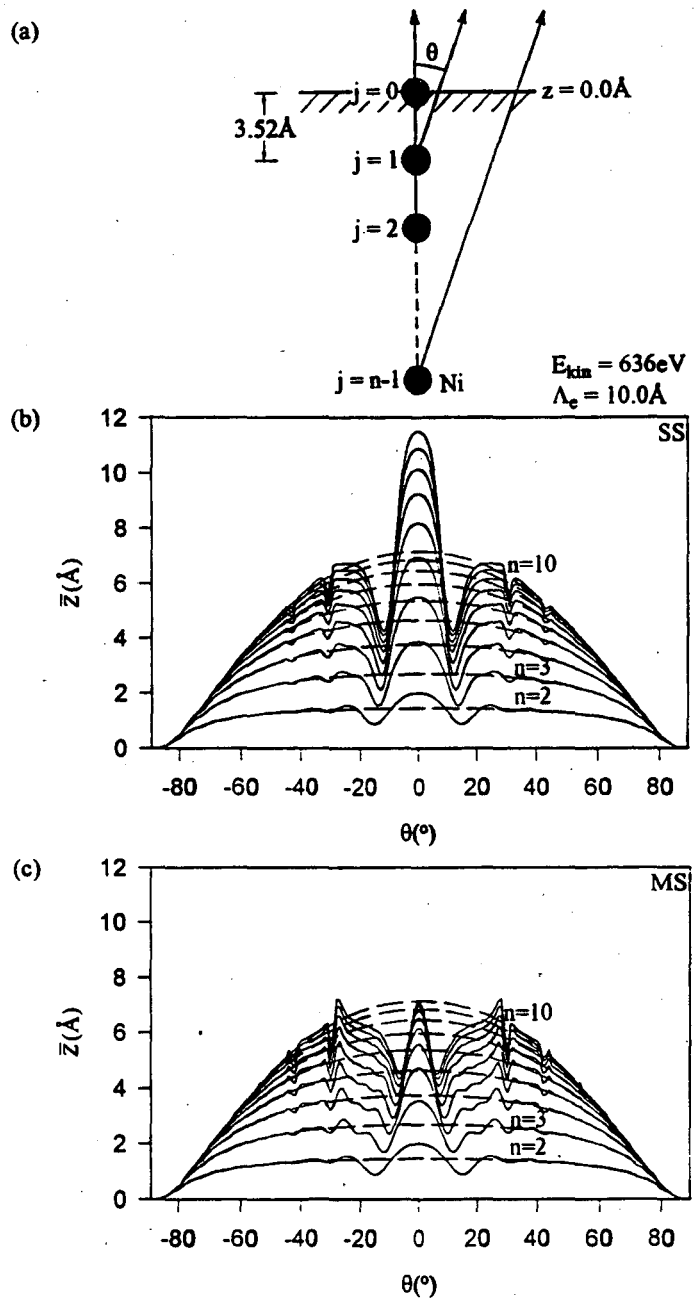
(a)
θ
j = 0
z = 0.0Å
3.52Å
j = 1
j = 2
j = n-1
Ni
E_{kin} = 636eV
Λ_e = 10.0Å
(b)
SS
n=10
n=3
n=2
$\bar{z}$(Å)
θ(°)
(c)
MS
n=10
n=3
n=2
$\bar{z}$(Å)
θ(°)

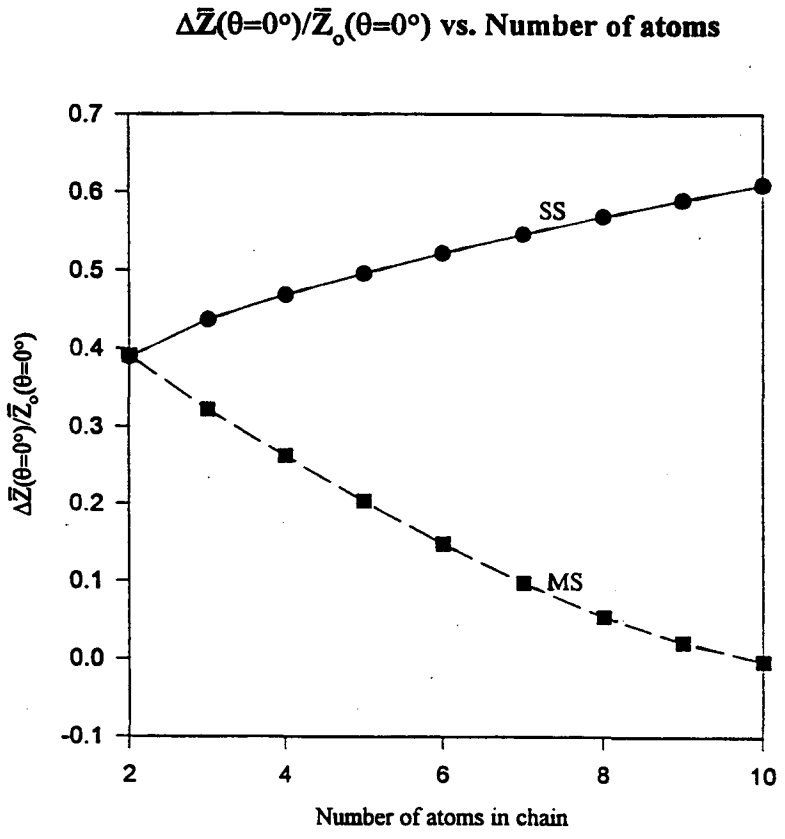

Fig. 3.2: The normalized difference between forward scattering intensities $\overline{Z}(\theta = 0^0)$ and the reference intensity $\overline{Z}_0(\theta = 0^0)$ (from Eq. 4) for a vertical Ni(001) chain; filled circles represent results for single scattering and filled squares represent results for multiple scattering.

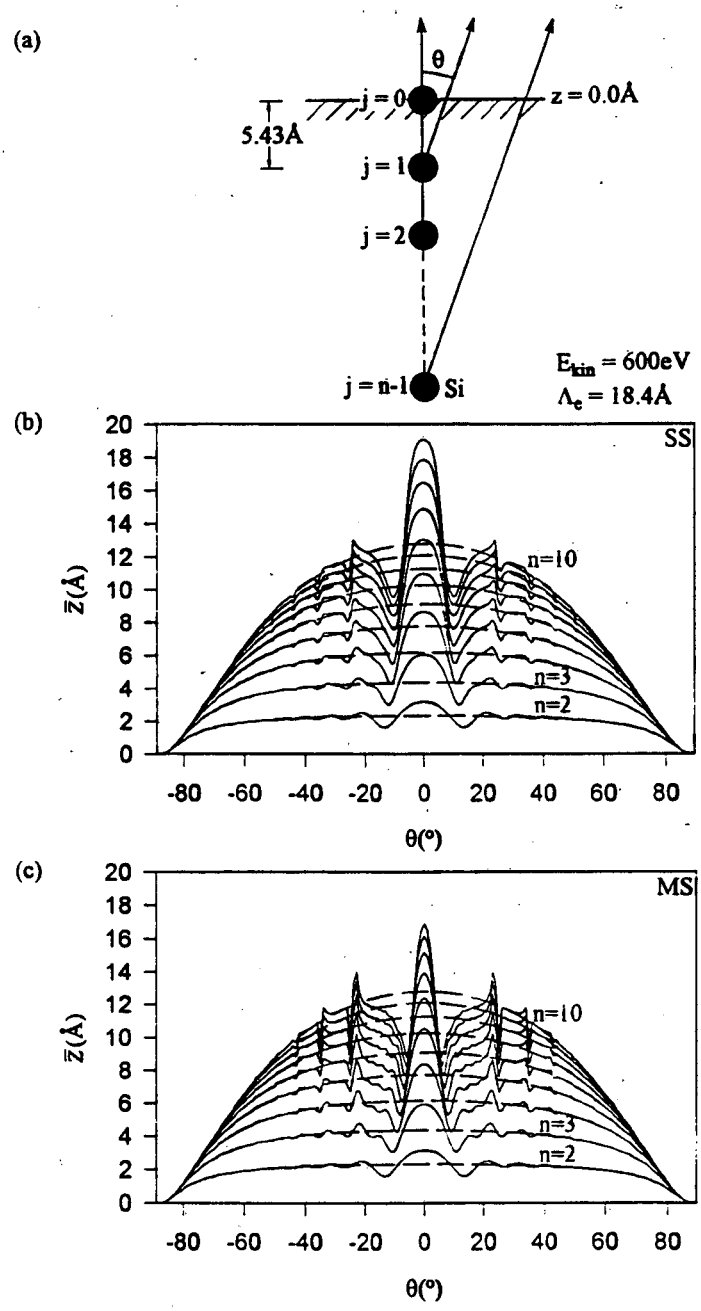

Fig. 3.3: As Fig. 1, but for Si 2p emission at 600 eV from vertical Si(001) chains with an interatomic spacing of 5.43 Å.

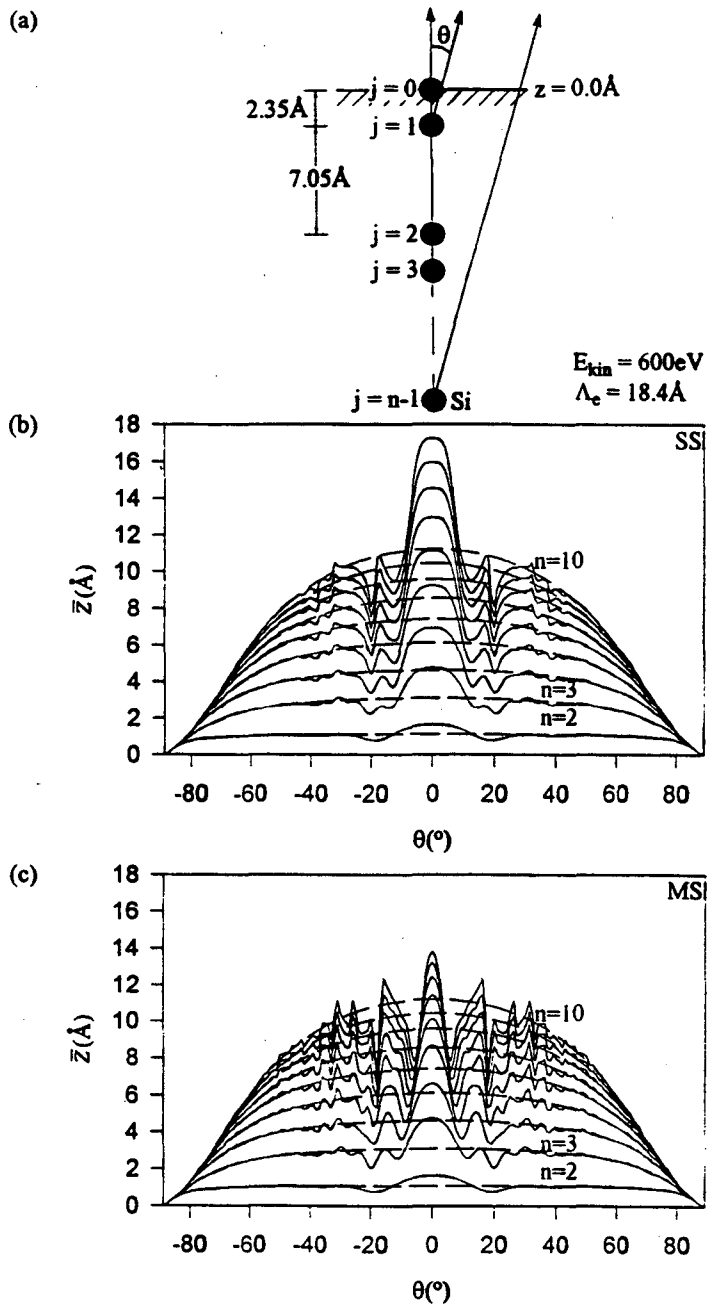

Fig. 3.4: As Fig. 1, but for Si 2p emission at 600 eV from vertical Si(111) chains with alternating interatomic spacings of 2.35 Å and 7.05 Å.

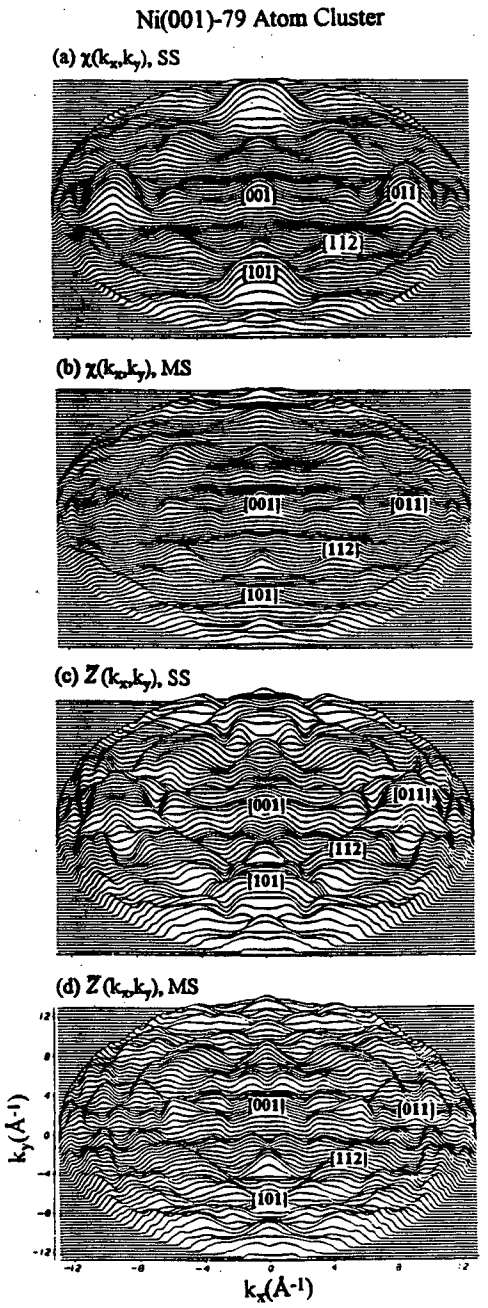

Fig. 3.5: Normalized intensities $\chi(\vec{k})$ and mean emission depths $\overline{Z}(\vec{k})$ over the full 2π solid angle for Ni 2p emission at 636 eV from a large cluster representing a Ni(001) single crystal. (a),(b): Three-dimensional renderings of $\chi(\vec{k})$ in single scattering and multiple scattering as projected down onto the k_X-k_Y plane. (c),(d) Three-dimensional renderings of $\overline{Z}(\vec{k})$ in single scattering and multiple scattering.

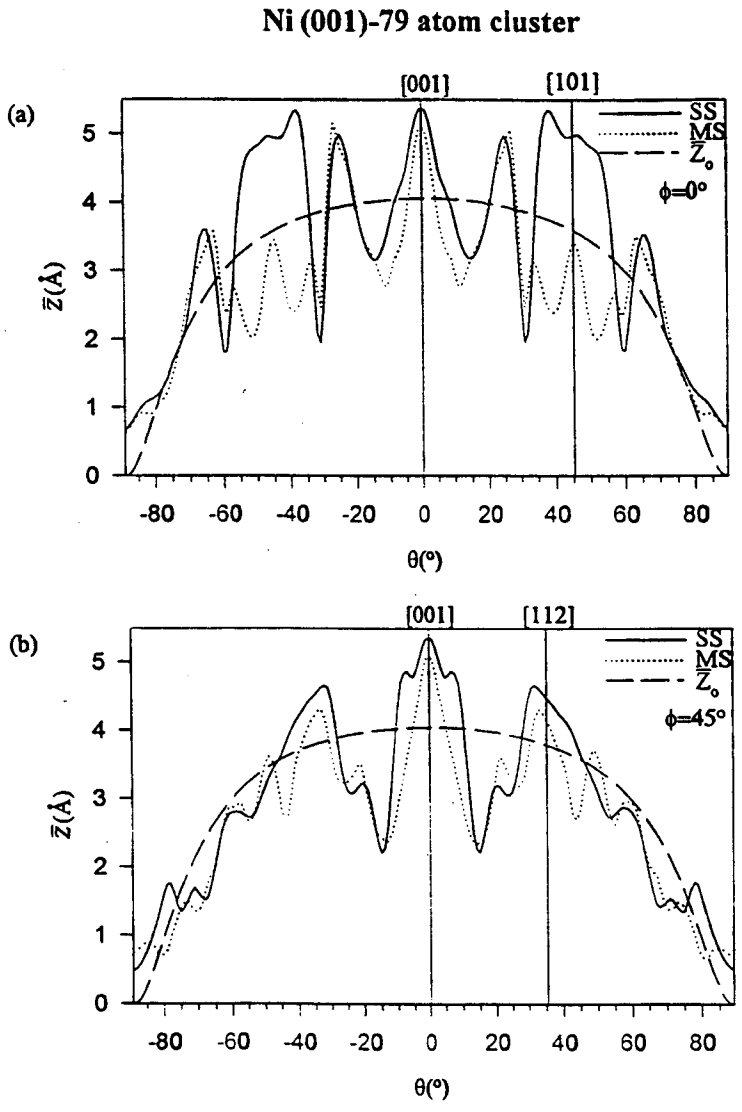

Fig. 3.6: $\bar{Z}(\vec{k})$ and $\bar{Z}_0(\vec{k})$ as a function of polar angle (θ) at two different azimuthal angles (a): ϕ = 0° and (b): 45°, as extracted from the results of Figs. 5(c),(d). $\bar{Z}(\vec{k})$ from multiple scattering is shown as a dotted curve, $\bar{Z}(\vec{k})$ from single scattering is shown as a solid curve, and the reference $\bar{Z}_0(\vec{k})$ is shown as a dashed curve.

Mean Emission Depth

2-beam Kikuchi Theory, 1420eV, Λ_e=9.8 Angstroms

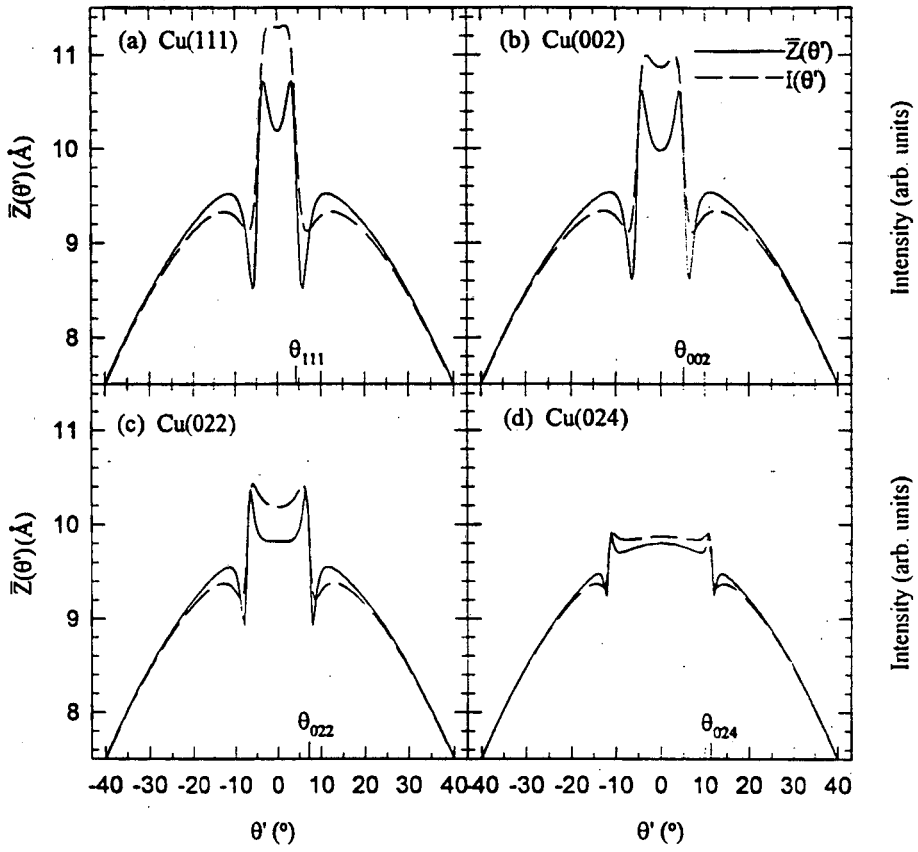

Fig. 3.7: Kikuchi-band calculations of $\bar{Z}(\theta')$ and $I(\theta')$ as a function of the deviation angle θ' from directions parallel to a given set of (hkl) planes. (a) Cu (111) planes. (b) Cu (002) planes. (c) Cu (022) planes. (d) Cu (024) planes.

Chapter 4

X-ray Photoelectron Diffraction Study of Thin Cu Films Grown on Clean Ru(0001) and O-Precovered Ru(0001)

Abstract

We have studied the epitaxial growth modes and near-surface interlayer relaxation of thin Cu films on Ru(0001) using x-ray photoelectron diffraction (XPD), measuring experimental Cu $2p_{3/2}$ (E_{kin} = 556 eV) and Ru 3d (E_{kin} = 1206 eV) intensities over 1/3 of the nearly full 2π solid angle above the surface for Cu coverages from submonolayer up to 40 monolayers. Reference Cu $2p_{3/2}$ data for a clean Cu(111) surface have also been obtained from Naumovic et al. and in our laboratory. These data have been compared to single scattering cluster (SSC) and more accurate multiple scattering cluster (MSC) calculations via a sum of five R-factors to derive precise structural information. MSC calculations are found to give a more accurate description for layers of ≥ 4 ML thickness, and comparisons of experiment and theory are also improved by systematically assessing the effective degree of angular averaging involved. Calculations for thicker layers are also found to converge by ~5 ML. Our analysis indicate that the first Cu layer grows pseudomorphically on Ru(0001), in agreement with prior studies. An R-factor analysis comparing MSC and SSC calculations to experimental results further indicates that the Cu-Ru interlayer spacing at 1 monolayer (ML) is about 2.15 Å, in excellent agreement with prior low energy ion scattering (LEIS) and low energy electron diffraction (LEED) experimental studies, as well as with prior linearized augmented plane wave (LAPW) calculations. At higher coverages, comparison of our data to SSC and MSC calculations for various atomic clusters indicate that the short-range structure is fcc Cu(111)-like, but with significant interlayer contraction that persists up to ≥ 5 ML coverage. Prior STM work by Behm et al. has shown a series of misfit dislocation structures in the top layer of the Cu film at higher coverages from 2 ML to 4 ML. Our data indicate that these misfit dislocation structures thread to the Cu/Ru interface rather than occurring only in the top

Cu layer or layers. An R-factor comparison of the more accurate MSC calculations to experiment also indicates that the ratio, $d_{\perp} / d_{\parallel}$, of the Cu-Cu interlayer distance ($d_{\perp}$) to the Cu-Cu in-plane nearest-neighbor distance ($d_{\parallel}$) = 0.729±0.034 at 2 ML, and reaches 0.777±0.020 by 25 ML. For reference, the bulk value is $d_{\perp} / d_{\parallel}$ = 0.816, and the analysis of our data for Cu(111) yields 0.801±0.035, in good agreement with this value and prior LEED studies. This analysis shows that there is significant interlayer contraction for very thin Cu layers, and that it persists (at least in the top few layers to which XPD is the most sensitive) for longer than would be expected on the basis of a prior theoretical analysis using the 2-D Frenkel-Kontorova model by Hamilton and Foiles, as turned into an estimate of via either a constant-atomic-volume assumption or the use of elasticity theory. In addition, the Cu overlayer grows in two possible orientations rotated by 180° on the Ru(0001) surface, with a preference towards one of the two possible orientations at certain coverages. Finally, we have investigated the effect of oxygen preadsorbed on the Ru(0001) surface on the growth of the Cu overlayer. For this case, we find that all of the oxygen floats on top of the Cu in a highly disordered configuration, and that the oxygen promotes multilayer or island growth relative to growth on the clean Ru surface up to at least 3 ML coverage, rather than to act as a surfactant promoting smoother growth.

4.1. Introduction

The growth of thin epitaxial metal films on metal substrates has attracted much interest recently due to the unusual catalytic, electronic, or magnetic properties such systems may exhibit [4.1]. The atomic scale structure of these systems plays an important role in their physical and chemical properties. Heteroepitaxial metal-on-metal systems are of particular interest because misfit between the substrate lattice geometry and the overlayer bulk geometry causes strain in the overlayer, which can in turn lead to altered growth modes and expansions or contractions of interatomic or interlayer distances in the

overlayer [4.1]. Such heteroepitaxial systems thus offer the possibility of producing novel atomic structures which may exhibit unique properties. An understanding of how the substrate lattice geometry influences overlayer growth and structure is thus vital to the development of nanostructured materials with new and useful properties. The heteroepitaxial system Cu/Ru(0001) has become a model system for such strained overlayer systems due to the several interesting structural transformations which occur in the Cu overlayer as the film thickness is increased, particularly in the range from 1 monolayer (ML) to 4 ML [4.2]. These structural transitions are driven by a balance between the misfit energy and the strain energy of the Cu overlayer [4.3]. The misfit is such that the lattice constant of fcc Cu(111) which ultimately grows in thicker layers is 5.5% smaller than that of hcp Ru(0001) substrate.

Early studies of the Cu/Ru(0001) system using Auger electron spectroscopy (AES), low energy electron diffraction (LEED), thermal desorption spectroscopy (TDS), and work function measurements concluded that the growth was Stranski-Krastonov in character [4.4-4.6]. However, more recent studies using scanning tunneling microscopy (STM) have provided a much more detailed and complex picture, and revealed that the Cu grows via a series of misfit dislocation structures [4.2]. These dislocation structures have also been predicted recently in a theoretical study by Hamilton and Foiles [4.3], who used a 2D Frenkel-Kontorova model to determine the minimum energy configuration for thin Cu films grown on Ru(0001), and obtained results in basic agreement with the STM structures. The STM studies [4.2] concluded that the first Cu layer expands 5.5% from the bulk Cu(111) lateral spacing to grow pseudomorphically, with the Cu atoms occupying the threefold hollow sites of the Ru(0001) surface. At 2 ML, a striped dislocation pattern was observed in which the layer is assumed to contract uniaxially from the pseudomorphic configuration via misfit dislocations. At 3 ML, the Cu surface layer contracts along three directions from the pseudomorphic configuration to form a complex network of triangular structures, but still with an overall expansion by about 2% from the

bulk fcc Cu(111) configuration. At 4 ML, a large scale incommensurate lateral superlattice or Moiré pattern was observed. At 4 ML and higher coverages, the Cu overlayer is thought to relax almost fully to a bulk fcc Cu(111) lateral spacing [4.2, 4.3], but two separate quantitative analyses of the 4 ML atomic-resolution STM Moiré pattern [4.2(d), 4.7] still indicate a 0.6% expansion relative to bulk Cu(111). These STM studies [4.2] also concluded that, at 300 K, the growth is layer-by-layer up to at least 2 ML, but that 3D islands and a distribution of island heights around the nominal thickness form at higher coverages. Detailed measurements of the distributions of different layer thicknesses for different coverages and thermal treatments have also been made [4.2(d)]. A very recent LEED study has permitted concluding, in addition, that the structural data derived on a local scale by STM are representative of the entire surface as analyzed by LEED, and also permitted determining both lattice periodicities and lattice rotations more exactly [4.8, 4.9]. From STM and LEED it is not, however, possible to determine whether the misfit dislocation structures thread to the Cu-Ru interface or occur only in the top Cu layer or layers. Nor does STM permit determining the vertical spacing between adjacent Cu layers. We have thus applied x-ray photoelectron diffraction (XPD) to both of these questions.

Other studies have found that the growth of thin epitaxial metal films on metal substrates may be strongly affected by contaminants, such as preadsorption of oxygen on the original substrate surface [4.10, 4.11]. In certain cases, such preadsorption can lead to smoother overlayer growth through what has been termed a surfactant role [4.12-4.14]. These studies have suggested that when oxygen is preadsorbed on the Ru(0001) substrate, the growth mode of the Cu overlayer may be changed from multilayer and/or 3D islands to a more nearly 2D layer-by-layer growth mode, thus achieving smoother film morphologies [4.12-4.14]. For example, work function studies [4.13, 4.14] reported oscillations in the work function starting at about 3 ML when Cu was grown at ~125°C on the O-precovered Ru(0001) surface and at an O precoverage of 0.4 ML.

Smoluchowski dipoles at island step edges tend to lower the work function, and thus, these work function oscillations were attributed to a changing Cu step edge length which grew large during nucleation of many small 2D Cu islands, grew smaller as the islands grew larger, and finally coalesced near the completion of a layer. Schmidt et al. [4.14] further concluded that when oxygen is preadsorbed on Ru(0001), Cu grows layer-by-layer up to as many as 50 ML, and that 85% of the oxygen floats on the Cu surface during the film growth, while the rest remains at the Cu/Ru interface. A more recent low energy ion scattering (LEIS) study concluded that 70% of the oxygen floats on the Cu surface, and in addition, that the oxygen layer is disordered on the Cu surface [4.15]. We have thus explored these questions using XPD as well.

X-ray photoelectron diffraction (XPD) is an excellent tool for deriving additional information about the Cu/Ru(0001) system [4.16]. The strong forward scattering effect along internuclear axes for core level emission at high energies ($E_{kin} \geq 500$ eV) permits quickly identifying buried species and determining the local structural environment around an emitting atom, and thus can provide information about epitaxial growth modes and lattice expansions or contractions. Since diffraction patterns for the overlayer element as well as the substrate element can be measured simultaneously, information about the preferred orientation of the overlayer relative to the substrate can be determined as well [4.16]. Finally, more detailed structural information can be determined by comparing experimental data to single-scattering cluster (SSC) and more accurate multiple-scattering cluster (MSC) diffraction calculations [4.17-4.19].

4.2. Experiment

The Ru(0001) surface was prepared by mechanically polishing a Ru single crystal, 0.5 inches in diameter, using a final abrasive of 0.05μ alumina. The polished crystal was oriented by Laue back reflection and the surface was found to be within 0.5° of the (0001)

orientation. The polished and oriented Ru(0001) crystal was cleaned further in a UHV chamber chamber attached to the photoelectron spectrometer, in which the base pressure was near $5x10^{-11}$ Torr. The *in situ* cleaning consisted of mild Ar^+ ion bombardment ($5.5x10^{-5}$ Torr, 800 eV, 30 mA) followed by several oxygen and heat treatments in which the Ru sample was heated to ~800°C in an oxygen atmosphere of $3x10^{-7}$ Torr for ~5 minutes and then briefly vacuum annealed at ~1400°C. Surface cleanliness was verified by x-ray photoelectron spectroscopy (XPS) [4.16]. Typical oxygen impurity levels were ≤ 0.05 ML. Carbon impurity levels were more difficult to estimate due to the overlap of the C 1s and Ru $3d_{3/2}$ levels; but cross comparisons of the intensities of the Ru $3d_{3/2}$ and Ru $3d_{5/2}$ peaks in different stages of cleanliness permit estimating that carbon was present at levels ≤ 0.1 ML. The presence of a well ordered Ru(0001) surface was verified by a sharp hexagonal LEED pattern. In order to insure that the Ru(0001) surface remained clean and well ordered, oxygen and heat treatments, XPS, and LEED were performed before each Cu deposition.

The thin Cu films were made by evaporating Cu onto the Ru substrate from a resistively heated W wire wrapped with high purity (99.998%) Cu wire. The Ru substrate temperature during deposition was ~ 600°C for Cu coverages ≤ 3 ML and ~300°C for Cu coverages ≥ 5 ML, with the lower temperature being used to suppress evaporation effects [4.4]. A 4.2 ML film of intermediate coverage, however, was obtained by initially depositing Cu at 300°C to a coverage of 7.7 ML and then heating to 600°C briefly to yield the final lower coverage via evaporation. After heating, XPS measurements indicated a Cu coverage of 4.2 ML. These preparation conditions thus correspond to those used in prior studies [4.2, 4.4-4.6], although we note that a very recent STM study has explored the detailed temperature dependence, and concluded that, for layers above 2 ML, higher substrate temperatures promote more multilayer/3D island growth [4.2(d)]. The Cu coverage was determined in two independent ways, via measurements of total deposition using a quartz crystal monitor (QCM--Leybold-Inficon Model 751-001-G1)

and angular-dependent XPS [4.15]. The QCM values should represent upper limits of coverage, with the XPS being affected by subsequent evaporation and/or 3D island formation of some of the Cu, especially for thicker films. The details concerning the XPS quantitative analysis appear elsewhere [4.7], but they involved determining a Cu $2p_{3/2}$/Ru 3d intensity ratio that was averaged over azimuthal angle and spline-smoothed over polar angle, and then applying standard surface analysis formulas. The deposition rates as measured by the QCM were between 0.4 and 1.3 ML/min. A tabulation of coverages determined from QCM and XPS measurements is shown in Table 4.1, and the values obtained from the two different measurements are in general in good agreement with each other; the XPS numbers are in any case viewed as a more accurate measure of the actual final coverages. For a very thick Cu overlayer, Cu was deposited until the substrate Ru 3d XPS signal could no longer be seen due to electron inelastic attenuation through the Cu overlayer, thus indicating an effectively infinitely thick Cu film. Based on the deposition rate as measured by the QCM, the thickness of this very thick Cu overlayer was ~25.2 ML. For Cu grown on O-precovered Ru(0001), the clean Ru surface was first exposed to 90 L of Oxygen until a saturation coverage of 0.5 ML was reached. This led to a well ordered p(2x1)-O/Ru(0001) structure as confirmed by LEED. Copper was then evaporated as for Cu/clean Ru(0001), but at a substrate temperature of ~125°C, in order to correspond to prior work on this system [4.12-4.14]. A 3.7 ML film, however, was obtained by briefly annealing a 6.5 ML Cu film at 325°C in order to obtain a $2\sqrt{3} \times 4\sqrt{3}R30$ LEED structure as seen in ref [4.13]. After annealing, XPS indicated a coverage of 3.7 ML. In Table 4.2, we present the Cu coverages as determined from both QCM and XPS measurements.

The experiments were performed with a Hewlett-Packard 5950A photoelectron spectrometer that has been specially modified for ultra-high vacuum XPD studies [4.16]. The base pressure of the experimental chamber was 5×10^{-11} torr. Al Kα radiation ($h\nu$ = 1486.6 eV) was used to excite Cu $2p_{3/2}$ (E_{kin} = 556 eV), Ru 3d (E_{kin} = 1206 eV), and O

1s (E_{kin} = 955 eV),) photoelectrons. A special non-monochromatized x-ray tube has been added to this system, and it yields about three times higher data acquisition rates than the normal monochromatized source [4.20]. The experimental geometry is shown in Fig. 4.1. The angle between photon incidence and electron exit was fixed at 72°. The intensities of all peaks were measured over one-third of the nearly full 2π solid angle above the sample surface, thus exploiting the threefold symmetry of the Cu/Ru system to reduce scan time. However, the threefold symmetry was verified for all overlayers studied by performing full 360° azimuthal scans at selected polar angles. Thus, both the polar (θ) and azimuthal (ϕ) emission angles were varied, with θ being measured from the sample surface, and ϕ from the [001] direction lying in the Ru surface. Scanning was over the ranges $6^o \leq \theta \leq 90^o$ and $0^o \leq \phi \leq 120^o$, with full-hemisphere intensity patterns then being generated by threefold repetition of each set of data. The step size in θ was 2°. The step size in ϕ was initially 2° at $\theta = 6^o$, and was increased as θ increased so that the data density in solid angle would remain roughly constant over the full data set above the sample surface. The formula used to adjust the size of the ϕ step was

$$\Delta\phi = \Delta\phi_{init.} \frac{\sin\left(\frac{90^\circ - \theta_{init.}}{2}\right)}{\sin\left(\frac{90^\circ - \theta}{2}\right)} \quad , \tag{4.1}$$

where $\Delta\phi_{init.} = 2^o$ and $\theta_{init.} = 6^o$ for our data.

Because the limit for thicker coverages is a Cu(111) epitaxial layer, we have also measured the Al Kα-excited Cu $2p_{3/2}$ XPD pattern at 556 eV from a bulk Cu(111) specimen. This was mechanically polished, chemically polished, and oriented (to within 0.5° of (111)) and cleaned *in situ* using standard methods. Additional Cu $2p_{3/2}$ XPD patterns at slightly different kinetic energies of 321 eV (Mg Kα) and 808 eV (Si Kα)

were also obtained from Naumovic and Osterwalder. [4.21]. These data provide an important reference for the ideal Cu(111) structure to which we will return later.

All of the XPD intensities from our experiments have been normalized so as to include only the diffraction features. The normalized intensity, $\chi(\vec{k})$, is defined as $\chi(\vec{k}) = [I(\vec{k}) - I_o(\vec{k})]/I_o(\vec{k})$, where $I(\vec{k})$ is the measured photoelectron intensity, $I_o(\vec{k})$ is the photoelectron intensity in the absence of any scattering, and $\vec{k}$ is the photoelectron wave vector. In presenting and analyzing the experimental data, we have estimated $I_o(\vec{k})$ by applying a spline smoothing routine [4.22] to $I(\vec{k})$ so that the diffraction features have been smoothed out . In this procedure, the data were first azimuthally averaged so that,

$$\bar{I}(\theta_i) = \frac{1}{n} \sum_{j=1}^{n} I(\theta_i, \phi_j), \tag{4.2}$$

where n = the number of ϕ_j steps at each θ_i. The spline function was then fit to $\bar{I}(\theta_i)$ to derive $I_o(\vec{k})$. The smoothing factor of this spline fit was adjusted so that it removed only a smooth background following the instrumental variation of intensity with polar angle, which in general shows an approximate *sin 6.* variation. Details of this procedure appear elsewhere [4.7], and it is very useful in amplifying weaker total-intensity features for lower takeoff angles that nonetheless contain considerable structural information.

4.3. Results and Discussion

4.3.1 Cu Grown on Clean Ru(0001)

4.3.1.1 XPD - Experimental Results

In Figs. 4.2(a)-(i), we present the measured XPD patterns for the Cu $2p_{3/2}$ peak at nine different Cu coverages from 0.4 ML to 25 ML. In Figs. 4.2(j)-(k), we show the same XPD pattern from a bulk Cu(111) crystal: in (k) the raw data with threefold symmetry are shown, and in (j) the same data which has been made sixfold via a 60° rotation and addition of two patterns is shown. In addition, for reference to the substrate, we show in Fig. 4.2(l) the measured XPD pattern for the Ru 3d peak for a clean Ru sample. The low-index direction, $[2\bar{1}\bar{1}]$, for Cu(111) is along the 90° azimuth in Fig. 4.2(k), and the low-index direction, [210], for Ru is along the 30° azimuth in Fig. 4.2(l). Note that the hcp Ru (0001) pattern is inherently sixfold, whereas that of fcc Cu(111) is threefold. This is due to the ABABAB...stacking in the hcp lattice, which inverts its threefold local-scattering symmetry pattern from one monatomic step to another. By contrast, the ABCABCABC...stacking in fcc does not invert its local symmetry across a monatomic step. The XPD pattern for Ru 3d does not change significantly as thicker Cu layers are grown, and so we do not show the XPD patterns for Ru 3d at each Cu coverage.

As a measure of the degree of diffraction present for these XPD patterns, we show in Fig. 4.3(a) the relative anisotropy = $\left[I_{\max}(\theta) - I_{\min}(\theta)\right]/I_{\max}(\theta) = \Delta I(\theta)/I_{\max}(\theta)$ as a function of polar angle and coverage; this is here computed for each azimuthal scan. The absolute anisotropies range from about 5% at the lowest points on the curves up to about 30% at the highest points on the curves. A scale is included in each panel to indicate the relative amounts of anisotropy versus polar angle. Comparing Figs. 4.2(a)-(b) and Fig. 4.3(a) for 0.4 ML and 1.1 ML, we see that the peak in anisotropy near 15° is due to the pronounced first-order diffraction rings originating in electrons scattered from nearest-neighbor and next-nearest-neighbor atoms in the surface plane of the hexagonal array of pseudomorphic Cu atoms, as we will confirm with a more detailed theoretical analysis of the XPD patterns below. Note also that the essential identity of Figs. 4.2(a) and 4.2(b) and of the anisotropy curves for 0.4 ML and 1.1 ML in Fig. 4.3(a) immediately implies that the Cu atoms at 0.4 ML are clustering together into pseudomorphic islands that are

large compared to the sensing diameter of XPD of ~20-30 Å. The peak in anisotropy at 0.4 ML and 1.1 ML near $\theta = 15^{o}$ is thus due to the variation in intensity caused by the diffraction rings at low θ. The anisotropy at higher angles is nearly zero for these two lowest coverages and is due mainly to noise, although a weak sixfold pattern is seen for the 1.1 ML case in Fig. 4.2(b). For thicker Cu layers, polar angles associated with near-neighbor interatomic directions should have the largest anisotropies since such directions imply strong forward scattering and a rapid variation in intensity. To provide some idea of where such directions occur, we show in Fig. 4.4 an atomic model for Cu(111) with a top view of the Cu(111) surface and also a cross section through the $[2\bar{1}\bar{1}]$ direction. The low index directions and most prominent forward scattering directions are also indicated in Fig. 4.4(b). Comparison of these forward scattering directions to the diffraction patterns and the experimental anisotropies suggests that the overlayer is Cu(111)-like. That is, peaks in the anisotropy first occur at 2 ML Cu coverage near 33°-34° and also near 55°, in good agreement with the forward scattering directions for bulk Cu(111). The increase in the relative heights of these two anisotropy peaks with coverage is due to the increasing atomic chain lengths along these forward scattering directions. For a thick enough layer (in fact 3 ML or more), a forward scattering peak near 70.5^{o} should also appear, and in fact, a small peak in the anisotropy near 70° does indeed appear at 25 ML; however, this feature is small enough that it may be strongly influenced by the higher-order interference effects from adjacent near-neighbor directions. Shown in Figs. 4.3(b) and 4.3(c) are the corresponding anisotropies from MSC and SSC calculations, respectively, for 1-5 ML thick ideal clusters. (The way in which these calculations were performed is discussed in the following section.) In general, the MSC curves agree very well with experiment as to peak positions and relative intensities, although the features in theory are often sharper than those in experiment. Beyond 2-3 ML, SSC theory diverges from MSC theory, and does not describe experiment as well; for example, due to the too-strong forward focusing in SSC calculations, the peak near

55° in the SSC anisotropy curves is too strong relative to MSC calculations and experiment. These differences between MSC and SSC will be discussed in more detail below when we fit theory to experiment for the entire XPD pattern.

We now discuss qualitatively the full diffraction patterns in Fig. 4.2. In Figs. 4.2(a) and 4.2(b), at 0.4 ML and 1.1 ML Cu coverages, respectively, we see no evidence whatsoever for forward scattering peaks; thus, the XPD data provide a clear indication that the first layer is fully completed before the second layer begins to grow. In addition, the clear sixfold ring pattern at low θ is indicative of a pseudomorphic first layer of Cu on Ru. Two sets of rings with sixfold symmetry rotated by 30° with respect to one another are seen. These are the first order diffraction rings caused by photoelectrons emitted from one Cu atom and then scattered from the nearest- and next-nearest-neighbor Cu atoms in a single hexagonal layer, and they have been seen before in adsorbate overlayer studies [4.16(d)] The polar angles at which these rings occur are, in fact, predicted quite well using a simple single-scattering calculation,

$$2\pi m = kr_k(1-\cos\theta_m) + \psi(\theta_m), \quad m = 1, 2, ..., \tag{4.3}$$

where θ_m is the polar angle, m is the diffraction order, r_k is the distance from an emitter to a given scatterer, $r_k(1-\cos\theta_m)$ is the path-length difference between direct and scattered waves, and $\psi(\theta_m)$ is the additional phase difference between direct and scattered waves produced by elastic scattering [4.16(b)]. To account for surface refraction, θ_m inside the surface is then adjusted to θ_m' outside the surface according to,

$$\theta_m' = \cos^{-1}\left[(1+V_0/E_{kin})^{1/2}\cos\theta_m\right] \tag{4.4}$$

where V_0 is the surface inner potential and E_{kin} is the electron kinetic energy.[4.16(b)]. Using V_0 = 14.4 eV [4.23], the positions of the rings centered along ϕ = 0°, 60°, etc., due

to nearest neighbors, are predicted to be at θ = 28° along these directions and are observed at θ = 26°; and the positions of the rings centered along ϕ = 30°, 90°, etc., due to next-nearest neighbors, are predicted to be at θ = 23° along these directions and are observed at θ = 20°. If we increase the inner potential to V_0 = 21 eV, this simple single scattering calculation gives ring positions which agree much better with the observed experimental positions. This may be a sign of an effectively higher inner potential for such low takeoff angles, but further more careful experimental and theoretical work will be needed to confirm this suggestion. As further evidence for an effectively higher inner potential, the peak in anisotropy for 1 ML near 15° is about 1.5° higher in the MSC calculation than in experiment. According to Eq. (4.3) above, this peak position should be adjustable to match experiment by raising V_0 by about 8 eV to about 22 eV. But whether or not V_0 is adjusted the first Cu layer appears to have conformed to the substrate lattice geometry as a pseudomorphic layer, and to have the simple diffraction pattern associated with such a layer.

In Fig. 4.2(c), at 2 ML Cu coverage, we still see the rings at low θ observed for ≤ 1 ML, but at a much higher $\theta \approx 50°$, three strong forward scattering peaks have appeared, indicating that the second layer has grown in the threefold hollow sites of the first layer. In addition, these 2 ML results immediately suggest that the uniaxial striped dislocation structure seen in STM [4.2] threads itself all the way to the Cu-Ru interface; i.e. the first pseudomorphic layer uniaxially contracts with the second layer when the second layer is grown. If the underlying layers did not reconstruct with the top layer, then the underlying emitters would each see scatterers in the top layer in several different orientations, and this would tend to smear out the XPD pattern; the sharp diffraction pattern seen for 2 ML makes it clear that this is not the case, as we further confirm below with comparisons to theoretical calculations. For 2 ML, a second weaker set of three forward scattering peaks at $\theta \approx 50°$ is also seen rotated 180° in ϕ from the first set; from this we conclude that the

second layer Cu atoms may sit in one of two possible threefold sites of the first Cu layer, but with one of the two sites being preferred.

At 3 ML, in Fig 4.2(d), a sharp sixfold pattern of strong forward scattering peaks at $\theta \approx 50°$ is seen, indicating that the Cu atoms still grow in the threefold hollow sites of the underlying Cu layers, and further confirming that the dislocation structures seen in STM thread to the Cu-Ru interface. However, at 3 ML, no preference is shown for the two possible growth orientations on the Ru substrate, leading to full sixfold symmetry. At 3 ML, theoretical calculations to be discussed further below indicate that both fcc and hcp stacking will lead to a threefold XPD pattern, although hcp appears slightly more sixfold and does not correctly converge to the correct sixfold pattern for thicker hcp layers (e.g. note the differences between the hcp Ru(0001) and sixfold Cu(111) patterns in Figs. 4.2(j) and 4.2(l)). Thus, if either type of stacking is to describe this data, the registry of the Cu layers with the Ru substrate must have two possible preferred orientations which are 180° apart in ϕ.

At 4 ML and 5 ML, in Figs. 4.2(e) and 4.2(f), a threefold pattern with more fine structure at higher θ associated with a thicker fcc Cu(111)-like overlayer is observed. By 6.5 ML and 8 ML, in Figs. 4.2(g) and 4.2(h), a nearly sixfold pattern is observed that will be seen to be best described as a superposition of two fcc Cu(111)-like XPD patterns rotated by 180° in ϕ with respect to one another, and this sixfold pattern is also observed for a very thick Cu layer of 25 ML in Fig. 4.2(i), as well as for the intentionally sixfolded Cu(111) data in Fig. 4.2(j). The sixfold pattern observed at these higher coverages cannot be attributed to equal amounts of fcc and hcp stacking of the Cu on itself, as an XPD pattern resulting from a thick hcp stacked layer is distinctly different from an XPD pattern resulting from a thick fcc stacked layer. For example, an hcp Ru 3d XPD pattern is shown in Fig. 4.2(j), and it is much different from the patterns seen in the 6.5 ML to 25 ML range. Therefore, the cause of the sixfold symmetry at these higher coverages must be two fcc Cu(111) domains 180° apart in ϕ. A possible explanation for the two

domains is the presence of monatomic steps on the Ru(0001) surface. With the ABABAB...stacking of the hcp structure, we thus suppose that one orientation grows on an "A" terrace, whereas the other orientation grows on a "B" terrace. That is, if we insert a "/" between Ru and Cu, the two growth modes could be: on an "A: step: ABABA/BCABCABC... and on a "B" step: ABABAB/CBACBACBA. This, however, still does not fully explain the interesting changes in the symmetry of the XPD patterns between threefold and sixfold as the coverage is increased, a point to which we return below.

4.3.1.2 XPD - Theoretical Calculations

We now make a more quantitative comparison of our XPD results to theoretical calculations. These calculations were performed at both the single-scattering cluster (SSC) [4.18] and multiple-scattering cluster (MSC) [4.19] levels, using a separable Green's function method developed by Rehr and Albers [4.17]. This approximation has been used in second-order (implying the use of 6x6 matrices), and recent extensive tests have shown this to be fully accurate for PD structural analyses [4.24] Scattering phase shifts were calculated using a standard muffin-tin approximation and program [4.25]. The electron inelastic attenuation length in the Cu overlayer was estimated from the empirical equation, $\Lambda_e[4.\text{Å}] = 0.54(E_{kin}[4.\text{eV}])^{0.5}$ [4.26]. Vibrational effects were included by Debye-Waller factors based on correlated vibrational motion, with the inputs being the bulk Cu Debye temperature and Debye wave vector [4.19(b), 4.27]. An inner potential of 14.4 eV was used to allow for electron refraction in crossing the surface barrier (cf. Eq. 4.3). As discussed earlier with reference to the diffraction rings at low θ for 1 ML, the effective inner potential at low takeoff angle may be higher than this value. We have therefore varied the inner potential in MSC calculations for the case of 1 ML and performed an R-factor comparison (with R-factors defined below) between these

calculations and experiment and found that the R-factor minimum occurs at $V_0 = 21$ eV, in excellent agreement with the simple single scattering calculation performed earlier. An inner potential of 14.4 eV, however, was used in the calculations for all remaining coverages. The cluster sizes varied from 43 to 80 atoms, and are described for each of the cases below. In cases with > 1 ML thickness, full advantage was taken of mirror-plane symmetry and the threefold symmetry of Cu(111). That is, an emitter was placed in each Cu layer of the cluster, with the emitter being near the apex of a wedge of atoms spanning and angle somewhat greater than 60° to avoid edge truncation effects. The XPD calculations were then performed over the 60° azimuthal angular range of this wedge from $\phi = 30^{\circ}$ to $\phi = 90^{\circ}$. The intensities from these calculations were then mirrored across the $\phi = 90^{\circ}$ plane and then threefold mapped to 360°. The final intensity for such cases is then the sum over the intensities for all emitters. The angular broadening induced by the spectrometer was included by doing a standard multi-point average over a cone of 3.0° half angle [4.28]; however, we discuss below an additional angular broadening procedure that was found to improve agreement with experiment. Before comparing to experiment, each theoretical pattern was converted to a normalized $\chi(\vec{k})$ by the same procedure used for the experimental patterns described above. Finally, because forward scattering peaks along near-neighbor directions will be important features of such XPD patterns for layers ≥ 2 ML in thickness, we also show in the figures below for each cluster a figure in which each scatterer is represented by a circle or dot whose diameter is inversely proportional to the distance from the emitter. For clusters with emitters in more than one layer, the contribution from all emitters are superposed in these figures. Note that for the coverages with sixfold symmetry (such as 3 ML), we have six-fold symmetrized the corresponding forward scattering plots.

The R-factors used in this analysis are based on a set of five first discussed for LEED analyses [4.29(a)] and then modified so as to be applicable to XPD by Saiki et al. [4.29(b)]. The first quantity, R_1, is a normalized sum of the absolute value of the

differences between the experimental and theoretical intensities; R_2 is a normalized sum of the square of the difference between the experimental and theoretical intensities; R_3 is the percentage of angle range over which the experimental and theoretical intensities have slopes of different sign (+/-); R_4 is a normalized sum of the absolute value of the difference between the first derivative of the experimental and theoretical intensities; and R_5 is a normalized sum of the square of the difference between the first derivatives of the experimental and theoretical intensities. These R-factors are discussed in more detail in ref. [4.29(b)]. These quantities have been determined by first calculating R_i at each individual polar angle in the nearly full 2π XPD pattern and then summing R_i over the polar angles from $\theta = 6^{\circ}$ to $\theta = 88^{\circ}$. We will refer to these summed R-factors as R_i^S. In most of our analysis, we have varied the interlayer spacing and calculated the resulting summed R-factors as a function of $d_\perp/d_\parallel$. In finally determining a structure, a global normalized-sum R-factor is then calculated by first normalizing R_2^S - R_5^S to the average of R_1^S, i.e.,

$$R_i^N\left(d_\perp/d_\parallel\right) = R_i^S\left(d_\perp/d_\parallel\right)\cdot\frac{\sum\limits_{d_\perp/d_\parallel} R_i^S\left(d_\perp/d_\parallel\right)}{\sum\limits_{d_\perp/d_\parallel} R_1^S\left(d_\perp/d_\parallel\right)},\ \text{i} = 2, 3, 4, \text{or } 5, \tag{4.5}$$

where $R_i^N(d_\perp/d_\parallel)$ is the ith normalized R-factor, and $R_1^N\left(d_\perp/d_\parallel\right) = R_1^S\left(d_\perp/d_\parallel\right)$. The global R-factor is then,

$$R_{global}\left(d_\perp/d_\parallel\right) = \tfrac{1}{5}\sum_{i=1}^{5} R_i^N\left(d_\perp/d_\parallel\right). \tag{4.6}$$

These global R-factors have been determined by comparing experiment to SSC and MSC calculations on an fcc Cu lattice with various interlayer spacings and also various degrees of mixing between the two possible domains. The R-factor minima for both the

interlayer spacing and relative domain occupation were determined in a self consistent manner by iteratively finding the minimum R-factor for interlayer spacing and then finding the minimum R-factor for the relative domain occupation at this interlayer spacing. This process was then repeated this process until the minimum R-factors for interlayer spacing and for relative domain occupation were consistent with each other.

Another consideration emerging from this analysis is that theoretical XPD patterns, and in particular MSC XPD patterns, tend to show much more fine structure than experimental XPD patterns. This may be due to several reasons. One is that the $\pm 3^{o}$ angular broadening included in our calculations may not accurately represent the true amount of angular broadening in our experimental system, with the latter actually being slightly larger. In addition, there may be other effects in experiment such as defects and imperfections in the sample which tend to smear out the experimental XPD patterns as compared to the theoretical XPD patterns. Finally, there may also be deficiencies in the way the MSC code includes the effects of both angular broadening and vibrational damping or smearing of diffraction structures. To account for such factors, we have thus also performed a systematic smoothing of the theoretical XPD patterns by convolution with a gaussian of various widths, and this has in fact been found to lower the overall R-factors and improve the visual comparison with experiment. The gaussian convolution procedure was developed by Len [4.30] and its application to XPD is described in more detail elsewhere [4.7]. To illustrate the effects of this additional broadening, we show, in Fig. 4.5(a), the experimental XPD pattern at 5 ML, and in Figs. 4.5(b)-4.5(e), the MSC calculations at different degrees of gaussian smoothing. Indicated next to each MSC calculation is the half width at half maximum (HWHM) of the gaussian used. Since a $\pm 3.0^{o}$ broadening has already been included in all of the MSC calculations in this work via a standard multi-point average, the amount of gaussian smoothing indicated in Fig. 4.5(b)-4.5(e) represents additional smoothing. A simple (but always important) visual comparison of experiment and theory suggests that a HWHM somewhere in the range of

2.4^{o} to 4.8^{o} provides the best fit to experiment, and in fact, the global R-factor is lowest at 4.8^{o}. We also show in Fig. 4.6 a plot of the R-factor versus HWHM for both SSC and MSC calculations, and the minimum R-factor for both is at a HWHM = 4.8^{o}, although the curve for SSC is not as convincing due to other deficiencies in single scattering theory for describing a thick overlayer. The optimum broadening is thus slightly larger than the $\pm 3^{o}$ angular broadening used in our MSC code. The minimum R-factor, in fact, is found to occur near a HWHM = 4.8^{o} for all of our coverages; however, visual comparison suggests using a HWHM slightly smaller than this and thus, the theoretical XPD patterns shown in this paper have all been smoothed with a gaussian of HWHM = 4.0^{o}. We have, however, used the more quantitatively derived HWHM = 4.8^{o} in all R-factor analyses for determining interlayer spacings and symmetries. Although the minimum R-factor at 1 ML also occured at a HWHM = 4.8^{o}, we have used a HWHM = 2.4^{o} at this coverage, again because the visual comparison appears much better. We have found that the choice of HWHM anywhere within the range of lowest-R-factor to best visual comparison does not significantly affect the position of the R-factor minimum, although the overall R-factors are higher for smaller values of HWHM.

The global R-factors used to determine interlayer spacings are shown in Fig. 4.7 for coverages from 1 ML up to 25 ML and for both SSC and MSC calculations. Due to the large amount of calculation time required for MSC calculations, the cluster sizes have been limited to a maximum of 80 atoms. We have also performed single scattering calculations on larger clusters, and while the larger cluster size has the effect of changing the overall R-factor slightly, it does not significantly change the position of the R-factor minima, and therefore we only show single scattering R-factors for the smaller clusters. The curves through the R-factor points have been determined by spline interpolation. The positions of the R-factor minima and the corresponding uncertainties have been roughly estimated by adding 3% to the minimum in the R-factor curve, and using the half-width of the curve at this point as a measure of the $\pm$ uncertainty. The minimum is

then taken to be at the midpoint of this width. We note immediately in Fig. 4.7 that the SSC and MSC global R-factors agree very well up to 2.9 ML, and then begin to diverge, with this divergence being much more severe for 4.9 ML and higher. For 2.0 ML and above, the MSC R-factor minima are always lower that those for SSC, and the shapes of the MSC curves are more well-behaved in permitting the determination of a unique minimum. This is due to the onset of significant multiple scattering effects along chains of atoms for the thicker layers, and indicates that the MSC results should be much more reliable for such layers.

In Fig. 4.8(a), we present the experimental XPD pattern of the Cu $2p_{3/2}$ peak at 556 eV kinetic energy for a Cu coverage of 1 ML, and in Figs. 4.8(b) and 4.8(c) are the calculated XPD patterns using the MSC and SSC methods, respectively. The XPD calculations were performed on a cluster which consisted of a single Cu layer on top of an hcp Ru(0001) cluster, with the Cu atoms sitting in the threefold hollow hcp sites of the Ru and at a vertical distance $Z_{Cu\text{-}Ru}$ of 2.15 Å corresponding the minimum of the R-factors in Fig. 4.7(a). There were a total of 38 Cu atoms and 40 Ru atoms in the cluster. Although the SSC calculation for this simple bilayer case is in good agreement with experiment, and in fact yields a slightly lower minimum R-factor, the MSC calculation does better in a visual sense at predicting the fine structure, including particularly the two sets of first-order diffraction rings seen at low θ. These rings become much sharper, and more like those seen in experiment, in a multiple scattering simulation. This implies that multiple-scattering pathways via forward scattering along the surface are important in analyzing such XPD patterns, even though the single monolayer morphology of the Cu makes multiple scattering at higher angles from the surface negligible. The plot of the global R-factor versus the vertical distance $Z_{Cu\text{-}Ru}$ in Fig. 4.5(a) has one other interesting feature: there are two minima of very nearly equal depth, one at 1.85 Å and one at 2.15 Å. This oscillation in the R-factor is due to pathlength-related variations of the phase between the direct photoelectron wave (emitted from the Cu monolayer) and its

components scattered off the dominant nearest-neighbor Ru scatterers underneath. This type of behavior in XPD R-factors has been pointed out before for the O/Ni system [4.29(a)], and it is reminiscent of things seen also in LEED analyses [4.31]. This oscillatory behavior is not expected to happen at higher Cu coverages, as the R-factor now becomes primarily sensitive to changes in the direction of the dominant forward scattering peaks and their associated higher-order fine structures, rather than changes in the backscattering from the substrate. The choice of the minimum at a vertical distance $Z_{Cu\text{-}Ru}$ = 2.15 Å is in excellent agreement with prior LEIS [4.32] and LEED [4.33] experimental studies (which gave 2.10±0.06 Å and 2.123 Å, respectively), as well as with LAPW theoretical calculations [4.33] (which gave 2.10 Å for Cu(1x1) growing in fcc sites on Ru(0001), and 2.07 Å for Cu(1x1)-hcp/Ru(0001)). This agreement is noteworthy, because at the high photoelectron kinetic energy ($E_{kin} \geq 500$ eV) studied here, XPD is not initially expected to be as sensitive a technique as LEED or LEIS for determining the substrate-overlayer distance, since photoelectron backscattering is weak at these higher energies. Nonetheless, we see that XPD can be quantitatively used for such cases, with the only caveat being the possibility of multiple minima in R-factors.

For 2 ML and higher coverages, the clusters for the MSC and SSC calculations consisted of the corresponding number of Cu layers with an fcc stacking sequence. Due to the weak backscattering at this high kinetic energy of 556 eV, Ru atoms were verified to have negligible effect on these simulations for these thicker layers, and were thus omitted from the cluster. Although it is known from STM that a distribution of island heights exists on such surfaces [4.2], this distribution is generally peaked around the nominal thickness = coverage [4.2(d)], and we have found it adequate to use this nominal thickness in our theoretical modeling. To best model the XPD patterns, which ranged from threefold to sixfold symmetric depending on coverage, two threefold fcc Cu(111) XPD patterns 180° apart in ϕ (denoted "1" and "2") were superimposed on each other and added with variable weighting factors f_1 and f_2, where $f_2 = (1 - f_1)$. The in-plane Cu-Cu

nearest-neighbor distance $d_{\parallel}$ in the calculations was set to 2.56 Å (as for bulk Cu(111)), and the Cu-Cu interlayer spacing $d_{\perp}$ was then varied to provide the best fit to experiment. We were thus able to finally determine the degree of interlayer relaxation via the ratio $d_{\perp}/d_{\parallel}$. The actual $d_{\parallel}$ may of course be slightly more than 2.56 Å due to interaction with Ru, and in fact it must vary from the 5.5%-expanded 2.70 Å for the pseudomorphic layer to 2.56 Å for the ultimate fully-relaxed Cu(111). But the calculations are found to be primarily sensitive to $d_{\perp}/d_{\parallel}$, and only very weakly sensitive to $d_{\parallel}$ for a given $d_{\perp}/d_{\parallel}$. Note also that the $d_{\perp}/d_{\parallel}$ values determined here represent an average over the several Cu layers, with the top layers being weighted more heavily due to the greater amount of inelastic attenuation of photoelectrons emitted from deeper layers. The individual Cu-Cu interlayer spacings between different pairs of layers may vary slightly from this average, but we have not attempted to determine this.

Shown in Fig. 4.8(e) is the experimental 2 ML XPD pattern and in Figs. 4.8(f) and 4.8(g) the corresponding MSC and SSC XPD calculations, respectively. The 2 ML cluster consisted of 22 atoms in the 1st layer and 21 atoms in the 2nd layer. The positions of the forward scattering peaks for this cluster are indicated in Fig. 4.8(h), and they are in excellent agreement with the positions of the strongest diffraction peaks seen in experiment. The SSC calculation agrees reasonably well with experiment, but the MSC calculation is still better at predicting the fine structure, particularly at low θ where multiple forward scattering is expected to be more important. A plot of the global R-factor versus $d_{\perp}/d_{\parallel}$ for 2 ML is shown in Fig. 4.7(b), and it confirms the better description of MSC. The global R-factor minimum for SSC theory compared to experiment indicates that the Cu bilayer is significantly contracted from the bulk fcc Cu(111) interlayer spacing, with $d_{\perp}/d_{\parallel}$ = 0.733±0.038 in the bilayer and $d_{\perp}/d_{\parallel}$ = 0.816 for bulk Cu(111). The global R-factor minimum for MSC theory compared to experiment indicates that $d_{\perp}/d_{\parallel}$ = 0.729±0.034, in good agreement with SSC theory. The R-factor analysis also indicates that, as averaged over different thicknesses, one of

the two possible orientations of Cu on the Ru substrate is favored by a 3:2 ratio, thus yielding a value of $f_1 = 0.66$.

Shown in Fig. 4.9(a) is the experimental 3 ML XPD pattern, and in Figs. 4.9(b) and 4.9(c) are the corresponding MSC and SSC XPD calculations, respectively. In addition, Fig. 4.9(d) shows a plot of the forward scattering directions for the cluster used in the MSC calculations. Initially, a 3 ML cluster consisting of 22 atoms in the 1st layer, 21 atoms in the 2nd layer, and 20 atoms in the 3rd layer was used to compare to experiment, however, the 2 ML calculation not only appeared to be a better fit, but also gave lower overall R-factors, and we have thus used the 2 ML calculation (although with sixfold symmetry and thus $f_1 = f_2$) for comparison to the 3 ML experiment. We are able to justify this by the fact that at the substrate temperature ($T \cong 600^{o}C$) at which we deposited Cu for 3 ML coverage, STM studies [4.2(d)] indicate that the first two layers grow layer-by-layer while the third layer grows as very tall 3D islands which cover only about 10% of the surface. Thus, the XPD pattern is expected to be dominated by the first two layers, while the 3D islands are expected to contribute only a little to the XPD pattern. Both 2 ML calculations are in good agreement with experiment, but again the MSC calculation is in better agreement with the fine structure at low θ. A plot of the global R-factor versus $d_{\perp}/d_{\parallel}$ is shown in Fig. 4.5(c). The R-factor minimum for experiment compared to SSC theory indicates that $d_{\perp}/d_{\parallel} = 0.740 \pm 0.026$, and that neither of the two possible orientations is favored: that is, they form in a 1:1 ratio with $f_1 = 0.50$, and so yield a sixfold pattern as seen in experiment. The R-factor minimum for experiment compared to MSC theory indicates $d_{\perp}/d_{\parallel} = 0.756 \pm 0.018$, and the same 1:1 ratio is found. Although we can justify comparing 3 ML experiment to 2 ML theory, it is interesting to note that the 3 ML experiment is sixfold whereas the 2 ML experiment is more threefold. This is not a random effect as the 2 ML and 3 ML experiments were repeated more than once and the symmetries did not change. It is not yet clear to us why

this change in symmetry occurs, but somehow having the extra monolayer of Cu for 3 ML forces the two domains of 2-ML growth into equal population.

Shown in Fig. 4.9(e) is the experimental 4.2 ML XPD pattern, in Figs. 4.9(f) and 4.9(g) are the 4 ML MSC and SSC XPD calculations, respectively, and in Fig. 4.9(h) is the forward scattering plot for the cluster used in the MSC calculation. The cluster consisted of 22 atoms in the 1st layer, 21 atoms in the 2nd layer, 20 atoms in the 3rd layer, and 16 atoms in the 4th layer. As noted before, above 4 ML, our Cu films were grown at a substrate temperature of T = 300°C, where STM [4.2(d)] predicts a more complete filling of each layer than for higher temperatures. Although the 4.2 ML film was heated briefly to 600°C, which should tend to promote the formation of 3D islands, we do not believe the 3D character is as great as in our 3 ML film since the anneal was very brief, and also due to the similarity of the 4.2 ML XPD pattern to the 4.9 ML XPD pattern. Thus, here we have used a 4 ML cluster to compare to experiment. For a 4 ML coverage in the fcc stacking, there are now multiple forward scattering paths along <110>-like directions (cf. Fig. 4.4(b)) and these directions are involved in the three strongest peaks seen in the SSC calculation. Here, the forward scattering peaks in the SSC calculation have become too strong due to a lack of consideration of multiple scattering [4.16]. That is, multiple scattering defocusing along chains of atoms reduces the intensities of forward scattering peaks [4.19], and thus the MSC calculation in Fig. 4.9(f) is in much better agreement with experiment over the full range of θ than the SSC calculation. An R-factor comparison of SSC calculations with experiment indicates that $d_{\perp}/d_{\parallel}$ = 0.773±0.022, and that one orientation is preferred again by about a 3:2 ratio (f_1 = 0.66). An R-factor comparison of MSC calculations to experiment indicates that $d_{\perp}/d_{\parallel}$ = 0.742±0.016, with the same domain ratio resulting. For this coverage, the $d_{\perp}/d_{\parallel}$ from SSC no longer agrees very well with $d_{\perp}/d_{\parallel}$ from MSC, as would be expected for a multilayer film where multiple scattering is expected to become more important. Above 4 ML, we thus do not expect the SSC analysis to be as accurate,

although a preliminary set of calculations based on it is found to yield results in essential agreement with the main conclusions of this study [4.34]

Shown in Fig. 10(a) is the experimental 4.9 ML XPD pattern, in Figs. 4.10(b) and 4.10(c) are the 5 ML MSC and SSC XPD calculations, respectively, and in 4.10(d) is the forward scattering plot. The cluster is the same as for the 4 ML MSC cluster but with an added (bottom) 5th layer consisting of 1 atom. The XPD patterns have not changed significantly from the 4 ML XPD patterns, and this is true also for the anisotropy curve in Fig. 4.2. An R-factor comparison of SSC calculations with experiment indicates that $d_{\perp}/d_{\parallel}$ = 0.769±0.047, and that one orientation is preferred again by a 3:2 ratio (f_1 = 0.66). An R-factor comparison of MSC calculations with experiment indicates that $d_{\perp}/d_{\parallel}$ = 0.718±0.018. Both a visual comparison of the XPD patterns in Figs. 4.10(a),(b), and (c) and the R-factor curves for this case in Fig. 4.7(e) makes it clear that the MSC result is the more reliable for $d_{\perp}/d_{\parallel}$.

Before proceeding to discuss the remaining experiment/theory comparisons in Figs. 4.10 and 4.11, we note that, due to multiple scattering defocusing, as well as inelastic attenuation of the outgoing photoelectrons, only the top 5 or so atomic layers are expected to contribute significantly to the XPD patterns. Thus, MSC calculations for substrate emission are expected to converge in about 5-10 layers, as verified in both this work and elsewhere [4.19(b), 4.35]. To illustrate this effect for the present case, we show, in Fig. 4.12, plots of MSC calculations for a Cu(111) cluster of 1 ML to 8 ML in thickness and with $d_{\perp}/d_{\parallel}$ = 0.816 as in bulk Cu. Visually, the MSC calculation appears to have converged by 5 ML, with no difference discernible among the 5, 6, 7, and 8 ML cases. To confirm this more quantitatively, we have performed an R-factor analysis in which the full pattern calculated for each coverage is compared to the 8 ML calculation; i.e. we have compared n ML to 8 ML for n = 1,2,...,8. A plot of this is shown in Fig. 4.13(a). The R-factor decreases quickly between n = 1 and n = 2 and then continues to decrease by small amounts up to n = 8, where it is required to go to zero from the 8 ML-

to-8 ML comparison. If we now compare 8 ML experiment to each coverage in the MSC calculations from 1 ML to 8 ML, the R-factor also decreases quickly between 1 and 2 ML and then decreases by small amounts up to 8 ML. A plot of this is shown in Fig. 4.13(b). Due to the large amount of computation time needed to do MSC calculations on several layers, we have only been able to go up to 8 ML. Although these comparisons of theory with theory and of experiment with theory do not indicate a complete convergence by 8 ML, using thicker layers for interlayer determination would not significantly change our results. We conclude from Figs. 4.12 and 4.13 that a 5-ML cluster should yield a very good agreement with experiment. In particular, since the shapes and sizes of the peaks and diffraction features in the XPD patterns, as well as the positions of the peaks and features do not change significantly after about 5 ML, we believe the small change in the R-factor for each succeeding layer thickness may be due to small subtle changes in the relative intensities of the peaks and features in the XPD pattern. Thus, it should not be necessary to perform MSC calculations on clusters much thicker than about 5 ML in order to model thicker experimental overlayers, and this should be a generally useful rule for analyzing epilayers of low-to-medium Z materials with XPD.

Due to the foregoing discussion and the large amount of computation time required to perform MSC and SSC calculations on multilayer clusters with several emitters, we have thus only performed extensive calculations for geometry determinations with clusters from 1 to 5 Cu layers. Therefore, Fig. 4.10(e) shows the experimental 6.5 ML XPD pattern, while Figs. 4.10(f) and 4.10(g) represent XPD calculations for a 5 ML cluster in MSC and SSC, respectively. The forward scattering plot is also shown in Fig. 4.10(h). By 6.5 ML, the symmetry of the experimental 6.5 ML XPD pattern is beginning to appear more sixfold, and in fact, an R-factor comparison of SSC calculations with experiment indicates that one orientation is now preferred by only a 5:3 ratio (f_1 = 0.60) and that $d_\perp/d_\parallel$ = 0.812±0.026. An R-factor comparison of MSC calculations with

experiment further indicates that $d_{\perp}/d_{\parallel}$ = 0.740±0.014, and we expect this to be the most reliable of the two determinations.

Shown in Fig. 4.11(a) is the experimental 8 ML XPD pattern, which is now essentially sixfold, and in Figs. 4.11(b) and 4.11(c) are the 5 ML MSC and SSC calculations, respectively. Here, the SSC calculation again does not model experiment very well due to the too-great strength of the dominant forward scattering peaks at $\theta \approx 52^{o}$. The MSC calculation with an equal mixture of the two orientations (f_1 = 0.50) however matches experiment very well. An R-factor comparison of SSC calculations to experiment indicates that $d_{\perp}/d_{\parallel}$ = 0.837±0.016. Comparison of the more accurate MSC calculations to experiment indicates that $d_{\perp}/d_{\parallel}$ = 0.766±0.018.

Shown in Fig. 4.11(e) is the experimental 25 ML XPD pattern, and in Figs. 4.11(f) and 4.11(g) are the 5 ML MSC and SSC calculations, respectively. An R-factor comparison of SSC calculations to experiment indicates that $d_{\perp}/d_{\parallel}$ = 0.835±0.014 and that neither orientation is preferred (f_1 = 0.50). By contrast, our most accurate MSC analysis of the XPD data indicates that $d_{\perp}/d_{\parallel}$ = 0.777±0.020. Thus, the MSC analysis for 25 ML indicates that the near-surface average Cu interlayer spacing is still contracted by about 4.8±2.5% from bulk fcc Cu(111). This is not a completely surprising result, as such contractions from bulk values have been observed in other metal-on-metal systems, as e.g. Ni/Cu(001) [4.36]. A LEED I-V structure determination of this system indicates that the average interlayer distance in the top 5 or so layers of an 11 ML Ni film is 1.72±0.03 Å, or about 2.3% smaller than the bulk interlayer distance of 1.76 Å [4.36].

We now summarize the predictions of the MSC analysis for $d_{\perp}/d_{\parallel}$ in Fig. 4.14(a), and for the determination of the pattern symmetry and f_1 in Fig. 4.14(b). Also shown in Fig. 4.14(a) is a theoretical estimate of $d_{\perp}/d_{\parallel}$ versus coverage in which we have taken areal Cu densities derived from 2D Frenkel-Kontorova calculations by Hamilton and Foiles [4.3 Ham], used these to derive $d_{\parallel}$, and then assumed a constant atomic volume to estimate $d_{\perp}$. This theoretical estimate suggests a fairly rapid convergence to the bulk

$d_{\perp}/d_{\parallel}$ = 0.816 by 4 ML. For 2 and 3 ML coverage, comparison of our XPD results with MSC calculations yields $d_{\perp}/d_{\parallel}$ values that agree rather well with this simple theoretical estimate. By contrast, for coverages from 4 ML to 8 ML, comparison of our data to to MSC calculations indicates a much slower convergence to the bulk Cu(111) interlayer spacing and suggests that the top 5 or so layers of the Cu overlayer have not quite converged to bulk Cu(111) interlayer spacings even up to 25 ML coverage. As another method of estimation, we have also used elasticity theory considering trigonal strain [4.37, 4.38]. That is, $d_{\parallel}$ was again taken from the Frenkel-Kontorova analysis, and elasticity theory then used to predict $d_{\perp}$ [4.7]. Elasticity theory predicts an even more rapid approach to the bulk values, as shown in Fig. 4.14(a). Taken together, these experimental results thus indicate a much higher degree of interlayer relaxation for thinner layers than predicted by applying either a constant volume assumption or elasticity theory to the results of the simple Frenkel-Kontorova model. This contraction has additional potential implications for the chemical reactivity of such Cu layers.

In Fig. 4.14(b), we present a plot of the fractional occupation of domain #1 (f_1, here in %) as a function of coverage. At 1 ML, the sixfold symmetry is expected, as an emitting atom in the pseudomorphic overlayer will have six nearest neighbors in a hexagonal pattern around it, thus producing the ring pattern in Figs. 4.2(a) and 4.2(b). At the higher coverages, for fcc growth in a single domain, the XPD pattern will be threefold (cf. Fig. 4.2(k)), but for fcc growth in two equally-populated domains 180° apart in ϕ, the XPD pattern will be sixfold (cf. Fig. 4.2(j)). We note interesting changes in the symmetry as we increased the coverage from 2 ML to 8 ML. At 2 ML, the symmetry is threefold, indicating a preference for a particular adsorption site of the second-layer atoms on the first Cu layer. According to STM [4.2] results, the uniaxial contraction may take place in three directions, 120° apart in ϕ. However, this will not produce the threefold symmetry seen in XPD since XPD is not sensitive to the long range features of the overlayer, but is rather a short range structural probe. Thus, locally, the structure is fcc Cu(111)-like, and

the threefold pattern results. At 3 ML, however, the symmetry is sixfold, and thus, at 3 ML, the two possible domains of fcc Cu(111) on Ru(0001) have become equally populated; we have commented before on the fact that this layer tends to be dominated by 2 ML surface, with small, thick islands to accommodate the additional material. At 4 and 5 ML, the symmetry becomes threefold again, and finally, the pattern returns to nearly sixfold symmetry at 8 ML and above, converging to the case of equal occupation of the two domains by 25 ML. A possible explanation for the jump to sixfold symmetry at 3 ML may be that, according to STM data [4.2(d)], the substrate temperature during deposition of 3 or more monolayers will significantly change the amount of 3D islanding, i.e. at lower temperatures the growth is more layer-by-layer with the 3D islands covering a large area of the surface, while at higher temperatures, the 3D islands grow thicker and covers less area of the surface. Between 3 and 5 ML, we lowered our substrate temperature, and thus, our 5 ML film should be smoother than our 3 ML film. At thicker coverages above about 8 ML, more 3D islanding occurs regardless of the deposition temperature. Perhaps the 3D islands allow for more randomness in domain occupation, whereas when the growth is more layer-by-layer, the film coalesces into a single domain. However, this would tend to suggest that our 4.2 ML film which we annealed at 600°C should be more sixfold due to the occurrence of 3D islanding. However, we only annealed the sample for a short time, and it may not have been able to attain as much 3D character as the 3 ML film which was at 600°C during deposition and also for a brief time after deposition before cooling down. Thus, at coverages where more 3D islanding occurs, we expect the symmetry to be more sixfold, and at coverages where the film is smoother, the symmetry should be more threefold.

4.3.1.3 Reference XPD results for bulk Cu(111) and comparison to theory

In assessing the accuracy of our XPD analysis, it is important to verify that it converges to a correct interlayer spacing for the limiting case of bulk Cu(111). Thus, we have compared MSC calculations at three photoelectron kinetic energies of 321 eV, 556 eV, and 808 eV to Cu $2p_{3/2}$ experimental XPD patterns taken from a Cu(111) single crystal at these energies. The data at 321 eV and 808 eV were obtained by Naumovic and Osterwalder [4.21], and made use of somewhat better angular resolution than ours. The data at 556 eV were obtained with the same system as all of the other patterns shown here, and have already been presented in Fig. 4.2(k). Shown first in Fig. 4.15(a) is the experimental 321 eV XPD pattern, and in Figs. 4.15(b) and 4.15(c) are the corresponding MSC and SSC calculations, respectively, for the optimized interlayer spacing. Shown in Fig. 4.15(d) is the experimental 556 eV XPD pattern, and in Figs. 4.15(e) and 4.15(f) are the corresponding MSC and SSC calculations, respectively. Shown in Fig. 4.15(g) is the experimental 808 eV XPD pattern, and in Figs. 4.15(h) and 4.15(i) are the corresponding MSC and SSC calculations, respectively. The MSC patterns are in excellent agreement with experiment, while the SSC patterns have too-strong forward scattering peaks, as noted previously. An R-factor comparison of the 321 eV XPD pattern to MSC indicates that $d_{\perp}/d_{\parallel}$ = 0.820±0.020, about 0.5% larger than bulk. An R-factor comparison of the 556 eV experimental XPD pattern to MSC indicates that $d_{\perp}/d_{\parallel}$ = 0.792±0.023, about 2.9% smaller than the bulk. An R-factor comparison of the 808 eV experimental XPD pattern to MSC indicates that $d_{\perp}/d_{\parallel}$ = 0.792±0.017, about 2.9% smaller than bulk, and in excellent agreement with the 556 eV result. Plots of the MSC global summed R-factor for 321 eV, 556 eV, and 808 eV XPD patterns are shown in Fig. 4.16, and Fig. 4.14(a) also shows the three Cu(111) interplanar distances determined from XPD as open symbols, with two points overlying one another. The average $d_{\perp}/d_{\parallel}$ over these three sets of Cu(111) data is thus 0.801, corresponding to a small interlayer contraction of -1.8%

(-0.04 Å); our overall error estimate for these numbers based on the 3% criterion on change in R-factor is ~±4.2% (±0.09 Å) and thus includes the case of no relaxation. For comparison, prior LEED studies of Cu(111) yield varying results for the topmost interlayer distance. Watson *et al* [4.39(a)] reported a surface relaxation of –4.1±0.6% (–0.085±0.012 Å) for Cu(111), in good agreement with our results. Tear *et al* [4.39(b)] reported a very small surface relaxation of –0.3±1% (–0.006±0.021 Å). Neve *et al* [4.39(c)] found the topmost copper layer to be relaxed by a somewhat larger-0.6% (–0.012 Å). Finally, Bartos *et al* [4.39(d)] found a +0.8±1.0% (+0.016±0.021 Å) expansion of the topmost Cu layer. These LEED values thus span essentially the same range as our XPD analysis and a simple arithmetic average of them yields a -1.06% (-0.022 Å) contraction, although we stress that LEED is measuring the relaxation of the topmost layer, whereas we are measuring an average over the first 5 layers, but with strong weighting toward the first few. Thus, within our range of error, our XPD results for $d_{\perp}/d_{\parallel}$ for a thick Cu film of 25 ML grown on Ru(0001) are lower than, but still can be considered to agree reasonably well with similar results obtained from a Cu(111) single crystal and from prior LEED analyses of the Cu(111) surface.

4.3.2 Cu Grown on O-Precovered Ru(0001)

4.3.2.1 Experimental Results and Comparison to Cu on clean Ru(0001)

Finally, we consider the effect on the Cu growth modes of preadsorbing oxygen on Ru(0001). First we show for reference in Fig. 4.17(a) the XPD pattern of the experimental O 1s (E_{kin} = 958 eV) peak for O/Ru(0001) at an oxygen saturation coverage of 0.5 ML; and in Figs. 4.17(b) and 4.17(c), the corresponding MSC and SSC calculations, respectively, as summed over the three domains of p(2x1)-O/Ru(0001) expected on this surface. For reference to the substrate, the experimental Ru 3d XPD

pattern is shown in Fig. 4.17(d). Due to the weak photoelectric cross section of the O 1s peak, the experimental data were rather noisy, and therefore the diffraction features at low θ were very faint in the initial XPD pattern. Thus, a more quantitative analysis of this data is not possible. For presentation purposes, we have also applied a significant amount of smoothing as well as symmetrization through a mirror plane on the experimental XPD pattern shown in Fig. 4.17(a). The final anisotropy is very small, being only about 15% over an azimuthal scan at $\theta = 12^{o}$ for which it is a maximum. Also, the features seen at high θ in the experimental XPD pattern are largely artifacts of the smoothing and symmetrization process. The Ru 3d XPD pattern is essentially identical to that for the clean surface, although the features at lower θ maybe somewhat weaker due to scattering in the O overlayer. Oxygen forms an ordered p(2x1) structure on Ru at the saturation coverage of 0.5 ML [4.40], although according to LEED it appears to form a p(2x2) structure due to the occurrence of three possible domains of p(2x1)-O. The actual p(2x2) structure will form at an oxygen coverage of 0.25 ML but is not possible at an oxygen coverage of 0.5 ML. The experimental O 1s XPD pattern shown in Fig. 17(a) has a sixfold symmetry for low polar angles, and weak threefold symmetry at higher angles. At low polar angles, there is also an indication of first-order diffraction rings similar to those in Figs. 4.2(a) and 4.2(b) that would have to be due to near-neighbor forward scattering in three p(2x1)-O domains 120° apart in azimuth. The MSC and SSC calculations have the correct sixfold symmetry and are in good qualitative agreement with experiment, showing also the strong minima at low θ and at $\phi = 0^{o}, 60^{o}, 120^{o}, ...$

For the Cu overlayers, we begin by considering the plots of the relative azimuthal anisotropies of the Cu $2p_{3/2}$ XPD patterns for Cu/O/Ru(0001) as a function of the polar angle, as shown in Fig. 4.3(b). For 2 ML and above, the anisotropies have very nearly the same shape as the anisotropies shown for Cu/Ru(0001) in Fig. 4.2. This similarity in anisotropy curves is an indication that the structure of the Cu overlayer is not significantly changed by the addition of oxygen for thicker overlayers. However, at 1 ML, the shape of

the anisotropy curve is different for Cu/O/Ru(0001) and Cu/Ru(0001), and in fact that for Cu/O/Ru(0001) looks more like that for 2 ML of Cu/Ru(0001). This suggests that double-layer stacking occurs at 1 ML in Cu/O/Ru(0001). The absolute anisotropies for Cu/O/Ru(0001) and for Cu/Ru(0001) also differ, with those for Cu/O/Ru(0001) being only about half as high as the anisotropies for Cu/Ru(0001).

In Figs. 4.18-4.21, we show O 1s and Cu $2p_{3/2}$ XPD results for Cu grown on oxygen precovered Ru(0001), and compare them directly to the corresponding Cu $2p_{3/2}$ results for Cu grown on clean Ru(0001) (shown in the bottom panels of each column). In Figs. 4.18(a) and 4.18(d) we show XPD results for the O 1s peak, and in Figs. 4.18(b) and 4.18(e), the Cu 2p3/2 peak, for Cu coverages on O/Ru(0001) of 1 ML and 2 ML, respectively. The comparison to the case of Cu grown on clean Ru(0001) is shown in Figs. 4.18(c) and 4.18(f). The O 1s XPD patterns shown in Figs. 4.18(a) and 4.18(d) show no diffraction features whatsoever. Although the oxygen XPD patterns shown here have not been smoothed as was Fig. 4.17(a), no diffraction features are visible in these XPD patterns, even after considerable smoothing. The lack of any forward scattering peaks indicates that all of the oxygen floats on the Cu overlayer, and that none of the oxygen is subsurface or remains at the Cu/Ru interface, in disagreement with some prior conclusions concerning this system [4.12-4.14]. If any oxygen were subsurface for these two cases, there would be the possibility of forward scattering through overlying Cu or O atoms, with the Cu clearly being in an ordered structure, as seen in the XPD patterns of Figs. 4.18(b) and 4.18(e). This result is further verified by XPS coverage calculations which indicate that the O coverage remains at ~ 0.5 ML after Cu deposition, although due to noise in the O 1s signal as well as to errors in parameters used in our coverage calculations, the error in the O coverage determination may be as high as $\pm$0.05 ML [4.7]. The further lack of any features at even low θ confirms the results of LEIS studies [4.15] that the oxygen overlayer is disordered and/or perhaps highly mobile as a sort of lattice gas on the Cu surface. This is in contrast to the features seen in the XPD pattern shown

in Fig. 4.18(a) for the ordered p(2x1)-O/Ru(0001) structure. This result is not surprising as several prior studies [4.41] have not reported an ordered oxygen structure on the Cu(111) surface. Consensus on the O/Cu(111) adsorption system, however, has not yet been reached, since ordered structures have been reported as well [4.42]. Shown in Fig. 4.18(b) is the Cu $2p_{3/2}$ XPD pattern for a Cu coverage of 1 ML on the O-precovered Ru(0001) surface. A nearly sixfold pattern of forward scattering peaks appears already, indicating that there are atoms sitting in the threefold hollow sites on top of the first layer before the first layer is complete, and that the two domain types are nearly equally occupied. This same sixfold pattern persists for 2 ML and 3 ML, as shown in Figs. 4.18(e) and 4.19(b), and all three of these patterns look very much like the pattern for 3 ML Cu on clean Ru(0001), as shown in Fig. 4.19(c). Thus, for Cu grown on O-precovered Ru in the 1-3 ML range, the growth appears to be initially via a Volmer-Weber (3D islands) mode rather than a Franck-Van der Merwe (layer-by-layer) mode. This is at first sight in disagreement with prior studies [4.12-4.15], which suggest layer-by-layer growth. For example, AES studies [4.12, 4.15] suggested the layer-by-layer mode based on agreement between the AES intensity ratio I_{Cu}/I_{Ru} as a function of coverage and a calculation based on the Gallon model [4.43] assuming layer-by-layer growth. Our findings are inconsistent with this AES study. Work function oscillations seen during Cu growth [4.13, 4.14] have also suggested surfactant-mediated layer-by-layer growth. However, these oscillations did not start until about 3 ML Cu coverage. Thus, our XPD results and the work function measurements [4.13, 4.14] can still be consistent with one another if the Cu initially grows as 3D islands, and then switches to layer-by-layer at thicker coverages above 3-4 ML. This type of growth has, for example, been seen by STM on the Co/Cu(100) system [4.44].

At thicker coverages ($\geq$ 4 ML), as shown in Figs. 4.19(a) , 4.19(d), 4.20(a), 4.20(d), 4.21(a) and 4.21(d), the XPD patterns for the O 1s peak again show absolutely no diffraction, again indicating that the oxygen floats on the Cu surface and is disordered

and/or mobile. The XPS coverage determination also again yields essentially the same value of ~0.5 ML as for the other Cu coverages [4.7], with no systematic variation in this coverage as the Cu thickness was increased. An interesting point to note at ~4 ML coverage (obtained as noted previously after annealing to 325°C), is that a $2\sqrt{3} \times 4\sqrt{3}R30^\circ$ LEED structure as reported in prior work was observed [4.13]; however the oxygen XPD pattern still reveals no ordered structure. This is noteworthy in that it might be expected that oxygen could preferentially bind to sites in the $2\sqrt{3} \times 4\sqrt{3}R30^\circ$ structure, in which case forward scattering features or diffraction rings could develop. In fact, the oxygen is still totally disordered and/or highly mobile. At ~4 ML, the XPD pattern for the Cu $2p_{3/2}$ peak shown in Fig. 4.19(e) looks like the XPD patterns for 4 ML and 5 ML of Cu on clean Ru(0001), as shown in Figs. 4.19(f) and 4.20(c). At 5 ML and higher coverages shown in Figs. 4.20(b), 4.20(e), 4.21(b), and 4.21(e), the Cu $2p_{3/2}$ XPD patterns look very much like the XPD patterns for 8 ML and 25 ML of Cu on clean Ru(0001), as shown in Figs. 4.21(c) and 4.21(f). For these higher coverages, the diffraction features at lower θ values are somewhat weaker and more smeared out with oxygen present, but this might be expected if growth is more multilayer and/or if there is diffuse scattering through the disordered oxygen overlayer. Thus, the structure is finally fcc Cu(111)-like with two domains, but the oxygen induces multilayer growth earlier than is the case of growth on clean Ru(0001). However, without a more detailed theoretical analysis, XPD does not allow us to determine whether the growth has become layer-by-layer at these thicker coverages. More studies of this system (e.g. with STM) may help to better understand the nature of the disorder in the oxygen overlayer, as well as the morphology of the surface at thicker Cu coverages with and without oxygen present.

We have also carried out an R-factor analysis of these O/Ru(0001) data so as to determine the ratio $d_\perp/d_\parallel$ for Cu coverages from 1 to 30 ML, and these curves as derived from MSC calculations are shown in Figs. 4.22(a)-4.22(h). Because of the greater uncertainty in the growth mode with oxygen present, it is more difficult to decide

what thickness of cluster best represents this data. At 1 ML coverage, we have compared experiment to 2 ML MSC calculations since we believe that stacking occurs before the first monolayer is completed. For the other cases, we have used the nominal thickness of the overlayer up to 5 ML, and we have used 5 ML calculations for comparison to thicker coverages. All of the R-factors shown in Fig. 4.22 have been determined by comparing experiment to the same fcc Cu(111) clusters as used for Cu/Ru(0001). That is, we have not included the oxygen overlayer in our calculations since the oxygen overlayer is disordered, and therefore should have little effect on the Cu XPD pattern other than acting as an attenuating overlayer, with more serious effects for lower θ, as noted above. The results of the R-factor analysis for both Cu/Ru(0001) and Cu/O/Ru(0001) are tabulated in Table 4.3.

A plot of the change in interlayer contraction for Cu grown on O-precovered Ru(0001) is presented in Fig. 4.23(a). These values do not significantly differ from those for Cu/Ru(0001), and thus the oxygen appears only to affect the growth and morphology rather than the short-range interplanar structure. Again we also show here a theoretical estimate of $d_{\perp}/d_{\parallel}$ versus coverage based on 2D Frenkel-Kontorova calculations and a constant atomic volume assumption. Shown in Fig. 4.23(b) is also a plot of the symmetry versus coverage for the Cu films grown on O-precovered Ru(0001). Here, with the exception of ~4 ML which was a special case where the film was annealed, all of the symmetries are nearly sixfold. Thus it would seem that the presence of oxygen promotes the formation of two domains, or perhaps the sixfold symmetry is due to a greater amount of 3D character in the films as was suggested earlier for Cu/Ru(0001); however this conclusion would then be in disagreement with the prior studies of this system [4.12-4.15].

4.4. Conclusions

This XPD analysis of the growth of Cu on clean and oxygen-recovered Ru(0001) permits several new structural conclusions, as well as some general comments concerning the application of XPD to such epitaxial systems.

For Cu growth on clean Ru(0001), the first monolayer is pseudomorphic, and even at partial monolayer coverages forms in large islands of the same structure. Our result of 2.15 Å for the distance between the Cu and the first Ru layer is consistent with prior experiments and theoretical studies of this first monolayer. For thicker overlayers, we have also shown that the short range structure of Cu/Ru(0001) is fcc Cu(111), but with significant interlayer contraction for coverages between 2 ML and 8 ML. Comparison of experiment to MSC calculations suggests that the interlayer contraction may persist even up to 25 ML Cu coverage, although within the range of error, the results for this coverage are also consistent with our own R-factor comparison of MSC calculations to XPD patterns from a Cu(111) single crystal at photoelectron kinetic energies of 321 eV, 556 eV, and 808 eV, as well as with LEED results from Cu(111) single crystals. The Cu-Cu interlayer spacing shows a slower approach to the bulk fcc Cu(111) interlayer spacing than a simple theoretical estimate based on the 2D Frenkel-Kontorova model [4.3] and either a constant atomic volume assumption or a more complex analysis using elasticity theory. The appearance of sharp forward scattering peaks with distinct orientations and the excellent agreement with theory demonstrates that the misfit dislocation structures seen in STM [4.2] for 2-4 ML coverage actually thread through to the Cu-Ru interface. We have also shown that the SSC model predicts experiment reasonably well, but MSC calculations do a better job of predicting the fine structure at low θ for lower coverages and at all θ for higher coverages. Thus, MSC calculations are important even at low coverages for a fully quantitative analysis of XPD data.

For Cu grown on O-precovered Ru(0001), we have shown that it initially forms 3D islands in the 1-3 ML range, and that all of the oxygen floats on the Cu overlayer and is highly disordered and/or mobile on the Cu surface. In addition, the presence of oxygen does not affect the interlayer contraction, but does affect the relative domain occupation of the Cu overlayer, leading to a dominance of sixfold character in the XPD patterns..

Finally, these results indicate that such XPD data, when combined with multiple scattering calculations and R-factor analysis, can yield quantitative information on such subtle issues as interlayer relaxations. Even the vertical position of a single-monolayer for which no forward scattering features exist has been successfully determined. Our results also indicate that the calculated XPD patterns converge rather quickly with layer thickness, so that the experiment is probing primarily the first 5 monolayers, and calculations can probably be truncated at about this level as well. We also have found that it is important to adequately allow for the various sources of broadening in the XPD features, and have used a gaussian angular broadening as part of the optimization of the fit of theory to experiment. Without this additional broadening, theory in our case usually predicts sharper features than experiment, which can adversely affect the final R-factor comparisons leading to a structural conclusion. Lastly, even at XPS energies of ≥500 eV, a proper allowance for surface refraction in electron escape is important, and our data may suggest using a slightly higher effective inner potential than one as usually estimated for the bulk (21 eV versus 14 eV). However, further investigation of this last point is needed to be more quantitative.

References:

[4.1] E. Bauer, Applic. Surf. Sci. **11/12,** 479 (1982).

[4.2] (a) G. Pötschke, J. Schröder, C. Günther, R.Q. Hwang, and R. J. Behm, Surf. Sci. **252,** 592 (1991); (b) G.O. Pötschke, and R.J. Behm, Phys. Rev. B **44,** 1442 (1991); (c) C.Günther, J. Vrijmoeth, R.Q. Hwang, and R.J. Behm, Phys. Rev. Lett. **74,** 754 (1995); (d) C. Günther, Ph.D. Thesis, Univ. Muenchen (1994).

[4.3] J. C. Hamilton and S.M Foiles, Phys. Rev. Lett. **75,** 882 (1995)

[4.4] K. Christmann, G. Ertl, and H. Shimizu, Thin Solid Films 57 (1979) 247; J. Catalysis **61,** 397 (1980).

[4.5] J.E. Houston, C.H.F. Peden, D.S. Blair, and D.W. Goodman, Surf. Sci. **167,** 427 (1986); J. E. Houston, C. H. F. Peden, and Peter J. Feibelman, Phys. Rev. Lett. **56,** 375 (1986); D. G. O'Neill and, J.E. Houston, Phys. Rev. B **42,** 2792 (1990)

[4.6] C. Park, E. Bauer, and H. Poppa, Surf. Sci. **187,** 86 (1987).

[4.7] S.D. Ruebush, Ph.D. Thesis, Univ. California, Davis (1997).

[4.8] Ch. Ammer, K. Meinel, H. Wolter, A. Beckmann and H. Neddermeyer, to be published in Surf. Rev. Lett.

[4.9] Ch. Ammer, K. Meinel, H. Wolter, A. Beckmann and H. Neddermeyer, submitted to Surf. Sci.

[4.10] W. F. Egelhoff, Jr. and D. A. Steigerwald, J. Vac. Sci. Technol. A **7**, 2167 (1989).

[4.11] A. Pavlovska, and E. Fauer, Surf. Sci. **175**, 369 (1986).

[4.12] K. Kalki, M. Schick, G. Ceballos, and K. Wandelt, Thin Solid Films **228**, 36 (1993).

[4.13] H. Wolter, M. Schmidt, and K. Wandelt, Surf. Sci., **298**, 173 (1993).

[4.14] M. Schmidt, H. Wolter, M. Nohlen, and K. Wandelt, J. Vac. Sci. Technol. A **12**, 1818 (1994).

[4.15] Y.G. Shen, D.J. O'Connor, H. van Zee, K. Wandelt, R.J. MacDonald, Thin Solid Films **263**, 72 (1995).

[4.16] C.S. Fadley, (a) Prog. in Surf. Sci. **16,** 275 (1984); (b) Synchrotron Radiation Research: Advances in Surface and Interface Science, R.Z. Bachrach, Ed. (Plenum Press, New York, 1992) pp. 421-517; (c) Surf. Sci. Reports **19**, 231 (1993); (d) C.S. Fadley et al., J. Elect. Spect. **68**, 19 (1994)..

[4.17] J.J. Rehr and R.C. Albers, Phys. Rev. B **41**, 8139 (1990);

[4.18] (a) D.J. Friedman and C.S. Fadley, J. Electron Spectrosc. Relat. Phenom. **48**, 689 (1990).

[4.19] (a) A.P. Kaduwela, G.S. Herman, D.J. Friedman, C.S. Fadley and J.J. Rehr, Phys. Scr. **41**, 948 (1990); (b) A.P. Kaduwela, D.J. Friedman, and C.S. Fadley, J. Electron Spectrosc. Relat. Phenom. **57**, 223 (1991).

[4.20] Z. Wang, Ph.D. Thesis, Univ. California, Davis (1997).

[4.21] D. Naumovic' and J. Osterwalder private communication; D. Naumovic', Ph.D. Thesis, Univ. Fribourg (1993).

[4.22] P. Dierckx, Journal of Computational and Applied Mathematics, **1** (1975), p. 165.

[4.23] (a) L.F. Mattheis, Phys. Rev., **134**, 970 (1964); (b) CRC Handbook of Chemistry and Physics, (CRC Press, Ed., David R. Lide), 72nd ed., 1991-1992. Mattheis determined the Fermi energy (E_F) of copper to be 9.5 eV from band structure calculations. Tables of work functions (ϕ) are available in the CRC Handbook and for Cu(111) $\phi = 4.94$ eV. The inner potential is then $V_0 = E_F + \phi = 14.44$ eV.

[4.24] Y. Chen, A. Chassé, J Garcia, M. A. Van Hove, and C. S. Fadley, private communication.

[4.25] J.B. Pendry, private communication.

[4.26] M.P. Seah and W.A. Dench, Surf. and Interface Anal. **1**, 2 (1979); C.J. Powell, A. Jablonski, S. Tanuma, and D.R. Penn, J. Elect. Spect. **68**, 605 (1994).

[4.27] A.P. Kaduwela, Ph.D. Thesis, Univ. Hawaii (1991).

[4.28] R.J. Baird, Ph.D. Thesis, Univ. Hawaii (1977).

[4.29] (a) M.A. Van Hove, S.Y. Tong and M.H. Elconin, Surf. Sci. **64**, 85 (1977); (b) R.S. Saiki, A.P. Kaduwela, M. Sagurton, J. Osterwalder, D.J. Friedman, C.S. Fadley, and C.R. Brundle, Surf. Sci. **282**, 33 (1993).

[4.30] P. M. Len, Ph.D. Thesis, Univ. California, Davis (1997).

[4.31] (a) S. Andersson and J.B. Pendry, Sol. St. Commun. **16**, 563 (1975): (b) M.A. Van Hove, W.H. Weinberg, and C.-M. Chan in *Low Energy Electron Diffraction, Experiment, Theory and Surface Structure Determination*, edited by G. Ertl, (Springer-Verlag, Berlin 1986), Vol. 6, pp. 246-248.

[4.32] Y.G. Shen, D.J. O'Connor, J. Yao, H. van Zee, R.H. Roberts, R.J. MacDonald, and K. Wandelt, J. Vac. Sci. Technol. A **13**, 1478 (1995).

[4.33] P.J. Feibelman, J.E. Houston, H.L. Davis, and D.G. O'Neill, Surf. Sci. **302**, 81 (1994).

[4.34] S.D. Ruebush, R.E. Couch, S. Thevuthasan, Z. Wang, C.S. Fadley, submitted to Surf. Sci. Lett.

[4.35] S.D. Ruebush, R.X. Ynzunza, S. Thevuthasan, A.P. Kaduwela, M.A. Van Hove, C.S. Fadley, Surf. Sci. **328**, 302 (1995).

[4.36] K. Baberschke, Appl. Phys. A **62**, 417 (1996); S. Müller, B. Schulz, G. Kostka, M. Farle, K. Heinz, K. Baberschke: Surf. Sci. (in press 1996).

[4.37] (a) P.R. Watson, F.R. Shepard, D.C. Frost and K.A.R. Mitchell, Surf. Sci. **72**, 562 (1978); (b) S.P. Tear, K. Roll and M. Prutton, J. Phys. C**14**, 3297 (1981); (c) J. Neve, P. Westrin and J. Rundgren, J. Phys. C**16**, 1291 (1983); (d) I. Bartos, P. Jaros, A. Barbieri, M.A. van Hove; and others, Surf. Rev. and Lett. **2**, 477 (1995).

[4.38] T. Kraft and P.M. Marcus, Phys. Rev. B**48**, 5886 (1993).

[4.39] P.M. Marcus and F. Jona, Surf. Rev. and Lett., **1**, 15 (1994).

[4.40] T.E. Madey, H.A. Engelhardt and D. Menzel, Surf. Sci. 48 (1975) 204.

[4.41] L.H. Dubois, Surf. Sci., **119**, 399 (1982); H. Niehus, Surf. Sci., **130**, 41 (1983); J. Haase and H.-J. Kuhr, Surf. Sci., **203**, L695 (1988).

[4.42] G.W. Simmons, D.F. Mitchell and K.R. Lawless, Surf. Sci., **8**, 130 (1967); J.H. Ho and R.W. Vook, J. Cryst. Growth, **44**, 561 (1978); R.W. Judd, P. Hollins and J. Pritchard, Surf. Sci., **171**, 643 (1986); F. Jensen, F. Besenbacher, E. Lægsgaard and I. Stensgaard, Surf. Sci., **259**, L774 (1991).

[4.43] T. E. Gallon, Surf. Sci., **17**, 486 (1969).

[4.44] C.M. Schneider, A.K. Schmid, P. Schuster, H.P. Oepen, and J. Kirschner in Magnetism and Structure in Systems of Reduced Dimensions, R.F.C. Farrow et al., Eds. (Plenum Press, New York, 1993) pp. 453-466.

Table 4.1: Cu coverages as determined by QCM and XPS for Cu/Ru(0001).

Cu (ML) by QCM	Cu (ML) by XPS
0.24	0.38
1.8	1.1
2.2	2.0
3.0	2.9
*	4.2
5.9	4.9
**	6.5
9.0	8.0
25.2	∞

*Sample was initially 7.7 ML and was annealed at 600°C to desorb Cu until a nominal coverage of ~ 4 ML was reached, therefore no QCM data is available for this coverage. The coverage after annealing was 4.2 ML according to XPS. **No QCM data taken at this coverage.

Table 4.2: Cu coverages determined by QCM and XPS for Cu/O/Ru(0001).

Cu (ML) by QCM	Cu (ML) by XPS
0.56	0.60
1.8	1.1
1.4	2.2
2.16	3.2
*	3.7
3.4	4.8
5.7	6.5
6.1	8.0
30.5	∞

*Sample was initially 6.5 ML and was annealed at 325°C in order to obtain a $2\sqrt{3} \times 4\sqrt{3}R30$ LEED structure as seen in ref. [4.12 Wolter]. The Cu coverage after annealing was 3.7 ML according to XPS.

Table 4.3: Values of $d_{\perp}/d_{\parallel}$ for Cu/Ru(0001) and Cu/O/Ru(0001) as determined by R-factor comparison of experiment to SSC and MSC calculations. The SSC values are much less reliable for coverages of ≥ 4 ML, and are thus shown in parentheses.

	$d_{\perp}/d_{\parallel}$			
	Cu/Ru(0001)		**Cu/O-precovered Ru(0001)**	
Cu coverage	**SSC**	**MSC**	**SSC**	**MSC**
1 ML	-	-	0.783±0.033	0.783±0.033
2 ML	0.733±0.038	0.729±0.034	0.761±0.042	0.753±0.042
3 ML	0.740±0.026	0.756±0.018	0.737±0.033	0.724±0.039
4 ML	(0.773±0.022)	0.742±0.016	(0.818±0.032)	0.764±0.033
5 ML	(0.769±0.047)	0.718±0.018	(0.825±0.013)	0.713±0.028
6.5L	(0.812±0.026)	0.740±0.014	(0.840±0.020)	0.729±0.020
8 ML	(0.837±0.016)	0.766±0.018	(0.828±0.021)	0.732±0.026
≥ 25 ML	(0.835±0.014)	0.777±0.020	(0.847±0.027)	0.786±0.032

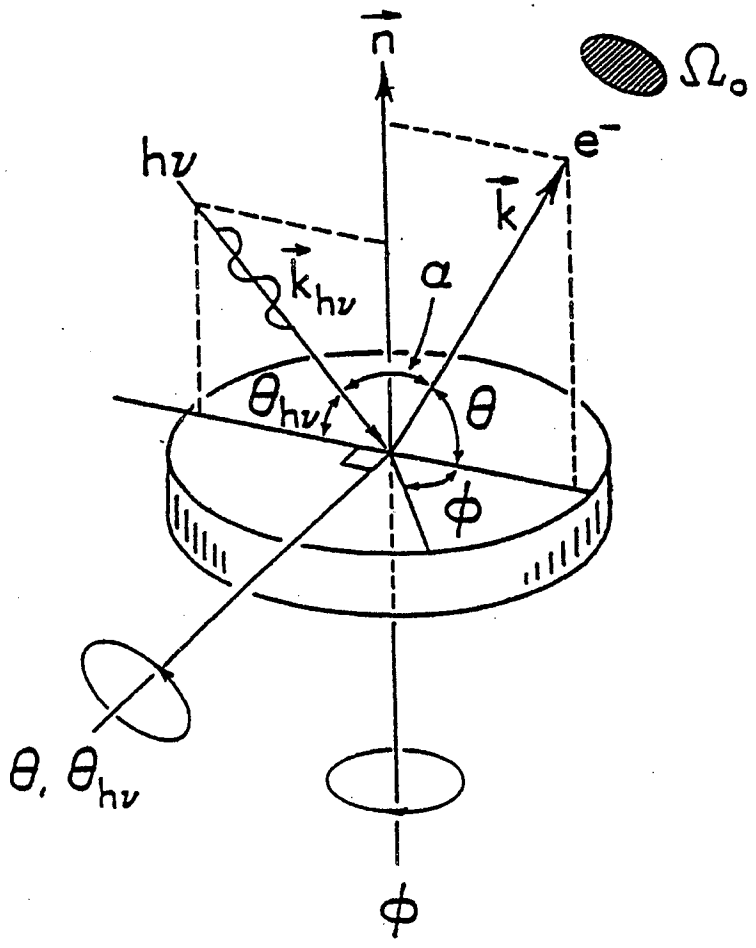

Fig. 4.1 Illustration of the basic experimental geometry in the XPD experiment. The polar angle θ of electron emission is measured from the surface. The angle α between th incoming radiation and the outgoing wave vector was fixed for the experiments in this dissertation at 72°.

Fig. 4.2 (a)-(i) Experimental XPD patterns for Cu $2p_{3/2}$ emission (E_{kin} = 556 eV) for several Cu coverages on clean Ru(0001): (a) 0.4 ML; (b) 1.1 ML; (c) 2.0 ML; (d) 2.9 ML; (e) 4.2 ML; (f) 4.9 ML; (g) 6.5 ML; (h) 8.0 ML; (i) 25.2 ML; (j) Experimental XPD patterns for Cu $2p_{3/2}$ emission from Cu(111) (E_{kin} = 556 eV), as artificially sixfold symmetrized by adding (k) and (k) with a 180° rotation; (k) As (j), but raw data from Cu(111) with expected threefold symmetry; (k) Experimental XPD pattern for Ru 3d emission (E_{kin} = 1206 eV) from clean Ru(0001).

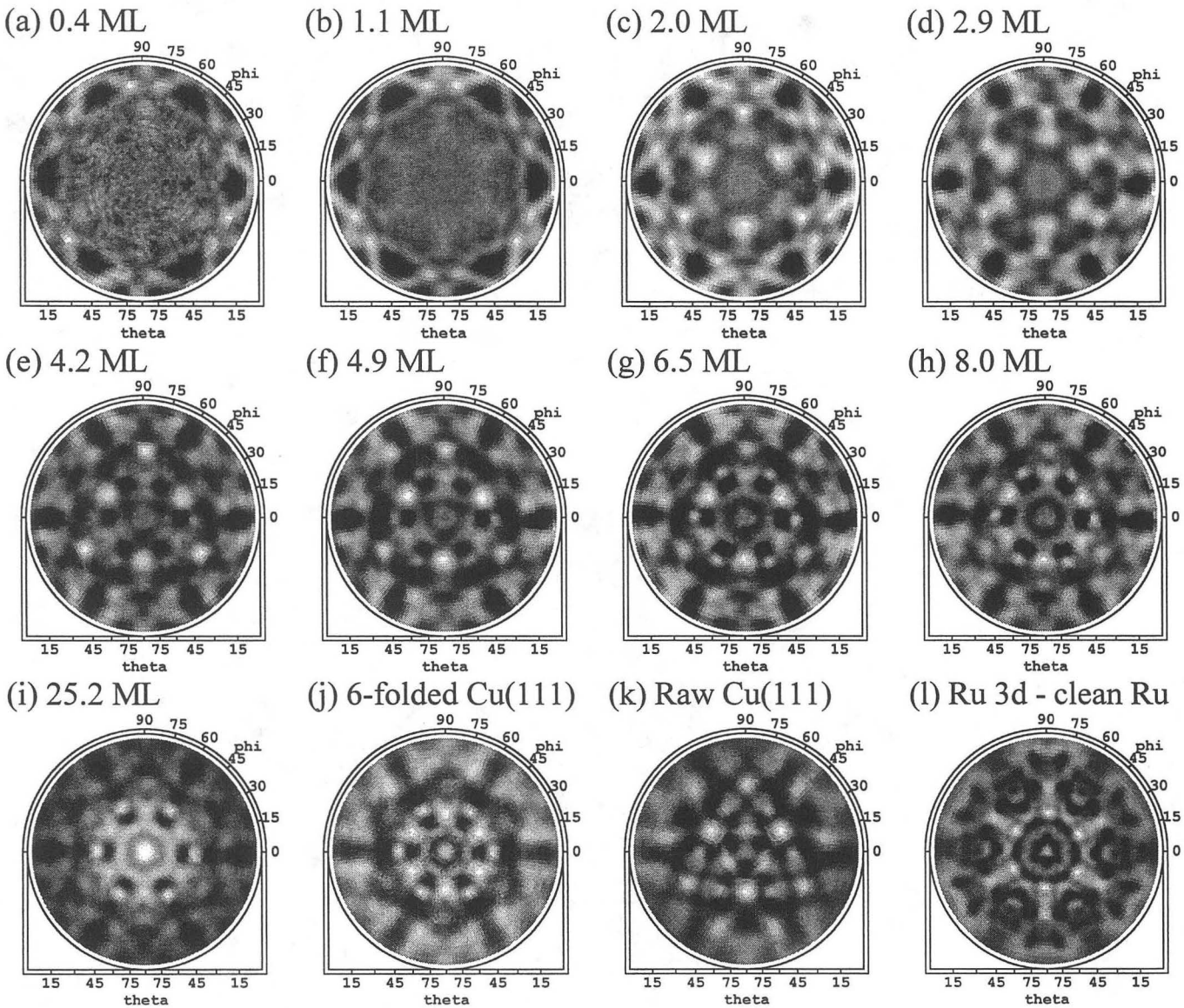
(a) 0.4 ML
(b) 1.1 ML
(c) 2.0 ML
(d) 2.9 ML
(e) 4.2 ML
(f) 4.9 ML
(g) 6.5 ML
(h) 8.0 ML
(i) 25.2 ML
(j) 6-folded Cu(111)
(k) Raw Cu(111)
(l) Ru 3d - clean Ru
phi
90 75 60 45 30 15 0
theta
15 45 75 75 45 15

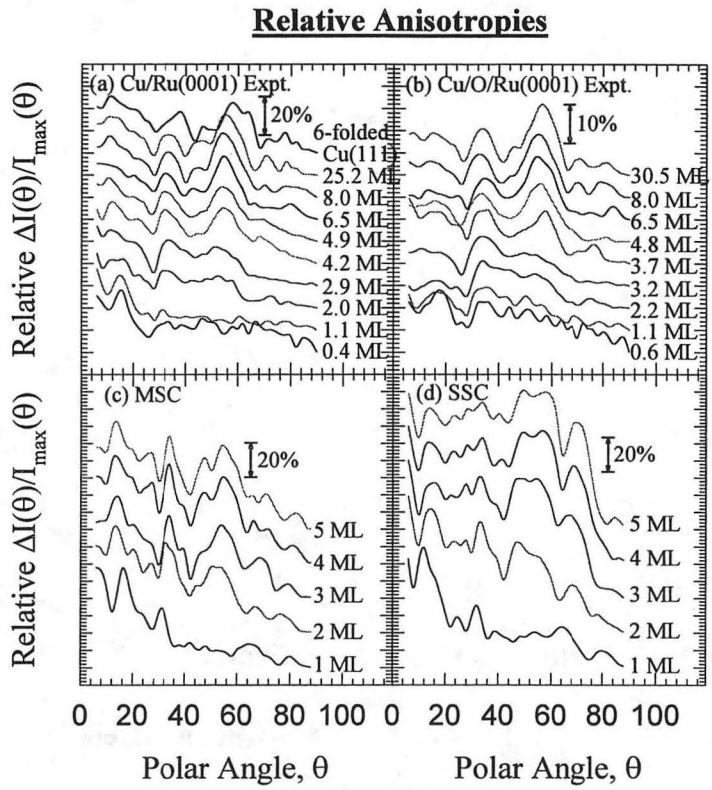

Fig. 4.3 (a) Experimental relative anisotropies = $\Delta I(\theta)/I_{max}(\theta)$ versus polar angle for various Cu coverages from 0.4 ML to 25.2 ML on clean Ru(0001) and for bulk Cu(111) with sixfold symmetrization; each value is calculated over a given azimuthal scan. These anisotropies range from 5% to 30% depending on the polar angle. (b) As (a), but for various Cu coverages from 0.6 ML to 30.5 ML on Ru(0001) precovered with 0.5 ML O. The magnitudes of the anisotropies here are about half as large as those for Cu grown on clean Ru(0001). (c) As (a), but derived from multiple scattering cluster (MSC) calculations, as described in the text. Here the magnitudes of the anisotropy here are slightly larger than in experiment in (a). (d) As (b), but derived from single scattering cluster (SSC) calculations. Here, the magnitudes are often significantly larger than in experiment in (a).

Fig. 4.4 (a) Atomic structure of the Cu(111) surface. The white circles represent the surface layer, the gray circles represent the second layer, and the black circles represent the third layer. Various low index azimuthal directions are indicated. (b) A cross section through a $(1\bar{1}0)$ plane at $\phi = 30^\circ$, with various forward scattering directions indicated. The white circles represent atoms in the plane of the cut, and the gray circles represent atoms just behind the cut.

(a) Cu(111) Surface:

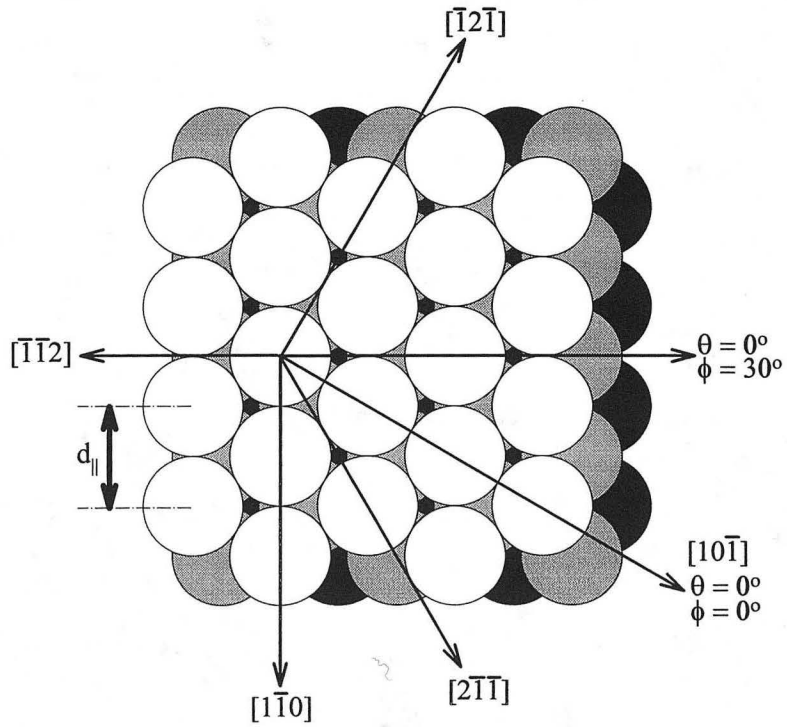

(b) Cross section through ϕ = 30°:

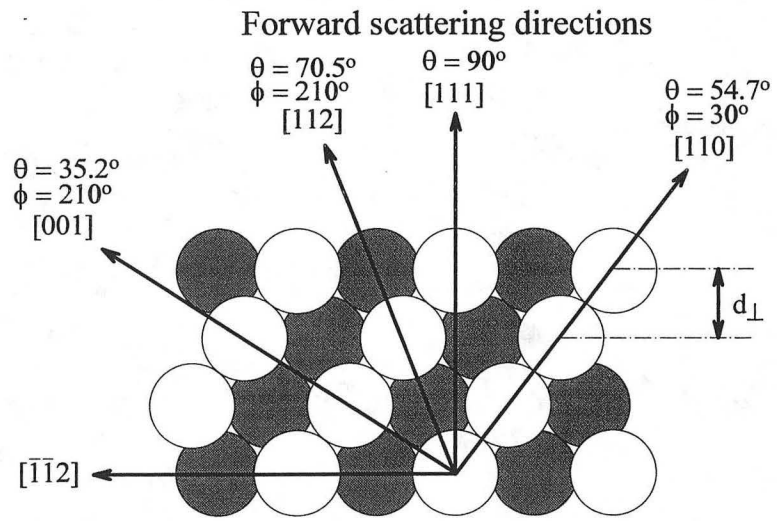

Fig. 4.5 Illustration of the effect angular broadening by gaussian smoothing on comparison of experiment and MSC theory: (a) 5.0 ML Experiment; (b) 5 ML MSC theory without gaussian smoothing (but with $\pm 3^{o}$ angular broadening using a multi-point average); (c) 5 ML MSC theory smoothed with a gaussian of half-width at half-maximum (HWHM) = 2.4^{o}; (d) As (c) but with HWHM = 4.8^{o}; (e) As (c) but with HWHM = 7.1^{o}.

XPD - Effect of Smoothing MSC Theory

(a)

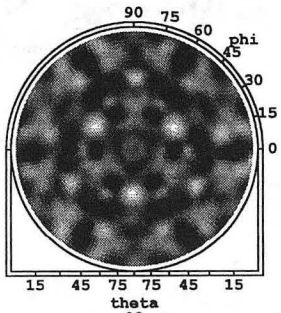

Experiment - 5 ML

(b)

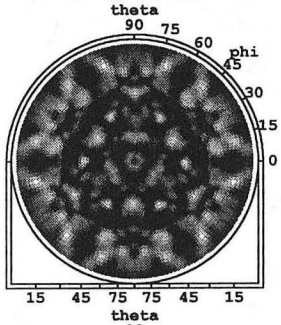

Theory - 5 ML

HWHM = 0o

(c)

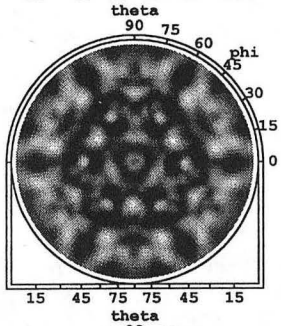

HWHM = 2.4o

(d)

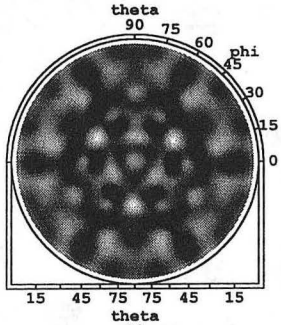

HWHM = 4.8o

(e)

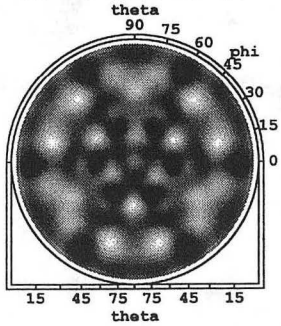

HWHM = 7.1o

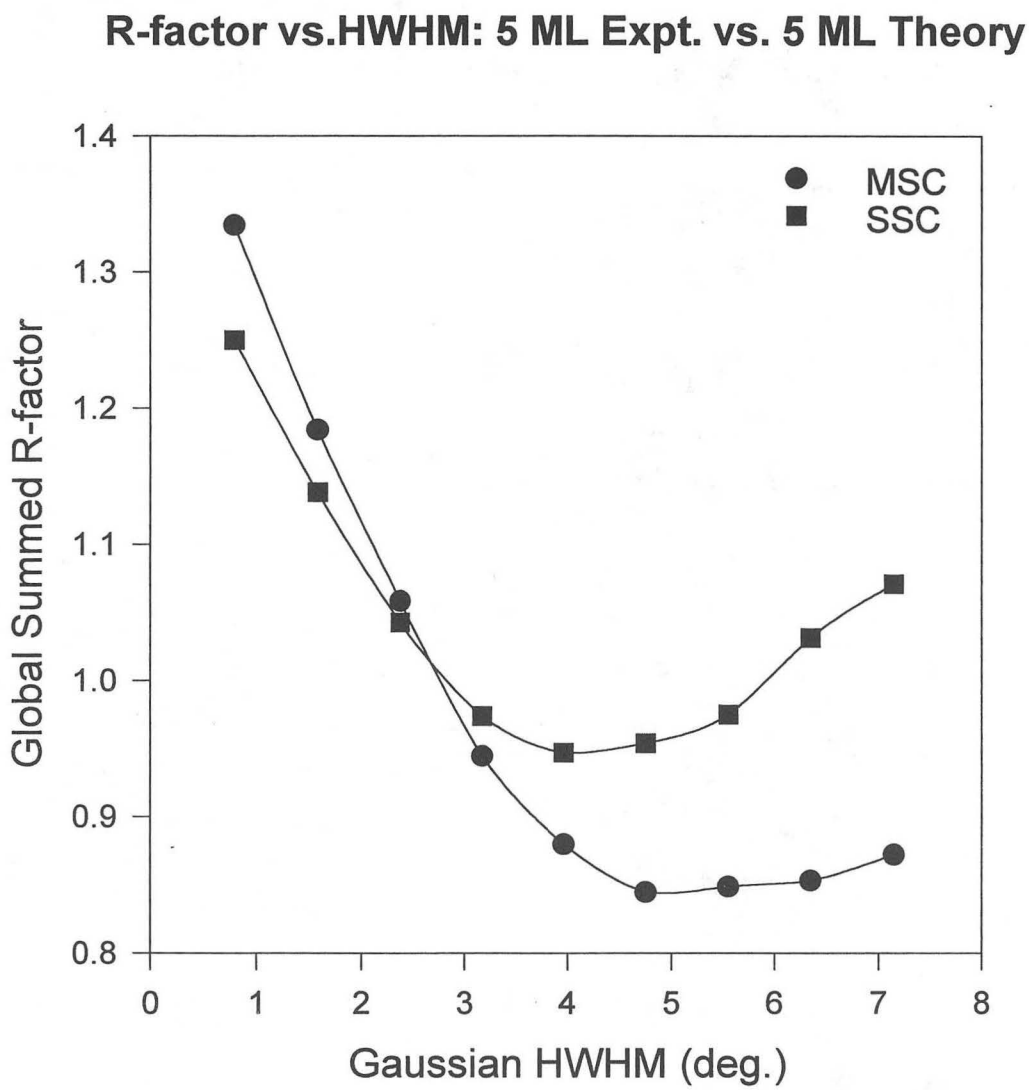

Fig. 4.6 Global sum over five normalized R-factors plotted for 5 ML SSC and 5 ML MSC calculations as compared to 5.0 ML experiment and for various degrees of gaussian angular smoothing.

Fig. 4.7 R-factor plots versus the structural parameters $Z_{Cu\text{-}Ru}$ and derived from comparing experiment to SSC and MSC calculations at various Cu coverages on Ru(0001): (a) 1 ML; (b) 2 ML; (c) 3 ML; (d) 4 ML; (e) 5 ML; (f) 6.5 ML; (g) 8 ML; (h) 25.2 ML. Note the divergence of results for SSC and MSC, which begins at about 4 ML as multiple scattering effects become more important. The fraction of occupation of domain #1 ($=f_1$) was also optimized for each case ≥2 ML, and is plotted in Fig. 4.16(b).

R-factor Analysis: Cu/Ru(0001) - Interlayer Distances

(a) 1.1 ML

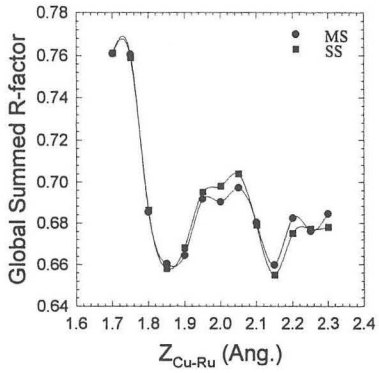

(b) 2.0 ML

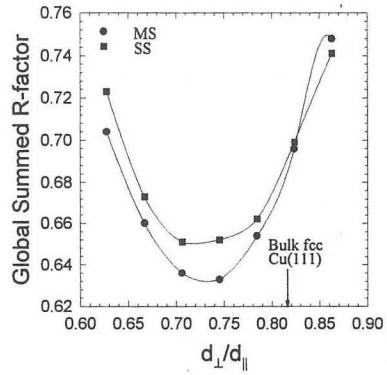

(c) 2.9 ML

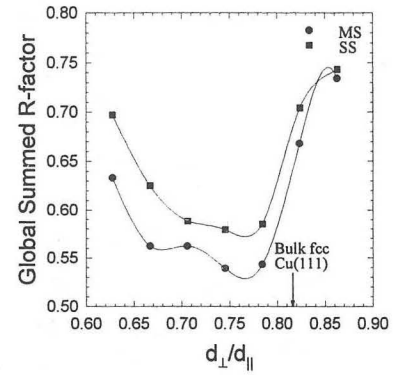

(d) 4.2 ML

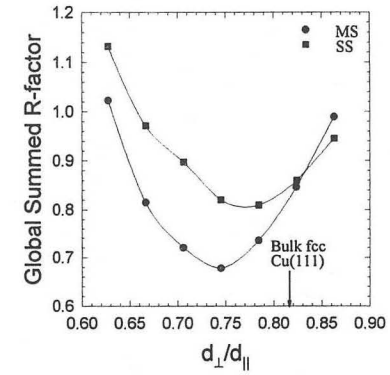

(e) 4.9 ML

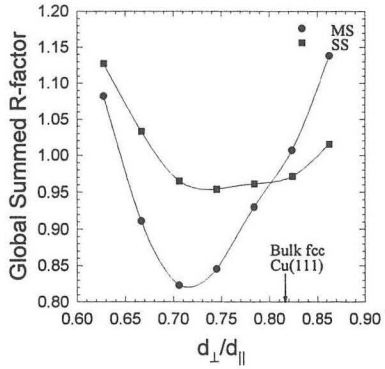

(f) 6.5 ML

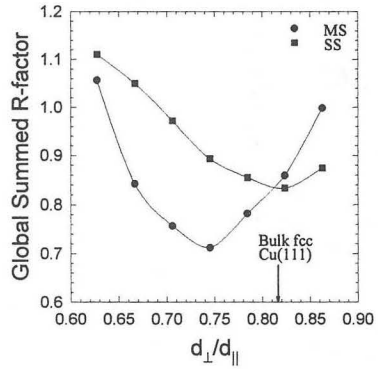

(g) 8.0 ML

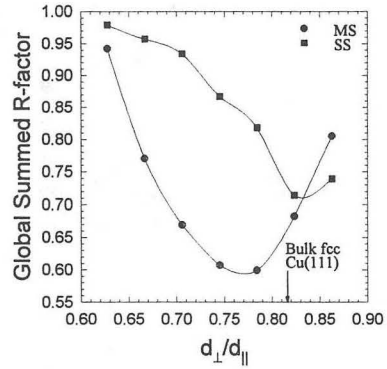

(h) 25.2 ML

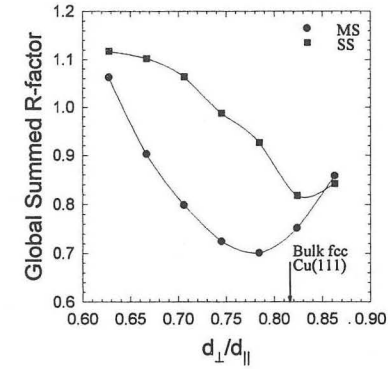

Fig. 4.8 Experimental and theoretical XPD patterns for Cu $2p_{3/2}$ emission: (a) 1.1 ML experiment; (b) 1 ML MSC theory; (c) 1 ML SSC theory; (d) Positions of simple forward scattering directions in the 1 ML, which in fact are not observable, (e) 2.0 ML experiment; (f) 2 ML MSC theory; (g) 2 ML SSC theory, (h) Positions of simple forward scattering directions in the 2 ML cluster.

1 ML Cu/Ru(0001) **2 ML Cu/Ru(0001)**

(a) Experiment (e) Experiment

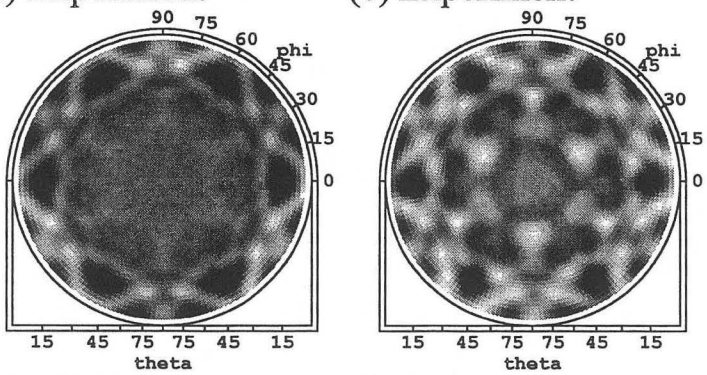

(b) MSC Theory (f) MSC Theory

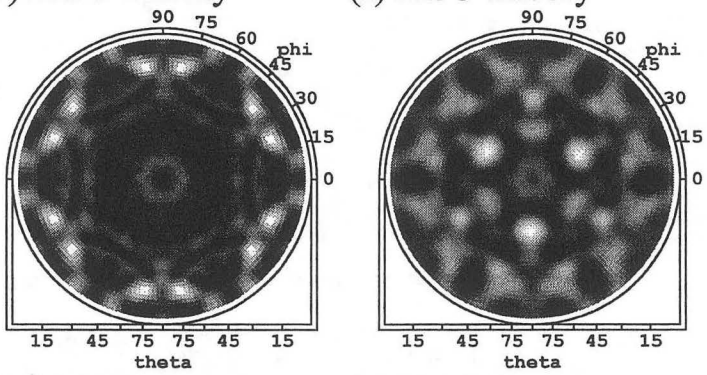

(c) SSC Theory (g) SSC Theory

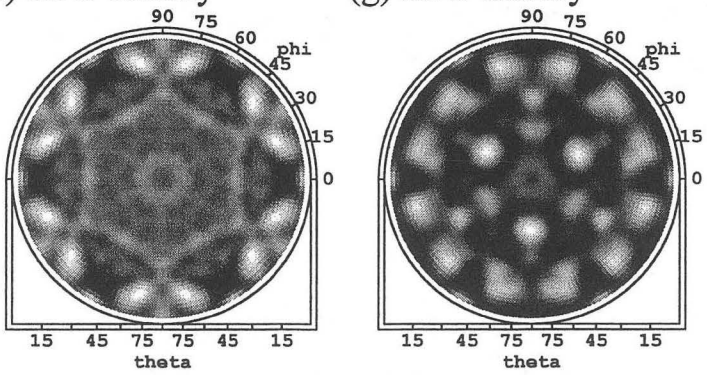

(d) Fwd. Scat. (h) Fwd. Scat.

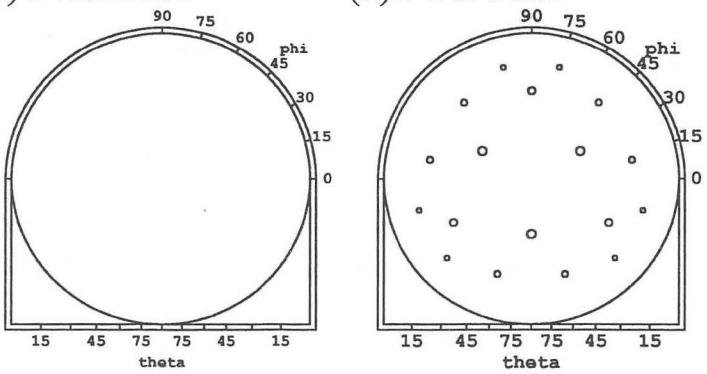

Fig. 4.9 Experimental and theoretical XPD patterns for Cu $2p_{3/2}$ emission: (a) 2.9 ML experiment; (b) 2 ML MSC theory (sixfold symmetrized); (c) 2 ML SSC theory (sixfold symmetrized); (d) Positions of simple forward scattering directions in the 2 ML cluster (sixfold symmetrized), (e) 4.2 ML experiment; (f) 4 ML MSC theory; (g) 4 ML SSC theory, (h) Positions of simple forward scattering directions in the threefold symmetric 4 ML cluster.

3 ML Cu/Ru(0001) **4 ML Cu/Ru(0001)**

(a) Experiment (e) Experiment

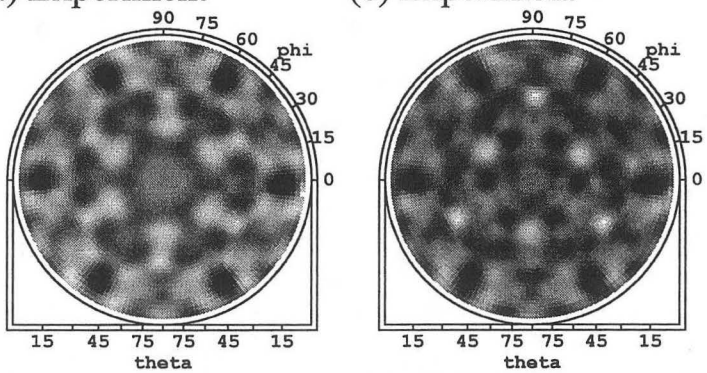

(b) MSC Theory (f) MSC Theory

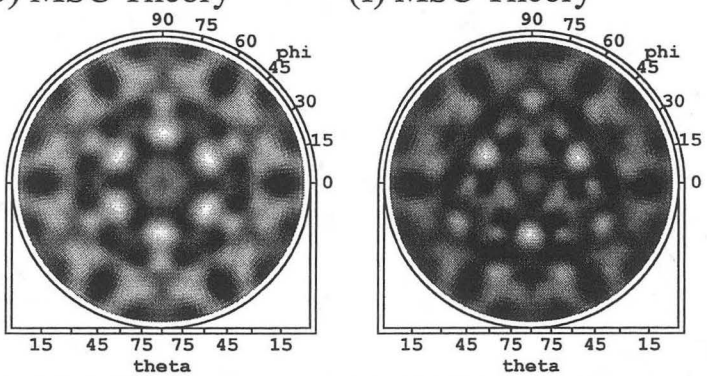

(c) SSC Theory (g) SSC Theory

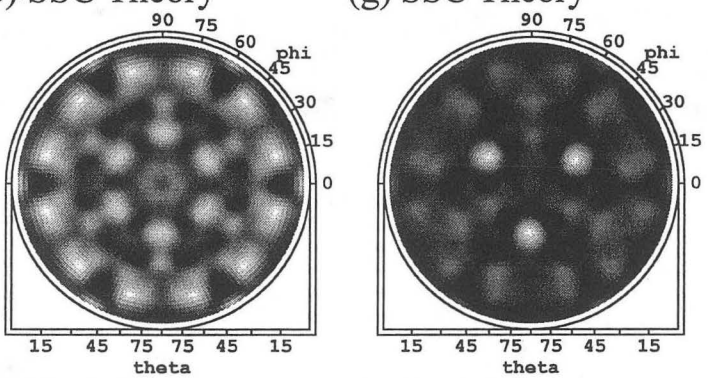

(d) Fwd. Scat. (h) Fwd. Scat.

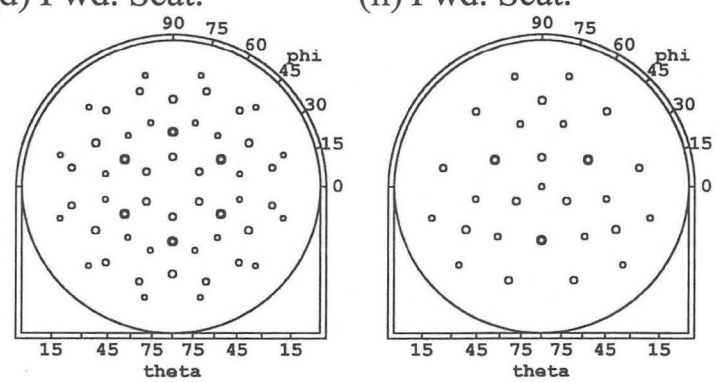

Fig. 4.10 Experimental and theoretical XPD patterns for Cu $2p_{3/2}$ emission: (a) 4.9 ML experiment; (b) 5 ML MSC theory; (c) 5 ML SSC theory; (d) Positions of simple forward scattering directions in the 5 ML cluster, (e) 6.5 ML experiment; (f) 5 ML MSC theory; (g) 5 ML SSC theory, (h) Positions of simple forward scattering directions in a 5 ML cluster.

5 ML Cu/Ru(0001) **6.5 ML Cu/Ru(0001)**

(a) Experiment (e) Experiment

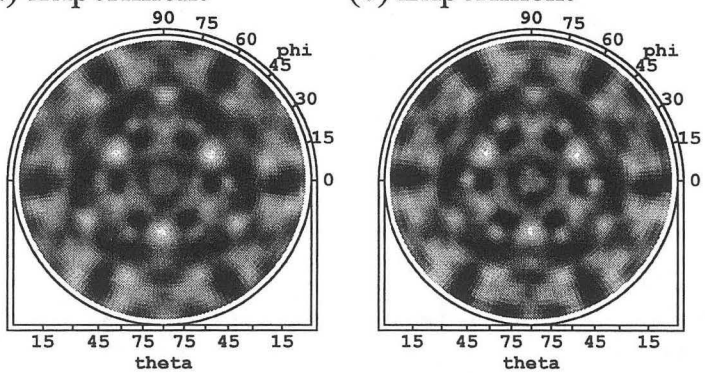

(b) MSC Theory (f) MSC Theory

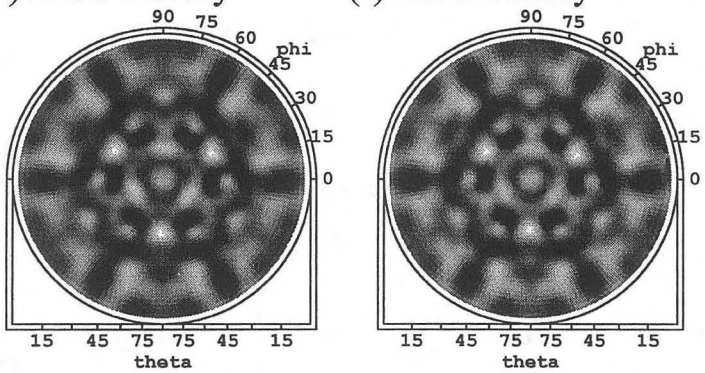

(c) SSC Theory (g) SSC Theory

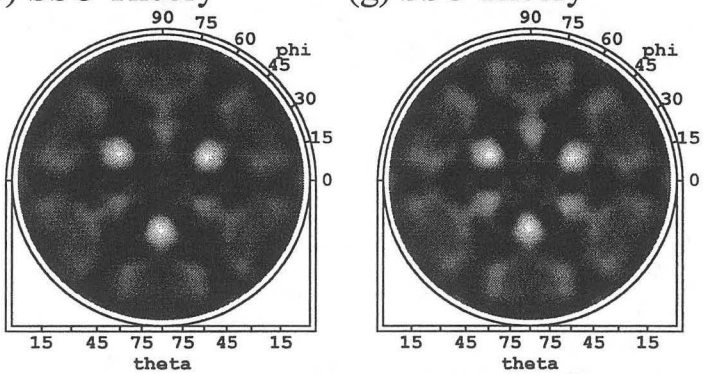

(d) Fwd. Scat. (h) Fwd. Scat.

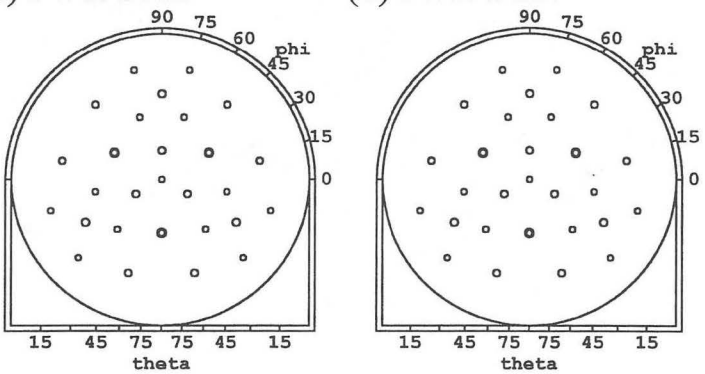

Fig. 4.11 Experimental and theoretical XPD patterns for Cu $2p_{3/2}$ emission: (a) 8.0 ML experiment; (b) 5 ML MSC theory; (c) 5 ML SSC theory; (d) Positions of simple forward scattering directions for a 5 ML cluster (sixfold symmetrized in order to simulate two domains); (e) 25.2 ML experiment; (f) 5 ML MSC theory; (g) 8 ML SSC theory, (h) Positions of forward scattering directions for a 5 ML cluster.

8 ML Cu/Ru(0001) **25 ML Cu/Ru(0001)**

(a) Experiment (e) Experiment

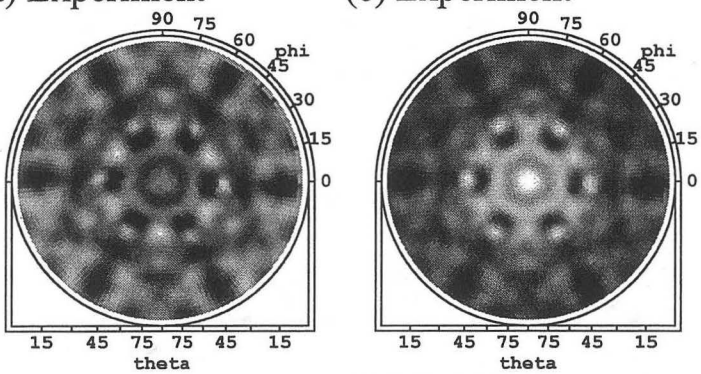

(b) MSC Theory (f) MSC Theory

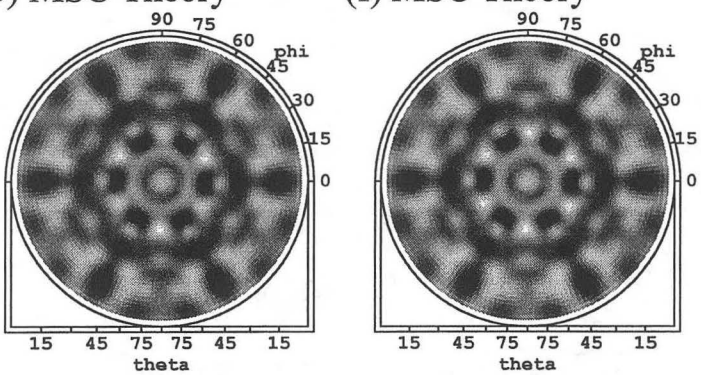

(c) SSC Theory (g) SSC Theory

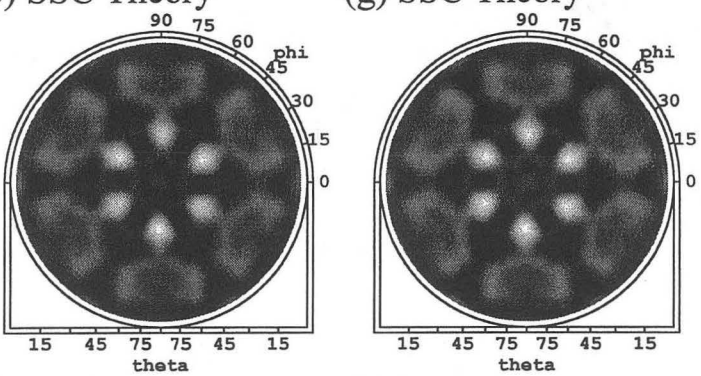

(d) Fwd. Scat. (h) Fwd. Scat.

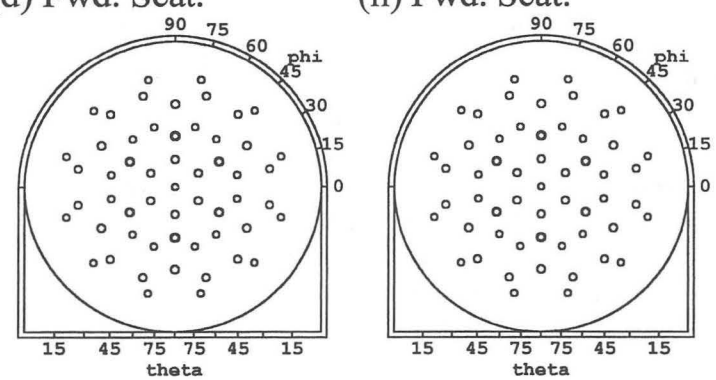

Fig. 4.12 MSC calculations from (a) 1 ML up to (h) 8 ML for the bulk value of $d_{\perp}/d_{\parallel}$ = 0.816. Visually, the MSC calculation appears to have converged to a bulklike description by about 5 ML.

XPD - MSC Theory 1-8 ML

(a) 1 ML

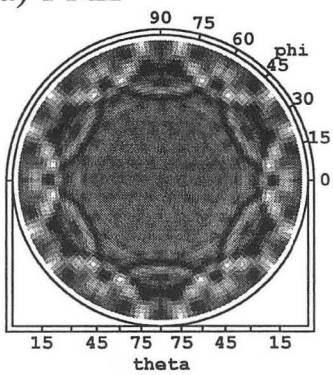

(e) 5 ML

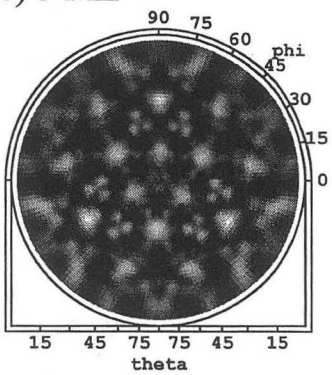

(b) 2 ML

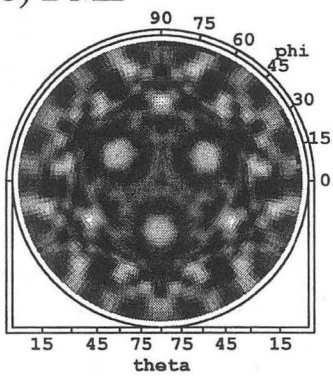

(f) 6 ML

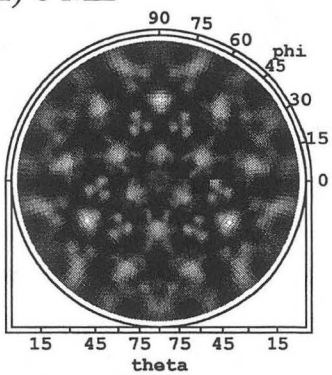

(c) 3 ML

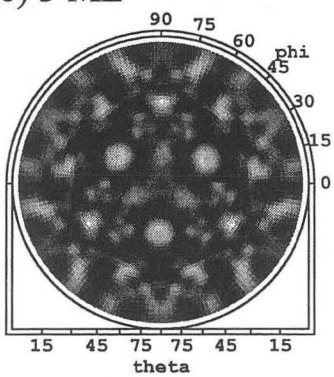

(g) 7 ML

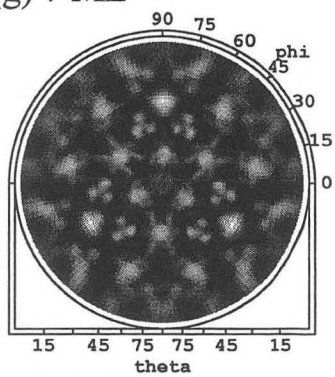

(d) 4 ML

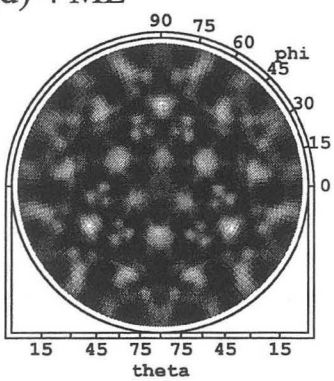

(h) 8 ML

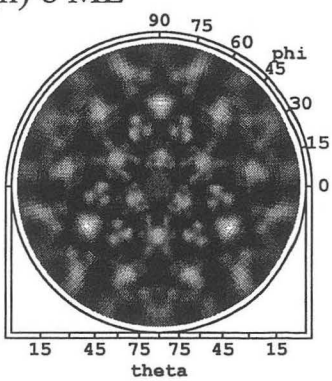

(a) n ML MSC Theory vs. 8 ML MSC Theory

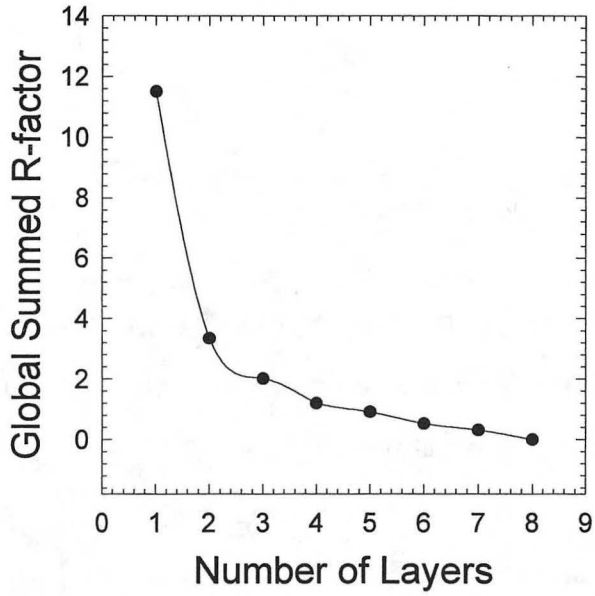

(b) n ML MSC Theory vs. Experiment

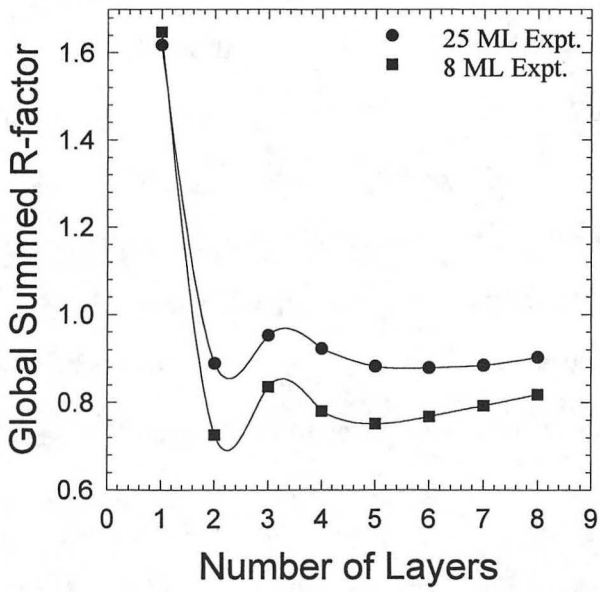

Fig. 4.13 (a) Global R-factor comparison of MSC theory for n ML to MSC theory for 8 ML, as shown in Fig. 4.12. (b) Global R-factor comparison of 25.2 ML experiment and 8 ML experiment to n ML theory for n = 1, 2, ..., 8.

Fig. 4.14 (a) Plot of $d_{\perp}/d_{\parallel}$ = (Cu-Cu interplanar distance)/(Cu-Cu in-plane nearest-neighbor distance) versus coverage in monolayers (ML), as derived by different methods. ● = Estimate of $d_{\perp}/d_{\parallel}$ using Cu areal densities derived from a 2D Frenkel-Kontorova model by Hamilton and Foiles [4.3] combined with a constant-atomic-volume assumption; ◊ = Estimate of $d_{\perp}/d_{\parallel}$ using Cu areal densities derived from a 2D Frenkel-Kontorova model by Hamilton and Foiles [4.3] combined elasticity theory [4.38, 4.39]; (■ = $d_{\perp}/d_{\parallel}$ determined by R-factor comparisons between experimental XPD data from various Cu coverages on Ru(0001) and MSC calculations for Cu $2p_{3/2}$ emission at a photoelectron kinetic energy of 556 eV; ◆ and □ = $d_{\perp}/d_{\parallel}$ determined by R-factor comparisons to experimental Cu $2p_{3/2}$ data obtained from Cu(111) by Naumovic et al. at photoelectron kinetic energies of 321 eV and 808 eV, respectively [4.21]; O = $d_{\perp}/d_{\parallel}$ determined by an R-factor comparison between experimental Cu $2p_{3/2}$ XPD data obtained in our laboratory from a Cu(111) single crystal and MSC calculations at an energy of 556 eV; (b) Plot of relative occupation of domain #1 versus coverage, with rotational symmetry indicated.

R-factor results - Cu/Ru(0001)

(a) $d_{\perp}/d_{\parallel}$ vs. Cu Coverage

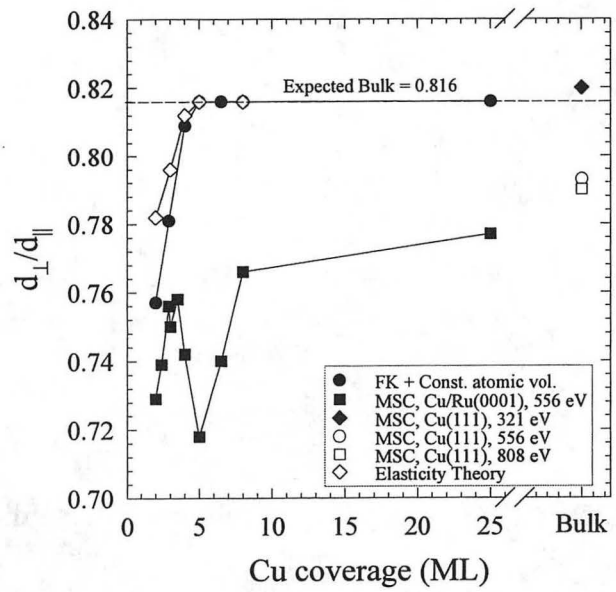

(b) Symmetry vs. Cu Coverage

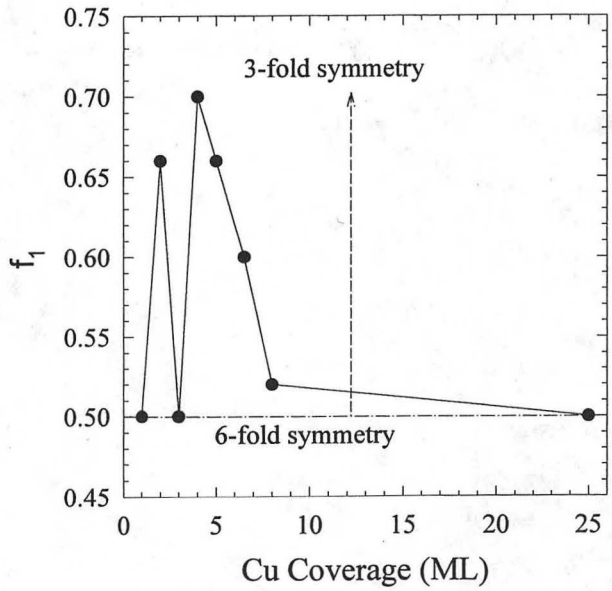

Fig. 4.15 Experimental XPD patterns for Cu $2p_{3/2}$ emission at three different energies from from a Cu(111) single crystal, as compared to corresponding MSC and SSC calculations for the optimum interlayer spacing; (a)-(c) Kinetic energy equals 321 eV. (d)-(f) Energy equals 556 eV. (g)-(i) Energy equals 808 eV. The 321 eV and 808 eV data are due to Naumovic and Osterwalder [4.21].

Cu(111) - 321 eV

(a) Experiment

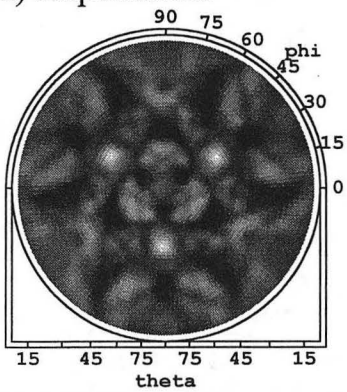

(b) MSC Theory

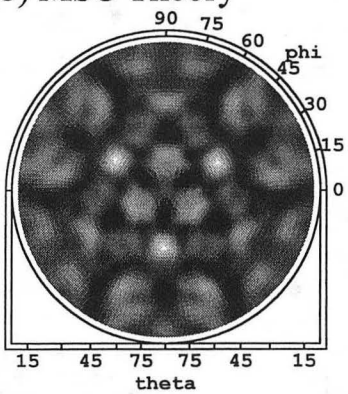

(c) SSC Theory

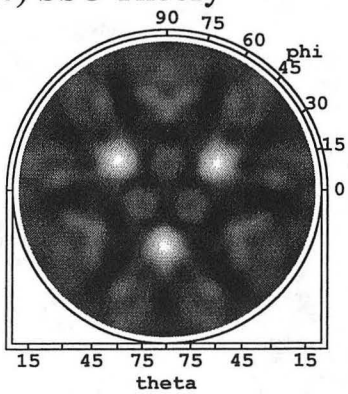

Cu(111) - 556 eV

(d) Experiment

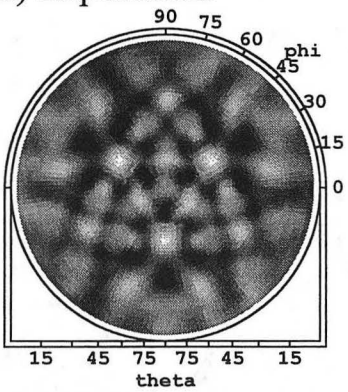

(e) MSC Theory

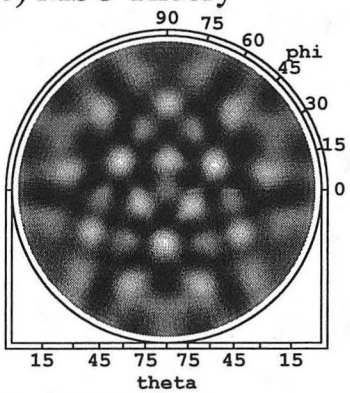

(f) SSC Theory

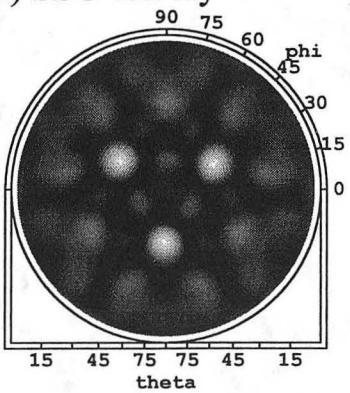

Cu(111) - 808 eV

(g) Experiment

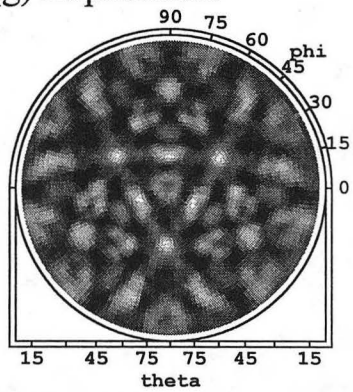

(h) MSC Theory

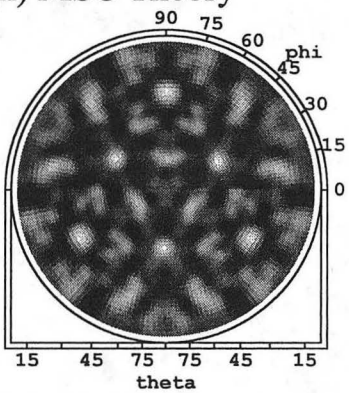

(i) SSC Theory

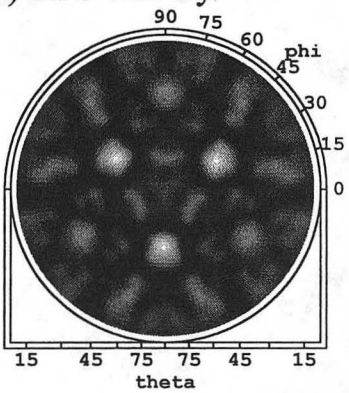

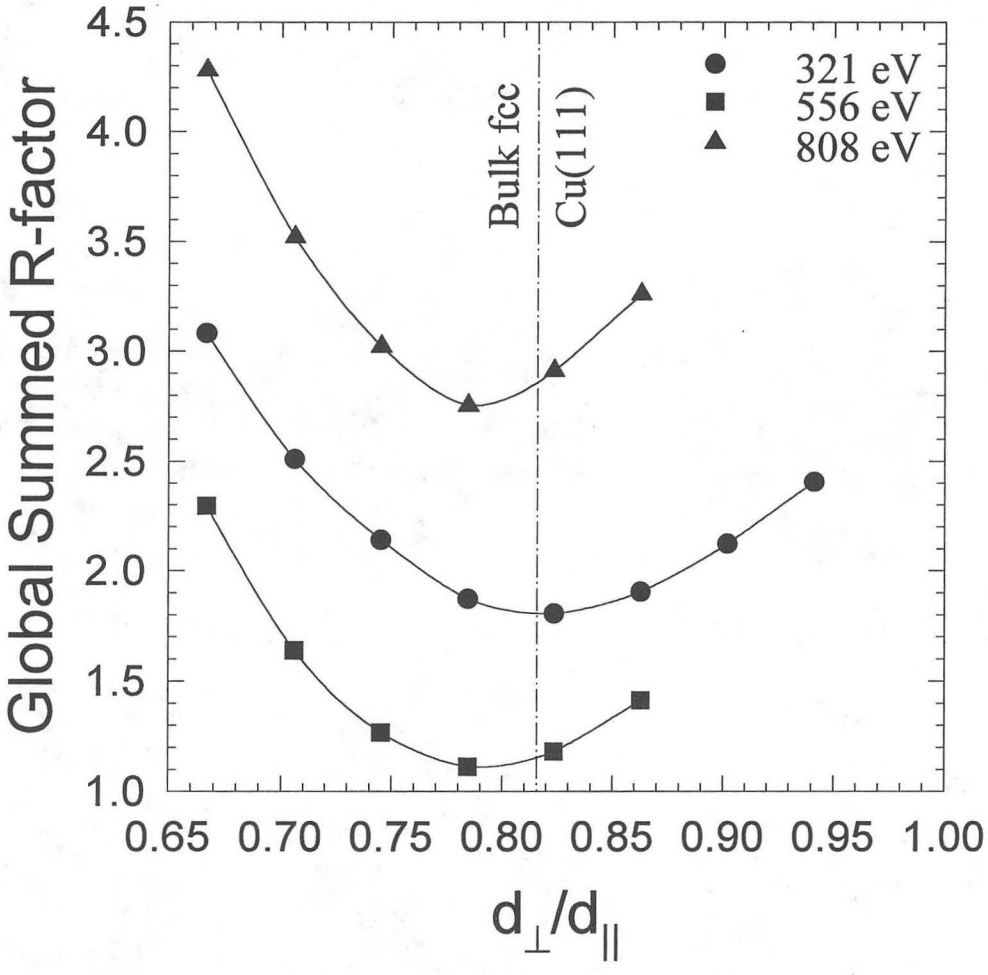

Fig. 4.16 Global summed R-factor plot for MSC comparisons to the Cu(111) data shown in Figs. 4.15(a), (d) and (g).

Fig. 4.17 XPD patterns from a 0.5 ML saturation coverage of oxygen on Ru(0001) for: (a) Experimental O 1s peak; (b) MSC calculation of O 1s pattern, assuming three domains of p(2x1)-O/Ru(0001); (c) As for (b) but SSC calculation; (d) Experimental Ru 3d pattern (cf. Fig. 4.2(l)).

XPD - O/Ru(0001)

(a) Experiment

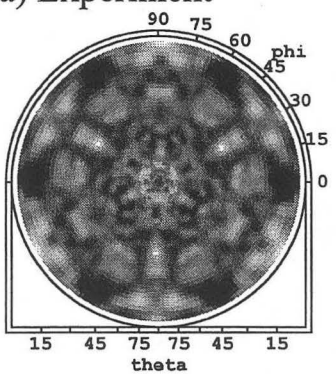

(b) MSC Theory

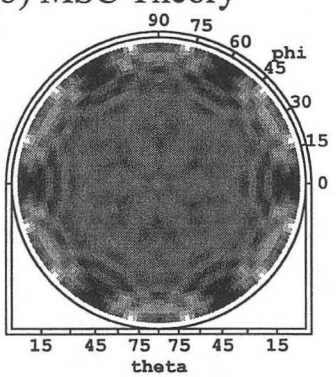

(c) SSC Theory

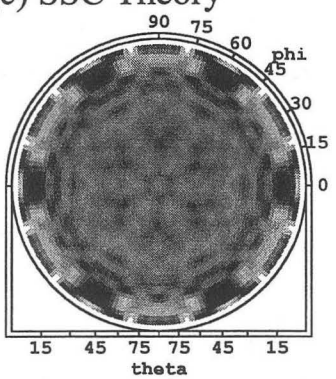

(d) Ru 3d

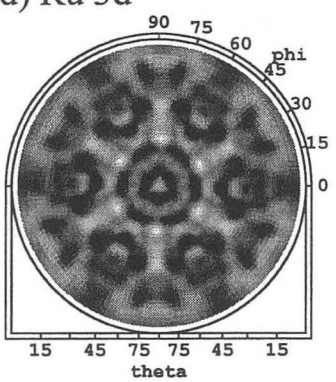

Fig. 4.18 Experimental XPD patterns from Cu/O/Ru(0001) at 1.1 ML and 2.2 ML Cu coverages: (a) O 1s emission at 1.1 ML Cu coverage; (b) Cu $2p_{3/2}$ emission at 1.1 ML Cu coverage; (c) comparison to Cu $2p_{3/2}$ emission at 1.1 ML Cu coverage on clean Ru(0001); (d) O 1s emission at 2.2 ML Cu coverage; (e) Cu $2p_{3/2}$ emission at 2.2 ML Cu coverage; (f) comparison to Cu $2p_{3/2}$ emission at 2.0 ML Cu coverage on clean Ru(0001).

1 ML Cu | **2 ML Cu**

(a) O 1s - Cu/O/Ru(0001)

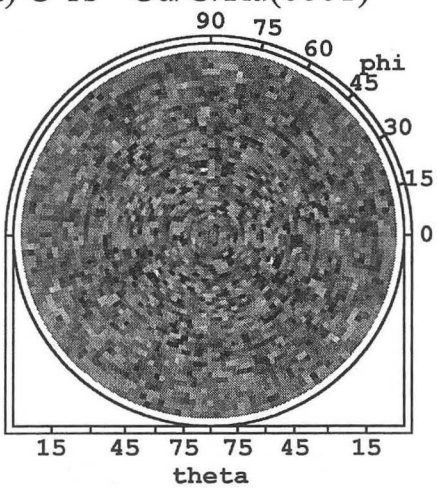

(d) O 1s - Cu/O/Ru(0001)

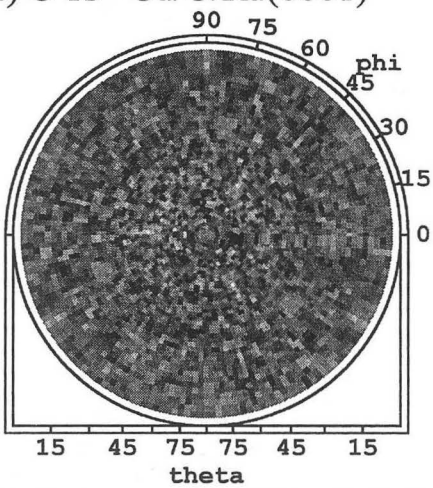

(b) Cu $2p_{3/2}$ - Cu/O/Ru(0001)

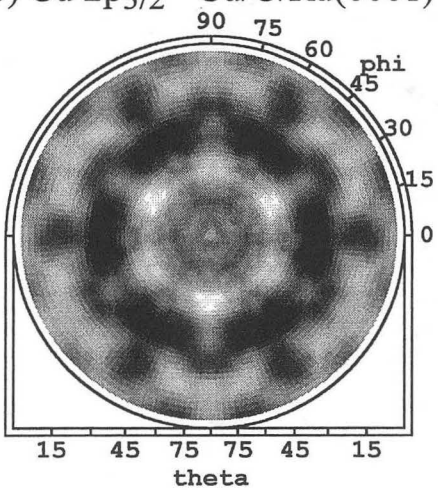

(e) Cu $2p_{3/2}$ - Cu/O/Ru(0001)

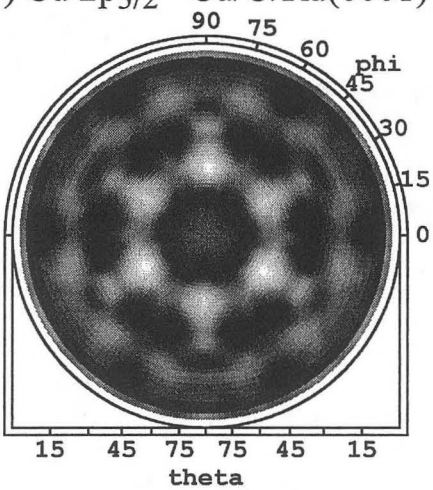

(c) Cu $2p_{3/2}$ - Cu/Ru(0001)

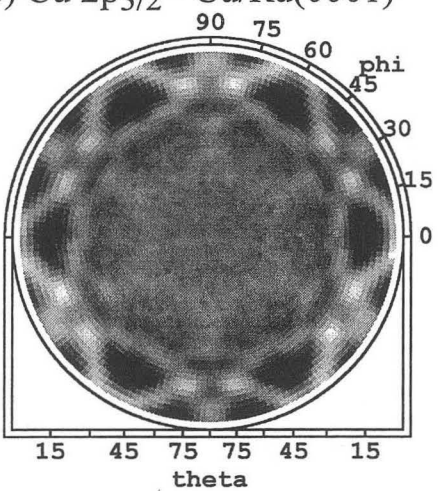

(f) Cu $2p_{3/2}$ - Cu/Ru(0001)

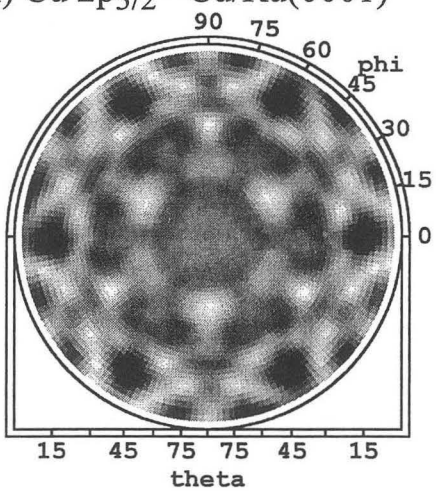

Fig. 4.19 Experimental XPD patterns from Cu/O/Ru(0001) at 3.2 ML and 3.7 ML Cu coverages: (a) O 1s emission at 3.2 ML Cu coverage; (b) Cu $2p_{3/2}$ emission at 3.2 ML Cu coverage; (c) comparison to Cu $2p_{3/2}$ emission at 2.9 ML Cu coverage on clean Ru(0001); (d) O 1s emission at 3.7 ML Cu coverage; (e) Cu $2p_{3/2}$ emission at 3.7 ML Cu coverage; (f) comparison to Cu $2p_{3/2}$ emission at 4.2 ML Cu coverage on clean Ru(0001).

3 ML Cu

(a) O 1s - Cu/O/Ru(0001)

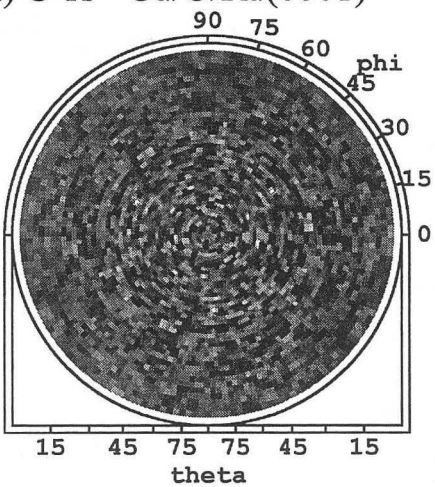

(b) Cu $2p_{3/2}$ - Cu/O/Ru(0001)

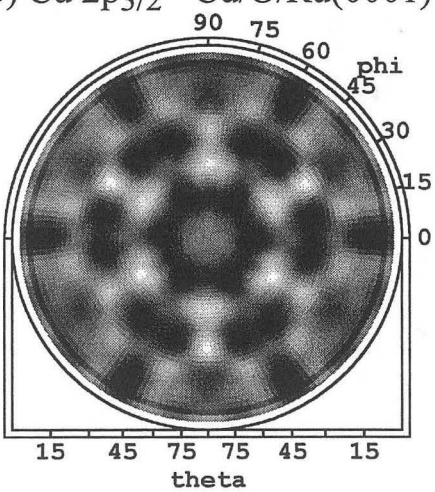

(c) Cu $2p_{3/2}$ - Cu/Ru(0001)

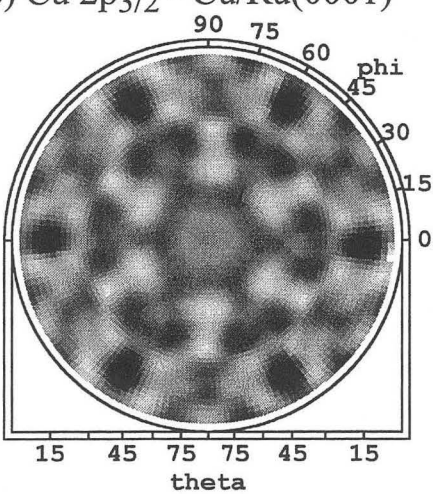

4 ML Cu

(d) O 1s - Cu/O/Ru(0001)

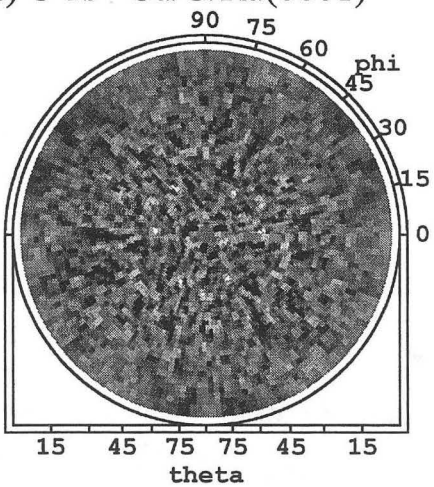

(e) Cu $2p_{3/2}$ - Cu/O/Ru(0001)

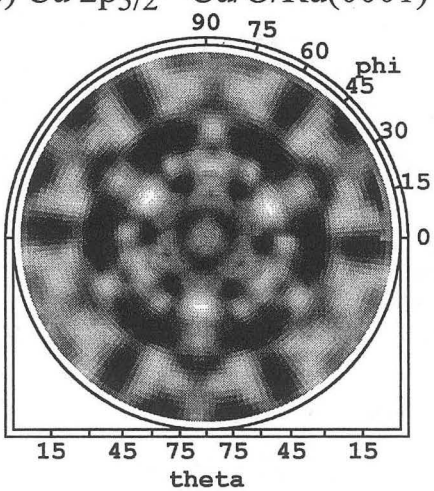

(f) Cu $2p_{3/2}$ - Cu/Ru(0001)

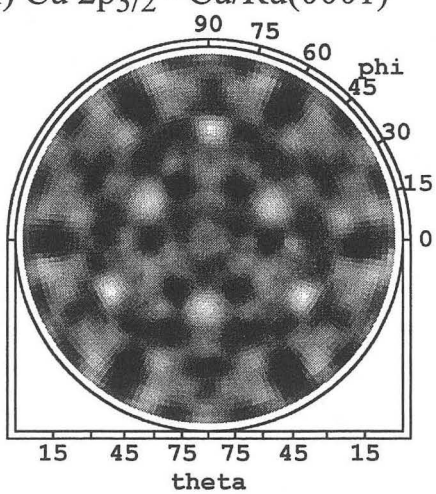

Fig. 4.20 Experimental XPD patterns from Cu/O/Ru(0001) at 4.8 ML and 6.5 ML Cu coverages: (a) O 1s emission at 4.8 ML Cu coverage; (b) Cu $2p_{3/2}$ emission at 4.8 ML Cu coverage; (c) comparison to Cu $2p_{3/2}$ emission at 4.9 ML Cu coverage on clean Ru(0001); (d) O 1s emission at 6.5 ML Cu coverage; (e) Cu $2p_{3/2}$ emission at 6.5 ML Cu coverage; (f) comparison to Cu $2p_{3/2}$ emission at 6.5 ML Cu coverage on clean Ru(0001).

5 ML Cu | **6.5 ML Cu**

(a) O 1s - Cu/O/Ru(0001)

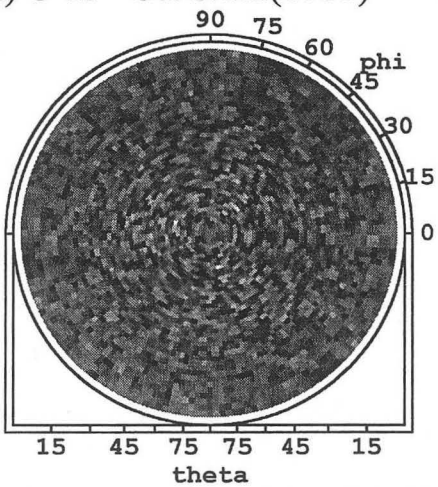

(d) O 1s - Cu/O/Ru(0001)

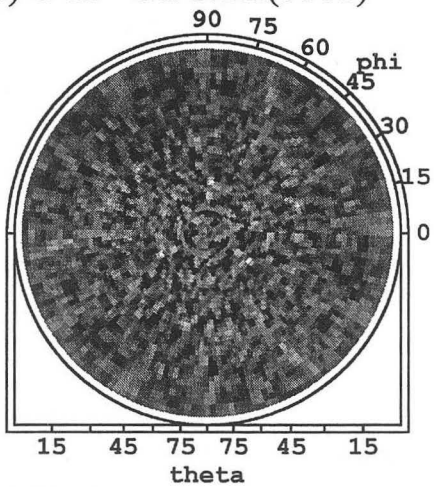

(b) Cu $2p_{3/2}$ - Cu/O/Ru(0001)

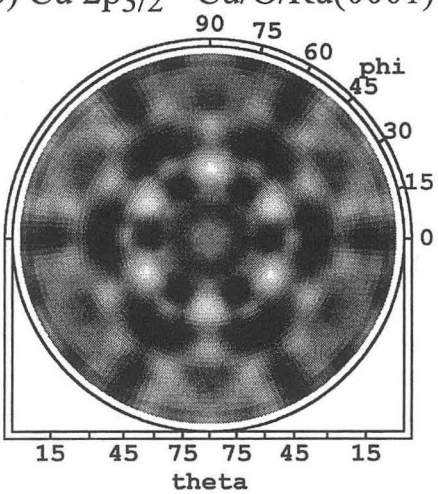

(e) Cu $2p_{3/2}$ - Cu/O/Ru(0001)

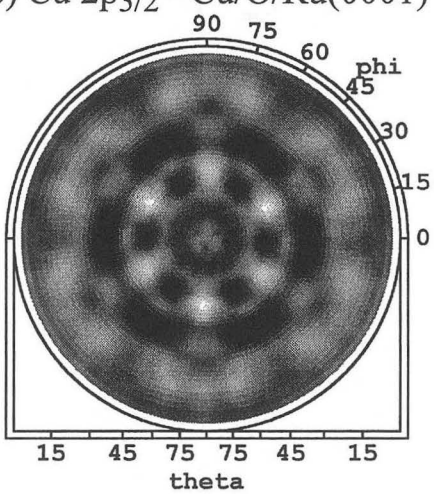

(c) Cu $2p_{3/2}$ - Cu/Ru(0001)

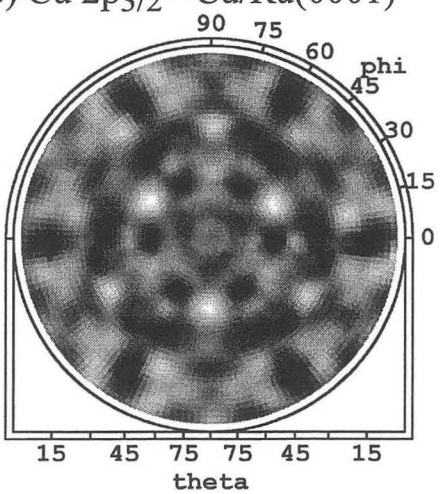

(f) Cu $2p_{3/2}$ - Cu/Ru(0001)

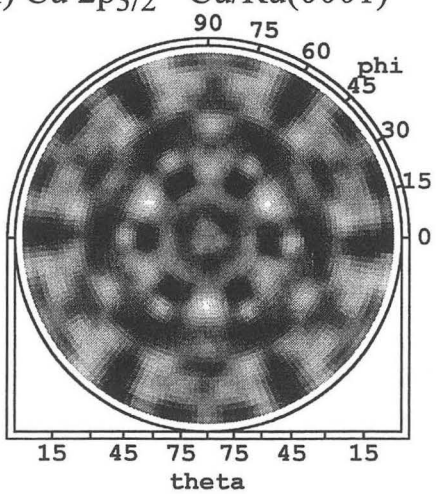

Fig. 4.21 Experimental XPD patterns from Cu/O/Ru(0001) at 8.0 ML and 30.5 ML Cu coverages: (a) O 1s emission at 8.0 ML Cu coverage; (b) Cu $2p_{3/2}$ emission at 8.0 ML Cu coverage; (c) comparison to Cu $2p_{3/2}$ emission at 8.0 ML Cu coverage on clean Ru(0001); (d) O 1s emission at ~30.5 ML Cu coverage; (e) Cu $2p_{3/2}$ emission at ~30.5 ML Cu coverage; (f) comparison to Cu $2p_{3/2}$ emission at ~25.2 ML Cu coverage on clean Ru(0001).

8 ML Cu | **30 ML Cu**

(a) O 1s - Cu/O/Ru(0001)

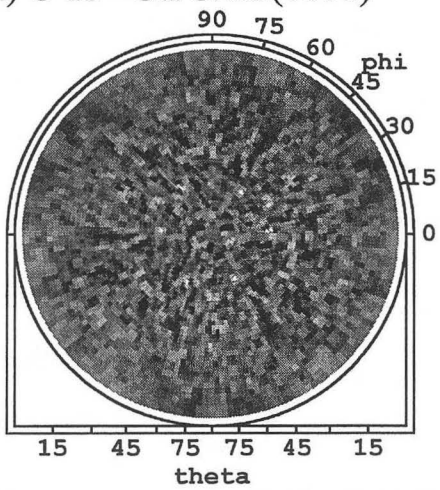

(d) O 1s - Cu/O/Ru(0001)

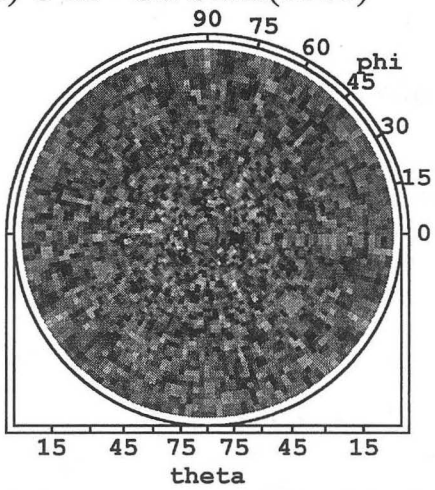

(b) Cu $2p_{3/2}$ - Cu/O/Ru(0001)

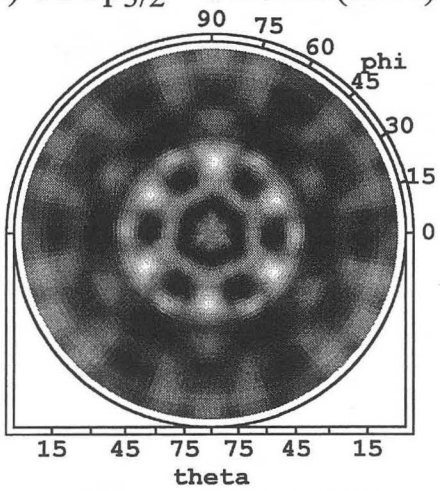

(e) Cu $2p_{3/2}$ - Cu/O/Ru(0001)

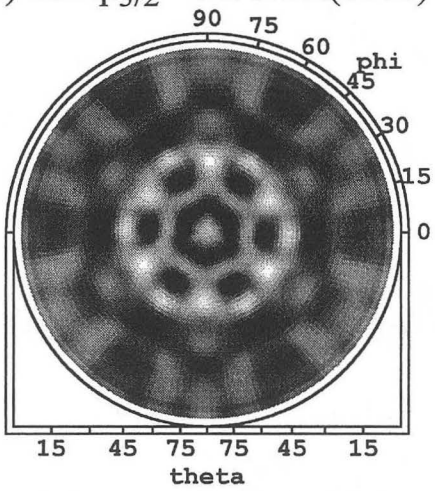

(c) Cu $2p_{3/2}$ - Cu/Ru(0001)

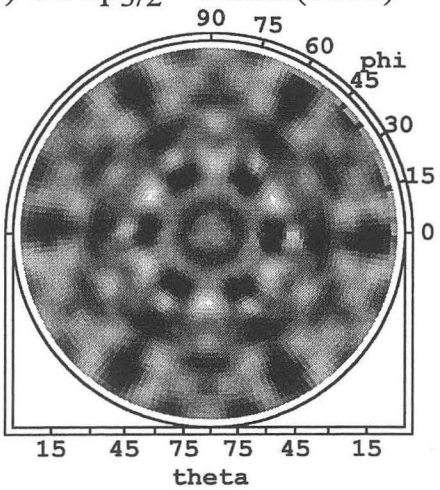

(f) Cu $2p_{3/2}$ - Cu/Ru(0001)

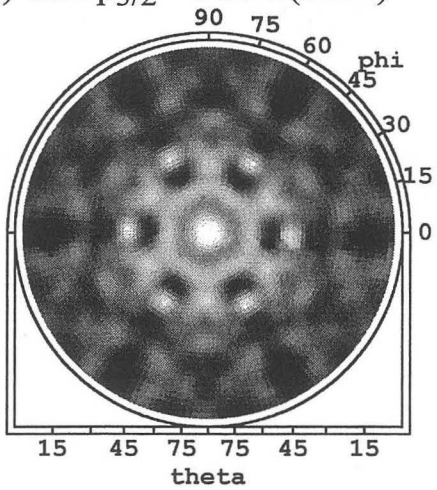

Fig. 4.22 Global R-factor plots comparing experiment to SSC calculations (for 1-3 ML) and MSC calculations (for all coverages) at various Cu coverages on O-precovered Ru(0001): (a) 1.1 ML; (b) 2.2 ML; (c) 3.2 ML; (d) 3.7 ML; (e) 4.8 ML; (f) 6.5 ML; (g) 8.0 ML; (h) 30.5 ML.

R-factor Analysis: Cu/O/Ru(0001) - Interlayer Distances

(a) 1.1 ML

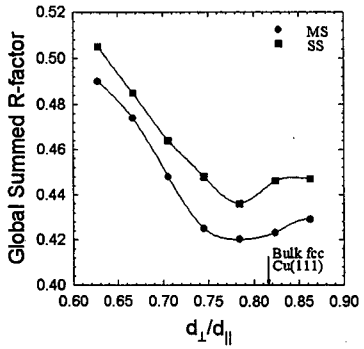

(b) 2.2 ML

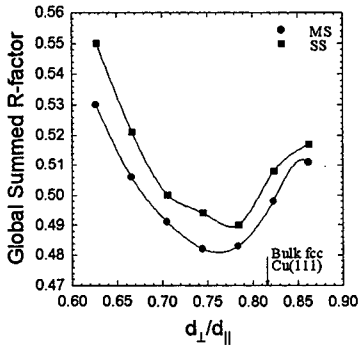

(c) 3.2 ML

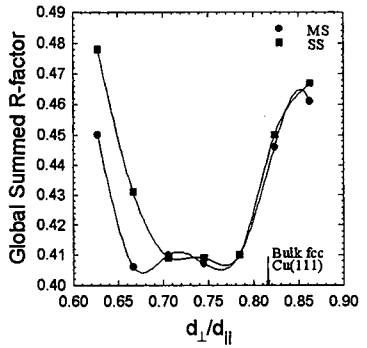

(d) 3.7 ML

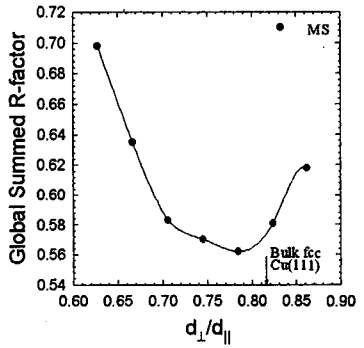

(e) 4.8 ML

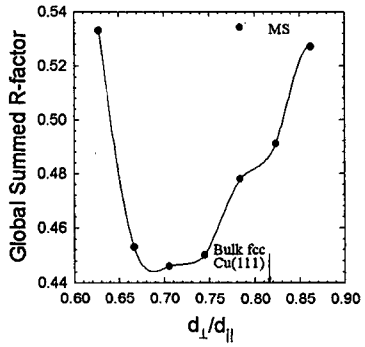

(f) 6.5 ML

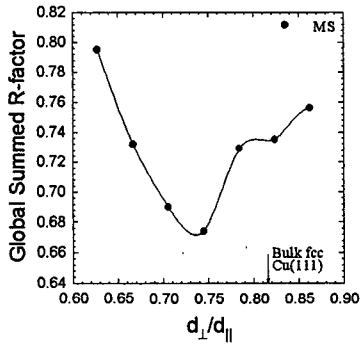

(g) 8.0 ML

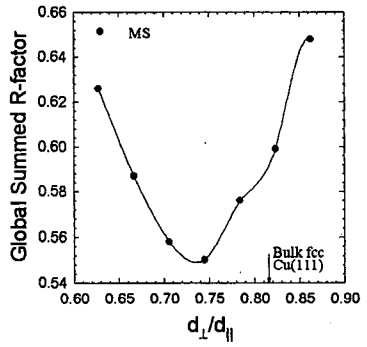

(h) 30.5 ML

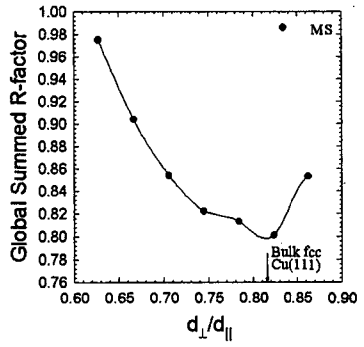

Fig. 4.23 As Fig. 4.14, but for oxygen-precovered Ru(0001). (a) Plot of $d_{\perp}/d_{\parallel}$ = (Cu-Cu interplanar distance)/(Cu-Cu in-plane nearest-neighbor distance) versus coverage in monolayers (ML): ● = Estimate of $d_{\perp}/d_{\parallel}$ using Cu areal densities derived from a 2 D Frenkel-Kontorova model by Hamilton and Foiles [4.3] combined with a constant-atomic-volume assumption; ■ = $d_{\perp}/d_{\parallel}$ determined by R-factor comparisons between experimental XPD data from Cu/O/Ru(0001) and MSC calculations for Cu $2p_{3/2}$ emission at a photoelectron kinetic energy of 556 eV; ◆ and □ = $d_{\perp}/d_{\parallel}$ determined by R-factor comparisons to experimental Cu $2p_{3/2}$ data obtained from Cu(111) by Naumovic and Osterwalder at photoelectron kinetic energies of 321 eV and 808 eV, respectively [4.21]; O = $d_{\perp}/d_{\parallel}$ determined by an R-factor comparison between experimental Cu $2p_{3/2}$ XPD data obtained in our laboratory from a Cu(111) single crystal and MSC calculations at an energy of 556 eV; (b) Plot of relative occupation of domain #1 versus coverage, with rotational symmetry indicated.

R-factor results - Cu/O/Ru(0001)

(a) $d_{\perp}/d_{\parallel}$ vs. Cu coverage

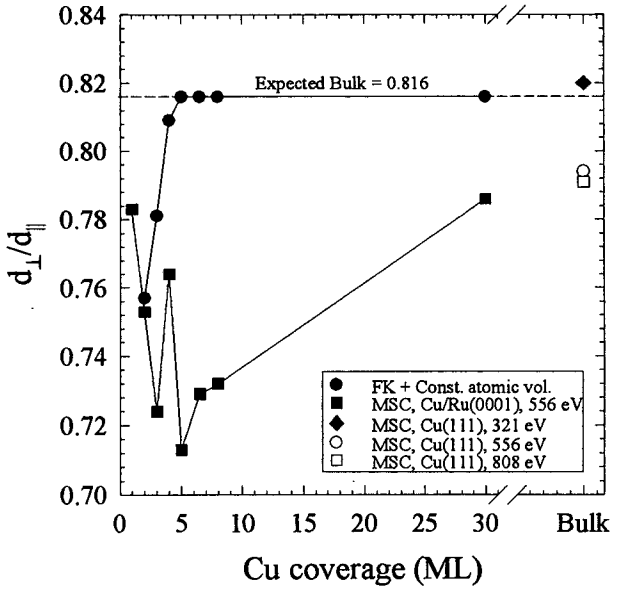

(b) Symmetry vs. Cu Coverage

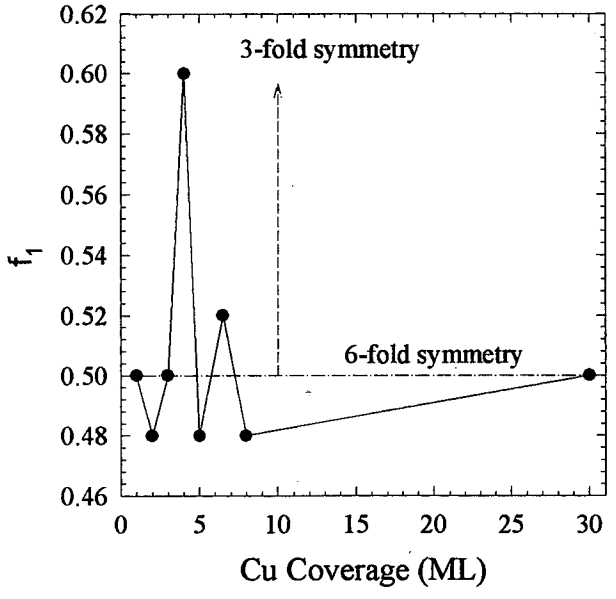

Chapter 5

Concluding Remarks

In chapter 3, we studied the directional dependence of the mean emitter depth for core-level photoelectron emission from single crystal overlayers and substrates, including both inelastic and elastic scattering and using both single-scattering and fully-converged multiple scattering approaches. In calculations on both isolated chains of Ni and Si atoms, and a more realistic large cluster of Ni atoms, we showed that this mean emission depth may vary by as much as $\pm$25-30% from a reference value based only upon isotropic inelastic scattering. In chapter 4, we studied the growth and structure of epitaxial Cu films grown on clean and O-precovered Ru(0001), and were able to make several structural conclusions. For growth on clean Ru(0001), the first monolayer is pseudomorphic, and even at partial monolayer coverages forms in large islands of the same structure. For thicker overlayers, we also showed that the short range structure of Cu/Ru(0001) is fcc Cu(111), but with significant interlayer contraction for coverages between 2 ML and 8 ML. The Cu-Cu interlayer spacing was found to have a slower approach to the bulk fcc Cu(111) interlayer spacing than a simple theoretical estimate based on the 2D Frenkel-Kontorova model and a constant atomic volume assumption. The appearance of sharp forward scattering peaks with distinct orientations and the excellent agreement with theory permitted us to demonstrate that the misfit dislocation structures seen in STM for 2-4 ML coverage actually thread through to the Cu-Ru interface. Finally, we showed that Cu grown on O-precovered Ru(0001) initially forms 3D islands, and that all of the oxygen floats on the Cu overlayer and is highly disordered and/or mobile on the Cu surface. In addition, the presence of oxygen does not affect the interlayer contraction, but does affect the relative domain occupation of the Cu overlayer.

As stated in the introduction, the ability to understand the atomic scale structure of thin films has become increasingly important because of the vast technological

applications of such films as well as to acquire a better fundamental understanding of atomic scale phenomena. Full-solid-angle x-ray photoelectron diffraction provides a powerful tool for determining such information about thin films. When high energy photoelectrons are used so that forward scattering peaks are present, full-solid-angle XPD patterns are quite easy to interpret regarding structures. By comparing experimental XPD patterns to single-scattering cluster (SSC) and multiple-scattering cluster (MSC) calculations via R-factors, it is possible to determine much more quantitative information such as the amount of interlayer contraction or expansion in overlayers, as well as identifying the presence of many domains, as was demonstrated in this dissertation. Although LEED may also provide such information, XPD has the advantage of being sensitive to the local atomic order, and can thus provide information even when the domain sizes are very small. In addition, XPD has the advantage that it can provide information about the relative positions of different atomic species, and thus can identify the presence of interdiffusion, species buried at an interface, or a species floating on a growing surface layer such as in the case of Cu/O-precovered Ru(0001) in this dissertation. While XPD is very powerful as a probe of surface structure, it is even more powerful when combined with complimentary surface structural techniques such as LEED and STM. For example, with XPD, it is not possible to detect the dislocation structures seen by STM in the Cu/Ru(0001) system, however, with XPD, it is possible to determine whether the dislocation structures thread to the interface or occur only in the top layer. In addition, it is difficult for us to determine with XPD the exact nature of the oxygen overlayer or if the Cu growth is layer-by-layer at very thick Cu coverages in the case of Cu/O-precovered Ru(0001). This type of information could more easily be determined with STM, for example.

Appendix A

Spline Smoothing Program and Input file for the determination of $I_O(\theta,\phi)$

Program smooth.f

```
C ************************************************************
c SPLINE SMOOTHING PROGRAM
c ************************************************************
c This program reads in XPD data as I(θ,φ), and then carries out both the
c azimuthal averaging to yield c Ī(θ,φ) and the spline fitting to Ī(θ,φ) necessary
c to generate the best final estimate of I_o(k̄). Finally, c χ(k̄) is determined
c for subsequent plotting, as in Fig. 2.9(b). The first line of the input file is
c the number of smoothed output files created.
c The second line is the name of the input XPD data file. The rest of
c the lines specify the smoothing factors used followed by the respective output
c smoothed file. The smoothing factor determines the degree of smoothing
c performed and can be any number between 0 and 1.0. Using a smoothing
c factor of 0 will cause the program to interpolate (i.e. the spline will go through
c all data points). Using a smoothing factor of 1.0 will cause the maximum amount
c of smoothing. The input data file is a full 2π XPD data set in a (θ, φ, Intensity)
c format. The output file is only in a (θ, Intensity) format. The program first
c averages over phi for each polar angle. These phi averaged intensities, Ī(θ),
c are then read into the spline smoothing routine and smoothed. The spline is
c forced to go to zero for a cutoff takeoff angle that is near the negative of the
c estimated half-angle of acceptance of the analyzer, and the parameter specifying
c this can be adjusted in the program (as the variable CUTOFFANG). The
c output is then in the (θ, Intensity) format. For I_o(θ,φ) subtraction,
c I_o(θ) = I_o(θ,φ) for all φ, and I_o(θ,φ) is then subtracted from the 2π
c XPD data.
c
c                                   S. Ruebush 9/7/94
c ************************************************************
c ************************************************************

c **Initialize things and read input**
      real calthe(93,363), calphi(93,363),i0(100),avint(93),
     &     chi1(93,363), the(32400),phi(32400),
     &     dphi(100), delthe(100),yy(100),xx(100),
     &     theta(100),x(100),y(100),t(108),c(108),
     &     w(100),wrk(3000),sp(100),spp(100),ww(100),
     &     cutoffang,imax,imin,ii0(100),wx(30)
      integer nphi(365),iwrk(100),i,ier,iopt,j,k,lwrk,m,
     &        n,nest,nk1,mm,kk,lnum
      character*20 fname2, fname3
c     write (*,*) 'Input data file:'
c     read (*,*) fname2
c     write (*,*) 'Output i0newfile:'
c     read (*,*) fname3
```

```
c     write(*,*) 'Smoothing parameter (between 0 and 1.0):'
c     read(*,*) s
      write(*,*) 'Cutoff angle = -4.0 deg'
c     read(*,*) cutoffang

      mm = 10000
      pi = 3.141592654
      rapi = pi/180.0
      cutoffang = -4.0

      open(unit=13, file = 'smooth.in')
      read(13,*) lnum
      read(13,*) fname2
      do 875 kk = 1, lnum
      read(13,*) fname3
      read(13,*) s
c
c **Finding how many values of theta**

      nthe = 0
      open (unit = 4, file = fname2)
      do 120 i = 1, mm
      read (4,*,end=999) the(i), phi(i), xxx
      if (i .gt. 1) then
        diff = the(i) - the(i-1)
        if (diff .ge. 0.10) then
          nthe = nthe+1
          delthe(nthe) = diff
         endif
      endif
 120  continue
 999  close (4)
      nthe = nthe+1

c ** reading the data and assigning each datum a place in the
c     <i,j> matrix**

      open (unit = 4, file = fname2)
      read (4,*) calthe(1,1), calphi(1,1), chi1(1,1)
      do 121 i = 1, nthe
      nphi(i) = 1
      dphi(i) = 0
      do 125 j = 2, 365
      read (4,*,end=998) calthe(i,j), calphi(i,j), chi1(i,j)
      if (j .gt. 1) then
        diff = calphi(i,j) - calphi(i,j-1)
        nphi(i)= nphi(i)+1
        dphi(i) = dphi(i) + diff
        if (diff .lt. 0.00) then
          nphi(i) = nphi(i) - 1
          dphi(i) = dphi(i)-diff
          calthe (i+1,1) = calthe(i,j)
          calphi(i+1,1) = calphi(i,j)
          chi1(i+1,1) = chi1(i,j)
          dphi(i) = dphi(i)/(nphi(i)-1)
```

```
        go to 121
       endif
    endif
125 continue
121 continue
998 dphi(i) = calphi(i,2)-calphi(i,1)
    close (4)

c **Average I(theta,phi) over phi**

    do 114 i = 1, nthe
    theta(i) = calthe(i,1)*pi/180.0
    sumint = 0.0
    do 115 j = 1, nphi(i)
    sumint = sumint+chi1(i,j)
115 continue
    avint(i) = sumint/nphi(i)
    ii0(i) = avint(i)
    yy(i) = ii0(i)
114 continue

c Mirror i0 over pi/2. It is assumed here that there is a data point
c right on pi/2.

    delthe(nthe) = delthe(nthe-1)
    do 116 i9 = nthe+1, 2*nthe-1
     theta(i9) = pi - theta(nthe-1-(i9-nthe-1))
     ii0(i9) = ii0(nthe-1-(i9-nthe-1))
     yy(i9) = ii0(i9)
     delthe(i9) = delthe(nthe-1-(i9-nthe-1))
116 continue

    m = 2*nthe-1
    do 117 i=1,m
    xx(i) = theta(i)*180.0/pi
    ww(i) = 1.0
117 continue
    m=m+1
    do 666 i=1,m
    y(i+1)=yy(i)
    i0(i+1)=ii0(i)
    x(i+1)=xx(i)
    w(i+1)=ww(i)
666 continue
    m=m+1
    y(1)=0.0
    i0(1)=0.0
    y(m)=0.0
    imin = y(1)
    x(1)=cutoffang
    x(m)=180.0-cutoffang
    imax = y(1)
    do 777 i=1,m
    if(imax .lt. y(i+1))then
    imax = y(i+1)
```

```
      endif
 777  continue
      do 779 i = 1,m
      y(i) = y(i)/imax
 779  continue
      xb = x(1)
      xe = x(m)
      open(unit=5, file='weights.in')
      do 177 i = 1,30
      read(5,*) wx(i)
      if(i .le. 15)then
      w(i) = wx(i)
      endif
      if(i .ge. 16)then
      w(m+16-i) = wx(i)
      endif
 177  continue
      close(5)

      k = 3.0
      nest = 100
      lwrk = 3000
      iopt = 0
      call curfit(iopt,m,x,y,w,xb,xe,k,s,nest,n,t,c,fp,wrk,lwrk,
     &      iwrk,ier)
      if(ier .eq. 10) go to 202
      call splev(t,n,c,k,x,sp,m,ier)

 202  continue
      do 888 i = 1,m
      spp(i) = (sp(i)+sp(m-i+1))/2.0
 888  continue
      open(unit = 7, file = fname3)
c     open(unit = 8, file = 'junk1')
c     open(unit = 9, file = 'junk2')
c     write(7,*) 'Smoothing factor:', s
c     write(7,*) 'Number of knots:', n
c     write(7,*) 'position of the knots:'
c     do 220 j = 1, n
c     write(7,*) j,t(j)
c 220 continue
c     write(7,*) 'dimension of s(x) (nk1=n-k-1):', n-k-1
c     write(7,*) 'coefficients of B-Spline rep. of s(x):'
      nk1 = n-k-1
c     do 225 j = 1, nk1
c     write(7,*) j, c(j)
c 225 continue
c     write(7,*) 'error code:', ier
      do  231 i = 2,m-1
      write(7,241) x(i), i0(i), spp(i)*imax
c     write(8,242) x(i), i0(i)
c     write(9,243) x(i), sp(i)*imax
 241  format(2x,f7.2,2x,e12.5,2x,e12.5)
c 242 format(2x,f7.2,2x,e12.5)
c 243 format(2x,f7.2,2x,e12.5)
```

```
 231  continue
      close(7)
c     close(8)
c     close(9)
 875  continue
      close(13)
      end

* ==========================================================================
* NIST Guide to Available Math Software.
* Fullsource for module CURFIT from package DIERCKX.
* Retrieved from NETLIB on Tue Jul 19 18:59:23 1994.
* ==========================================================================
      subroutine curfit(iopt,m,x,y,w,xb,xe,k,s,nest,n,t,c,fp,
     * wrk,lwrk,iwrk,ier)
c  given the set of data points (x(i),y(i)) and the set of positive
c  numbers w(i),i=1,2,...,m,subroutine curfit determines a smooth spline
c  approximation of degree k on the interval xb <= x <= xe.
c  if iopt=-1 curfit calculates the weighted least-squares spline
c  according to a given set of knots.
c  if iopt>=0 the number of knots of the spline s(x) and the position
c  t(j),j=1,2,...,n is chosen automatically by the routine. the smooth-
c  ness of s(x) is then achieved by minimalizing the discontinuity
c  jumps of the k-th derivative of s(x) at the knots t(j),j=k+2,k+3,...,
c  n-k-1. the amount of smoothness is determined by the condition that
c  f(p)=sum((w(i)*(y(i)-s(x(i))))**2) be <= s, with s a given non-
c  negative constant, called the smoothing factor.
c  the fit s(x) is given in the b-spline representation (b-spline coef-
c  ficients c(j),j=1,2,...,n-k-1) and can be evaluated by means of
c  subroutine splev.
c
c  calling sequence:
c     call curfit(iopt,m,x,y,w,xb,xe,k,s,nest,n,t,c,fp,wrk,
c    * lwrk,iwrk,ier)
c
c  parameters:
c   iopt  : integer flag. on entry iopt must specify whether a weighted
c           least-squares spline (iopt=-1) or a smoothing spline (iopt=
c           0 or 1) must be determined. if iopt=0 the routine will start
c           with an initial set of knots t(i)=xb, t(i+k+1)=xe, i=1,2,...
c           k+1. if iopt=1 the routine will continue with the knots
c           found at the last call of the routine.
c           attention: a call with iopt=1 must always be immediately
c           preceded by another call with iopt=1 or iopt=0.
c           unchanged on exit.
c   m     : integer. on entry m must specify the number of data points.
c           m > k. unchanged on exit.
c   x     : real array of dimension at least (m). before entry, x(i)
c           must be set to the i-th value of the independent variable x,
c           for i=1,2,...,m. these values must be supplied in strictly
c           ascending order. unchanged on exit.
c   y     : real array of dimension at least (m). before entry, y(i)
c           must be set to the i-th value of the dependent variable y,
c           for i=1,2,...,m. unchanged on exit.
c   w     : real array of dimension at least (m). before entry, w(i)
```

```
c        must be set to the i-th value in the set of weights. the
c        w(i) must be strictly positive. unchanged on exit.
c        see also further comments.
c  xb,xe : real values. on entry xb and xe must specify the boundaries
c        of the approximation interval. xb<=x(1), xe>=x(m).
c        unchanged on exit.
c  k     : integer. on entry k must specify the degree of the spline.
c        1<=k<=5. it is recommended to use cubic splines (k=3).
c        the user is strongly dissuaded from choosing k even,together
c        with a small s-value. unchanged on exit.
c  s     : real.on entry (in case iopt>=0) s must specify the smoothing
c        factor. s >=0. unchanged on exit.
c        for advice on the choice of s see further comments.
c  nest  : integer. on entry nest must contain an over-estimate of the
c        total number of knots of the spline returned, to indicate
c        the storage space available to the routine. nest >=2*k+2.
c        in most practical situation nest=m/2 will be sufficient.
c        always large enough is  nest=m+k+1, the number of knots
c        needed for interpolation (s=0). unchanged on exit.
c  n     : integer.
c        unless ier =10 (in case iopt >=0), n will contain the
c        total number of knots of the spline approximation returned.
c        if the computation mode iopt=1 is used this value of n
c        should be left unchanged between subsequent calls.
c        in case iopt=-1, the value of n must be specified on entry.
c  t     : real array of dimension at least (nest).
c        on succesful exit, this array will contain the knots of the
c        spline,i.e. the position of the interior knots t(k+2),t(k+3)
c        ...,t(n-k-1) as well as the position of the additional knots
c        t(1)=t(2)=...=t(k+1)=xb and t(n-k)=...=t(n)=xe needed for
c        the b-spline representation.
c        if the computation mode iopt=1 is used, the values of t(1),
c        t(2),...,t(n) should be left unchanged between subsequent
c        calls. if the computation mode iopt=-1 is used, the values
c        t(k+2),...,t(n-k-1) must be supplied by the user, before
c        entry. see also the restrictions (ier=10).
c  c     : real array of dimension at least (nest).
c        on succesful exit, this array will contain the coefficients
c        c(1),c(2),..,c(n-k-1) in the b-spline representation of s(x)
c  fp    : real. unless ier=10, fp contains the weighted sum of
c        squared residuals of the spline approximation returned.
c  wrk   : real array of dimension at least (m*(k+1)+nest*(7+3*k)).
c        used as working space. if the computation mode iopt=1 is
c        used, the values wrk(1),...,wrk(n) should be left unchanged
c        between subsequent calls.
c  lwrk  : integer. on entry,lwrk must specify the actual dimension of
c        the array wrk as declared in the calling (sub)program.lwrk
c        must not be too small (see wrk). unchanged on exit.
c  iwrk  : integer array of dimension at least (nest).
c        used as working space. if the computation mode iopt=1 is
c        used,the values iwrk(1),...,iwrk(n) should be left unchanged
c        between subsequent calls.
c  ier   : integer. unless the routine detects an error, ier contains a
c        non-positive value on exit, i.e.
c   ier=0  : normal return. the spline returned has a residual sum of
```

```
c          squares fp such that abs(fp-s)/s <= tol with tol a relat-
c          ive tolerance set to 0.001 by the program.
c   ier=-1 : normal return. the spline returned is an interpolating
c          spline (fp=0).
c   ier=-2 : normal return. the spline returned is the weighted least-
c          squares polynomial of degree k. in this extreme case fp
c          gives the upper bound fp0 for the smoothing factor s.
c   ier=1  : error. the required storage space exceeds the available
c          storage space, as specified by the parameter nest.
c          probably causes : nest too small. if nest is already
c          large (say nest > m/2), it may also indicate that s is
c          too small
c          the approximation returned is the weighted least-squares
c          spline according to the knots t(1),t(2),...,t(n). (n=nest)
c          the parameter fp gives the corresponding weighted sum of
c          squared residuals (fp>s).
c   ier=2  : error. a theoretically impossible result was found during
c          the iteration proces for finding a smoothing spline with
c          fp = s. probably causes : s too small.
c          there is an approximation returned but the corresponding
c          weighted sum of squared residuals does not satisfy the
c          condition abs(fp-s)/s < tol.
c   ier=3  : error. the maximal number of iterations maxit (set to 20
c          by the program) allowed for finding a smoothing spline
c          with fp=s has been reached. probably causes : s too small
c          there is an approximation returned but the corresponding
c          weighted sum of squared residuals does not satisfy the
c          condition abs(fp-s)/s < tol.
c   ier=10 : error. on entry, the input data are controlled on validity
c          the following restrictions must be satisfied.
c          -1<=iopt<=1, 1<=k<=5, m>k, nest>2*k+2, w(i)>0,i=1,2,...,m
c          xb<=x(1)=(k+1)*m+nest*(7+3*k)
c          if iopt=-1: 2*k+2<=n<=min(nest,m+k+1)
c                  xb=0: s>=0
c                  if s=0 : nest >= m+k+1
c          if one of these conditions is found to be violated,control
c          is immediately repassed to the calling program. in that
c          case there is no approximation returned.
c
c  further comments:
c   by means of the parameter s, the user can control the tradeoff
c   between closeness of fit and smoothness of fit of the approximation.
c   if s is too large, the spline will be too smooth and signal will be
c   lost ; if s is too small the spline will pick up too much noise. in
c   the extreme cases the program will return an interpolating spline if
c   s=0 and the weighted least-squares polynomial of degree k if s is
c   very large. between these extremes, a properly chosen s will result
c   in a good compromise between closeness of fit and smoothness of fit.
c   to decide whether an approximation, corresponding to a certain s is
c   satisfactory the user is highly recommended to inspect the fits
c   graphically.
c   recommended values for s depend on the weights w(i). if these are
c   taken as 1/d(i) with d(i) an estimate of the standard deviation of
c   y(i), a good s-value should be found in the range (m-sqrt(2*m),m+
c   sqrt(2*m)). if nothing is known about the statistical error in y(i)
```

```
c  each w(i) can be set equal to one and s determined by trial and
c  error, taking account of the comments above. the best is then to
c  start with a very large value of s ( to determine the least-squares
c  polynomial and the corresponding upper bound fp0 for s) and then to
c  progressively decrease the value of s ( say by a factor 10 in the
c  beginning, i.e. s=fp0/10, fp0/100,...and more carefully as the
c  approximation shows more detail) to obtain closer fits.
c  to economize the search for a good s-value the program provides with
c  different modes of computation. at the first call of the routine, or
c  whenever he wants to restart with the initial set of knots the user
c  must set iopt=0.
c  if iopt=1 the program will continue with the set of knots found at
c  the last call of the routine. this will save a lot of computation
c  time if curfit is called repeatedly for different values of s.
c  the number of knots of the spline returned and their location will
c  depend on the value of s and on the complexity of the shape of the
c  function underlying the data. but, if the computation mode iopt=1
c  is used, the knots returned may also depend on the s-values at
c  previous calls (if these were smaller). therefore, if after a number
c  of trials with different s-values and iopt=1, the user can finally
c  accept a fit as satisfactory, it may be worthwhile for him to call
c  curfit once more with the selected value for s but now with iopt=0.
c  indeed, curfit may then return an approximation of the same quality
c  of fit but with fewer knots and therefore better if data reduction
c  is also an important objective for the user.
c
c other subroutines required:
c   fpback,fpbspl,fpchec,fpcurf,fpdisc,fpgivs,fpknot,fprati,fprota
c
c references:
c  dierckx p. : an algorithm for smoothing, differentiation and integ-
c            ration of experimental data using spline functions,
c            j.comp.appl.maths 1 (1975) 165-184.
c  dierckx p. : a fast algorithm for smoothing data on a rectangular
c            grid while using spline functions, siam j.numer.anal.
c            19 (1982) 1286-1304.
c  dierckx p. : an improved algorithm for curve fitting with spline
c            functions, report tw54, dept. computer science,k.u.
c            leuven, 1981.
c  dierckx p. : curve and surface fitting with splines, monographs on
c            numerical analysis, oxford university press, 1993.
c
c author:
c   p.dierckx
c   dept. computer science, k.u. leuven
c   celestijnenlaan 200a, b-3001 heverlee, belgium.
c   e-mail : Paul.Dierckx@cs.kuleuven.ac.be
c
c creation date : may 1979
c latest update : march 1987
c
c ..
c ..scalar arguments..
    real xb,xe,s,fp
    integer iopt,m,k,nest,n,lwrk,ier
```

```
c ..array arguments..
    real x(m),y(m),w(m),t(nest),c(nest),wrk(lwrk)
    integer iwrk(nest)
c ..local scalars..
    real tol
    integer i,ia,ib,ifp,ig,iq,iz,j,k1,k2,lwest,maxit,nmin
c ..
c we set up the parameters tol and maxit
    write(*,*) 'Starting curfit.'
    maxit = 20
    tol = 0.1e-02
c before starting computations a data check is made. if the input data
c are invalid, control is immediately repassed to the calling program.
    ier = 10
    if(k.le.0 .or. k.gt.5)then
    write(*,*) '0 > k or k > 5'
    go to 50
    endif
    k1 = k+1
    k2 = k1+1
    if(iopt.lt.(-1) .or. iopt.gt.1)then
    write(*,*) 'iopt < -1 or iopt > 1'
    go to 50
    endif
    nmin = 2*k1
    if(m.lt.k1 .or. nest.lt.nmin)then
    write(*,*) 'm < k+1 or nest < nmin'
    go to 50
    endif
    lwest = m*k1+nest*(7+3*k)
    if(lwrk.lt.lwest)then
    write(*,*) 'lwrk < lwest'
    go to 50
    endif
    if(xb.gt.x(1) .or. xe.lt.x(m) .or. w(1).le.0.)then
    write(*,*) 'xb > x(1) or xe < x(m) or w(1) < 0'
    go to 50
    endif
    do 10 i=2,m
      if(x(i-1).ge.x(i) .or. w(i).le.0.)then
      write(*,*) 'x(i-1) > x(i) or w(i) < 0 for :i =', i
      go to 50
      endif
 10 continue
    if(iopt.ge.0) go to 30
    if(n.lt.nmin .or. n.gt.nest)then
    write(*,*) 'n < nmin or n > nest'
    go to 50
    endif
    j = n
    do 20 i=1,k1
      t(i) = xb
      t(j) = xe
      j = j-1
 20 continue
```

```
      call fpchec(x,m,t,n,k,ier)
      if(ier) 50,40,50
   30 if(s.lt.0.)then
      write(*,*) 's < 0'
      go to 50
      endif
      if(s.eq.0. .and. nest.lt.(m+k1))then
      write(*,*) 's=0 and nest < m+k+1'
      go to 50
      endif
      ier = 0
c we partition the working space and determine the spline approximation.
   40 ifp = 1
      iz = ifp+nest
      ia = iz+nest
      ib = ia+nest*k1
      ig = ib+nest*k2
      iq = ig+nest*k2
      call fpcurf(iopt,x,y,w,m,xb,xe,k,s,nest,tol,maxit,k1,k2,n,t,c,fp,
     * wrk(ifp),wrk(iz),wrk(ia),wrk(ib),wrk(ig),wrk(iq),iwrk,ier)
      write(*,*) 'Leaving curfit.'
   50 return
      end
      subroutine fpcurf(iopt,x,y,w,m,xb,xe,k,s,nest,tol,maxit,k1,k2,
     * n,t,c,fp,fpint,z,a,b,g,q,nrdata,ier)
c ..
c ..scalar arguments..
      real xb,xe,s,tol,fp
      integer iopt,m,k,nest,maxit,k1,k2,n,ier
c ..array arguments..
      real x(m),y(m),w(m),t(nest),c(nest),fpint(nest),
     * z(nest),a(nest,k1),b(nest,k2),g(nest,k2),q(m,k1)
      integer nrdata(nest)
c ..local scalars..
      real acc,con1,con4,con9,cos,half,fpart,fpms,fpold,fp0,f1,f2,f3,
     * one,p,pinv,piv,p1,p2,p3,rn,sin,store,term,wi,xi,yi
      integer i,ich1,ich3,it,iter,i1,i2,i3,j,k3,l,l0,
     * mk1,new,nk1,nmax,nmin,nplus,npl1,nrint,n8
c ..local arrays..
      real h(7)
c ..function references
      real abs,fprati
      integer max0,min0
c ..subroutine references..
c   fpback,fpbspl,fpgivs,fpdisc,fpknot,fprota
c ..
c set constants
      one = 0.1e+01
      con1 = 0.1e0
      con9 = 0.9e0
      con4 = 0.4e-01
      half = 0.5e0
cccccccccccccccccccccccccccccccccccccccccccccccccccccccccccccccccccccccc
c part 1: determination of the number of knots and their position     c
c ************************************************************     c
```

```
c given a set of knots we compute the least-squares spline sinf(x),   c
c and the corresponding sum of squared residuals fp=f(p=inf).        c
c if iopt=-1 sinf(x) is the requested approximation.                 c
c if iopt=0 or iopt=1 we check whether we can accept the knots:      c
c   if fp <=s we will continue with the current set of knots.        c
c   if fp > s we will increase the number of knots and compute the   c
c     corresponding least-squares spline until finally fp<=s.        c
c   the initial choice of knots depends on the value of s and iopt.  c
c   if s=0 we have spline interpolation; in that case the number of  c
c   knots equals nmax = m+k+1.                                       c
c   if s > 0 and                                                     c
c     iopt=0 we first compute the least-squares polynomial of        c
c     degree k; n = nmin = 2*k+2                                     c
c     iopt=1 we start with the set of knots found at the last        c
c     call of the routine, except for the case that s > fp0; then    c
c     we compute directly the least-squares polynomial of degree k.  c
cccccccccccccccccccccccccccccccccccccccccccccccccccccccccccccccccccccccc
c determine nmin, the number of knots for polynomial approximation.
      nmin = 2*k1
      if(iopt.lt.0) go to 60
c calculation of acc, the absolute tolerance for the root of f(p)=s.
      acc = tol*s
c determine nmax, the number of knots for spline interpolation.
      nmax = m+k1
      if(s.gt.0.) go to 45
c if s=0, s(x) is an interpolating spline.
c test whether the required storage space exceeds the available one.
      n = nmax
      if(nmax.gt.nest) go to 420
c find the position of the interior knots in case of interpolation.
   10 mk1 = m-k1
      if(mk1.eq.0) go to 60
      k3 = k/2
      i = k2
      j = k3+2
      if(k3*2.eq.k) go to 30
      do 20 l=1,mk1
        t(i) = x(j)
        i = i+1
        j = j+1
   20 continue
      go to 60
   30 do 40 l=1,mk1
        t(i) = (x(j)+x(j-1))*half
        i = i+1
        j = j+1
   40 continue
      go to 60
c if s>0 our initial choice of knots depends on the value of iopt.
c if iopt=0 or iopt=1 and s>=fp0, we start computing the least-squares
c polynomial of degree k which is a spline without interior knots.
c if iopt=1 and fp0>s we start computing the least squares spline
c according to the set of knots found at the last call of the routine.
   45 if(iopt.eq.0) go to 50
      if(n.eq.nmin) go to 50
```

```
      fp0 = fpint(n)
      fpold = fpint(n-1)
      nplus = nrdata(n)
      if(fp0.gt.s) go to 60
   50 n = nmin
      fpold = 0.
      nplus = 0
      nrdata(1) = m-2
c main loop for the different sets of knots. m is a save upper bound
c for the number of trials.
   60 do 200 iter = 1,m
      if(n.eq.nmin) ier = -2
c find nrint, tne number of knot intervals.
      nrint = n-nmin+1
c find the position of the additional knots which are needed for
c the b-spline representation of s(x).
      nk1 = n-k1
      i = n
      do 70 j=1,k1
       t(j) = xb
       t(i) = xe
       i = i-1
   70 continue
c compute the b-spline coefficients of the least-squares spline
c sinf(x). the observation matrix a is built up row by row and
c reduced to upper triangular form by givens transformations.
c at the same time fp=f(p=inf) is computed.
      fp = 0.
c initialize the observation matrix a.
      do 80 i=1,nk1
       z(i) = 0.
       do 80 j=1,k1
        a(i,j) = 0.
   80 continue
      l = k1
      do 130 it=1,m
c fetch the current data point x(it),y(it).
       xi = x(it)
       wi = w(it)
       yi = y(it)*wi
c search for knot interval t(l) <= xi < t(l+1).
   85  if(xi.lt.t(l+1) .or. l.eq.nk1) go to 90
       l = l+1
       go to 85
c evaluate the (k+1) non-zero b-splines at xi and store them in q.
   90  call fpbspl(t,n,k,xi,l,h)
       do 95 i=1,k1
        q(it,i) = h(i)
        h(i) = h(i)*wi
   95  continue
c rotate the new row of the observation matrix into triangle.
       j = l-k1
       do 110 i=1,k1
        j = j+1
        piv = h(i)
```

```
      if(piv.eq.0.) go to 110
c  calculate the parameters of the givens transformation.
      call fpgivs(piv,a(j,1),cos,sin)
c  transformations to right hand side.
      call fprota(cos,sin,yi,z(j))
      if(i.eq.k1) go to 120
      i2 = 1
      i3 = i+1
      do 100 i1 = i3,k1
       i2 = i2+1
c  transformations to left hand side.
       call fprota(cos,sin,h(i1),a(j,i2))
 100   continue
 110  continue
c  add contribution of this row to the sum of squares of residual
c  right hand sides.
 120   fp = fp+yi**2
 130  continue
    if(ier.eq.(-2)) fp0 = fp
    fpint(n) = fp0
    fpint(n-1) = fpold
    nrdata(n) = nplus
c  backward substitution to obtain the b-spline coefficients.
    call fpback(a,z,nk1,k1,c,nest)
c  test whether the approximation sinf(x) is an acceptable solution.
    if(iopt.lt.0) go to 440
    fpms = fp-s
    if(abs(fpms).lt.acc) go to 440
c  if f(p=inf) < s accept the choice of knots.
    if(fpms.lt.0.) go to 250
c  if n = nmax, sinf(x) is an interpolating spline.
    if(n.eq.nmax) go to 430
c  increase the number of knots.
c  if n=nest we cannot increase the number of knots because of
c  the storage capacity limitation.
    if(n.eq.nest) go to 420
c  determine the number of knots nplus we are going to add.
    if(ier.eq.0) go to 140
    nplus = 1
    ier = 0
    go to 150
 140  npl1 = nplus*2
    rn = nplus
    if(fpold-fp.gt.acc) npl1 = rn*fpms/(fpold-fp)
    nplus = min0(nplus*2,max0(npl1,nplus/2,1))
 150  fpold = fp
c  compute the sum((w(i)*(y(i)-s(x(i))))**2) for each knot interval
c  t(j+k) <= x(i) <= t(j+k+1) and store it in fpint(j),j=1,2,...nrint.
    fpart = 0.
    i = 1
    l = k2
    new = 0
    do 180 it=1,m
     if(x(it).lt.t(l) .or. l.gt.nk1) go to 160
     new = 1
```

```
      l = l+1
160     term = 0.
      l0 = l-k2
      do 170 j=1,k1
        l0 = l0+1
        term = term+c(l0)*q(it,j)
170     continue
      term = (w(it)*(term-y(it)))**2
      fpart = fpart+term
      if(new.eq.0) go to 180
      store = term*half
      fpint(i) = fpart-store
      i = i+1
      fpart = store
      new = 0
180   continue
     fpint(nrint) = fpart
     do 190 l=1,nplus
c  add a new knot.
      call fpknot(x,m,t,n,fpint,nrdata,nrint,nest,1)
c  if n=nmax we locate the knots as for interpolation.
      if(n.eq.nmax) go to 10
c  test whether we cannot further increase the number of knots.
      if(n.eq.nest) go to 200
190   continue
c  restart the computations with the new set of knots.
200  continue
c  test whether the least-squares kth degree polynomial is a solution
c  of our approximation problem.
250  if(ier.eq.(-2)) go to 440
cccccccccccccccccccccccccccccccccccccccccccccccccccccccccccccccccccccccc
c  part 2: determination of the smoothing spline sp(x).          c
c  ***************************************************           c
c  we have determined the number of knots and their position.      c
c  we now compute the b-spline coefficients of the smoothing spline   c
c  sp(x). the observation matrix a is extended by the rows of matrix   c
c  b expressing that the kth derivative discontinuities of sp(x) at   c
c  the interior knots t(k+2),...t(n-k-1) must be zero. the corres-    c
c  ponding weights of these additional rows are set to 1/p.        c
c  iteratively we then have to determine the value of p such that    c
c  f(p)=sum((w(i)*(y(i)-sp(x(i))))**2) be = s. we already know that   c
c  the least-squares kth degree polynomial corresponds to p=0, and    c
c  that the least-squares spline corresponds to p=infinity. the      c
c  iteration process which is proposed here, makes use of rational    c
c  interpolation. since f(p) is a convex and strictly decreasing      c
c  function of p, it can be approximated by a rational function       c
c  r(p) = (u*p+v)/(p+w). three values of p(p1,p2,p3) with correspond-  c
c  ing values of f(p) (f1=f(p1)-s,f2=f(p2)-s,f3=f(p3)-s) are used     c
c  to calculate the new value of p such that r(p)=s. convergence is   c
c  guaranteed by taking f1>0 and f3<0.                              c
cccccccccccccccccccccccccccccccccccccccccccccccccccccccccccccccccccccccc
c  evaluate the discontinuity jump of the kth derivative of the
c  b-splines at the knots t(l),l=k+2,...n-k-1 and store in b.
    call fpdisc(t,n,k2,b,nest)
c  initial value for p.
```

```
      p1 = 0.
      f1 = fp0-s
      p3 = -one
      f3 = fpms
      p = 0.
      do 255 i=1,nk1
        p = p+a(i,1)
 255  continue
      rn = nk1
      p = rn/p
      ich1 = 0
      ich3 = 0
      n8 = n-nmin
c  iteration process to find the root of f(p) = s.
      do 360 iter=1,maxit
c  the rows of matrix b with weight 1/p are rotated into the
c  triangularised observation matrix a which is stored in g.
        pinv = one/p
        do 260 i=1,nk1
          c(i) = z(i)
          g(i,k2) = 0.
          do 260 j=1,k1
            g(i,j) = a(i,j)
 260      continue
        do 300 it=1,n8
c  the row of matrix b is rotated into triangle by givens transformation
          do 270 i=1,k2
            h(i) = b(it,i)*pinv
 270        continue
          yi = 0.
          do 290 j=it,nk1
            piv = h(1)
c  calculate the parameters of the givens transformation.
            call fpgivs(piv,g(j,1),cos,sin)
c  transformations to right hand side.
            call fprota(cos,sin,yi,c(j))
            if(j.eq.nk1) go to 300
            i2 = k1
            if(j.gt.n8) i2 = nk1-j
            do 280 i=1,i2
c  transformations to left hand side.
              i1 = i+1
              call fprota(cos,sin,h(i1),g(j,i1))
              h(i) = h(i1)
 280          continue
            h(i2+1) = 0.
 290        continue
 300      continue
c  backward substitution to obtain the b-spline coefficients.
      call fpback(g,c,nk1,k2,c,nest)
c  computation of f(p).
      fp = 0.
      l = k2
      do 330 it=1,m
        if(x(it).lt.t(l) .or. l.gt.nk1) go to 310
```

```
      l = l+1
 310    l0 = l-k2
      term = 0.
      do 320 j=1,k1
        l0 = l0+1
        term = term+c(l0)*q(it,j)
 320    continue
      fp = fp+(w(it)*(term-y(it)))**2
 330  continue
c test whether the approximation sp(x) is an acceptable solution.
      fpms = fp-s
      if(abs(fpms).lt.acc) go to 440
c test whether the maximal number of iterations is reached.
      if(iter.eq.maxit) go to 400
c carry out one more step of the iteration process.
      p2 = p
      f2 = fpms
      if(ich3.ne.0) go to 340
      if((f2-f3).gt.acc) go to 335
c our initial choice of p is too large.
      p3 = p2
      f3 = f2
      p = p*con4
      if(p.le.p1) p=p1*con9 + p2*con1
      go to 360
 335  if(f2.lt.0.) ich3=1
 340  if(ich1.ne.0) go to 350
      if((f1-f2).gt.acc) go to 345
c our initial choice of p is too small
      p1 = p2
      f1 = f2
      p = p/con4
      if(p3.lt.0.) go to 360
      if(p.ge.p3) p = p2*con1 + p3*con9
      go to 360
 345  if(f2.gt.0.) ich1=1
c test whether the iteration process proceeds as theoretically
c expected.
 350  if(f2.ge.f1 .or. f2.le.f3) go to 410
c find the new value for p.
      p = fprati(p1,f1,p2,f2,p3,f3)
 360 continue
c error codes and messages.
 400 ier = 3
     go to 440
 410 ier = 2
     go to 440
 420 ier = 1
     go to 440
 430 ier = -1
 440 return
     end
     real function fprati(p1,f1,p2,f2,p3,f3)
c given three points (p1,f1),(p2,f2) and (p3,f3), function fprati
c gives the value of p such that the rational interpolating function
```

```
c  of the form r(p) = (u*p+v)/(p+w) equals zero at p.
c  ..
c  ..scalar arguments..
      real p1,f1,p2,f2,p3,f3
c  ..local scalars..
      real h1,h2,h3,p
c  ..
      if(p3.gt.0.) go to 10
c  value of p in case p3 = infinity.
      p = (p1*(f1-f3)*f2-p2*(f2-f3)*f1)/((f1-f2)*f3)
      go to 20
c  value of p in case p3 ^= infinity.
   10 h1 = f1*(f2-f3)
      h2 = f2*(f3-f1)
      h3 = f3*(f1-f2)
      p = -(p1*p2*h3+p2*p3*h1+p3*p1*h2)/(p1*h1+p2*h2+p3*h3)
c  adjust the value of p1,f1,p3 and f3 such that f1 > 0 and f3 < 0.
   20 if(f2.lt.0.) go to 30
      p1 = p2
      f1 = f2
      go to 40
   30 p3 = p2
      f3 = f2
   40 fprati = p
      return
      end
      subroutine fpdisc(t,n,k2,b,nest)
c  subroutine fpdisc calculates the discontinuity jumps of the kth
c  derivative of the b-splines of degree k at the knots t(k+2)..t(n-k-1)
c  ..scalar arguments..
      integer n,k2,nest
c  ..array arguments..
      real t(n),b(nest,k2)
c  ..local scalars..
      real an,fac,prod
      integer i,ik,j,jk,k,k1,l,lj,lk,lmk,lp,nk1,nrint
c  ..local array..
      real h(12)
c  ..
      k1 = k2-1
      k = k1-1
      nk1 = n-k1
      nrint = nk1-k
      an = nrint
      fac = an/(t(nk1+1)-t(k1))
      do 40 l=k2,nk1
        lmk = l-k1
        do 10 j=1,k1
          ik = j+k1
          lj = l+j
          lk = lj-k2
          h(j) = t(l)-t(lk)
          h(ik) = t(l)-t(lj)
   10   continue
        lp = lmk
```

```
      do 30 j=1,k2
        jk = j
        prod = h(j)
        do 20 i=1,k
          jk = jk+1
          prod = prod*h(jk)*fac
 20       continue
        lk = lp+k1
        b(lmk,j) = (t(lk)-t(lp))/prod
        lp = lp+1
 30     continue
 40   continue
      return
      end
      subroutine fpknot(x,m,t,n,fpint,nrdata,nrint,nest,istart)
c  subroutine fpknot locates an additional knot for a spline of degree
c  k and adjusts the corresponding parameters,i.e.
c    t     : the position of the knots.
c    n     : the number of knots.
c    nrint : the number of knotintervals.
c    fpint : the sum of squares of residual right hand sides
c            for each knot interval.
c    nrdata: the number of data points inside each knot interval.
c  istart indicates that the smallest data point at which the new knot
c  may be added is x(istart+1)
c  ..
c  ..scalar arguments..
      integer m,n,nrint,nest,istart
c  ..array arguments..
      real x(m),t(nest),fpint(nest)
      integer nrdata(nest)
c  ..local scalars..
      real an,am,fpmax
      integer ihalf,j,jbegin,jj,jk,jpoint,k,maxbeg,maxpt,
     * next,nrx,number
c  ..
      k = (n-nrint-1)/2
c  search for knot interval t(number+k) <= x <= t(number+k+1) where
c  fpint(number) is maximal on the condition that nrdata(number)
c  not equals zero.
      fpmax = 0.
      jbegin = istart
      do 20 j=1,nrint
        jpoint = nrdata(j)
        if(fpmax.ge.fpint(j) .or. jpoint.eq.0) go to 10
        fpmax = fpint(j)
        number = j
        maxpt = jpoint
        maxbeg = jbegin
 10     jbegin = jbegin+jpoint+1
 20   continue
c  let coincide the new knot t(number+k+1) with a data point x(nrx)
c  inside the old knot interval t(number+k) <= x <= t(number+k+1).
      ihalf = maxpt/2+1
      nrx = maxbeg+ihalf
```

```
      next = number+1
      if(next.gt.nrint) go to 40
c  adjust the different parameters.
      do 30 j=next,nrint
        jj = next+nrint-j
        fpint(jj+1) = fpint(jj)
        nrdata(jj+1) = nrdata(jj)
        jk = jj+k
        t(jk+1) = t(jk)
   30 continue
   40 nrdata(number) = ihalf-1
      nrdata(next) = maxpt-ihalf
      am = maxpt
      an = nrdata(number)
      fpint(number) = fpmax*an/am
      an = nrdata(next)
      fpint(next) = fpmax*an/am
      jk = next+k
      t(jk) = x(nrx)
      n = n+1
      nrint = nrint+1
      return
      end
      subroutine fpback(a,z,n,k,c,nest)
c  subroutine fpback calculates the solution of the system of
c  equations a*c = z with a a n x n upper triangular matrix
c  of bandwidth k.
c  ..
c  ..scalar arguments..
      integer n,k,nest
c  ..array arguments..
      real a(nest,k),z(n),c(n)
c  ..local scalars..
      real store
      integer i,i1,j,k1,l,m
c  ..
      k1 = k-1
      c(n) = z(n)/a(n,1)
      i = n-1
      if(i.eq.0) go to 30
      do 20 j=2,n
        store = z(i)
        i1 = k1
        if(j.le.k1) i1 = j-1
        m = i
        do 10 l=1,i1
          m = m+1
          store = store-c(m)*a(i,l+1)
   10   continue
        c(i) = store/a(i,1)
        i = i-1
   20 continue
   30 return
      end
      subroutine fprota(cos,sin,a,b)
```

```
c  subroutine fprota applies a givens rotation to a and b.
c  ..
c  ..scalar arguments..
      real cos,sin,a,b
c ..local scalars..
      real stor1,stor2
c  ..
      stor1 = a
      stor2 = b
      b = cos*stor2+sin*stor1
      a = cos*stor1-sin*stor2
      return
      end
      subroutine fpgivs(piv,ww,cos,sin)
c  subroutine fpgivs calculates the parameters of a givens
c  transformation .
c  ..
c  ..scalar arguments..
      real piv,ww,cos,sin
c  ..local scalars..
      real dd,one,store
c  ..function references..
      real abs,sqrt
c  ..
      one = 0.1e+01
      store = abs(piv)
      if(store.ge.ww) dd = store*sqrt(one+(ww/piv)**2)
      if(store.lt.ww) dd = ww*sqrt(one+(piv/ww)**2)
      cos = ww/dd
      sin = piv/dd
      ww = dd
      return
      end
      subroutine splev(t,n,c,k,x,y,m,ier)
c  subroutine splev evaluates in a number of points x(i),i=1,2,...,m
c  a spline s(x) of degree k, given in its b-spline representation.
c
c  calling sequence:
c     call splev(t,n,c,k,x,y,m,ier)
c
c  input parameters:
c    t   : array,length n, which contains the position of the knots.
c    n   : integer, giving the total number of knots of s(x).
c    c   : array,length n, which contains the b-spline coefficients.
c    k   : integer, giving the degree of s(x).
c    x   : array,length m, which contains the points where s(x) must
c          be evaluated.
c    m   : integer, giving the number of points where s(x) must be
c          evaluated.
c
c  output parameter:
c    y   : array,length m, giving the value of s(x) at the different
c          points.
c    ier : error flag
c      ier = 0 : normal return
```

```
c     ier =10 : invalid input data (see restrictions)
c
c  restrictions:
c   m >= 1
c   t(k+1) <= x(i) <= x(i+1) <= t(n-k) , i=1,2,...,m-1.
c
c  other subroutines required: fpbspl.
c
c  references :
c   de boor c  : on calculating with b-splines, j. approximation theory
c            6 (1972) 50-62.
c   cox m.g.   : the numerical evaluation of b-splines, j. inst. maths
c            applics 10 (1972) 134-149.
c   dierckx p. : curve and surface fitting with splines, monographs on
c            numerical analysis, oxford university press, 1993.
c
c  author :
c   p.dierckx
c   dept. computer science, k.u.leuven
c   celestijnenlaan 200a, b-3001 heverlee, belgium.
c   e-mail : Paul.Dierckx@cs.kuleuven.ac.be
c
c  latest update : march 1987
c
c  ..scalar arguments..
      integer n,k,m,ier
c  ..array arguments..
      real t(n),c(n),x(m),y(m)
c  ..local scalars..
      integer i,j,k1,l,ll,l1,nk1
      real arg,sp,tb,te
c  ..local array..
      real h(6)
c  ..
c  before starting computations a data check is made. if the input data
c  are invalid control is immediately repassed to the calling program.
      ier = 10
      if(m-1) 100,30,10
   10 do 20 i=2,m
        if(x(i).lt.x(i-1)) go to 100
   20 continue
   30 ier = 0
c  fetch tb and te, the boundaries of the approximation interval.
      k1 = k+1
      nk1 = n-k1
      tb = t(k1)
      te = t(nk1+1)
      l = k1
      l1 = l+1
c  main loop for the different points.
      do 80 i=1,m
c  fetch a new x-value arg.
        arg = x(i)
        if(arg.lt.tb) arg = tb
        if(arg.gt.te) arg = te
```

```
c  search for knot interval t(l) <= arg < t(l+1)
 40    if(arg.lt.t(l1) .or. l.eq.nk1) go to 50
       l = l1
       l1 = l+1
       go to 40
c  evaluate the non-zero b-splines at arg.
 50    call fpbspl(t,n,k,arg,l,h)
c  find the value of s(x) at x=arg.
       sp = 0.
       ll = l-k1
       do 60 j=1,k1
         ll = ll+1
         sp = sp+c(ll)*h(j)
 60    continue
       y(i) = sp
 80  continue
 100 return
     end
     subroutine fpbspl(t,n,k,x,l,h)
c  subroutine fpbspl evaluates the (k+1) non-zero b-splines of
c  degree k at t(l) <= x < t(l+1) using the stable recurrence
c  relation of de boor and cox.
c  ..
c  ..scalar arguments..
     real x
     integer n,k,l
c  ..array arguments..
     real t(n),h(6)
c  ..local scalars..
     real f,one
     integer i,j,li,lj
c  ..local arrays..
     real hh(5)
c  ..
     one = 0.1e+01
     h(1) = one
     do 20 j=1,k
       do 10 i=1,j
         hh(i) = h(i)
 10    continue
       h(1) = 0.
       do 20 i=1,j
         li = l+i
         lj = li-j
         f = hh(i)/(t(li)-t(lj))
         h(i) = h(i)+f*(t(li)-x)
         h(i+1) = f*(x-t(lj))
 20  continue
     return
     end
     subroutine fpchec(x,m,t,n,k,ier)
c  subroutine fpchec verifies the number and the position of the knots
c  t(j),j=1,2,...,n of a spline of degree k, in relation to the number
c  and the position of the data points x(i),i=1,2,...,m. if all of the
c  following conditions are fulfilled, the error parameter ier is set
```

```
c to zero. if one of the conditions is violated ier is set to ten.
c     1) k+1 <= n-k-1 <= m
c     2) t(1) <= t(2) <= ... <= t(k+1)
c        t(n-k) <= t(n-k+1) <= ... <= t(n)
c     3) t(k+1) < t(k+2) < ... < t(n-k)
c     4) t(k+1) <= x(i) <= t(n-k)
c     5) the conditions specified by schoenberg and whitney must hold
c        for at least one subset of data points, i.e. there must be a
c        subset of data points y(j) such that
c           t(j) < y(j) < t(j+k+1), j=1,2,...,n-k-1
c ..
c ..scalar arguments..
      integer m,n,k,ier
c ..array arguments..
      real x(m),t(n)
c ..local scalars..
      integer i,j,k1,k2,l,nk1,nk2,nk3
      real tj,tl
c ..
      k1 = k+1
      k2 = k1+1
      nk1 = n-k1
      nk2 = nk1+1
      ier = 10
c check condition no 1
      if(nk1.lt.k1 .or. nk1.gt.m) go to 80
c check condition no 2
      j = n
      do 20 i=1,k
        if(t(i).gt.t(i+1)) go to 80
        if(t(j).lt.t(j-1)) go to 80
        j = j-1
 20   continue
c check condition no 3
      do 30 i=k2,nk2
        if(t(i).le.t(i-1)) go to 80
 30   continue
c check condition no 4
      if(x(1).lt.t(k1) .or. x(m).gt.t(nk2)) go to 80
c check condition no 5
      if(x(1).ge.t(k2) .or. x(m).le.t(nk1)) go to 80
      i = 1
      l = k2
      nk3 = nk1-1
      if(nk3.lt.2) go to 70
      do 60 j=2,nk3
        tj = t(j)
        l = l+1
        tl = t(l)
 40     i = i+1
        if(i.ge.m) go to 80
        if(x(i).le.tj) go to 40
        if(x(i).ge.tl) go to 80
 60   continue
 70   ier = 0
```

```
80 return
   end
```

Input file for smooth.f - smooth.in

```
10
cums5ml200.nb.int
jnk05
0.05
jnk10
0.10
jnk15
0.15
jnk20
0.20
jnk25
0.25
jnk30
0.30
jnk35
0.35
jnk40
0.40
jnk45
0.45
jnk50
0.50
```

Appendix B

Gaussian Convolution Program and Input File

Program filter.f

```
c filter.f
c
c This program reads in XPD patterns and then convolutes them with a
c gaussian with a full width at half maximum = 2*bangle, where bangle
c the angular width over which the XPD data is smoothed. This program
c is essentially a 2D low-pass filter, and can be used for filtering
c noise out of experimental XPD patterns as well as for changing the
c broadening angle in theoretical XPD patterns. This program will read
c in XPD patterns in a (theta,phi,intensity) format where the step sizes
c in theta and phi do not need to be constant. However, the number of
c phi steps at each theta must be the same. For XPD patterns with variable
c phi step size, map.f must be used. map.f simply repeats the last point
c at each azimuthal scan, so that all azimuthal scans in the XPD pattern
c have the same number of phi steps. The program was modified
c so that the output is in a (theta,phi,intensity) format, but with a
c 2 degree step size in both theta and phi. This modification allows
c individual polar cuts to be taken from XPD patterns. Another modification
c has been to replace the sigma smoothing factor input with the less abstract
c bangle. That is, we can now input a smoothing factor in terms of the
c angle over which we would like the data to be smoothed. sigma is then
c calculated from this bangle. sigma = (k/0.8344)*sin(bangle).
c
c jul 95,  p. len (wrote original program)
c aug 95,  p. len (corrections)
c apr 96   s. ruebush (modified for 2x2 deg. output in theta and phi)
c mar 97,  s. ruebush (modified for bangle input)
c
c initialization and parameterization
      real theta(43,183), phi(43,183), xK(11,43,183)
      real rtheta(43,183), rphi(43,183)
      real kx(11,43,183), ky(11,43,183), kz(11,43,183)
      real kx1(11,43,183), ky1(11,43,183), kz1(11,43,183)
      real k(11), k0, kkx, kky, kkz
      integer ntheta, nphi
      character*40 rawxK, lopassxK
cccc  character*40 rawxK, hipassxK, lopassxK
      parameter(pi = 3.141592654)
      parameter(degtorad = pi/180.0)
      real ctheta(43,183)
      real crtheta(43,183)
c
c read in reconstruction integration parameters
      open(unit = 10, file = 'filter.in')
       read(10,10) rawxK
       read(10,*) ntheta
       read(10,*) nphi
       read(10,*) k0
```

```
          read(10,*) dk
          read(10,*) nk
cccc      read(10,10) hipassxK
          read(10,10) lopassxK
          read(10,*) bangle
cccc      read(10,*) symmetry
         close(10)
10       format(a40)
c
c calculate sigma
         sigma = (k0/0.8344)*sin(bangle)
c
c initialize k
     do 90 ik = 1, nk
       k(ik) = k0 + (ik-1)*dk
90     continue
c
c main read-in routine
         open(unit = 20, file = rawxK)
         do 100 ik = 1, nk
          do 101 itheta = 1, ntheta
           do 102 iphi = 1, nphi
            read (20,*) theta(itheta,iphi), phi(itheta,iphi),
  &                          xK(ik,itheta,iphi)
102         continue
101        continue
100      continue
         close(20)
c
c calculation of cos and sin functions.  All input angles are
c now converted to radians.
c
     do 200 itheta = 1, ntheta
      do 201 iphi = 1, nphi
       ctheta(itheta,iphi) = cos(theta(itheta,iphi)*degtorad)
           stheta = sin(theta(itheta,iphi)*degtorad)
           cphi = cos(phi(itheta,iphi)*degtorad)
           sphi = sin(phi(itheta,iphi)*degtorad)
           do 202 ik = 1, nk
            kx(ik,itheta,iphi) = k(ik)*ctheta(itheta,iphi)*cphi
            ky(ik,itheta,iphi) = k(ik)*ctheta(itheta,iphi)*sphi
            kz(ik,itheta,iphi) = k(ik)*stheta
202        continue
201       continue
200      continue
c
c calculation of cos and sin functions at 2deg. x 2 deg. increments in
c theta and phi.  This is the modification made for 2x2 output.  All
c input angles are now converted to radians.
c
     do 210 ktheta = 1,43
      do 211 kphi = 1,180
       rtheta(ktheta,kphi) = ktheta*2.0 + 4.0
       rphi(ktheta,kphi) = kphi*2
       crtheta(ktheta,kphi) = cos(rtheta(ktheta,kphi)*degtorad)
```

```
            srtheta = sin(rtheta(ktheta,kphi)*degtorad)
            crphi = cos(rphi(ktheta,kphi)*degtorad)
            srphi = sin(rphi(ktheta,kphi)*degtorad)
            do 212 kk = 1, nk
              kx1(kk,ktheta,kphi) = k(kk)*crtheta(ktheta,kphi)*crphi
              ky1(kk,ktheta,kphi) = k(kk)*crtheta(ktheta,kphi)*srphi
              kz1(kk,ktheta,kphi) = k(kk)*srtheta
212         continue
211       continue
210     continue
c
c  loop over each direction in x(K)
        open (unit = 30, file = lopassxK)
cccc    open (unit = 31, file = hipassxK)
        do 300 kk = 1, nk
          do 301 ktheta = 1, 43
cccc        do 302 kphi = 1, symmetry
            do 302 kphi = 1, 180
              xKlo = 0.0
              A = 0.0
c  integrate over all K' directions in x(K')
              do 303 jk = 1, nk
                do 304 jtheta = 1, ntheta
                      do 305 jphi = 1, nphi
c  find the Gaussian weighing function
                    kkx = (kx1(kk,ktheta,kphi) - kx(jk,jtheta,jphi))
                    kky = (ky1(kk,ktheta,kphi) - ky(jk,jtheta,jphi))
                    kkz = (kz1(kk,ktheta,kphi) - kz(jk,jtheta,jphi))
                    deltak2 = kkx*kkx + kky*kky + kkz*kkz
                        egauss = exp(-deltak2/(sigma*sigma))
                    xKlo = xKlo +
   &                     xK(jk,jtheta,jphi)*egauss*crtheta(jtheta,jphi)
                    A = A + egauss*crtheta(jtheta,jphi)
305                   continue
304               continue
303             continue
                xKlo = xKlo/A
cccc            xKhi = xK(kk,ktheta,kphi) - xKlo
        if(rphi(ktheta,kphi) .ge. 360.0)then
              rphi(ktheta,kphi) = rphi(ktheta,kphi) - 360.0
        endif
                write(30,3000) rtheta(ktheta,kphi), rphi(ktheta,kphi), xKlo
cccc            write(31,3000) rtheta(ktheta,kphi), rphi(ktheta,kphi), xKhi
302           continue
301         continue
300       continue
3000      format(2f6.1,2x,e14.7)
c
          stop
          end
```

Input file for filter.f - filter.in

```
gauss.map        !name of input XPD file
39               !number of thetas in XPD file
180              !number of phis at each theta (must be same for all theta)
9.18        !k0 = 0.5124*sqrt[E0(eV)], initial k value.
0.0        !dk = delta k, step size in k. 0 for single energy.
1                !nk = number of k. 1 for single energy.
gauss.lp  !output low-pass filtered XPD file.
3.0              !bangle = HWHM of gaussian in degrees.
```

Program map.f - used for preparing the input XPD file for filtering in filter.f

```
c*********************************************************************
c  This program prepares exptl. or thyl. data for filtering via filter.f
c*********************************************************************

      real calthe(93,363), calphi(93,363),
     &     chi1(93,363), the(32400),phi(32400),
     &     dphi(95)
      integer nphi(365)
      character*20 fname2, fname3
c      write (*,*) 'Input file:'
c      read (*,*) fname2
c      write (*,*) 'Output file:'
c      read (*,*) fname3
c
      mm = 32403
      pi = 3.141592654
      rapi = pi/180.0
c
c     ** Finding the number of different theta values **
c
      nthe = 0
      open (unit = 4, file = 'map.in')
      do 120 i = 1, mm
      read (4,*,end=999) the(i), phi(i), xxx
      if (i .gt. 1) then
        diff = the(i) - the(i-1)
        if (diff .ge. 0.10) then
          nthe = nthe+1
         endif
      endif
 120  continue
 999  close (4)
      nthe = nthe+1
      write(*,*) 'nthe=', nthe
c
c     ** reading the data and assigning each datum a place
c     in the i,j matrix **
c
      open (unit = 4, file = 'map.in')
      read (4,*) calthe(1,1), calphi(1,1), chi1(1,1)
      do 121 i = 1, nthe
      nphi(i) = 1
      dphi(i) = 0
      do 125 j = 2, 365
      read (4,*,end=998) calthe(i,j), calphi(i,j), chi1(i,j)
      if (j .gt. 1) then
        diff = calphi(i,j) - calphi(i,j-1)
        nphi(i)= nphi(i)+1
        dphi(i) = dphi(i) + diff
        if (diff .lt. 0.0) then
          nphi(i) = nphi(i) - 1
          dphi(i) = dphi(i)-diff
```

```
          calthe (i+1,1) = calthe(i,j)
          calphi(i+1,1) = calphi(i,j)
          chi1(i+1,1) = chi1(i,j)
         if (nphi(i) .eq. 1) then
         dphi(i) = 0.0
         else
          dphi(i) = dphi(i)/(nphi(i)-1)
         endif
          go to 121
        endif
      endif
 125  continue
 121  continue
 998  dphi(i) = calphi(i,2)-calphi(i,1)
      close (4)
      write(*,*) 'nphi(1)=',nphi(1)
c
        open (unit =7, file = 'map.out')
c
c     ** writing the mapped data **
c
      do 202 i = 1, nthe
      do 201 j = 1, nphi(1)
      if(i .gt. 1)then
       if(j .gt. nphi(i))then
       calthe(i,j) = calthe(i,nphi(i))
       calphi(i,j) = calphi(i,nphi(i))
       chi1(i,j) = chi1(i,nphi(i))
       endif
      endif
 201  continue
 202  continue
c
      do 222 i = 1, nthe
      do 220 j = 1,nphi(1)
      write(7,240) calthe(i,j),calphi(i,j),chi1(i,j)
 240  format (2x,f5.2,2x,f6.2,2x,e12.5)
 220  continue
 222  continue
      close (7)
      end
```

Ernest Orlando Lawrence Berkeley National Laboratory
One Cyclotron Road | Berkeley, California 94720

Prepared for the U.S. Department of Energy under Contract No. DE-AC03-76SF00098